Nano-meter 3D characterization of an aluminum alloy designed for laser-based 3D-Printing

Von der Fakultät für Georessourcen und Materialtechnik der
Rheinisch-Westfälische Technische Hochschule Aachen

zur Erlangung des akademischen Grades eines

Doktors der Ingenieurwissenschaften

genehmigte Dissertation

vorgelegt von

Deepak Mani, M.Sc.

Berichtende: Univ.-Prof. Dr. techn. Guillermo Carlos Requena
Univ.-Prof. Dr.-Ing. habil. Brita Daniela Zander

Tag der mündlichen Prüfung: 25.09.2025

Abstract

Laser powder bed fusion enables exceptional design flexibility in metal additive manufacturing. However, a detailed microstructural analysis is crucial to fully understand its material performance and overcome challenges in process optimization. This thesis investigates the microstructural properties of the Al-1Fe-1Zr alloy (Constellium Aheadd® CP1) specifically tailored to the physical conditions of LPBF. The rapid solidification conditions inherent to LPBF promote the formation of metastable intermetallic particles, requiring high-resolution synchrotron-based 3D imaging for precise characterization. LPBF processing parameters significantly influence melt pool morphology, grain growth, and intermetallic formation. This work leverages nanoscale imaging at the ID16A Nano Imaging beamline of the ESRF to elucidate the spatial distribution of Fe- and Zr-rich intermetallics under different LPBF processing conditions and evolution during heat treatment. Investigations of prior melt pools show that a stable melt pool with a good width-to-depth ratio promotes well-defined columnar grain growth under moderate scan speeds with continuous wave laser mode, whereas increased scan speeds result in shallower melt pools. Pulsed wave modulation laser mode with higher energy density leads to deeper melt pools, disrupting columnar grain growth and increasing grain boundary density. HXCT and FXCT imaging demonstrate that Fe-rich intermetallics accumulate at grain boundaries, forming stable $Al_{13}Fe_4$. In contrast, Zr predominantly remains either trapped within the Al matrix or present as nanoscale $L1_2$-Al_3Zr precipitates dispersed within the matrix. Quantitative analysis after heat treatment at 400°C/4h confirms a uniform background level of Fe (0.56 wt%) and Zr (0.96 wt%) concentrations. Meanwhile, overaging at 530°C/24h promotes intermetallic coarsening driven by Oswald ripening. Fe-rich intermetallics transform, with Al_6Fe evolving into stable globular $Al_{13}Fe_4$ at grain boundaries and possibly transforming to Al_3Fe within larger grains adopting rod-like morphology, while Zr remains in its nanoscale form, with partial transformation to the stable $D0_{23}$-Al_3Zr at the grain boundaries and smaller spherical particles of the stable phase within the grains. First of its kind, high resolution FXCT quantification reveals that nano Zr-rich particles form 0.95% volume fraction (0.5wt%), while Fe-rich nanoparticles account for 0.03% (0.008wt%), suggesting that nearly half of Zr and only a fraction of Fe, are at this scale after overaging. This study establishes the capability of synchrotron 3D imaging to elucidate the nanoscale intermetallics and quantitative local elemental distributions. By refining high-resolution imaging techniques, this research contributes to the broader applications of advanced materials and additive manufacturing strategies.

Kurzfassung

Das Laser-Pulverbett-Schmelzen (Laser Powder Bed Fusion, LPBF) ermöglicht eine außergewöhnliche Gestaltungsfreiheit in der metallischen additiven Fertigung. Eine detaillierte mikrostrukturelle Analyse ist jedoch entscheidend, um das Werkstoffverhalten vollständig zu verstehen und Herausforderungen bei der Prozessoptimierung zu überwinden. Diese Arbeit untersucht die mikrostrukturellen Eigenschaften der speziell für die physikalischen Bedingungen des LPBF angepassten Al-1Fe-1Zr-Legierung (Constellium Aheadd® CP1). Die für das LPBF typischen raschen Erstarrungsbedingungen begünstigen die Bildung metastabiler und stabiler intermetallischer Phasen, deren präzise Charakterisierung eine hochauflösende, synchrotronbasierte 3D-Bildgebung erfordert. Die LPBF-Prozessparameter beeinflussen maßgeblich die Schmelzbadmorphologie, das Kornwachstum und die Bildung intermetallischer Phasen. Diese Arbeit nutzt fortschrittliche Bildgebung im Nanomaßstab an der ID16A Nano Imaging Beamline der ESRF, um die räumliche Verteilung von Fe- und Zr-reichen Intermetallverbindungen unter verschiedenen LPBF-Prozessbedingungen sowie deren Entwicklung während der Wärmebehandlung zu untersuchen. Die Analyse früherer Schmelzbäder zeigt, dass ein stabiles Schmelzbad mit einem günstigen Breiten-Tiefen-Verhältnis unter moderaten Scangeschwindigkeiten im kontinuierlichen Lasermodus ein gut definiertes säulenartiges Kornwachstum fördert, während erhöhte Scangeschwindigkeiten zu flacheren Schmelzbädern führen. Der gepulste Lasermodus mit höherer Energiedichte erzeugt tiefere Schmelzbäder, stört das säulenartige Kornwachstum und erhöht die Korngrenzendichte. HXCT- und FXCT-Bildgebung zeigen, dass sich Fe-reiche Intermetallverbindungen bevorzugt an Korngrenzen ansammeln und dort stabile $Al_{13}Fe_4$-Phasen bilden, während Zr überwiegend als nanoskalige $L1_2$-Al_3Zr-Präzipitate innerhalb der Matrix vorliegt. Eine quantitative Analyse nach der Wärmebehandlung bei 400 °C für 4 h bestätigt ein homogenes Hintergrundniveau von Fe (0,56 Gew. %) und Zr (0,96 Gew. %). Eine Überalterung bei 530 °C für 24 h fördert eine Vergröberung der Intermetallphasen, getrieben durch Ostwald-Reifung. Fe-reiche Intermetallphasen transformieren dabei, wobei Al_6Fe sich in stabiles, globuläres $Al_{13}Fe_4$ an Korngrenzen umwandelt und möglicherweise innerhalb größerer Körner in die stabilere Phase Al_3Fe mit stabförmiger Morphologie übergeht. Zr verbleibt überwiegend in nanoskaliger Form, zeigt jedoch teilweise eine Umwandlung zur stabilen $D0_{23}$-Al_3Zr-Phase an Korngrenzen sowie in Form kleiner sphärischer Partikel innerhalb der Körner. Die FXCT-Quantifizierung zeigt, dass nanoskalige Zr-reiche Partikel einen Volumenanteil von 0,95 % (0,5 Gew. %) bilden, während Fe-reiche Nanopartikel 0,03 % (0,008 Gew. %) ausmachen. Dies deutet darauf hin,

dass nach der Überalterung nahezu die Hälfte des Zr und nur ein kleiner Anteil des Fe in dieser Skala vorliegt.

Diese Studie zeigt das Potenzial der synchrotronbasierten 3D-Bildgebung zur Aufklärung nanoskaliger Intermetallphasen und lokaler quantitativer Elementverteilungen. Durch die Weiterentwicklung hochauflösender Bildgebungstechniken leistet diese Forschung einen Beitrag zu den breit gefächerten Anwendungen fortschrittlicher Werkstoffe und Strategien der additiven Fertigung.

Acknowledgment

This thesis marks the culmination of an extraordinary chapter in my academic and personal journey. It has been shaped by the guidance, encouragement, and generosity of many remarkable individuals, to whom I owe my deepest gratitude.

First and foremost, I would like to extend my sincerest thanks to Dr. Peter Cloetens. From the very beginning, Dr. Cloetens has provided not only expert scientific supervision but also personal support that went far beyond expectations. His guidance was instrumental in every stage of my development. What stands out most is the time he invested in my growth, he was always approachable, patient, and generous with his advice. I am truly honoured to have worked under his leadership.

I am grateful to Dr. Dmitry Karpov, who not only served as scientific advisor but also a trusted friend throughout my PhD. His insightful feedback and willingness to engage in deep discussions helped me navigate many scientific challenges. Every conversation with him was an opportunity to learn, reflect, and see problems from a new angle. His enthusiasm for science and his clarity in explaining complex phenomena made a significant impact on my work.

My heartfelt thanks also go to Dr. Federico Monaco, who provided valuable support and guidance during the early stages of my PhD. His expertise and mentorship helped me build a strong foundation and gave me confidence as I took my first steps in this research.

I would like to thank all the members of the ID16A Nano-Imaging Beamline team at the ESRF. I am truly grateful for the countless scientific and informal conversations we shared, which enriched my experience and made my time at ESRF all the more special. It was a privilege to work in such an inspiring, collaborative, and friendly environment.

I would also like to extend my sincere appreciation to Dr. Bechir Chehab and Dr. Ravi Shahani from Constellium, for their outstanding industrial collaboration and ongoing support. Their openness, scientific insight, and constant willingness to engage in discussions added immense value to my research. They ensured I remained informed and actively involved in the industrial aspects of the project throughout, bridging the gap between academic inquiry and practical application.

To my collaborators at the German Aerospace Center (DLR), I offer my warmest thanks. I am especially grateful to Dr. Katrin Bugelnig for her continuous support during my PhD and during my secondment at DLR. Her assistance at international conferences, and her help with logistics

and scientific coordination during my stay, were invaluable. I also wish to thank Dr. Klemens Klem, Mr. Frédéric Kreps, and Mr. Alexander Francke for their time, expertise, and contributions to the metallography work and sample preparation processes essential to this research.

My most sincere and profound gratitude goes to Prof. Dr. Guillermo Requena, the Principal Investigator of this project and my academic supervisor. His role in the success of this thesis cannot be overstated. Prof. Requena provided not only the vision and structure behind the research project, but also unwavering encouragement and critical feedback that pushed me to grow both scientifically and professionally. His strategic insight, passion for materials science, and continued faith in my potential have been cornerstones of my academic journey. I am especially grateful for the opportunity to carry out my doctoral research under his supervision. This work, and the broader scope of the project, would not have been possible without his initiative and guidance. For all this and more, I am deeply indebted to him.

I would also like to express my sincere appreciation to the InnovaXN doctoral program for providing the framework, funding, and collaborative environment that made this research possible. Being part of a program that bridges large-scale research infrastructures with industrial partners was an invaluable experience that significantly shaped my academic and professional development.

Finally, and most importantly, I wish to thank my beloved parents, Mr. Mani and Mrs. Manjula, whose love, sacrifice, and steadfast support have made all of this possible. Their constant encouragement, wisdom, and belief in me provided the emotional strength to persevere through every challenge. They are the reason I have the strength and ability to pursue such goals, and their words of advice and encouragement have always been my greatest source of comfort. They are my inspiration, my motivation, and my greatest blessing.

To all those who contributed to this journey—whether through mentorship, collaboration, or quiet support—I offer my heartfelt thanks.

List of Content

List of abbreviations

ACOM - Automated Crystal Orientation Mapping

AM - Additive Manufacturing

AP – Alternating Projection

BF – Bright Field

BSE – Backscattered Electrons

CAD – Computer Aided Design

CALPHAD - Computer Coupling of Phase Diagrams and Thermochemistry

CGM – Conjugate Gradient Method

CT- Computed Tomography

CW – Continuous Wave

CZ – Columnar Zone

DM – Difference Map

EBM – Electron Beam Melting

EBSD – Electron Backscatter Diffraction

FBP – Filtered Back Projection

FCC – Face Centred Cubic

FEZ – Fine Equiaxed Zone

FIB – Focused Ion Beam

FOV – Field of View

FSC – Fourier Shell Correlation

FXCT – X-Ray Fluorescence Computed Tomography

HXCT – Holographic X-Ray Computed Tomography

IPF – Inverse Pole Figure

KB – Kirkpatrick-Baez

LPBF – Laser Powder Bed Fusion

MLEM – Maximum Likelihood Expectation Maximization

MPB – Melt Pool Boundaries

NFPXCT – Near-Field Ptychographic X-Ray Computed Tomography

PFZ – Precipitate Free Zone

PWM – Pulse Width Modulation

SEM – Scanning Electron Microscopy

SNR – Signal to Noise Ratio

SR – Stress Relieved

STEM – Scanning Transmission Electron Microscope

TEM – Transmission Electron Microscopy

XRF - X-Ray Fluorescence

List of Figures

List of tables

1 Introduction

As global demands for lightweight, high-strength, and sustainable materials continue to rise - driven by sectors such as aerospace, automotive, energy, and consumer electronics - there is an increasing interest in advanced materials and manufacturing processes capable of meeting these requirements. The increasing demand for advanced design strategies that incorporate complex geometries tailored to specific applications, coupled with the necessity for improved performance across diverse industries, highlights the pivotal role of innovations in materials science and cutting-edge manufacturing technologies. Metal additive manufacturing (AM) technologies have revolutionized industrial production by enabling the fabrication of intricate metallic components that are challenging or inefficient to produce using traditional manufacturing methods. Unlike conventional techniques, which often involve multiple processing steps such as machining, joining, or casting, AM consolidates these processes into a single operation, thereby streamlining production. Among the various AM techniques, Laser Powder Bed Fusion (LPBF) stands out for its ability to create components with complex geometries and exceptional precision. Despite these advancements, significant challenges remain before metal AM can fully transition from a niche technology to a mainstream manufacturing approach. Critical issues such as process optimization, material performance, scalability, and cost-effectiveness need to be addressed to unlock its full potential and establish its viability as a major manufacturing technique.

Aluminium alloys are essential to sectors like aerospace due to their exceptional strength-to-weight ratio and resistance to corrosion. In this research, an Al-1Fe-1Zr alloy (Constellium alloy, Aheadd® CP1) specifically designed for the processing conditions of LPBF is investigated. Due to the complex thermal conditions during LPBF, distinct microstructures are formed that directly impact the material properties. 2D analyses, such as electron or optical microscopy, that are routinely used for analyses fail to provide the full 3D spatial complexity of the alloy's microstructures. Thus, advanced characterization techniques beyond traditional 2D analyses are required to understand these microstructures comprehensively. This research focuses on the high-resolution, 3D characterization of the microstructures in the Al-1Fe-1Zr alloy, utilizing the advanced capabilities of the ID16A Nano Imaging beamline at the European Synchrotron Radiation Facility (ESRF). The ID16A beamline, renowned for its state-of-the-art X-ray nano-imaging technology, enables precise visualization and quantification of features at the nanoscale, within the alloy matrix. By utilizing these advanced techniques, this study aims

to address critical gaps in the understanding of the microstructures formed during the LPBF. This knowledge is essential for correlating microstructural features with alloy performance and for developing strategies to tailor material properties. Furthermore, this work transcends the limitations of conventional 2D analytical approaches, contributing to a deeper understanding of LPBF-processed alloys and advancing the design of materials optimized for additive manufacturing.

This thesis presents an in-depth study of the spatial distribution, morphology, and chemical composition of microstructural features in the Al-1Fe-1Zr alloy, with a primary focus on understanding the influence of Laser Powder Bed Fusion (LPBF) process parameters on microstructure formation. Leveraging advanced non-destructive 3D X-ray characterization techniques, the analysis enables repeated investigations on the same sample before and after heat treatments, facilitating a thorough evaluation of microstructural evolution induced by annealing. By examining variations in microstructural characteristics within prior melt pools and their evolution under different heat treatments, this work seeks to provide a detailed understanding of the alloy's phase stability and distribution of intermetallic phases.

These insights address critical gaps in understanding the interplay between LPBF parameters and the resultant microstructures, further advancing the scientific basis for alloy design and processing optimization. Beyond the primary materials analysis, this thesis places a significant emphasis on optimizing experimental methodologies and beamline parameters for high-resolution imaging in additive manufacturing research. The objective is to refine synchrotron-based techniques to achieve superior data quality, reduced acquisition times, and cost-efficiency, thereby enhancing their applicability to real-world investigations. These improvements not only benefit ongoing research but also extend the suitability of these methods to a broader range of metallic systems and experimental conditions.

The outcomes of this study hold profound implications for both academic and industrial research, particularly within the scope of the InnovaXN doctoral program, which bridges large-scale research infrastructure with industrial R&D needs. By addressing key challenges in materials characterization and experimental efficiency, this work contributes to establishing robust methodologies that support the development of advanced materials and innovative manufacturing technologies for diverse applications.

2 Motivation

AM metal technologies are having a profound impact on industrial manufacturing, presenting significant opportunities, especially gaining traction in high-technology sectors, even though they currently represent only a small fraction of global metal production [1]. In aerospace applications, for example, approximately 10 - 15% of certain components, such as turbine blades and fuel nozzles, are now produced via AM [2–4]. LPBF has emerged as a transformative technology for producing metallic components with very high precision in the fabrication of complex geometries. In essence, LPBF operates by local melting of layers of metal powder using a high-energy laser, which subsequently solidifies to form the component. LPBF involves rapid heating and cooling cycles, leading to complex thermal histories and solidification dynamics. These conditions lead to the formation of distinctive microstructural features and elemental distributions.

Al alloys are crucial in the aerospace industry due to their high strength-to-weight ratio and excellent corrosion resistance. However, Al alloys commonly used in LPBF are often adapted from conventional manufacturing processes and typically require extensive post-processing to achieve the desired performance characteristics. In principle, parts manufactured through AM should be ready for immediate use and produced as needed, thereby minimizing the necessity for complex post-processing procedures. Such procedures often include machining to achieve final dimensional accuracy, heat treatments, etc., to optimize microstructural properties, and surface finishing to improve fatigue life or corrosion resistance. In response to these challenges, the Al-1Fe-1Zr alloy investigated here has been specifically tailored to the physical conditions of LPBF, thereby reducing the need for extensive post-processing. The objective of this research is to examine the microstructures of the Al-1Fe-1Zr alloy, thereby to bridge rigorous academic approaches with pressing industrial questions to address the existing knowledge gap of elucidating microstructure-property relationships.

Although 2D microstructural analyses such as electron or optical microscopy, etc., offer valuable information on the microstructures of the alloy, they are inherently limited by their inability to capture the full spatial complexity. Consequently, in-depth investigations into the fundamental aspects of microstructural architecture demand 3D nanoscale characterization to accurately capture these intricate features. Synchrotron-based techniques offer unparalleled spatial resolution and sensitivity for thoroughly examining such complex microstructures. However, practical constraints including limited beamtime availability and lengthy acquisition

periods, pose significant challenges. As a result, optimizing these characterization methodologies becomes essential, ensuring that maximum information is gleaned from each experiment while maintaining feasibility for both academic research and industrial applications. In this study, the following methodological issues are addressed:

- *What are the capabilities of the different 3D Synchrotron-Based X-ray Imaging Techniques available at the ID16A Nano-Imaging beamline of the ESRF, and how can they be optimally applied to characterize the Al-1Fe-1Zr alloy?*
- *What methodological optimizations and parameter modifications were introduced to the experimental setup to enable a comprehensive 3D characterization of the microstructures?*

While these investigations provide important insights into the internal architecture of this alloy, several aspects need to be addressed, exploring the impact of additive manufacturing process parameters on microstructural features. As usual for LPBF production, the initial step is to optimize and validate the manufacturing parameters to achieve the highest possible material density. Indeed, the optimization of manufacturing parameters should not only aim for defect-free conditions but also consider the attainability of microstructures that are stable during service conditions. In this sense, heat treatment can be a critical step in additive manufacturing, aimed at tailoring the microstructure of alloys to enhance their performance. The non-destructive nature of the 3D characterization techniques used in this work allows us to study the same sample before and after heat treatment. Therefore, in terms of microstructural evolution, the following issues are considered:

- *How does the variation of LPBF processing parameters influence microstructural formation?*
- *How do microstructural constituents, their architecture, and chemistry vary within a prior melt pool?*
- *How do heat treatments affect element distribution within a prior melt pool?*
- *How do different heat treatments influence the microstructural evolution of the Al-1Fe-1Zr alloy manufactured via LPBF?*
- *Is it possible to image and quantify nano-sized precipitates present in Al-1Fe-1Zr?*

Thus, the present work aims to bridge the knowledge gap regarding how processing parameters and heat treatments affect the spatial distribution and morphology of microstructural features in the Al-1Fe-1Zr alloy by employing advanced 3D characterization methods.

3 State of the Art

3.1 Additive Manufacturing

Additive manufacturing, also known as 3D printing, is revolutionizing production methods in various industries, such as medical, aerospace, transportation, and energy [5–7]. Originally developed for rapid prototyping of non-structural components [8], AM has since advanced significantly. The modern field of metal AM enables the creation of complex structural shapes that are challenging or impossible to produce using traditional methods. While it is necessary to address metallurgical issues such as mechanical anisotropy, residual stress, and unique defects, the potential of this technology to revolutionize manufacturing is clear. AM involves the layer-by-layer deposition of material to construct a three-dimensional object from a digital model. This method allows for the direct manufacture of intricate and custom components from CAD models, eliminating the need for costly machining and reducing the number of traditional machining steps. As a result, manufacturing processes are streamlined, decreasing the need to assemble multiple components. AM presents a range of notable advantages when compared to traditional manufacturing techniques, including economic efficiency, heightened productivity, improved quality, innovative design capabilities, and optimized supply chain management [5]. In the last two decades, there have been notable advances in metal AM processes, which include the development of reliable industrial lasers, high-performance computing hardware and software, and metal powder feedstock technology. These developments have contributed to the growing acceptance of AM, with commercial systems undergoing a period of rapid expansion [9]. Despite this progress, a comprehensive understanding of feedstock materials, processes, structures, properties, and performance is essential for producing defect-free, structurally robust, and reliable AM components.

The evolution of AM, particularly for metallic materials, is driven by increasing research and development. Although the existing knowledge base from metal powder technology, high-energy beam welding, cladding, and prototyping provides a foundation, many aspects of AM still require further exploration. The rapidly evolving AM field necessitates periodic evaluations to bridge gaps in scientific knowledge and identify research needs. The primary challenge in AM is a thorough understanding of the relationship between processing parameters and the resulting properties of the final parts and the materials used. This challenge is particularly pronounced for metallic parts due to the complex thermal histories involved in the AM process, which can lead to significant property variability [10]. There are metallurgical

differences between AM parts and those produced through conventional methods, such as residual stresses [11], anisotropy [12], and defects [13]. Addressing these unique characteristics is essential to meet the high-performance requirements of applications, e.g., where components are exposed to high temperature fatigue. Powder bed-based methods like LPBF, electron beam melting (EBM), and directed energy deposition (DED) are commonly used to manufacture dense metallic parts [14]. These processes involve fed powder interacting with a laser or electron beam, creating a melt pool that rapidly melts the material.

In this study, only LPBF will be considered, as the Al-1Fe-1Zr alloy examined here is specifically designed for this additive manufacturing process.

3.1.1 Laser Powder Bed Fusion Additive Manufacturing Technique

LPBF is a highly complex and precise AM technique. The process begins with setting up a powder bed. A uniform layer of metallic powder is deposited across the build platform. The quality of the powder bed is crucial as it directly affects the consistency and properties of the final product [15]. The key characteristics of the powder, such as heat conduction, flowability, packing density, internal porosity, and particle size and shape, all play crucial roles in determining the final properties of the component. It is important to note that dense and defect-free layers require both high packing density and a uniform distribution of particles [15]. Once the powder bed is prepared, a high-powered laser scans the selected area, melting the powder according to a digital design provided by CAD software. The laser's power, wavelength, spot size, pulse duration, and pulse frequency are crucial parameters that determine the energy input into the powder [16–18]. For example, increased laser power can enhance melting depth and layer adhesion, but excessive power may cause vaporization and flaws. Similarly, the laser wavelength must match the material's absorption characteristics to ensure efficient melting [19]. The spot size of the laser beam influences the resolution and detail of the printed part; smaller spot sizes yield finer details but may increase the build time [20]. In the context of metal AM, a keyhole refers to a deep, narrow melt cavity that forms when the laser energy input is high enough to partially vaporize the molten metal. This vaporization creates recoil pressure, which pushes the liquid metal away from the laser focal point, producing a distinct, elongated "keyhole" shape in cross-section. While keyhole mode

welding can improve fusion depth and powder consolidation, it also raises the risk of pore formation and other defects if process parameters are not carefully controlled.

In the LPBF process, the laser beam fuses the powder to the underlying solid material through complete melting. After each laser melting step, the powder bed is lowered by a precise thickness, and a new layer of powder is spread over the previous one by a recoater. Schematics of the LPBF process are shown in Fig. 3.1. Although the layer thickness is typically a few tens of micrometers, the heat from the laser can penetrate several layers below, causing the already solidified layers to be reheated and sometimes remolten, which affects the microstructure [21]. The scanning speed and strategy are also pivotal in the LPBF process. Scanning speed determines the rate at which the laser moves across the powder bed, influencing the energy deposition and melting quality [22]. Faster speeds can lead to insufficient melting and increased porosity, while slower speeds provide more energy, promoting better fusion but potentially causing overheating and thermal stresses. The scanning strategy, which includes the pattern and sequence of laser scans, affects thermal gradients and stress distribution within the part.

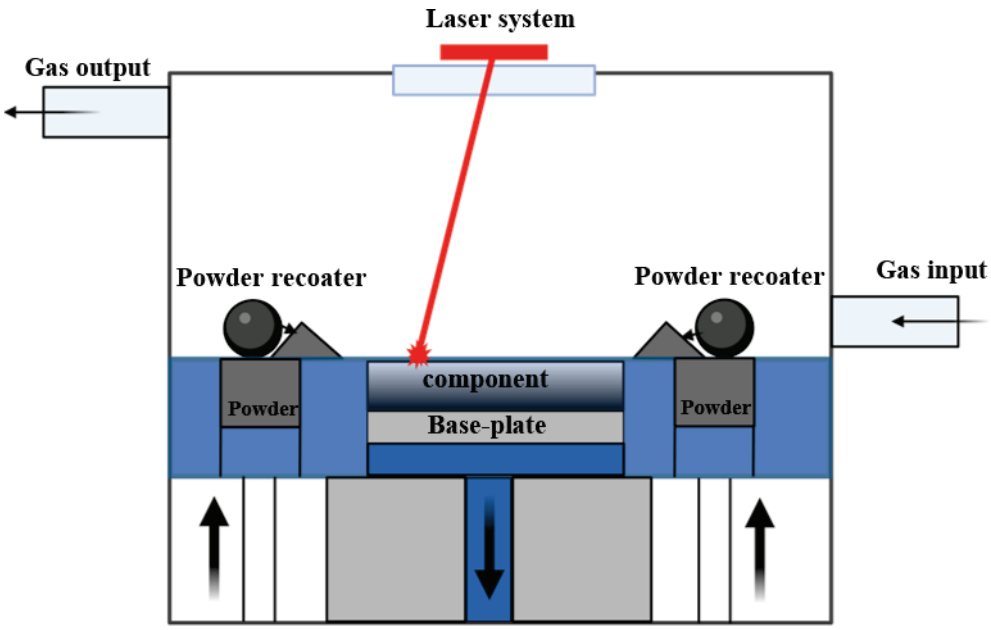

Fig. 3.1 Schematic representation of the LPBF process.

It is crucial to manage the temperature during the LPBF process. Controlling the powder bed temperature is important to avoid oxidation and uphold uniform thermal conditions. Preheating the powder bed can reduce thermal gradients, minimizing residual stresses and warping [23]. Ensuring an even temperature distribution throughout the powder bed is crucial to prevent

localized defects like warping, cracking, or incomplete melting. Consistently maintaining the optimal temperature of the powder feeder is crucial for ensuring a reliable and stable powder flow throughout the entire build process. The complex thermal cycles inherent in the LPBF process result in significant variability in the properties of the final parts, particularly for metallic components [24]. The variability in question stems from the rapid melting and solidification of the powder, potentially leading to residual stresses, anisotropy, and unique defects that are not typically encountered in conventionally manufactured parts. Addressing these issues is imperative to meeting the stringent performance requirements of critical applications such as aerospace components.

The advancement of reliable industrial lasers, high-performance computing hardware and software, and metal powder feedstock technology has been a significant driving force behind the developments in LPBF technology. Nevertheless, a comprehensive grasp of the interdependencies between processing parameters, material characteristics, and the resulting microstructure remains vital for optimizing LPBF processes and producing consistent, high-quality components.

3.1.2 Laser Powder Bed Fusion of Aluminium alloys

Aluminum alloys are indispensable in sectors such as aerospace, automotive, and marine, owing to their high strength-to-weight ratio and excellent corrosion resistance. Over several decades, specialized aluminum alloys have been developed to meet stringent performance requirements in these industries. However, adapting such alloys to LPBF processing introduces significant challenges, necessitating further optimization of their composition and fabrication parameters.

Commonly used alloys in LPBF, such as AlSi10Mg and AlSi7Mg, are traditional shape-casting alloys and are favoured for their excellent printability [25–27]. However, these alloys offer only moderate mechanical performance and often require extensive post-processing to meet performance standards. In contrast, higher-strength wrought alloys like AA6061, AA7050, and AA2195 are prone to hot cracking during LPBF [28–30]. This is primarily due to their relatively large solidification intervals, the rapid cooling rates and thermal stresses inherent in the LPBF process, which lead to crack formation during solidification.

Both Al-Si-Mg casting alloys and high-strength wrought alloys encounter issues due to their reliance on precipitation hardening. These alloys are designed to undergo heat treatments involving solution treatment, quenching, and aging to improve mechanical properties [31,32]. The complex thermal cycle in LPBF exacerbates problems like residual stresses and porosity, significantly reducing the mechanical integrity of the components. Many studies have reported that the LPBF process for aluminium alloys is generally critical [33]. A significant issue is the difficulty in spreading the powder bed due to poor flowability. Additionally, the high reflectivity of aluminium powders and the high thermal conductivity of the solidified material necessitate high laser power. The presence of a thin oxide film on gas-atomized particles and solidified layers further reduces processability by lowering wettability and hindering remelting of the previous layer, resulting in porosities within the built parts [34].

Despite the aforementioned challenges, the LPBF processing of aluminium alloys has emerged as a promising avenue of research due to the unique microstructures and enhanced mechanical properties that can be achieved. Near- and hypo- eutectic Al-Si alloys, such as AlSi10Mg, AlSi12, AlSi7Mg, are commonly used in AM processes, with AlSi10Mg being the most extensively studied [35–38]. The success of AlSi10Mg is primarily due to its silicon content, which is close to the eutectic composition and helps prevent solidification cracking [28]. The presence of 10 wt.% silicon in AlSi10Mg results in a narrow solidification range of about 30°C, which is significantly lower than that of high-strength aluminium alloys like the 2024 series, with a solidification range of 135°C [39]. Silicon improves the fluidity of molten aluminium, reduces solidification shrinkage, and lowers the coefficient of thermal expansion (CTE) [40–43]. Furthermore, the addition of silicon to the alloy enhances laser absorption, with silicon particles absorbing approximately 70% of the laser energy [44]. Studies have demonstrated that as-built AlSi10Mg samples exhibit superior mechanical properties compared to cast and conventionally solution-aged T6-treated samples of the same composition [43,45]. With the promising results with AlSi10Mg, a few other casting alloys have also been successfully processed with LPBF. High-strength aluminium alloys such as the 2xxx, 6xxx, and 7xxx series are challenging to process using LPBF due to their susceptibility to solidification cracking and the volatility of alloying elements like Zn, Mg, and Li, which can easily evaporate during the building process.

There is therefore considerable industrial interest in developing high-strength aluminium alloys suitable for LPBF processing. Although research in this area began only a few years ago, there

has been a significant increase in scientific publications on new aluminium alloys designed for AM processes. This growing interest highlights the potential for developing alloys to achieve the necessary mechanical properties and processability for advanced applications. Innovative alloy design and process optimization strategies, including tailored heat treatments and controlled cooling rates, are essential to mitigate these issues mentioned above and enhance the performance of aluminium alloys in LPBF applications.

3.1.3 The Al-Fe alloy system

The addition of Fe to aluminum enhances high-temperature strength due to the dispersion of second-phase particles [46]. However, the equilibrium solubility of Fe in aluminium is exceptionally low, approximately 0.03 atomic percent, limiting the ability to achieve precipitation strengthening through traditional aging treatments [47]. This low solubility results in limited strengthening under equilibrium conditions, making the development of Al–Fe alloys reliant on non-equilibrium processing techniques, such as rapid solidification, to achieve improved mechanical properties [48,49]. Despite their limitations in strength compared to precipitation-hardenable alloys (e.g., Al–Mg–Si systems), Al–Fe alloys offer distinct advantages, including high thermal conductivity [50–52]. This is attributed to the low solubility of Fe in the α-Al (FCC) matrix. Increasing the Fe content in Al–Fe systems promotes the formation of intermetallic phases, such as $Al_{13}Fe_4$, which can contribute to strengthening [53]. However, the morphology, distribution, and size of these intermetallics are also critical to the alloy's overall performance.

The Al–Fe binary system is particularly notable for its eutectic decomposition (occurring at 1.85 wt% Fe and 654 °C), where the liquid phase solidifies into α-Al and θ-$Al_{13}Fe_4$ phases under conventional casting conditions [54,55]. This process leads to the formation of plate-shaped θ-$Al_{13}Fe_4$, which is in equilibrium with the surrounding α-Al matrix. In contrast, under high cooling rates and temperature gradients, the eutectic reaction is altered, leading to the formation of metastable Al_6Fe phases alongside α-Al [56]. This transition occurs at cooling rates exceeding 1 K/s and is further influenced by solidification conditions such as growth rate and thermal gradients [57]. The Al–Fe intermetallics formed during various processing methods have been reported in the literature [58]. The metastable and ductile Al_6Fe phase has been observed in high-pressure die casting [59], Tungsten inert gas (TIG) welding-brazing [60], and AM via LPBF [56]. These findings suggest that Al_6Fe is an intermetallic that forms under high-pressure conditions. Moreover, most stable and metastable Al–Fe intermetallics,

such as $Al_{13}Fe_4$, Al_6Fe, Al_5Fe_2, Al_2Fe, AlFe, and $AlFe_3$, have been observed in AM processes (Fig. 3.2) [56,61,62]. These observations underscore the unique capability of AM processes to precisely tailor alloy compositions, enabling the formation of targeted intermetallic phases to achieve desirable material properties.

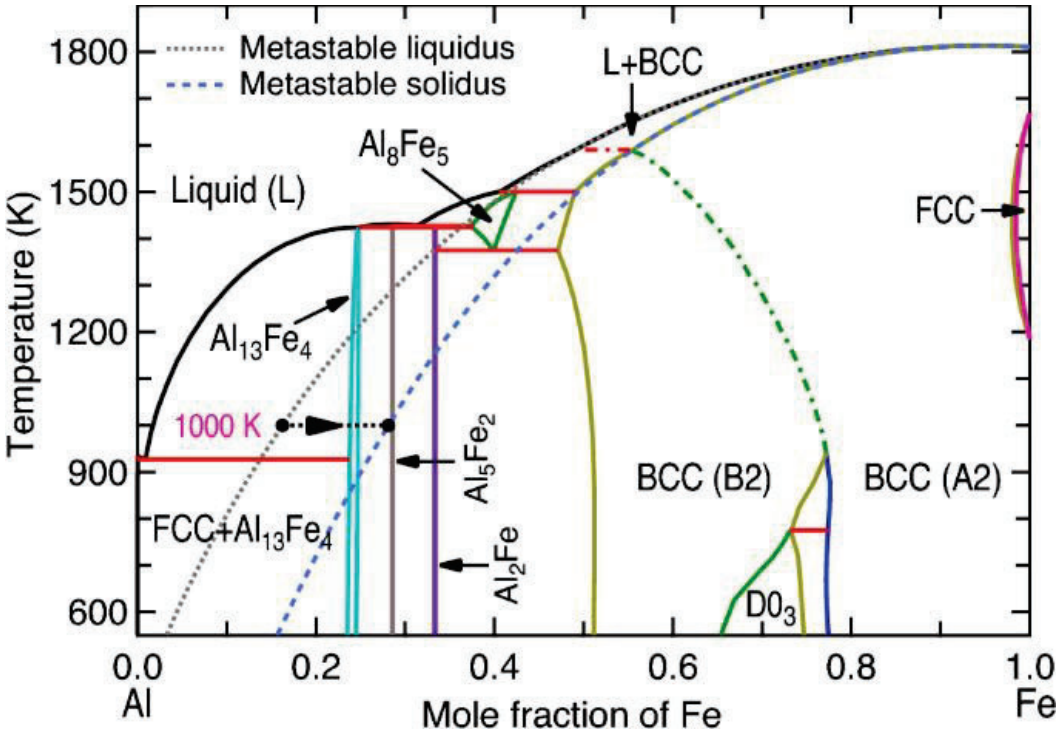

Fig. 3.2 CALPHAD-based calculated phase diagram of the Al–Fe system [63], showing metastable liquidus and solidus lines to evaluate the formation of non-equilibrium phases from the supersaturated solution. Taken from [58].

LPBF operates with extremely high cooling rates (~ 10^5K/s), which enable the formation of fine microstructures and metastable phases that are unattainable under conventional casting conditions. These rapid cooling rates enhance solute trapping, extending the solubility of Fe in the α-Al matrix and promoting the formation of nanoscale intermetallics [54]. In LPBF-fabricated Al–Fe alloys, the rapid cooling dramatically affects phase formation and distribution. X-ray diffraction analysis of LPBF samples has shown small fractions of the θ-$Al_{13}Fe_4$ phase, commonly observed in as-cast samples, and the presence of the metastable Al_6 Fe phase [56]. For instance, specific diffraction peaks corresponding to θ-$Al_{13}Fe_4$ are absent or significantly diminished in LPBF samples, while reflections associated with Al_6Fe become prominent. This suggests that the rapid solidification inherent to LPBF favours the partial replacement of stable θ-$Al_{13}Fe_4$ with metastable Al_6Fe [64]. The increased lattice parameter of

the α-Al matrix observed in LPBF samples further supports the enhanced solubility of Fe, attributed to the atomic size mismatch between Al and Fe atoms [65,66].

The high cooling rates in LPBF not only alter phase formation but also influence the morphology of intermetallics. While conventional solidification results in the formation of rod-shaped Al_6Fe phases, LPBF produces spherical or granular Al_6Fe particles, along with nanoscale dispersions of these intermetallics (<100 nm) within the melt pool [56]. These morphological differences may be attributed to the interplay of rapid solidification mechanisms and subsequent thermal effects from laser-induced reheating of the material [67]. The ability of LPBF to refine microstructures and influence phase formation provides a unique opportunity to optimize Al–Fe alloys for applications requiring a balance of high strength and thermal conductivity. For example, LPBF-fabricated Al–2.5Fe alloys exhibit enhanced mechanical properties, such as improved strength and ductility, due to the refined dispersion of intermetallics and the suppression of coarse eutectic phases [56]. These refined microstructures also contribute to better corrosion resistance, making these alloys highly suitable for demanding environments, including heat exchanger components [68]. Understanding and controlling the size, morphology, and distribution of Al–Fe intermetallics during LPBF processing are critical to maximizing the performance of these alloys.

3.1.4 Al-Fe-Zr alloy system

Al–Zr and Al–Fe–Zr alloys are recognized for their exceptional combination of mechanical strength, thermal stability, and corrosion resistance [69,70]. Small additions of Zr (0.05–0.13 wt%) play a crucial role in these alloys by forming coherent, metastable Al_3Zr dispersoids with an $L1_2$ crystal structure [71]. These nano-sized dispersoids inhibit recrystallization through the Zener mechanism, where grain boundary motion is effectively restricted during hot deformation and annealing [72–74]. This mechanism enhances the material's creep resistance and ensures superior high-temperature stability. Zr can form Al_3Zr precipitates during aging treatments [71].

The efficacy of Al_3Zr dispersoids in recrystallization resistance depends critically on their size, number density, and spatial distribution. Ideally, a high number density of uniformly distributed, fine dispersoids is desired to maximize pinning forces [72,75]. However, during solidification, Zr exhibits significant segregation behaviour, concentrating near dendrite cores in accordance with the Scheil model, which predicts a partition coefficient of k_{Zr}=1.4 [76].

This leads to the formation of dispersoid-free zones near grain boundaries, which are particularly vulnerable to recrystallization [76,77]. Furthermore, insoluble Fe-containing intermetallic phases can form near grain boundaries, further promoting recrystallization in these regions [71].

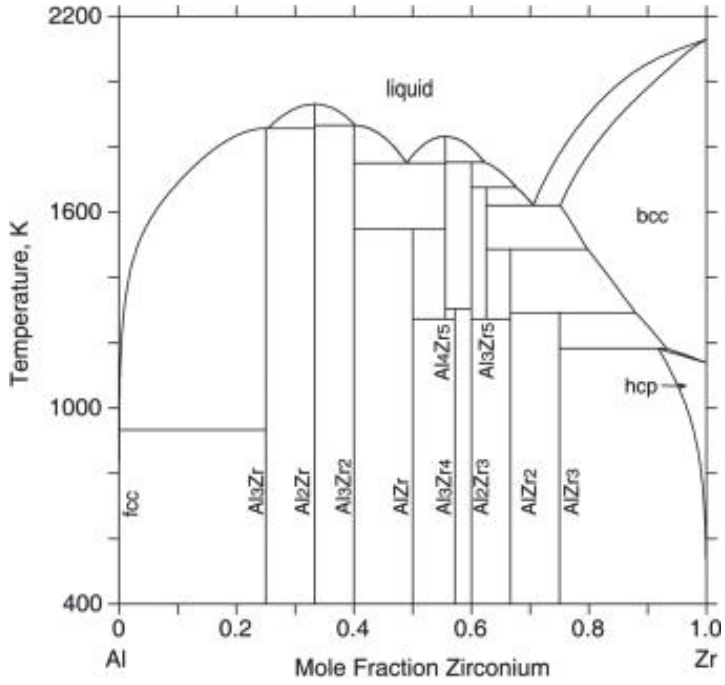

Fig. 3.3 Phase diagram of the Al–Zr system as optimized by Wang et al. [78].

The precipitation behaviour of Al_3Zr is influenced by Zr concentration and homogenization temperature. A higher Zr content generally enhances the number density of dispersoids, while optimized homogenization practices are critical for promoting fine, uniform dispersoid distributions [71]. Conventional homogenization aims primarily at reducing microsegregation and dissolving interdendritic intermetallic phases, but modified practices designed to enhance Al_3Zr precipitation are of interest. Techniques such as directional rapid solidification can further reduce segregation effects by controlling the distribution of alloying elements along the solidification front [79].

In the Al–Zr binary system, numerous stoichiometric intermetallic compounds, including $AlZr_3$, $AlZr_2$, Al_3Zr, and Al_2Zr, are well-documented (Fig. 3.3) [80]. In Al–Fe–Zr ternary systems, these compounds are represented as $(Al,Fe)_mZr_n$, where Al and Fe occupy the first sublattice, and Zr occupies the second [80–82]. Among these, Al_3Zr is particularly notable for its metastable cubic structure, which is coherent with the α-Al (FCC) matrix [74]. This

coherence enables Al_3Zr to act as an effective heterogeneous nucleation site for α-Al grains during solidification, promoting fine and equiaxed grain structures. The addition of Fe is not anticipated to directly influence the solubility of Zr in aluminum or the overall volume fraction of Al_3Zr precipitates [83]. However, an evident increase in both the number density and volume fraction of Al_3Zr precipitates has been observed with Fe additions [84]. This effect may be attributed to a mechanism similar to that of Si, where Fe atoms facilitate the nucleation of Al_3Zr by forming clusters that serve as preferential nucleation sites, thereby reducing the energy barrier for Al_3Zr precipitation [83]. Conversely, Zr exhibits a strong tendency to segregate at the solid-liquid interfaces during solidification, inhibiting Fe diffusion and thereby refining the morphology of Al_3Fe intermetallic phases [85].

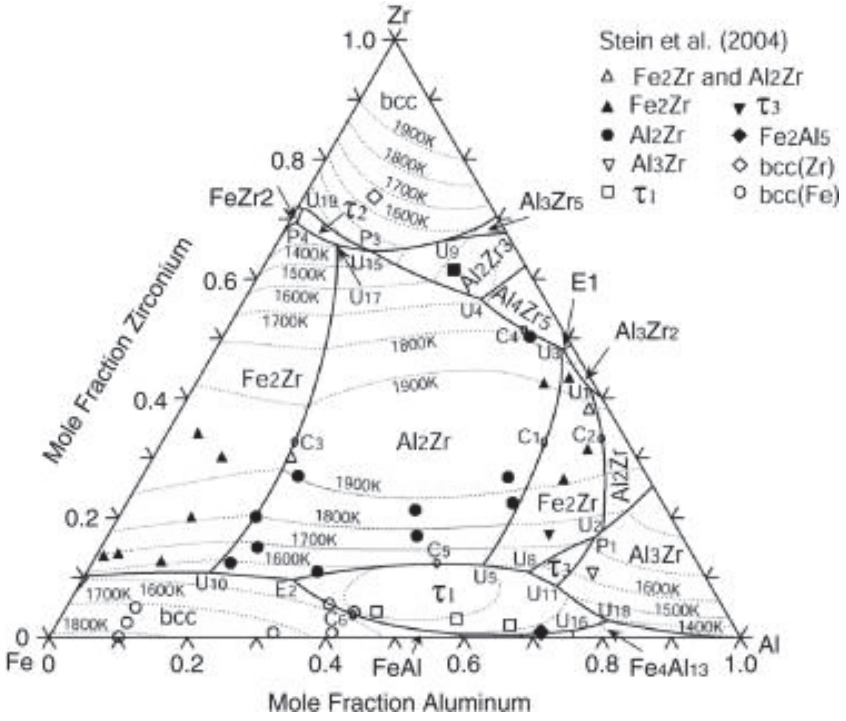

Fig. 3.4 Calculated liquidus surface projection for the Al–Fe–Zr ternary alloy system, providing insights into phase stability and solidification pathways. Taken from [86].

Upon prolonged heat treatment, Al_3Zr is characterized by transforming from the metastable $L1_2$ phase into the equilibrium DO_{23} phase [76]. Optimal precipitation kinetics occur at homogenization temperatures between 400°C and 500°C, resulting in fine, spherical Al_3Zr dispersoids (≈20 nm) in commercial Al alloys [87–89]. However, dispersoid-free zones adjacent to grain boundaries and the presence of large primary particles can significantly reduce recrystallization resistance in these regions [77]. To mitigate these effects, alloying strategies, such as combined microalloying with Scandium (Sc) and Erbium (Er), have been explored

[90]. The resulting $Al_3(Sc, Zr)$ precipitates enhance the stability of the θ’ phase and improve both creep resistance and strength by suppressing undesirable diffusion processes [91]. The localized reheating effect of overlapping laser scans may also contribute to slight coarsening or decomposition of metastable phases, transitioning them toward more stable forms [76]. The precise control over thermal gradients and cooling rates in LPBF allows for tailoring the size, shape, and distribution of these intermetallics to achieve the desired balance of strength and ductility. Zr plays a dual role during LPBF: It segregates to solid-liquid interfaces during solidification, effectively pinning grain boundaries and refining the morphology of intermetallic phases [76]. Simultaneously, Al_3Zr precipitates act as potent heterogeneous nucleation sites for α-Al grains, promoting a fine, equiaxed grain structure and mitigating columnar grain growth [92]. The ability of LPBF to manipulate solidification dynamics and microstructural evolution underscores its potential for producing high-performance Al–Fe–Zr alloys.

3.1.5 Aheadd® CP1: Al-1Fe-1Zr alloy

Recent advancements in aluminium alloys for LPBF have introduced innovative compositions tailored specifically for additive manufacturing. One such development is the Al-1Fe-1Zr alloy, commercially known as Aheadd® CP1, developed by Constellium [93]. This alloy is designed to overcome the limitations of traditional aluminum alloys used in LPBF, especially the 6xxx series, known for their susceptibility to hot cracking [94–97]. Various strategies, such as the addition of grain refiners and high-temperature powder bed pre-heating, have been employed to mitigate these issues with limited success [98,99]. The Al-1Fe-1Zr alloy is designed to address the challenges associated with LPBF, particularly by improving strength and thermal conductivity properties [92]. In a comprehensive study employing 2D multiscale characterisation techniques, Pauzon et al. investigated the microstructural evolution of the alloy and its impact on mechanical and electrical properties [100]. After direct aging for 4 hours at 400°C, Aheadd® CP1 exhibits a yield strength of 310 MPa and thermal conductivity of 180 W/m.K, compared to 130 MPa and 122 W/m.K, respectively, in a stress-relieved condition [92]. The tensile behaviour of the stress-relieved and aged conditions is shown in Fig. 3.5 (a) and (b). The Ashby chart in Fig. 3.5 (c) positions the performance of the new Al-1Fe-1Zr alloy in relation to the cast and wrought Al series based on yield strength (YS) and thermal conductivity. Thermal conductivity is essential in applications requiring efficient heat dissipation such as electronic devices, heat exchangers, or aerospace cooling systems, where improved conduction can significantly enhance performance and reliability. The objective of attaining the desired material properties was achieved through the strategic selection of elements with low vapor pressure and slow diffusion rates in aluminium, coupled with the low solubility of Fe in Al.

Both layer-by-layer processing and the melt pools that solidify under the effect of the laser during LPBF manufacturing usually result in periodic structures along the build direction.

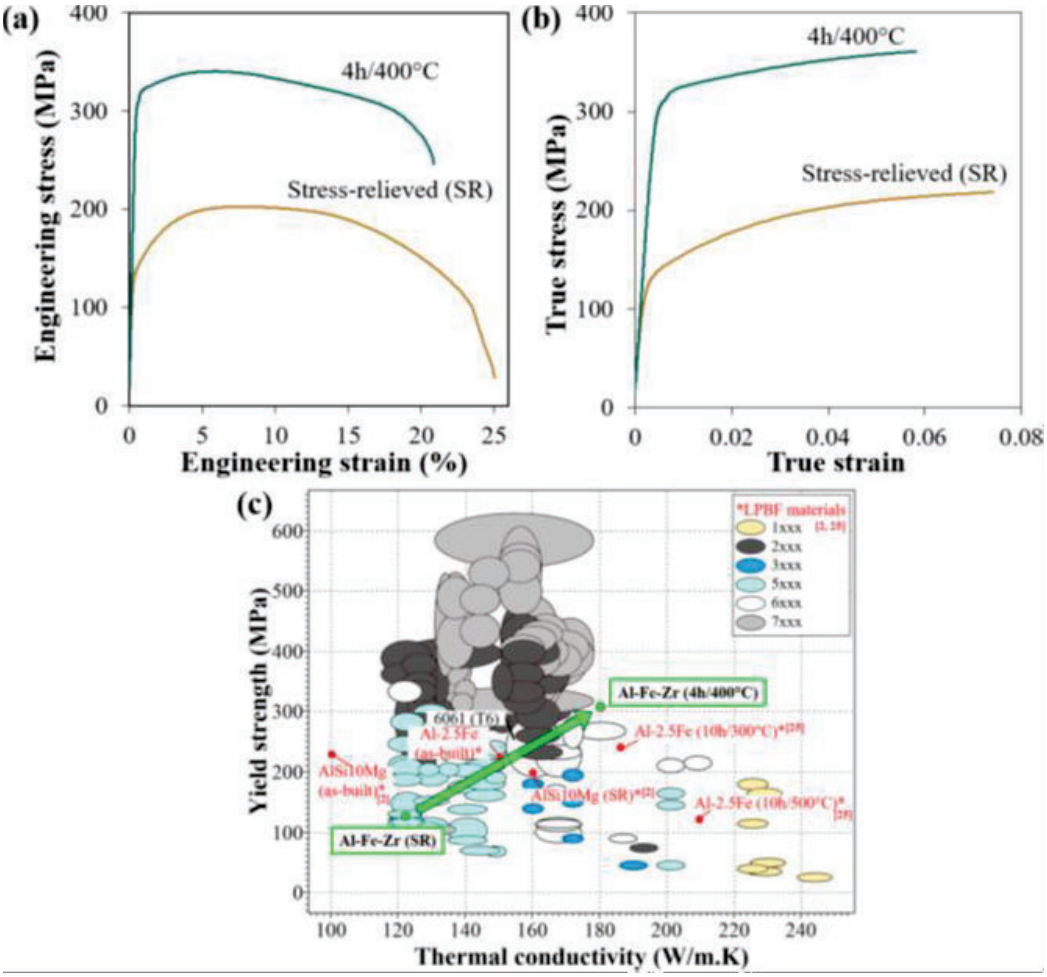

Fig. 3.5 (a) Engineering and (b) true tensile stress-strain curves for LPBF Al-1Fe-1Zr in both stress-relieved (SR) and peak-aged states. (c) Ashby chart showing the relationship between yield strength and thermal conductivity, comparing typical wrought and casting Al alloys with the new Al-1Fe-1Zr alloy presented here. Taken from [92].

Depending on the LPBF processing conditions, microstructural features within these melt pools can vary significantly in terms of grain size, precipitation types, phases formed, etc. [101–103]. Particularly for the Al-1Fe-1Zr alloy studied here, microstructural analysis was conducted in [92,100] using Scanning Electron Microscopy (SEM), Transmission Electron Microscopy (TEM) with Energy Dispersive Spectroscopy (EDS), and Automated Crystal Orientation Mapping (ACOM).

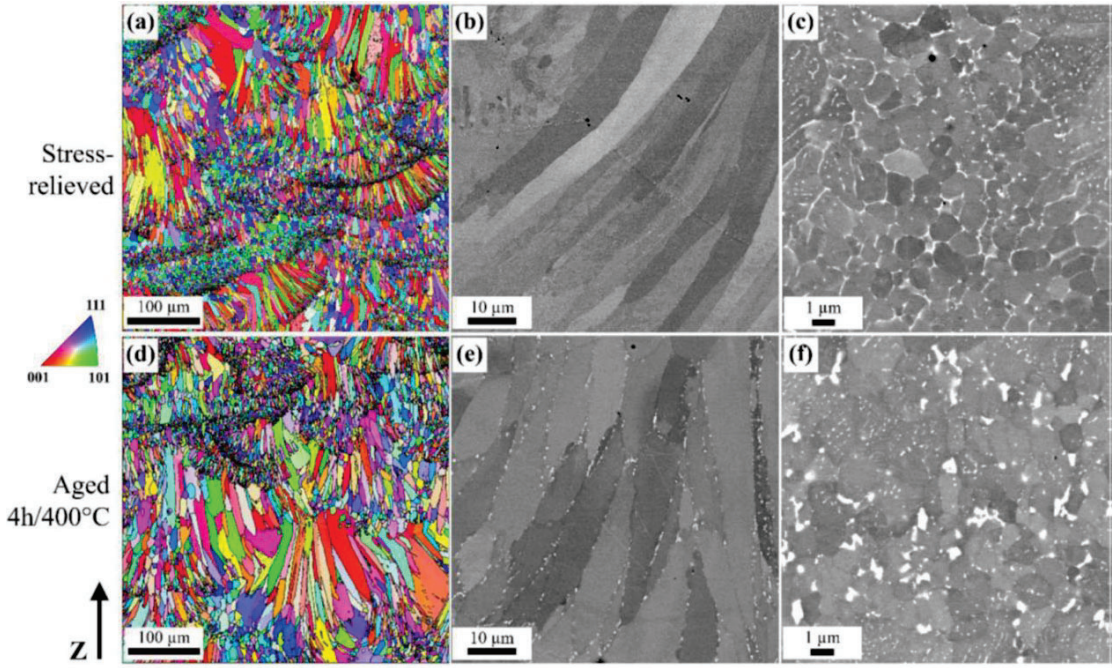

Fig. 3.6 (a) EBSD orientation maps in inverse pole figure (IPF) colouring for stress-relieved, and (d) peak-aged (4h at 400°C) conditions. Backscattered electron (BSE) images showing typical microstructures within (b, e) the columnar zone (CZ) and (c, f) the fine equiaxed zone (FEZ). Taken from [92]

The characterizations show the complex grain structures formed during LPBF with a periodicity of ~100-200µm [92]. Fig. 3.6 provides a detailed overview of the microstructure along the building direction (Z) for both the stress-relieved and aged conditions of the material. Fig. 3.6 (a) and (d) shows columnar Al grains (columnar zone, CZ) within the melt pools, that are elongated in the direction of solidification, while small equiaxed grains (fine equiaxed zone, FEZ) decorate their boundaries [92]. A significant feature is the presence of FEZ, as illustrated in Fig. 3.6 (c), where grains have a mean equivalent diameter of less than 1 µm. This fine-grained structure is partially due to the formation of primary $L1_2$-Al_3Zr particles, which promote heterogeneous nucleation of aluminium grains at the melt pool boundary, a region characterized by a relatively low solid-liquid front velocity. This phenomenon has been corroborated by thermal calculations from various studies (e.g., [104–106]). Further examination through BSE-SEM imaging reveals very less and sporadic bright grain boundary particles within the CZ of the stress-relieved material, with an estimated presence of around 0.3%, as observed in Fig. 3.6 (b). In contrast, the grain boundaries within the FEZ are more densely decorated with thin films and particles, accounting for approximately 3% of the observed area in Fig. 3.6 (c). In the aged condition, the decoration of grain boundaries by

coarser bright particles becomes more pronounced in both the FEZ and CZ, with particle sizes reaching up to several hundred nanometers, as depicted in Fig. 3.6 (e) and 3.6 (f).

The SEM techniques were employed to examine the alloy in both as-built and aged conditions, providing detailed insights into the solidification process and subsequent microstructural evolution. Properties such as hardness and electrical conductivity were investigated to evaluate the alloy's performance. The impact of post-fabrication stress-relief heat treatment, performed at 300°C for 2 hours, was studied in conjunction with subsequent aging treatments at 400°C for varying durations of 1, 4, and 7 hours. These conditions were also compared to the properties of the material in its as-built state. Both the as-built and stress-relieved materials exhibited identical hardness values (HV1 = 67 kgf/mm^2), though the stress-relieved material demonstrated a slightly higher electrical conductivity (18 MS/m compared to 17 MS/m for the as-built state). Peak aging was observed between 4 and 7 hours, with conductivity continuing to increase with extended aging. The hardness remained relatively stable between the 4-hour and 7-hour aging treatments at 400°C, but a noticeable decline was observed with longer aging times. In contrast, the material's conductivity, which was measured at 26.5 MS/m after 4 hours of aging at 400°C, continued to increase with extended aging durations. This increase in conductivity, reaching 30 MS/m after 96 hours at 400°C, can be attributed to the progressive depletion of solute atoms from the solid solution as the aging time increases. The alloy exhibited considerable enhancements in strength from its as-built to peak-aged condition, accompanied by a relatively slight decline in ductility. It is reported Fe is expected to form the $Al_{13}Fe_4$ phase (monoclinic) [92] at the grain boundaries, with globular morphology in the as-built state and particles further evolving during aging. The fraction of Fe-rich particles increased from 6% in the as-built state to 9% after aging at 400°C for 4 hours. Zr forms Al_3Zr primary cubic intermetallics, which presumably act as nucleation sites for the fine equiaxed Al grains [92,100]. The aged specimen exhibits a uniform distribution of coherent nano-sized precipitates within the aluminium grains, a feature that is absent in the as-built state. In the as-built material, only a few coarser primary $L1_2$-Al_3Zr particles are present, primarily contributing to the formation of FEZ. Upon aging at 400°C for 4 hours, the material shows a dense population of $L1_2$-Al_3Zr nanoprecipitates, which are finely dispersed throughout the aluminium matrix. However, regions adjacent to Fe-rich globular particles show a noticeable depletion of these nano-precipitates, forming precipitate-free zones (PFZ). This depletion is likely due to the peritectic reaction associated with Zr, coupled with a reduced concentration of vacancies near the interface between the Fe-rich intermetallics and the matrix. The lower

vacancy concentration limits the diffusion of Zr, thereby hindering the formation of nano-sized $L1_2$-Al_3Zr precipitates in these areas. Furthermore, adding Zr improves the alloy's resistance to recrystallization, maintaining a stable microstructure during post-processing heat treatments. This stability is essential for applications requiring high thermal and mechanical performance over extended periods.

The formation of melt pools was found to be associated with the depletion of Fe caused by the presence of early planar growth fronts. The microstructural evolution of these zones upon aging offers insights into the solidification process and its impact on alloy properties. The results of the tensile tests revealed differences in the work-hardening behaviour between the as-built and aged samples, indicating a need for further investigation into these variations. The solidification process was characterised by epitaxial growth, $L1_2$-Al_3Zr induced nucleation, and a solidification velocity-dependent partition coefficient, all contributing to the alloy's microstructural stability and performance [100]. The aging process resulted in the discontinuous precipitation, which influenced the distribution and morphology of Fe-rich particles [100]. The strengthening observed in the as-built specimen was primarily due to solid solution strengthening and the formation of fine grain structures. In contrast, the aging process introduced precipitation hardening via $L1_2$-Al_3Zr nanoparticles and the growth of intermetallic particles [92,100]. A detailed analysis of the microstructure at the scale of the melt pools reveals distinctive melt pool boundaries (MPBs), highlighted with yellow dashed lines in Fig. 3.7 (a). It is important to note that these MPBs do not always precisely align with the FEZ but are positioned several microns below them, as shown in Fig. 3.7 (c).

One key observation is the change in grain growth direction, clearly visible within the purple-oriented grain in the bottom left section of the EBSD map in Fig. 3.7 (b). Additionally, intragranular misorientation is particularly notable at the uppermost MPBs, as indicated by the yellow arrow in Fig. 3.7 (a). This local misorientation becomes even more apparent in the orientation map obtained through automated crystal orientation mapping (ACOM) on a TEM lamella across a MPB, illustrated in Fig. 3.7 (d-e). The misorientation reaches approximately 3.5° at this boundary, as shown in Fig. 3.7 (f). Furthermore, the nano-scale $L1_2$-Al_3Zr precipitation observed within the Fe-depleted zones at the MPBs aligns with the distribution of Zr, as depicted in Fig. 3.7 (g).

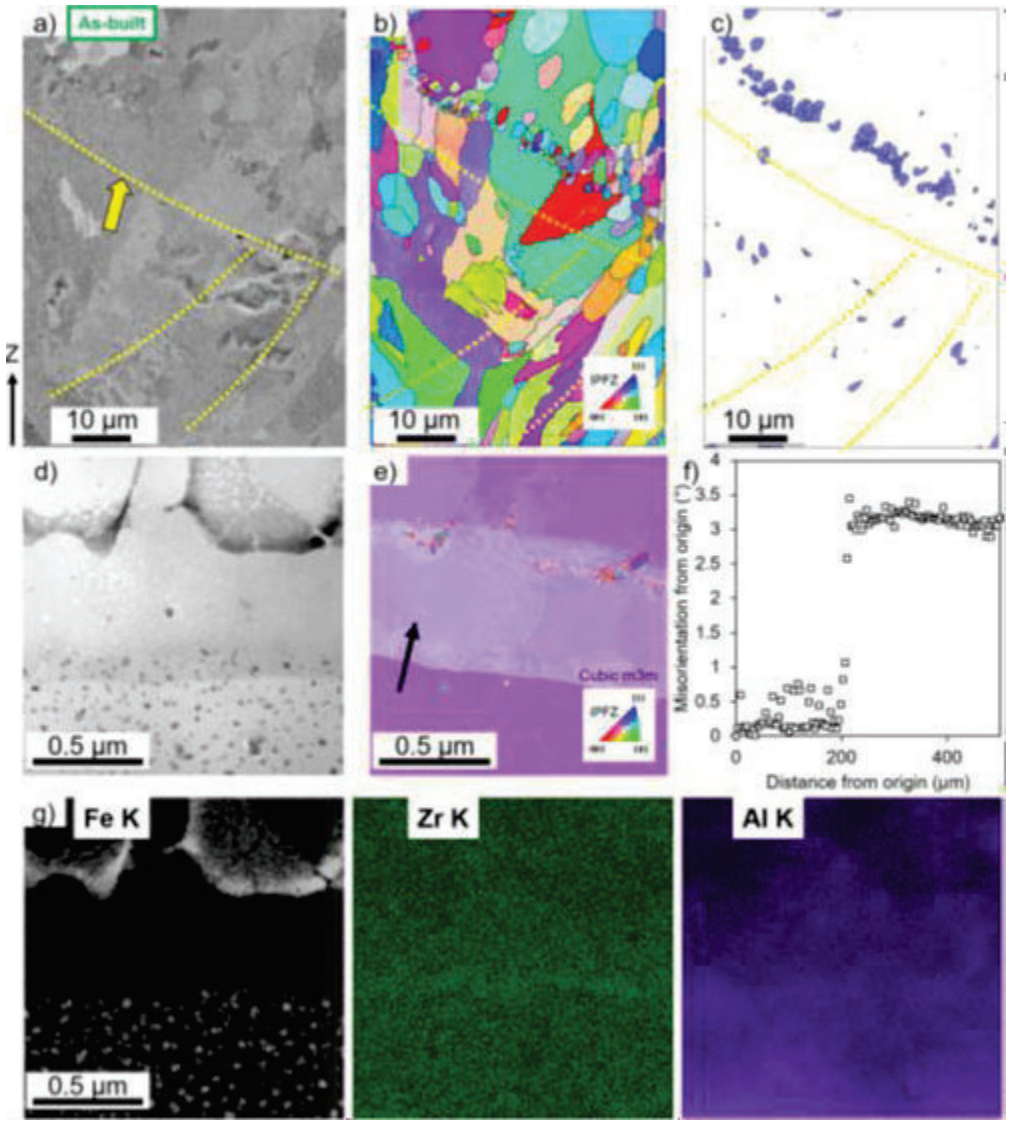

Fig. 3.7 (a) BSE image displaying multiple melt pool boundaries, (b) EBSD orientation map with IPF Z colouring, (c) Fine grains in the area with diameters below 5 µm and a sphericity index > 0.35, (d) STEM BF image of a melt pool boundary, (e) ACOM orientation map (IPF colour) in the Z direction, (f) Local misorientation across the melt pool boundary, (g) EDS maps showing Fe, Zr, and Al distribution in the same area. Taken from [100].

Understanding the interaction between spatter dynamics and keyhole morphology is crucial for comprehending the LPBF process [107,108]. Guo et al. explored the connections between vapor depression shape and spatter dynamics during LPBF of Al-1Fe-1Zr alloy using high-speed synchrotron X-ray imaging [109]. The study employs a methodology, utilizing *in-operando* synchrotron X-ray imaging to observe and analyze the LPBF process in real-time [110–112]. The *in-operando* experiments were performed at the high-speed imaging beamline ID19 at the European Synchrotron Radiation Facility (ESRF) [113]. They used synchrotron

radiography at a 40 kHz image acquisition rate to monitor and quantify the relationship between spatter ejection and vapor depression dynamics during LPBF. The study highlights the importance of linear energy density in shaping keyhole and spatter characteristics. The LPBF processing parameters were chosen to span a range of linear energy densities (El), from 210 $J \cdot m^{-1}$ to 840 $J \cdot m^{-1}$. The research provides practical recommendations for optimizing LPBF parameters by correlating spatter behaviour with keyhole morphologies. The study also proposed two novel spatter mechanisms: rear rim droplet spatter and spatter-induced surface cavities [109]. Rear rim droplet spatter occurs when metal vapor jets overcome surface tension at the keyhole's rear rim, while spatter-induced cavities form when the laser's radiation force dislodges particles from the melt pool. The analysis reveals that scan speed significantly affects spatter trajectory more than laser power, suggesting that optimized scan speeds can reduce spatter-related defects [109]. Higher scan speeds and appropriate lower linear energy densities (in the range that avoids lack-of-fusion defects) can minimize spatter formation and improve component quality [109].

Additionally, Klamann et. al., aimed at developing the process windows for processing the Al-1Fe-1Zr alloy on a Concept Laser® M2 system with a 400W NdYAG laser, for different layer thicknesses (30 µm, 60 µm and 120 µm) and to characterize the produced materials [114] . In addition, the effects of a remelting strategy were investigated, in which the already solidified material is re-exposed. Investigations revealed that layer thicknesses of 30 µm and 60 µm are optimal for LPBF with a 400 W laser, yielding porosity below 0.15% and material densities above 99.85%. However, a higher layer thickness of 120 µm was found to be unsuitable due to inadequate densification. A 30 µm layer thickness offers the most robust process window, reducing sensitivity to positioning effects and ensuring high dimensional accuracy, making it ideal for fine structures. In contrast, a 60 µm layer thickness enhances productivity but is less effective for intricate geometries. Microstructural formation depends on scanning speed and melt track overlap, influencing grain morphology and the precipitation of primary Al_3Zr particles. A fine layer thickness and optimized parameters promote controlled microstructural evolution. Additionally, double exposure effectively reduces porosity and bonding defects without significantly impacting build time.

The in-depth understanding of the Al-1Fe-1Zr alloy and LPBF processes is essential for advancing its application in producing high-quality components. The alloy demonstrates excellent LPBF processability due to its ability to utilize high cooling rates, taking advantage

of the thermal gradients and the solid-liquid interface during the process. The successful adaptation of the Al-1Fe-1Zr alloy for LPBF not only addresses the limitations of traditional aluminium alloys but also paves the way for the design of high-performance components, including, but not limited to, those required for aerospace and automotive applications. The development of such specialized alloys underscores the importance of integrated approaches combining material science, and process engineering.

3.2 Microstructural Characterization

Although traditional two-dimensional (2D) analytical techniques, such as electron or optical microscopy, have been invaluable in providing insights into the microstructures of alloys, these methods are fundamentally limited by their inability to capture the complete spatial complexity of these structures. This may result in the crucial 3D features being obscured, leading to an incomplete and potentially misleading understanding of the material's microstructure. While FIB-SEM tomography can address this challenge by reconstructing 3D data from serial sectioning, it is a destructive technique and thus not always suitable for repeated or large-scale analyses. Recent technological advancements have enabled the non-destructive investigation of three-dimensional microstructures at the nanoscale, thereby facilitating a more comprehensive understanding of an alloy's internal architecture. Such techniques reveal the true spatial relationships and orientations of microstructural constituents, which are often obscured in two-dimensional images. Furthermore, 3D characterisation provides precise data on the morphology, dimensions, and distribution of microstructural features, including precipitates, grains, and inclusions, without prior assumptions. These attributes are crucial for correlating microstructure with material properties, as they frequently influence mechanical behaviour, thermal stability, and other critical performance aspects. For instance, in precipitation-hardened alloys, the size, distribution, and coherence of precipitates with the matrix can significantly impact strength and ductility.

Furthermore, non-destructive characterisation techniques, such as X-ray radiography and X-ray computed tomography (XCT), enable subsequent analyses or mechanical testing. This ability is particularly advantageous for the study of microstructure evolution under different processing conditions. 3D characterization can elucidate how these conditions contribute to phase transformations, grain growth, and defect formation. This insight is of importance for the optimisation of manufacturing processes and the reliability of the final components. In the context of novel alloys such as the Al-1Fe-1Zr alloy, which has been specifically developed for LPBF, 3D microstructural investigations are indispensable. It is essential to understand the spatial distribution and morphology of the Fe- and Zr- phases. 3D microstructural investigations provide a more comprehensive and precise understanding of the material and the optimisation of processing techniques to enhance their properties.

3.2.1 X-ray Imaging

Imaging can be performed using a range of probes, including light, electrons, electromagnetic waves, ultrasound, neutrons, and X-rays, each offering distinct advantages in terms of resolution, penetration depth, and the physical properties they reveal. X-ray imaging is a powerful technique widely used to visualize the internal structures of objects and biological tissues. X-rays, a form of high-energy electromagnetic radiation, are used to penetrate materials and produce images based on the varying degrees of interaction between the X-rays and the material's internal components.

In the field of X-ray imaging, the use of synchrotron radiation has become a significant innovation. A synchrotron is a type of particle accelerator that produces high-energy, highly collimated beams of radiation. The primary principle of a synchrotron is to accelerate charged particles, typically electrons or protons, to nearly the speed of light and maintain them in a closed path using powerful magnetic fields. As these particles travel along the curved trajectory, they emit electromagnetic radiation, which spans a wide range of the electromagnetic spectrum, including X-rays. In the context of X-ray sources, brightness (often referred to as *brilliance*) is a key figure of merit that quantifies the photon flux (photons per second) emitted per unit area, per unit solid angle, and within a specified spectral bandwidth. The brightness of synchrotron X-rays is several orders of magnitude higher than that of conventional X-ray sources. The phase imaging techniques discussed in this study depend on coherence. Coherence is the property that enables waves to exhibit observable interference and diffraction phenomena, and it measures the degree of correlation between two points in a wavefield over time and space. The coherent nature of synchrotron X-rays enhances phase contrast imaging, which is particularly useful for visualizing low-density materials like aluminium. Within synchrotron facilities, synchrotron radiation is directed and extracted from the main storage ring to various experimental stations by specialized setups known as beamlines. Each beamline is customized for particular experiments and techniques.

X-ray imaging relies on multiple interaction mechanisms to extract comprehensive information about a material’s internal composition and structure. X-ray diffraction serves a distinct but complementary role in structural analysis. Coherent interactions within ordered structures (e.g., crystals) give rise to Bragg diffraction. When crystalline regions in a material satisfy the Bragg condition, coherent elastic scattering reveals the atomic lattice arrangement, while shifts in diffraction intensities can pinpoint defects or heterogeneities.

When a material is exposed to high-energy X-rays, the incident radiation can impart sufficient energy to the electrons within the atoms of the material. If the absorbed energy exceeds the binding energy of the electrons, they may be excited and promoted from their ground state to higher energy levels or to a free state with some residual kinetic energy as in our case (Fig. 3.8). This excitation creates a vacancy in the lower energy level, rendering the atom unstable. To restore stability, electrons from higher energy levels fall back to fill the vacancy in the lower energy shell. During this transition, the energy difference between the higher and lower energy levels is released in the form of electromagnetic radiation. The energy of this emitted radiation is characteristic of the specific elements present in the material and typically falls within the X-ray region of the electromagnetic spectrum. This phenomenon is referred to as X-ray fluorescence. Each element has a unique set of energy levels, leading to a characteristic X-ray emission spectrum that acts as a fingerprint for that element. By analyzing the emitted X-ray spectrum, it is possible to determine the elemental composition of the material with high accuracy.

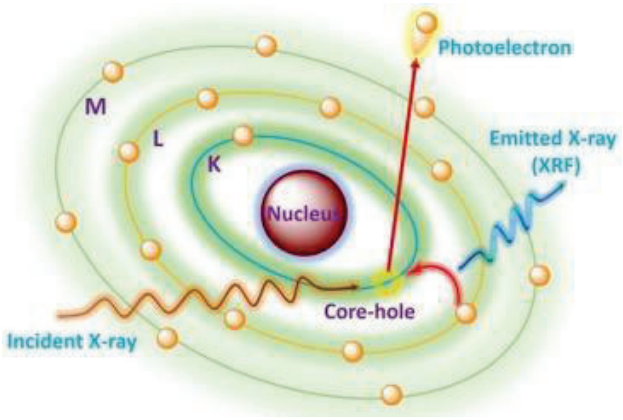

Fig. 3.8 Representation of the X-ray fluorescence phenomenon, illustrating core electron excitation by incident X-rays and the subsequent emission of characteristic fluorescence radiation during electron relaxation. Taken from [115].

Traditionally, X-ray imaging has relied on absorption contrast, where denser or thicker regions of a sample attenuate the beam more strongly. X-rays are absorbed or scattered out of the beam. This forms the basis of absorption radiography, the earliest and still most common form of X-ray imaging in many conventional applications. The Lambert-Beer law describes the relationship between the incoming and outgoing intensities through the material at zero distance (absorption only):

$$I_{out} = I_{in} exp(-\mu L) \tag{3.1}$$

The weak interaction of X-rays with matter, however, can limit contrast, especially for thin or low-density features. Classical absorption radiography has found extensive use in industrial non-destructive testing and medical diagnostics; however, it frequently proves inadequate for high-resolution examinations of low-absorbing materials.

To address this shortcoming, phase-contrast imaging has emerged as an effective alternative. It exploits the phase shift experienced by an X-ray wave as it encounters refractive index variations. The interaction of X-rays with matter, defined by a wavelength λ, can be described using the complex refractive index:

$$n(\lambda) = 1 - \delta(\lambda) + i\beta(\lambda) \tag{3.2}$$

Here, δ mediates phase shifts, while β governs attenuation. When X-rays traverse materials in which δ is non-negligible, subtle refraction and phase retardation effects arise, leading to significantly enhanced contrast for features that would otherwise remain indistinguishable in purely absorption-based imaging. Even minute changes in δ can produce significant enhancements in image contrast once translated into intensity fluctuations at the detector plane, particularly in weakly absorbing materials such as light alloys or soft tissues. In this context, δ is responsible for the phase shift experienced by the X-rays as they travel through the material:

$$\Phi = \frac{2\pi}{\lambda}\int_0^L \delta(\lambda)dz \tag{3.3}$$

β pertains to the absorption process, which is quantified by the absorption coefficient μ, given by:

$$\mu = \frac{4\pi}{\lambda}\beta \tag{3.4}$$

The dependence of these parameters on wavelength originates from the complex atomic scattering factor [116]:

$$f(\lambda) = Z + f_1(\lambda) + i\, f_2(\lambda) \tag{3.5}$$

The real and imaginary components of this factor, $Z + f_1(\lambda)$ and $f_2(\lambda)$ are related to δ and β as follows:

$$\delta(\lambda) = \frac{r_0}{2\pi}\,\lambda^2\, n_{at}\,[Z + f_1(\lambda)] \tag{3.6}$$

$$\beta(\lambda) = \frac{r_0}{2\pi} \lambda^2 n_{at} f_2(\lambda) \tag{3.7}$$

where r_0 denotes the classical electron radius, n_{at} atomic number density and Z represents the atomic number.

For the X-ray energy range commonly employed in imaging, results in a real part of the refractive index that lies slightly below unity. Consequently, δ remains positive and is proportional to λ^2. Away from absorption edges, where the real anomalous scattering factor f_1 vanishes, δ provides a direct measure of the electron density, and to a close approximation, the mass density of the material. Given that the ratio of the number of electrons to the atomic weight is similar for many atomic species ($\approx 1/2$), δ serves as an effective measure of the material's mass density, allowing its estimation [117],

$$\delta \approx 1.3\ 10^{-6}\ \rho\ \lambda^2 \tag{3.8}$$

where ρ is in g/cm3 and λ in Å.

One of the most straightforward forms of phase-sensitive imaging is propagation-based phase contrast, often made feasible by highly coherent synchrotron sources. Immediately after the sample, the transmitted beam can be expressed as a complex transmission function $T(x, y)$, which incorporates both attenuation and phase shifts. Over a propagation distance z, Fresnel diffraction transforms these phase modulations into measurable intensity variations at the detector:

$$I_d(x, y; z) = |U_d(x, y; z)|^2 \tag{3.9}$$

where U_d is the wavefield at the detector, obtained via a Fresnel propagator applied to $T(x, y)$.

This process effectively converts phase gradients into intensity contrast. In X-ray imaging, detectors primarily record intensity, losing the direct phase information of the wavefield. However, to quantitatively reconstruct the sample's internal structure, particularly its electron density, it is necessary to recover the phase shift Φ. To recover the missing phase component, various retrieval techniques have been developed. Two principal approaches are employed: One approach is the multi-distance Holography where images are acquired at different propagation distances z. The resulting intensity patterns collectively provide the constraints needed to solve for the phase distribution [118]. Another approach is the Near-Field Ptychography where the sample is scanned in multiple lateral positions relative to a coherent beam, and an iterative reconstruction algorithm recovers both the object's transmission function and the probe (incident beam) [119]. This method can achieve very high spatial

resolution without relying on additional optical elements. The reconstruction in X-ray phase imaging involves retrieving the sample's transmission function, T (r), and the incident illumination function, $\psi(r)$, from a set of measured intensities, I_j(r). These intensity measurements can be expressed as [119]:

$$I_j(r) = |D_z T(r - r_j)\psi(r)|^2 \tag{3.10}$$

here D_z represents the free-space propagation over a distance z, and r_j indicates the lateral displacement of the sample relative to the illumination for the j-th measurement. Both T(r) and $\psi(r)$are two-dimensional complex-valued functions, encoding the amplitude and phase information. For effective propagation distances, where the Fresnel number much larger than unity, the free-space propagator D_z is numerically stable and can be computed efficiently. The propagation is represented as a sequence of two fast Fourier transforms[119]:

$$D_z \chi(r) = \mathcal{F}^{-1}\left[\mathcal{F}[\chi(r)] e^{-2\pi i z/\lambda \sqrt{1-q^2\lambda^2}}\right] \tag{3.11}$$

where $\mathcal{F}$ denote the Fourier transform, q represents the reciprocal space coordinate, λ is the X-ray wavelength, z is the propagation distance.

In materials science, X-ray imaging is used to examine the internal structure of materials, identifying defects, inclusions, and the distribution of different phases within a sample. This information is crucial for understanding material properties and behaviours. It is extensively used in both industrial non-destructive testing and research fields, encompassing techniques like computed tomography (CT) that enable 3D imaging. This involves acquiring multiple two-dimensional X-ray images from different angles around the sample. These images are then reconstructed using computational algorithms to create a detailed 3D representation of the internal structures [120]. It allows for more precise and comprehensive analysis compared to traditional 2D imaging.

Synchrotron X-ray science can investigate matter across a wide range of scales, from interatomic crystal planes with angstrom-level spacing to time-resolved computed tomography. Important parameters for these techniques include spatial resolution, maximum sample size, acquisition time, and dose efficiency. There is often a trade-off among these parameters, as enhancing one may lead to compromises in others. As synchrotron X-ray techniques continue to evolve, they promise to provide even greater insights into the microscopic and nanoscopic investigations, driving forward research and innovation in numerous fields.

3.2.2 ID16A Nano-Imaging Beamline, ESRF

The 3D characterization experiments were conducted at the ID16A Nano Imaging beamline of the European Synchrotron Radiation Facility (ESRF), utilizing advanced nanotomography techniques.

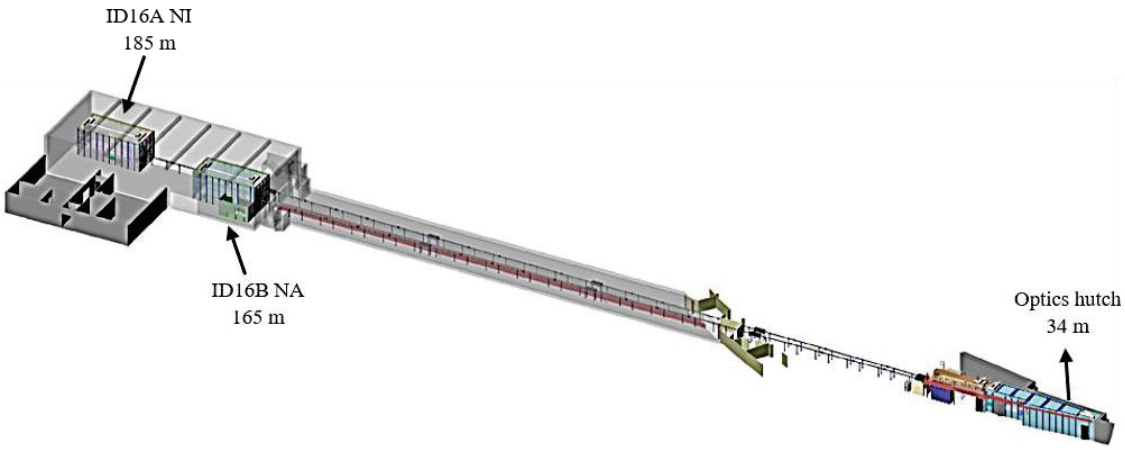

Fig. 3.9 ID16A beamline of the ESRF, one of the long beamlines where the end-station (X-ray focus) is at 185 m from the source.

This beamline is specifically designed for hard X-ray imaging and is highly suitable for materials characterization, achieving spatial resolutions down to approximately 30 nm while maintaining a relatively large field of view of 30 µm [7]. Additionally, larger fields of view and sample sizes can be accommodated, with spatial resolutions systematically adjusted to preserve imaging fidelity and ensure high-quality data acquisition. The beamline operates at two distinct energies, 17.1 keV and 33.35 keV, with the X-ray beam focused into a round spot of about 20 nm diameter using multilayer-coated fixed curvature Kirkpatrick-Baez (KB) mirrors [121–123]. To accommodate both energies, two pairs of KB mirrors have been specially designed. The distance between the source and the focusing element is set at 185 meters to ensure a beam with a high degree of spatial coherence. After the focal point, the beam diverges with a well-defined cone geometry and a divergence of ~5mrad in both directions.

To optimize beamline stability and fully exploit the intrinsic coherence properties of the beam, the number of optical elements is minimized. The beamline's design is largely achromatic, allowing for microscopy across a broad energy bandwidth. Multilayer-coated mirrors are employed for their high efficiency, while the Kirkpatrick-Baez crossed geometry in the nano-

focusing optics allows for independent optimization of the horizontal and vertical directions. All primary optics, including the multilayer monochromator and attenuators, are strategically positioned close to the source to preserve the coherence properties of the beam. The nano-focusing optics, on the other hand, are integrated into the sample stage and positioned near the sample for optimal performance.

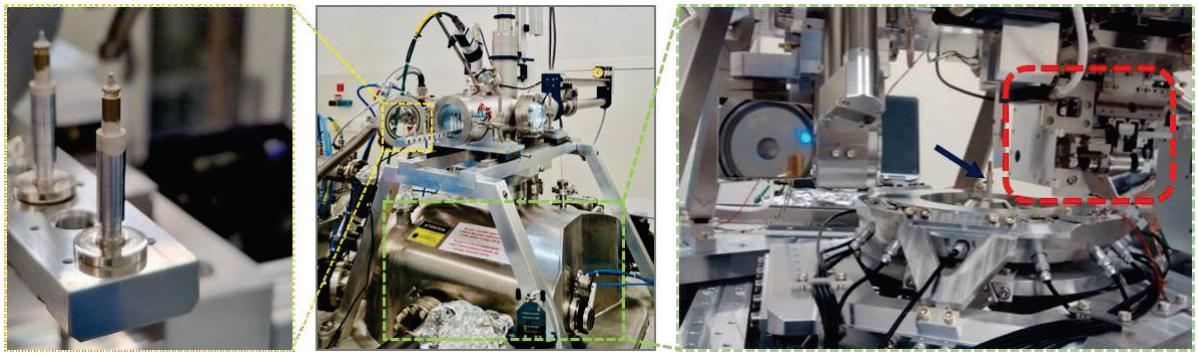

Fig. 3.10 Picture of the ID16A end-station with the vacuum vessel in the closed position (center). On the left, the room temperature sample transfer stage is enlarged, capable of accommodating up to 13 samples in the loadlock. On the right, the end-station is shown with the vacuum vessel open. The blue arrow indicates the sample positioned in the nanopositioning stage, while the housing of the two KB mirrors is highlighted in red.

For scanning the sample and correcting run-out errors of the rotation stage, a short-range piezo-driven hexapod and a metrology framework based on twelve capacitive sensors are used, ensuring accurate nano-positioning and high stability [123]. Translation scanning speeds of 4 µm/s and 1 µm/s in the horizontal and vertical directions, respectively, are achieved. The entire KB nano-focusing optics system and the sample stage are housed within a large vessel under high vacuum (10^{-7} to 10^{-8} mbar). This vacuum environment ensures the stability required for high-precision measurements, while also serving to accommodate cryo experiments (not employed here) and to protect the KB optics from oxidation.

The nanotomography techniques available at the ID16A beamline are Holographic X-ray Computed Tomography (HXCT) [124] and Near-Field Ptychographic X-ray Computed Tomography (NFPXCT) [125] in the phase contrast domain. They are complemented by X-ray Fluorescence Computed Tomography (FXCT) [126] to provide the 3D concentration distributions of individual chemical elements. HXCT and NFPXCT are sophisticated full-field coherent X-ray imaging techniques, both employing the same experimental setup at the ID16A

beamline. The detector is fixed at a focus-to-detector distance of $z_{12} = z_1 + z_2 = 1.265$ m (Fig. 3.11).

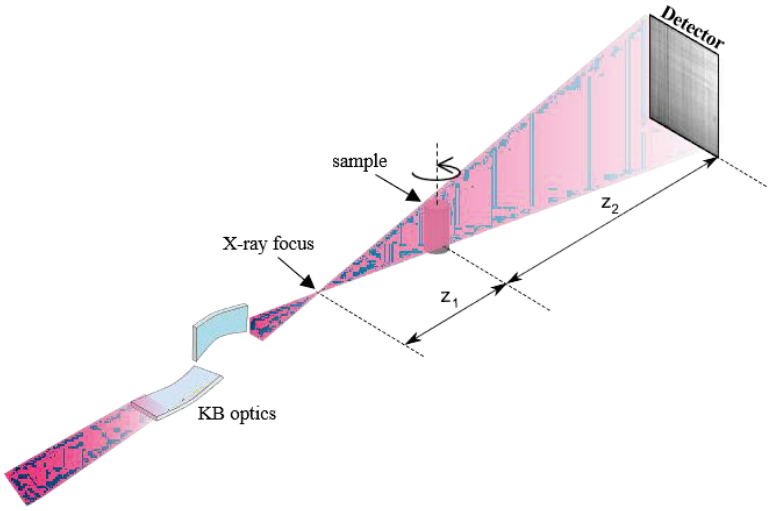

Fig. 3.11 Schematics of the experimental setup at the ID16A beamline. The detector is fixed at a focus-to-detector distance of 1.265 m.

By adjusting the sample's position along the divergent cone beam axis, it is possible to control the target pixel size in the projections, capitalizing on the X-ray magnification. This setup results in the generation of phase contrast images on the detector, where the geometrical magnification M is defined as

$$M = \frac{z_1 + z_2}{z_1} \tag{3.12}$$

with z_1 being the distance from the focus to the sample and z_2 being the distance from the sample to the detector, both measured along the X-ray beam's path.

The effective equivalent propagation distance, D, is defined as:

$$D = \frac{z_1 z_2}{z_1 + z_2} \tag{3.13}$$

In our setup, where the magnification is large ($z_2 >> z_1$), the equivalent propagation distance D is approximately equal to z_1 [118].

The following sections provide detailed descriptions of each imaging technique.

3.3 X-ray Imaging Methods

3.3.1 Holographic X-ray Computed Tomography

Holographic X-ray Computed Tomography is an amalgamation of in-line X-ray holography and computed tomography. This technique exploits the magnification effect of the divergent cone geometry of the beam to achieve the required voxel size in the final reconstructed volume [127]. Due to free-space propagation and the high degree of coherence of the beam, the recorded radiographs are actually magnified Fresnel diffraction patterns in the holographic regime, briefly in-line holograms. They contain both attenuation and phase information. Accurate and robust phase retrieval is achieved by combining radiographs recorded at different sample-to-detector distances along the X-ray beam [124]. For the experiments, usually 2000 projections over 180° are acquired at 4 different focus-to-sample distances with an exposure time of 0.3s per projection. The number of projections was optimized according to the requirements of each experiment and will be outlined in the respective description of the experiments.

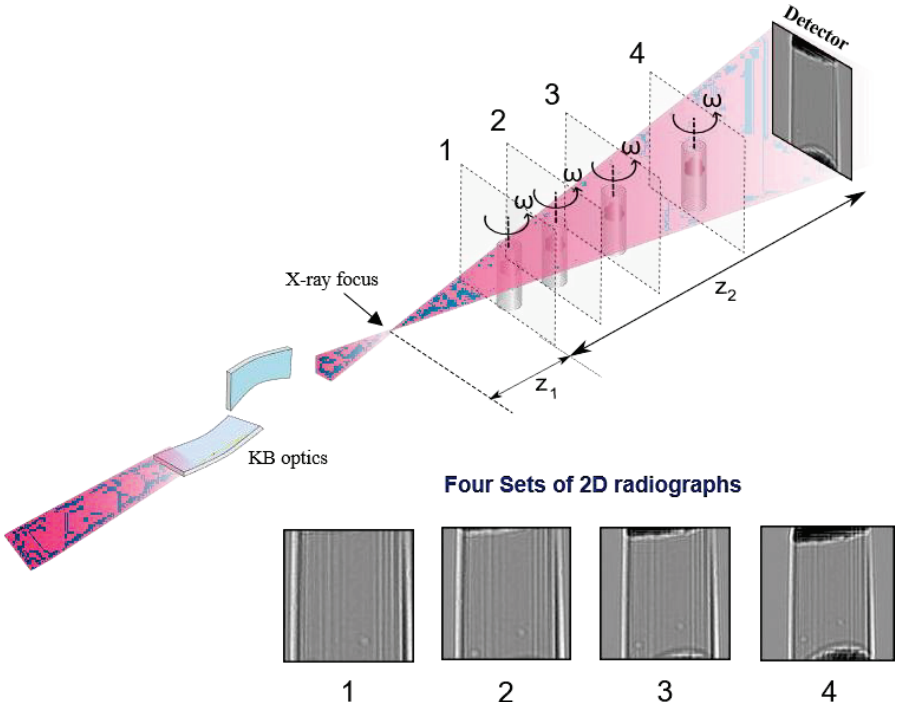

Fig. 3.12 Schematic representation of the Holographic X-ray computed tomography setup at the ID16A beamline. The incoming X-ray beam is focused by the KB optics and the sample is positioned at a distance z_1 from the focus. This configuration produces a phase contrast image on the detector. For tomography, a large number of projections are acquired at various

angular positions (ω), typically across four distinct sample-to-detector distances. Projections or 2D radiographs of a sample are shown at 4 different distances (marked 1-4).

In the case of small samples, the first distance with the highest magnification will be set at the desired voxel size, typically allowing the entire sample to be in the field of view. At each angle, a random (but known) lateral motion is added to the sample to avoid ring artefacts in the final reconstructed volume [128]. To perform a flat-field correction, projections without the sample and dark images were recorded at each distance as well. Prior to phase retrieval, the projections at different distances are interpolated to match the pixel size of the first distance and aligned precisely. The phase maps are obtained by an iterative holographic phase retrieval procedure for each angle.

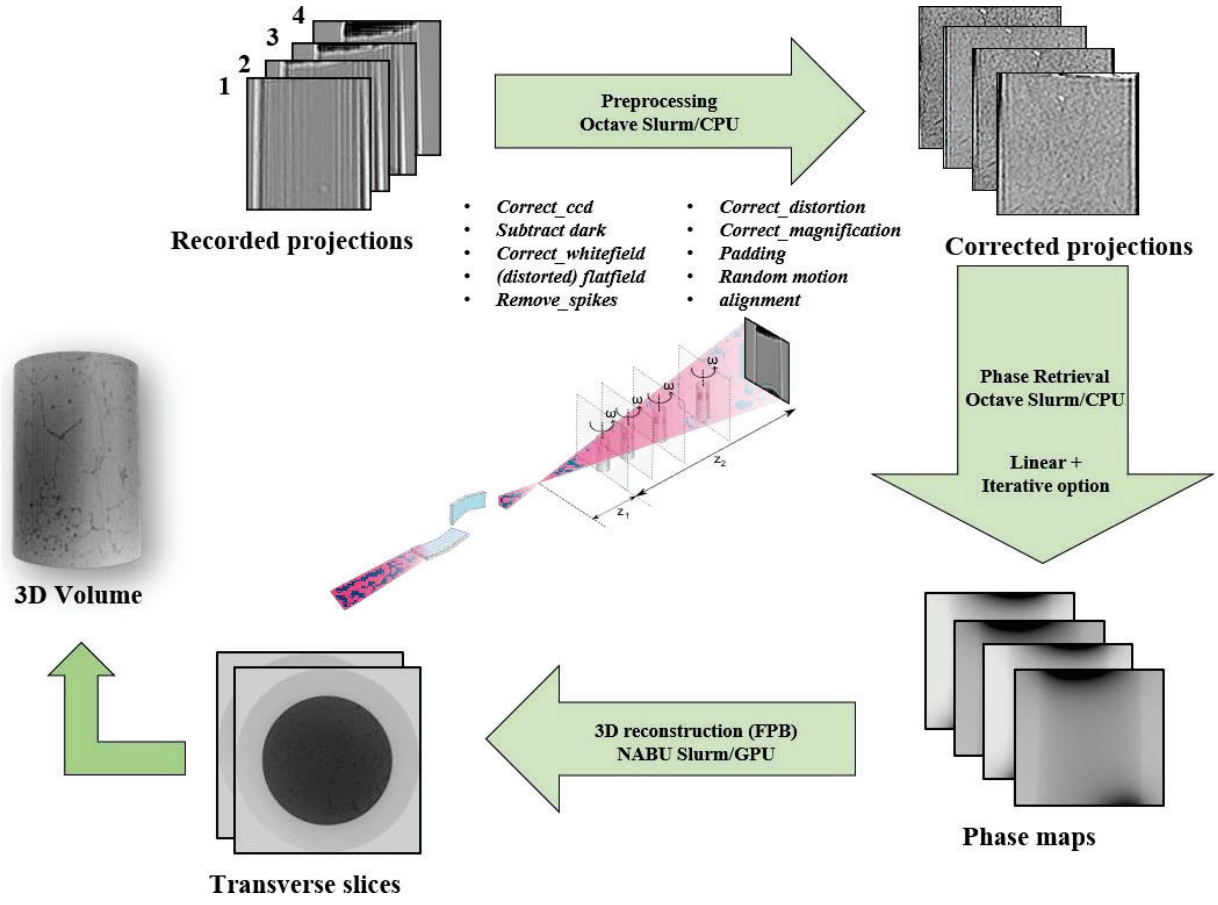

Fig. 3.13 Data processing workflow for HXCT: The workflow outlines the sequential steps from raw data acquisition to 3D reconstruction. Pre-processing and phase retrieval are carried out simultaneously in a single computational step.

The procedure begins by employing the Paganin methodology [129], presuming the sample is comparatively homogenous. This assumption allows for the evaluation of the ratio of refractive

index decrement to absorption coefficient δ/β ≈ 554 at 33.35 keV and δ/β ≈ 201 at 17.1 keV for the Al-1Fe-1Zr alloy. An iterative nonlinear conjugate gradient method (CGM) using this estimation as a starting point enables convergence in 10 -15 iterations to a good solution for the phase map at each angle. The phase retrieval is performed with ESRF in-house code using GNU Octave and ImageJ. As a sufficient number of angles are recorded, the tomographic reconstruction is done using the analytic Filtered Back-Projection (FBP) algorithm on the aligned phase maps with the ESRF in-house Nabu software [130]. Initially, this was conducted with PyHST2 software [131] . The value provided by the reconstruction is

$$\omega = -\frac{2\pi}{\lambda}\delta \tag{3.14}$$

here ω is the grey value of the voxel and δ is the refractive index decrement in the tomogram.

The X-ray wavelength λ is calculated from the energy (λ = 0.3717A˚ and 0.72505 A˚ for E = 33.35 keV and 17.1 keV, respectively). Assuming the 'Guinier' approximation (Z/A ≈ ½), the grey values in the tomograms are essentially proportional to the mass density of the metallurgical phase [132]. With this approximation, the mass density (ρ) was calculated for each voxel as,

$$\rho[g/cm^3] = -\frac{10^{-2}\omega[cm^{-1}]}{1.3\lambda[A^\circ]2\pi} \tag{3.15}$$

3.3.2 Near-Field Ptychographic X-ray Computed Tomography

Near-Field Ptychographic X-ray Computed Tomography (NFPXCT) is an efficient way to retrieve the sample transmission function, T (r) (object) and the incident illumination function, $\psi(r)$ (probe), eqn. (3.10) [119]. Compared to HXCT, this technique can provide higher quality data in terms of signal-to-noise ratio and potentially spatial resolution. A key advantage is that no prior knowledge of sample composition is required, unlike HXCT, which requires to choose the δ/β ratio. However, the acquisition time is longer due to the need to acquire more data. A sequence of holograms is collected at different lateral translations of the sample at a fixed focus-to-sample distance z_1.

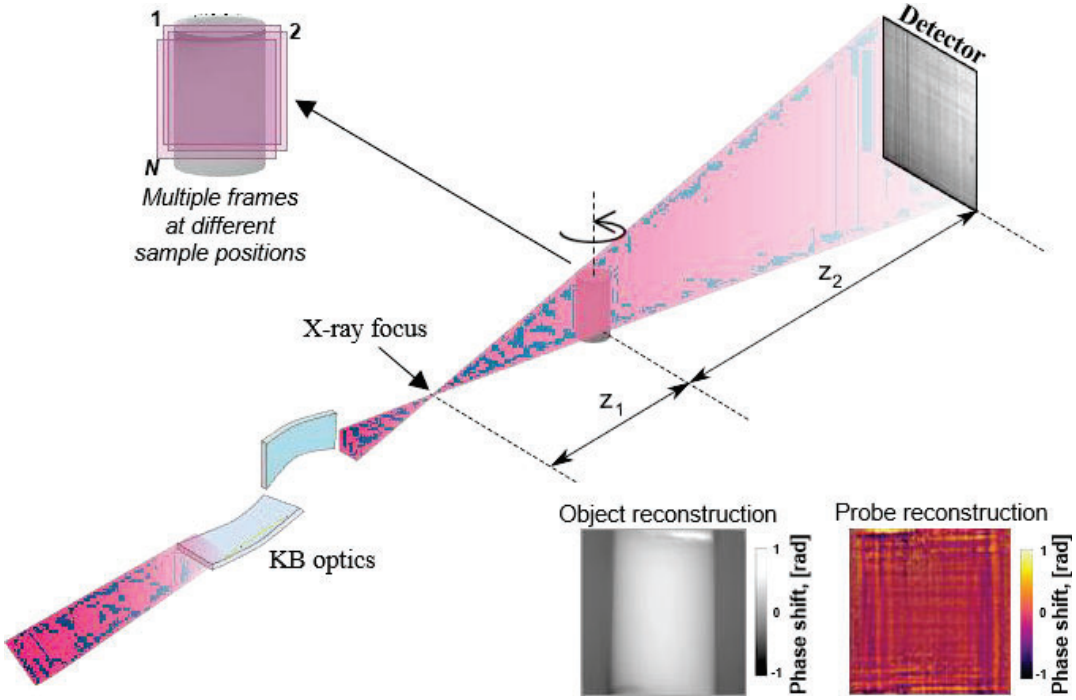

Fig. 3.14 Schematic representation of the Near-field ptychographic X-ray computed tomography setup. The incoming X-rays are focused by Kirkpatrick-Baez (KB) optics, with the sample placed at a fixed distance z_1 beyond the focus. The detector acquires data at 16 different lateral positions of the sample with respect to the illumination. The data is then subjected to an iterative reconstruction process, whereby both the phase shift introduced by the sample transmission function (object) and the incident illumination function (probe) are retrieved. From the four retrieved real-valued images, two are shown in the figure inset; the phase of both the object and the probe reconstruction. In tomography, the procedure is repeated for a large number of angular positions of the sample.

The phase retrieval process in this approach fundamentally relies on the use of structured illumination. Structured illumination introduces a complex mixture between the illumination wavefront and the object, enabling the encoding of both amplitude and phase information into the recorded holograms. In our case, the structured illumination created by the KB optics is leveraged for efficient phase retrieval from the holograms. For the experiments, holograms at 16 lateral pseudo-random (but known) positions [119] of the sample are collected with respect to the illumination for each projection angle, where the sample was at a focus-to-sample distance z1 that defines the desired voxel size in the final 3D volume. To avoid residual ring artefacts a random lateral motion is added to the average sample position at each angle, similar to HXCT [128].

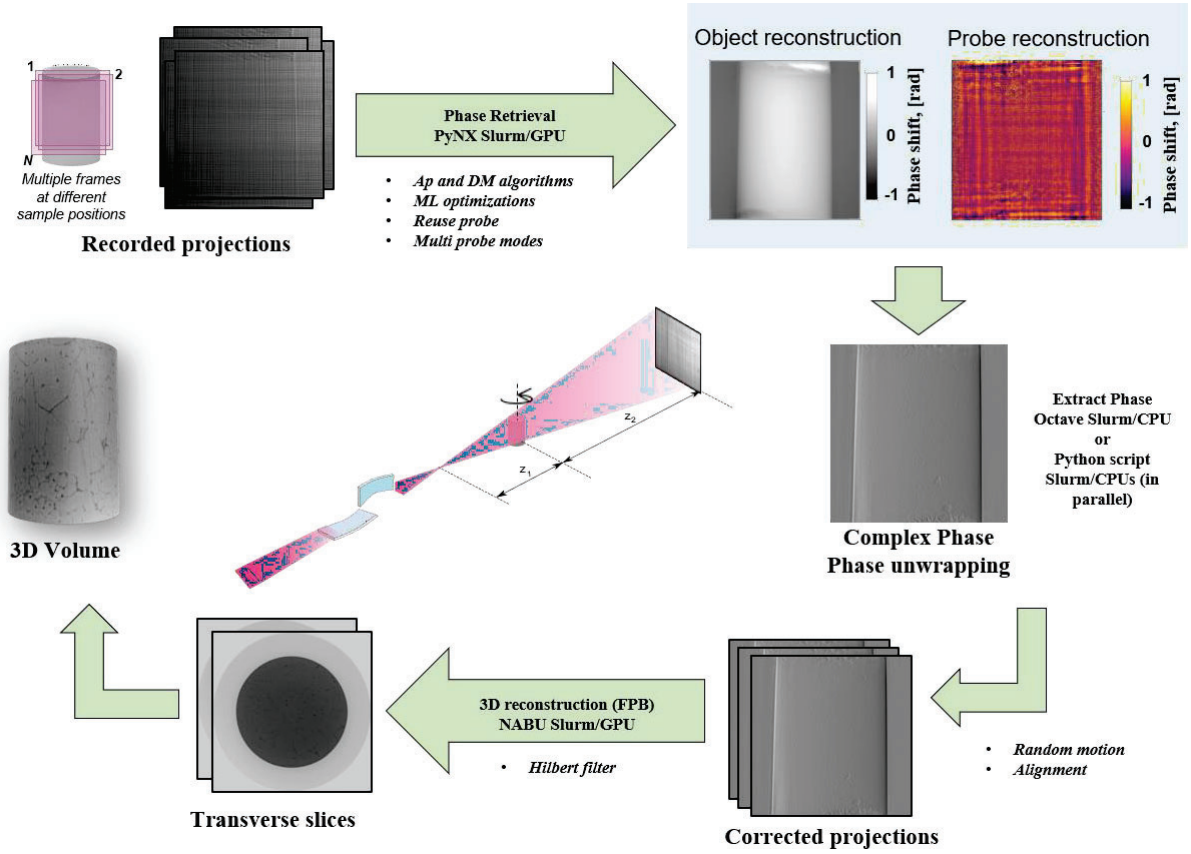

Fig. 3.15 NFPXCT data processing workflow: A step-by-step outline from raw data to the final 3D reconstructions.

The number of projections is optimized similarly to HXCT, according to the requirements of the experiment. The phase retrieval is performed with the Python package PyNX [133]. The phase retrieval of the projections is always initialized using one iteration of Alternating Projections [134]. This is followed by Maximum Likelihood optimization [135], and/or Difference Maps, and/or additional iterations of Alternating Projections. The selection of algorithms, as well as the choice to update the probe or not, was determined on a case-by-case basis, with the number of iterations and sequence of operations tailored to achieve optimal results for each case. Subsequent projections typically used the previous reconstruction as an initial estimate, with further refinements made as necessary to achieve optimal convergence. Finally, in order to avoid phase unwrapping, the tomographic reconstructions are carried out on the horizontal derivative of the phase maps using the FBP method with a Hilbert filter[136] with the ESRF in-house software NABU [130]. The calculation of the mass density (ρ) for the volumes is similar to the HXCT method [132].

3.3.3 X-ray Fluorescence Computed Tomography

XRF provides access to elemental concentrations with high efficiency, down to trace elements. The XRF setup uses two energy resolving X-ray detectors based on multi-element Silicon Drift Detector (SSD) technology.

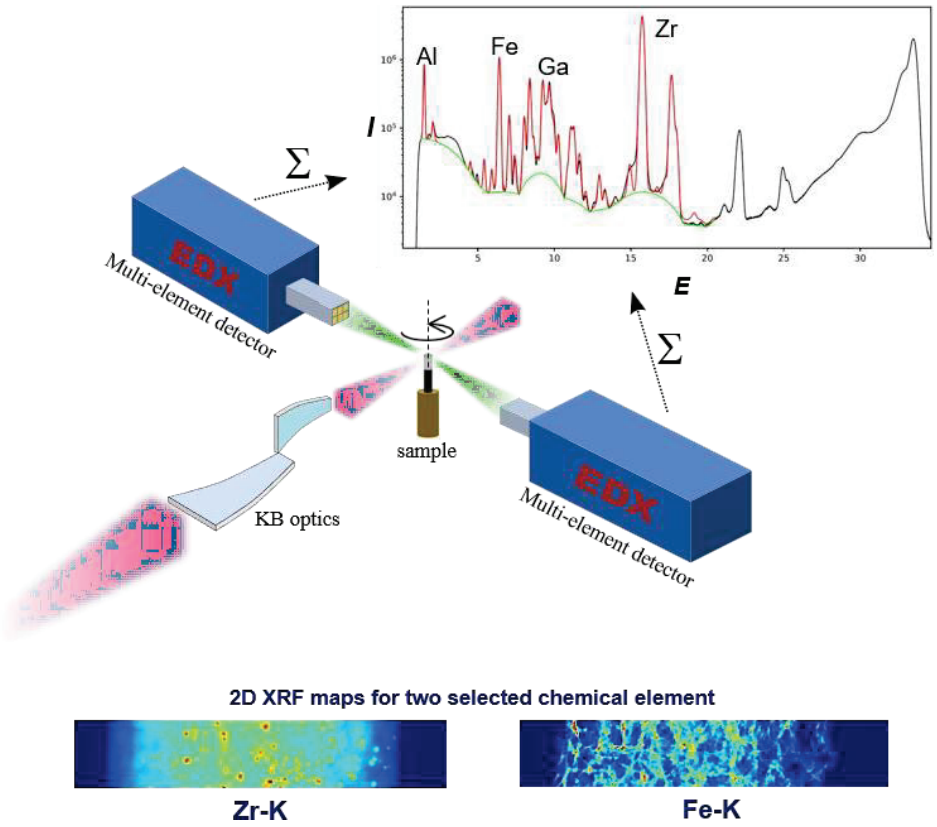

Fig. 3.16 Schematic representation of X-ray fluorescence setup. The incoming X-rays are focused by the KB optics, and the sample is positioned in the focal plane. 2D XRF maps are acquired by scanning the sample on-the-fly through the nanofocus while collecting full X-ray fluorescence emission spectra with energy dispersive detectors. The raw X-ray fluorescence spectra of the extracted sample, summed over the different detector.

The first detector is a custom Ardesia-16 detector from Politecnico di Milano [137] consisting of a monolithic SDD with 16 elements, whereas the second detector is a commercial Vortex ME7 from Hitachi High-Tech Science America consisting of 7 individual close-packed SDD elements. At the X-ray focus, the detectors are positioned on either side of the sample, perpendicular to the beam direction in the horizontal plane. The sample is scanned on-the-fly (grid scan) through the nanofocus while the emitted X-ray fluorescence signal is recorded.

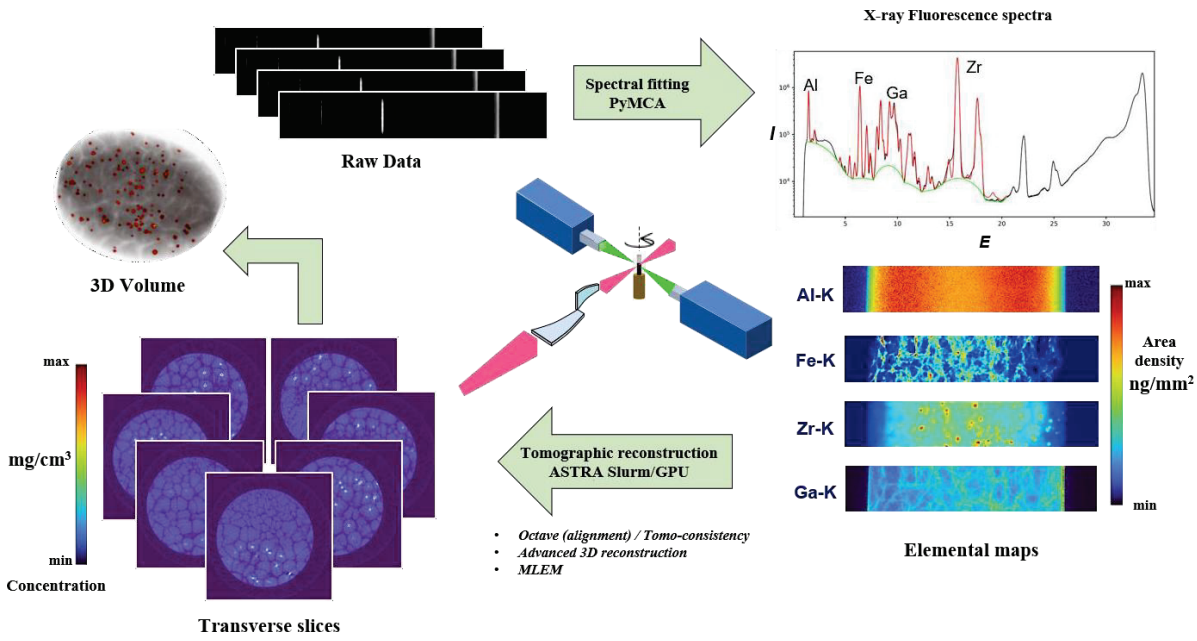

Fig. 3.17 3D-XRF (Fluorescence X-ray computed tomography) data processing workflow: Sequential steps from raw data to the final 3D reconstructions.

Being a scanning method, FXCT is typically orders of magnitude slower than full-field phase imaging methods. To obtain 2D XRF maps the full X-ray fluorescence emission spectra are collected using the energy-dispersive detectors. They are stored for each individual detector element. In addition, a sum spectrum of all detector elements is generated and saved owing to the common energy calibration. The same procedure is repeated for different angular positions of the sample for FXCT. For the experiments, to provide more information about the sample, typically a region of interest was selected based on the observation of more intra- and intergranular features in the reconstructed phase contrast tomography volumes. The field-of-view and pixel step size in the x-y plane are configured according to experimental requirements. Given the extended acquisition times typically required for tomography, scans are divided into sub-tomograms, each spanning a complete 0 – 180° angular range with evenly distributed alternating projections. In this study, the total number of projections necessary for the reconstruction was determined to ensure adequate sampling over the full angular range, with uniform alternate angular spacing maintained within each sub-tomogram. For example, with 64 projections, the first sub-tomogram uses the angular spacing corresponding to the projections 1, 3, 5, ..., 31 (0–180°), while the second uses 32, 30, 28, ..., 2 (180–0°).This approach serves to mitigate potential issues during data acquisition; in the event of an interruption, a single sub-tomogram covering a complete 0 – 180° dataset can still be utilized to reconstruct a fairly good volume. This strategy minimizes the impact of missing angular data

and ensures the reliability of the reconstructed volumes. To improve projection alignment, an additional projection is acquired at 180° if not already included in the sub-tomograms. We usually choose a setting that provides the best compromise between the target resolution and the field of view, while still having a sufficient number of projections.

The spectral fitting and normalization of the XRF data are performed with a Python script using the PyMCA library [138]. The results are 2D maps of the areal mass density (in ng/mm^2) of the different elements in the sample with atomic number $Z > 12$. The projections are then precisely aligned based on the tomographic consistency [139,140]. Contrary to HXCT and NFPXCT, the tomographic reconstruction of each chemical element is done using an advanced algebraic reconstruction method – regularized Maximum Likelihood Expectation Maximization (MLEM) [141] implemented with ESRF in-house software using the ASTRA Toolbox [142].

While the general methodology for HXCT, NFPXCT, and FXCT remains largely consistent, there may be slight variations in the experimental parameters and data processing tailored to the specific cases in the following chapters. The corresponding sections of each chapter will outline these nuanced differences as they apply to each individual study.

4 Phase Contrast and Element-Sensitive Synchrotron Nanotomography of Al-1Fe-1Zr Alloy

4.1 Introduction

The properties of materials are intricately linked to their internal architecture, necessitating detailed non-destructive characterization of microstructural features using 3D X-ray imaging techniques. This relationship is particularly complex in the context of AM materials, where the microstructures are significantly influenced by the complex thermal cycles and high anisotropy inherent to AM processes. These factors result in microstructures that differ from those found in conventionally manufactured materials. Such inconsistencies are evident in the variations observed in grain size, phase distribution, and porosity, not only between AM and traditional materials but also within different regions of the same AM part, depending on the specific processing parameters employed during fabrication. It is therefore essential to gain an understanding of these microstructural variations in order to accurately evaluate the material's properties using 3D X-ray imaging techniques. It is of the utmost importance that the correct imaging parameters are selected and that the microstructural data is accurately interpreted in order to ensure the reliability of the conclusions drawn about the material's properties. Additionally, optimizing acquisition parameters is essential to achieve the best possible balance between characterization quality and the required time and cost. This optimization also facilitates a compromise between spatial resolution and field of view, as exemplified in techniques such as FXCT, enabling efficient and high-quality characterization of the material.

As discussed in the previous chapters, the microstructural features in the Al-1Fe-1Zr alloy exhibit a significant level of complexity, shaped by the material's processing history. At the ID16A Nano-Imaging beamline of the ESRF, advanced 3D X-ray imaging techniques are employed for the detailed characterization of these microstructures. Each of these methods leverages the coherent nature of synchrotron-generated X-rays to produce high-resolution volumetric data, offering unique advantages depending on the application. However, a significant challenge lies in the optimization of experimental parameters to enhance imaging quality and the fidelity of the reconstructed volumes.

The full potential of these techniques can only be realized through meticulous optimization of the experimental parameters, which must be tailored to the specific material and the microstructures under investigation. This chapter aims to explore how these experimental strategies can be optimized, not only for the current samples but also for similar samples that could benefit from these investigations in the future. Special attention will be given to optimizing parameters such as the number of projections, the energy of the X-rays, and the application of techniques like random displacement to improve the overall quality of the data and the efficiency of the imaging process. The goal is to establish a robust framework that facilitates the best possible evaluation of microstructures, enhancing both the resolution and the accuracy of the data obtained.

Moreover, this study aims to provide a detailed examination of the ultrafine internal structure, morphology, and local mass density of the Al-1Fe-1Zr alloy. This is done by employing the phase-contrast nanotomography techniques. Additionally, a comparative evaluation of HXCT and NFPXCT was conducted, focusing on their performance in terms of acquisition and reconstruction time, and the quality of the reconstructed volumes. Both techniques offer critical insights into the internal architecture of the alloy but differ in their approaches to the reconstruction process and the trade-offs between speed and resolution. These insights are further complemented by FXCT, which provides a comprehensive view of the internal structure and composition, enabling the quantitative analysis of local elemental distributions in 3D.

The principal goal of the research presented in this chapter is to address the following key questions:

- *What are the capabilities of the different 3D Synchrotron-Based X-ray Imaging Techniques available at the ID16A Nano-Imaging beamline of the ESRF and how can they be optimally applied to characterize Al-1Fe-1Zr alloy?*
- *What methodological optimizations and parameter modifications were introduced to the experimental setup to enable a comprehensive 3D characterization of the microstructures?*

To answer these questions, several samples of the alloy were systematically studied. While the primary focus remained on investigating the microstructures, various experimental optimizations were also explored to enhance the effectiveness of these advanced imaging techniques.

4.2 X-ray Energy Criterion

The choice of X-ray energy at the ID16A beamline is a nuanced decision that must consider the specific demands of the imaging technique and the material under study. The different techniques may necessitate a tailored approach to X-ray energy, particularly when investigating materials with varying densities and compositions or when conducting correlative studies that require both phase contrast imaging and X-ray fluorescence analysis.

For the Al-1Fe-1Zr alloy, the choice of X-ray energy directly impacts the balance between contrast, spatial resolution, and the minimization of artefacts. The ID16A beamline provides two primary X-ray energies: 17.1 keV and 33.35 keV, each offering distinct advantages depending on the specific imaging requirements.

For HXCT, to illustrate the impact of the two X-ray energies, measurements were conducted using the same pixel size of 10 nm, acquiring 2000 projections with an exposure time of 0.3 seconds per radiograph and applying a random displacement of 50 pixels.

The phase maps obtained at 17.1 keV (Fig. 4.1 a) demonstrate that this lower energy X-ray provides enhanced contrast, which is particularly effective for highlighting fine features within the alloy. This effect arises from the increased interaction of lower-energy X-rays with the sample, which enhances differential interactions and emphasizes variations in density and composition within the material. As described in equation (3.3), the phase shift Φ is proportional to the X-ray wavelength λ and thus inversely proportional to the energy E. Specifically, the phase shifts are approximately halved due to the shorter wavelength at the higher energy, when switching from 17.1 keV to 33.35 keV. This results in a greater differential interaction, thereby accentuating the differences in density and composition within the material. However, this advantage is accompanied by a drawback in the form of pronounced artefacts, which must be taken into account when interpreting the results. Fig. 4.1(c) illustrates the phase map after applying a bandpass filter for the purpose of normalizing the cylindrical profile of the sample. The aforementioned artefacts become evident, which are predominantly associated with inhomogeneous wavefront correction. As previously stated in section 3.2.2, two KB mirrors are available, one for each energy. It can be observed that the artefacts are pronounced, which is likely attributed to the specific characteristics of the beam features produced by the KB mirror of 17.1 keV energy. The corresponding line profile plot (Fig. 4.1 e) serves to further highlight these artefacts, which are particularly evident at the sample edges, where they have the potential to significantly obscure image information.

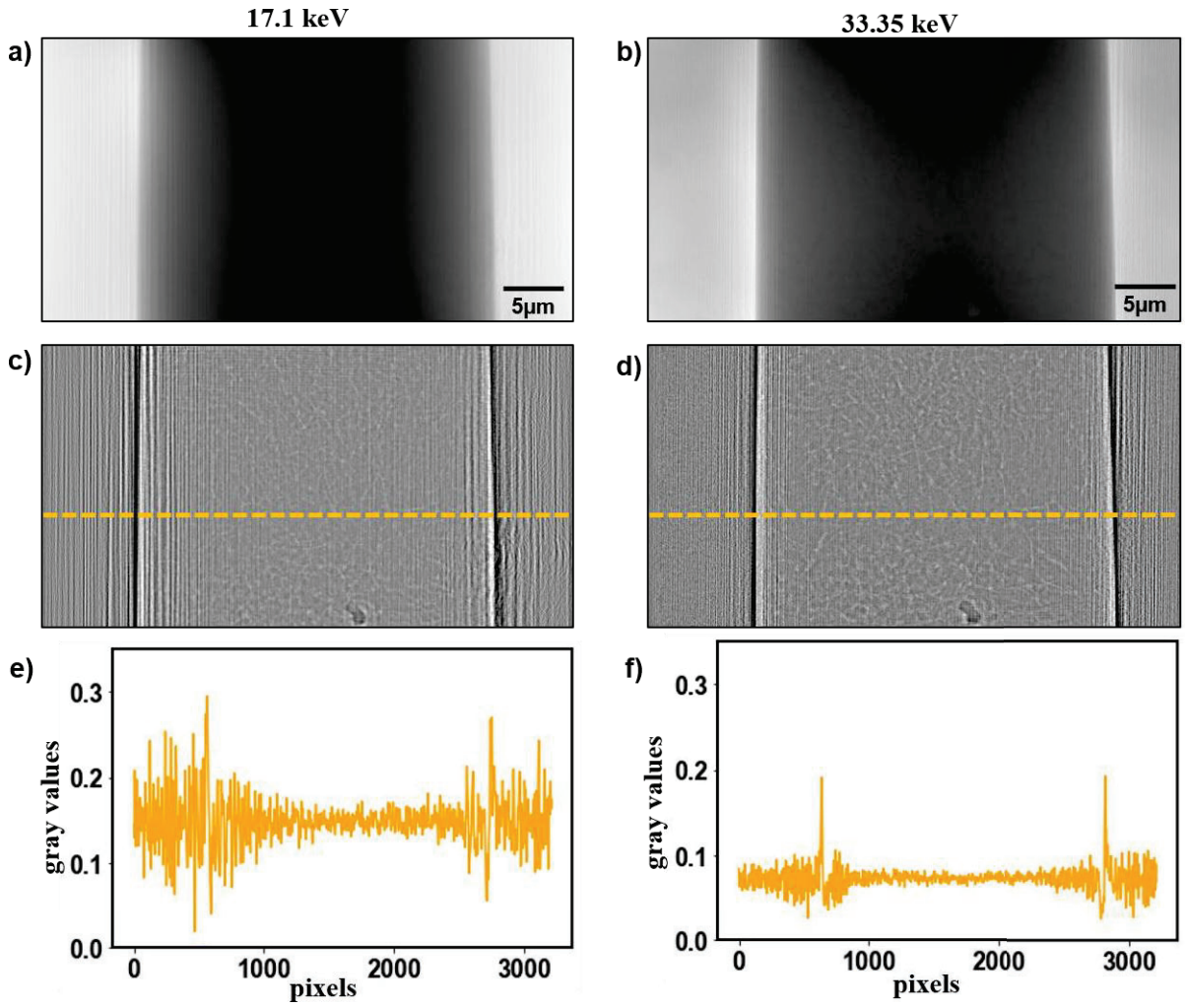

Fig. 4.1 Phase maps from HXCT at 17.1 keV and 33.35 keV are presented in (a) and (b), respectively. Images (c) and (d) show the phase maps after applying a bandpass filter to normalize the cylindrical profile of the sample, allowing for better visualization of residual artefacts for the respective energies. The corresponding line profile plots in (e) and (f), along the marked orange line, illustrate the presence of strong artefacts at 17.1 keV, which are significantly reduced at 33.35 keV. The pixel size in all images is 10 nm.

In contrast, the phase maps at 33.35 keV (Fig. 4.1 b) demonstrate a substantial reduction in these artefacts, as seen in the bandpass filtered image (Fig. 4.1 d) and the line profile plot (Fig. 4.1 f). Although the overall contrast at this higher energy is reduced by approximately a factor of two compared to 17.1 keV, the enhanced image quality, characterized by a reduction in artefacts, facilitates a more precise analysis of the sample's internal structure. This reduction in artefacts at 33.35 keV is of critical importance for the reliable acquisition of data, particularly in situations where the subsequent post processing of microstructural features is required.

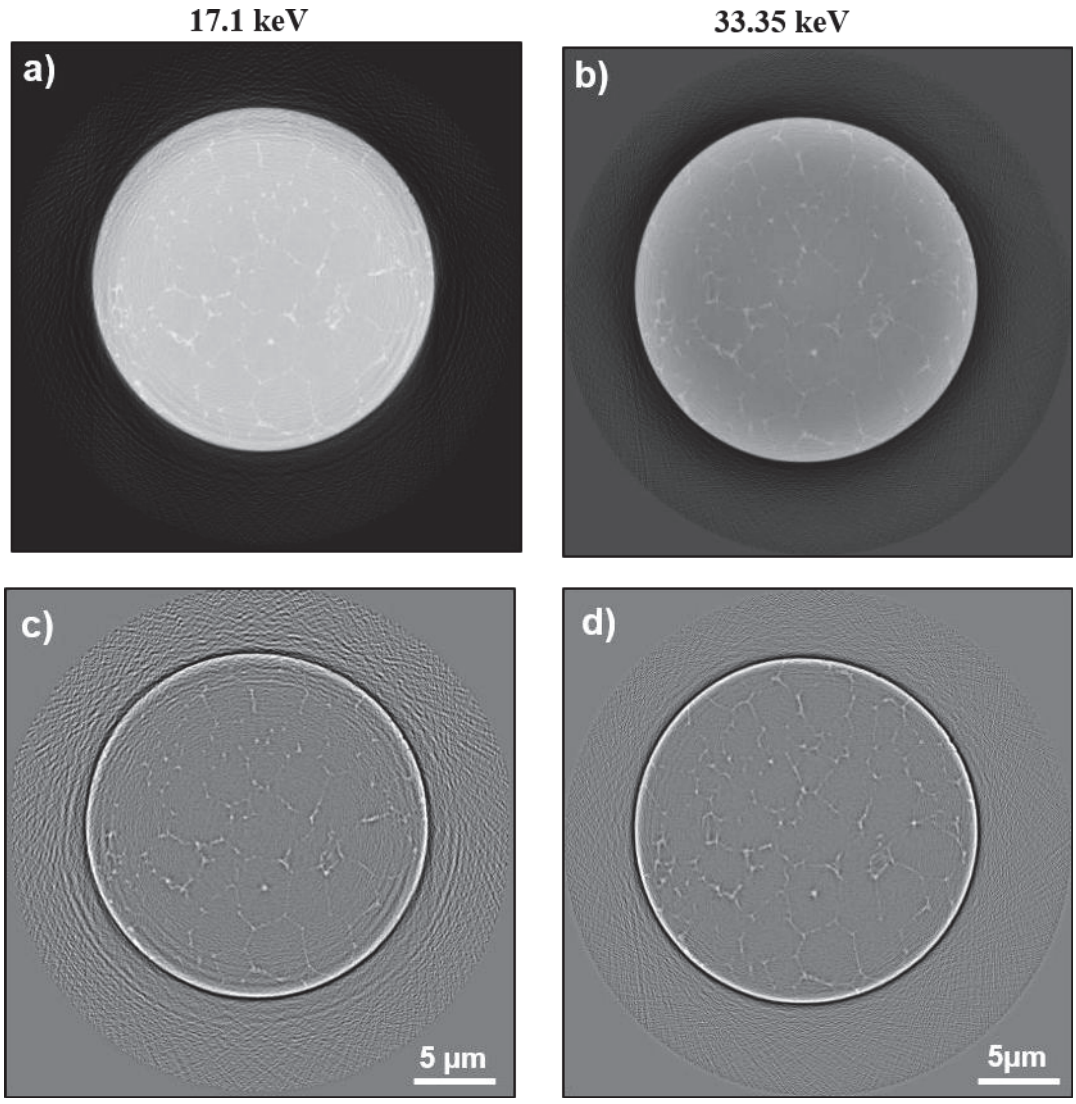

Fig. 4.2 The radial slices of the reconstructed HXCT volumes at 17.1 keV and 33.35 keV are shown in (a) and (b), respectively. While the contrast is noticeably higher at 17.1 keV, this comes at the expense of strong ring artefacts, particularly evident in the bandpass-filtered images (c) and (d) corresponding to each energy, with the most pronounced artefacts appearing at the sample periphery.

The reconstructed HXCT volumes demonstrate the result of these artefacts. As illustrated in Fig. 4.2 (a), the 17.1 keV energy yields volumes with markedly enhanced contrast, which is beneficial for visualizing the intricate details of the alloy's microstructure. However, this advantage is counterbalanced by the emergence of pronounced ring artefacts, as evidenced in the bandpass-filtered images (Fig. 4.2 c), especially at the periphery of the sample. Such ring artefacts have the potential to restrict the accuracy during image analysis, which could result in misinterpretations of the image information.

Conversely, the reconstructed volumes at 33.35 keV (a slice is shown in Fig. 4.2 b) demonstrate a notable decrease in these ring artefacts, as shown by the bandpass filtered image (Fig. 4.2 d). Although the contrast at this higher energy is reduced, the considerable reduction in artefacts results in a more accurate and reliable extraction of information and visualization. This makes 33.35 keV a more suitable option for HXCT measurements.

In the context of Near-Field Ptychographic X-ray Computed Tomography (NFPXCT), both the sample transmission function (object) and the incident illumination function (probe) are retrieved simultaneously. The experimental conditions were identical, including a pixel size of 5 nm, 2400 projections with a 0.3 seconds exposure per radiograph, and a random displacement of 50 pixels at the two energies. The phase retrieval for both energies was done using one iteration of Alternating Projections [134] followed by Difference map [143] for 400 and Maximum Likelihood optimization [135] for 200 iterations while updating the probe.

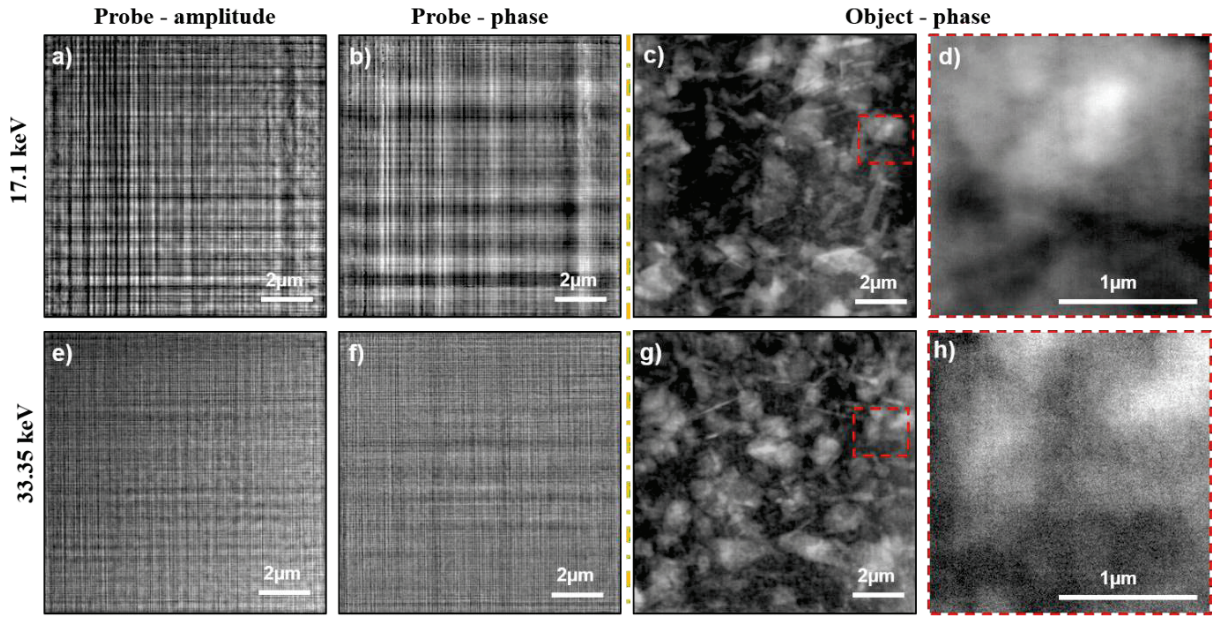

Fig. 4.3 Amplitude and phase maps of the probe at 17.1 keV are shown in (a) and (b), respectively, while the corresponding maps for 33.35 keV are displayed in (e) and (f) (same sample but different regions). The reconstructed phase maps of the object at 17.1 keV and 33.35 keV are presented in (c) and (g). Enlarged regions (marked red in c and g) of the object phase maps are provided in (d) and (h).

The phase maps reconstructed at 17.1 keV exhibit considerably enhanced clarity, with minimal noise, thereby demonstrating the superior performance of this lower energy setting in capturing fine structural details. This is especially pertinent for NFPXCT, where the objective is to attain

high-quality phase contrast imaging, particularly for such high-resolution measurements. The minimal noise at 17.1 keV enables a more precise interpretation of the specimen's internal features and is also crucial for microstructural post-processing analysis. Conversely, the phase maps acquired at 33.35 keV demonstrate a notable increase in the level of noise, particularly in the finer details of the reconstructed phase maps. This elevated noise level is discernible in the magnified regions, where it becomes evident that the phase maps at 33.35 keV are susceptible to potentially lower object information. The increased noise at this higher energy likely stems from the reduced interaction at 33.35 keV, leading to less intrinsic contrast in the KB beam at higher energy and less 'mixing' of the probe and object information. As a consequence, the extraction of phase information is less efficient. This indicates that, although higher X-ray energies can be advantageous in certain circumstances, they are less appropriate for NFPXCT when the main aim is to obtain high-resolution phase contrast images with minimal noise.

For correlative studies combining phase-contrast imaging with X-ray fluorescence, 33.35 keV is the required energy. This choice is driven by the need to excite the K-edge of Zr, which is critical for effective fluorescence imaging. Additionally, using this energy increases the efficiency of fluorescence imaging by minimising the self-attenuation of the emitted radiation, while also allowing the simultaneous acquisition of both phase contrast and fluorescence data.

4.3 Random Displacement Technique

The 3D data generated by X-ray nanotomography provide critical insights into the properties of materials; however, the extraction of precise information is often compromised by the presence of ring-shaped artefacts in the reconstructed slices . These artefacts, which result from imperfections in the X-ray optics, residually present after flatfield correction or non-uniform detector pixel response, are localized at specific pixels across all angular projections, producing rings in the transverse cross-sections of the 3D dataset [144–146].

To mitigate these artefacts, a technique known as random displacement is employed during the scans at the beamline [147]. This method involves randomly moving the sample orthogonally to the incoming beam between successive tomographic angles. By realigning the projections during data processing, the essential information about the object is correctly overlaid while the artefacts introduced by the beam's amplitude and phase gradients are smeared out [147].

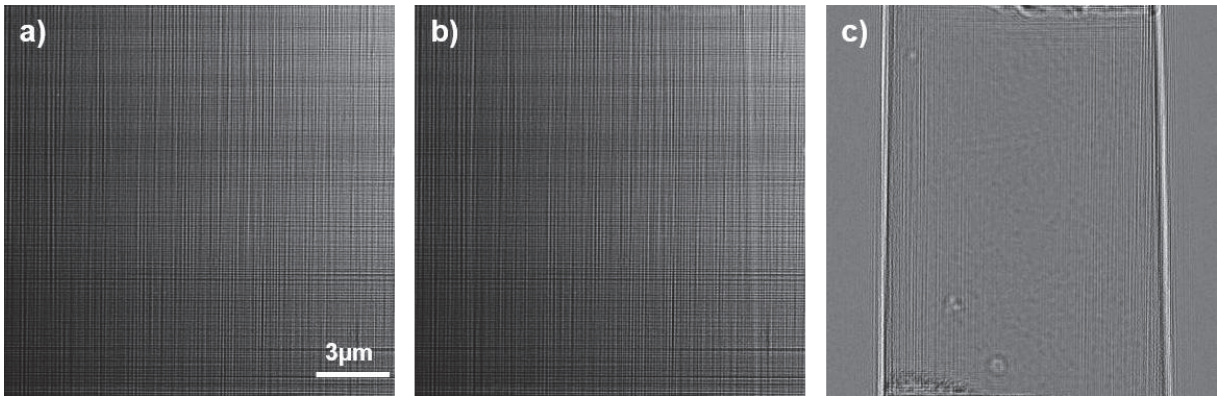

Fig. 4.4 Illustration of the object-probe mixing in a sample. Image (a) shows the projection without the sample, while (b) displays the raw projection with the sample present. (c) presents the projection after correcting for the empty beam, it shows the prominent residues from the probe at the edges of the sample that remain after flat field correction.

The range of the random displacement is carefully determined by several factors, including the speed of the piezoelectric stages, the scan duration, and the characteristic size of the beam features that could degrade the 3D reconstruction [128]. To streamline the process, the lateral movement of the piezo stages is synchronized with the incremental rotation of the sample, ensuring high spatial resolution while maintaining stability at each angle. The exact positions of the sample for each angle and displacement are recorded during the scan and later used during phase retrieval to realign the projections. This approach eliminates the need for additional post-processing, as the phase maps are automatically aligned. Displacement ranges of 25, 50, 100, and 150 pixels were tested for a study to understand the effect of random displacement with the same other experimental parameters. The corresponding reconstructed volumes are shown in Fig. 4.5. This was employed during a HXCT scan at 33.35 keV, with a pixel size of 10 nm. Generally, for larger pixel sizes, a displacement range of 25 pixels is commonly used to minimize the impact on scan time.

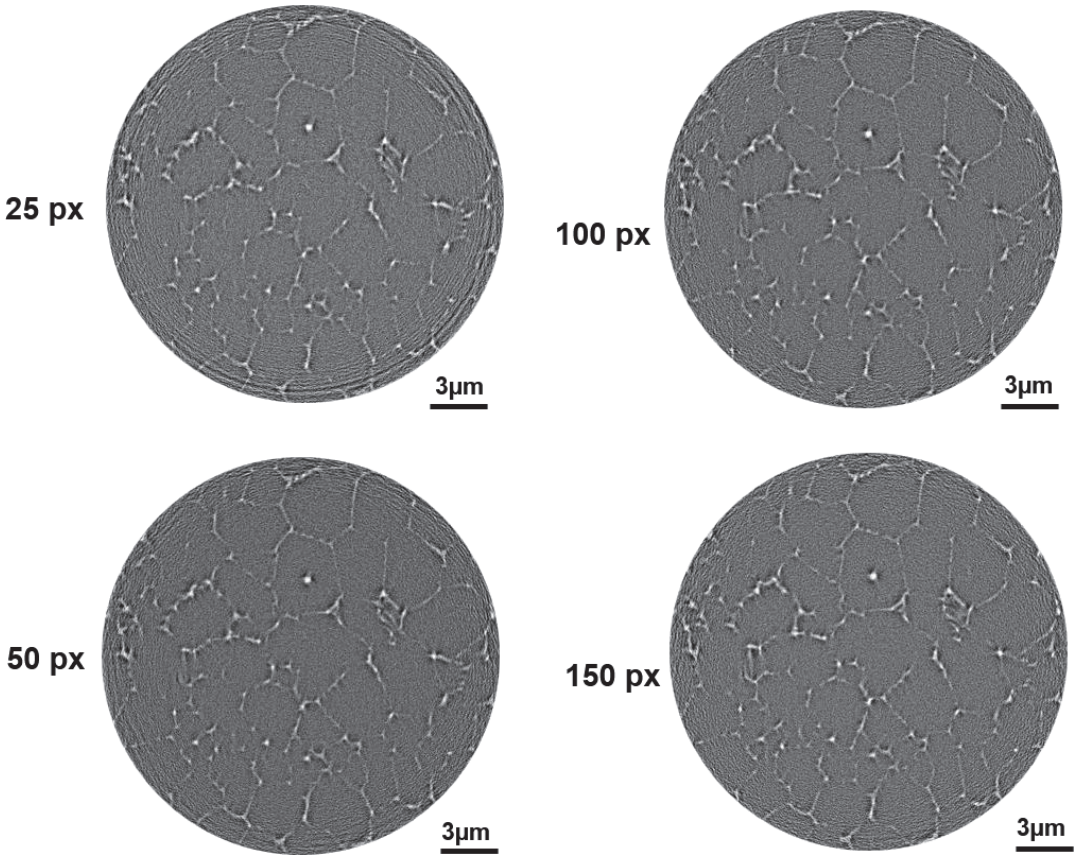

Fig. 4.5 Comparison of the effects of varying ranges of random displacement on the image quality of the same radial slice of a HXCT volume. The 25px displacement exhibits pronounced ring artefacts due to the characteristic size of the beam features, while a 50px displacement shows a modest reduction in these artefacts. A 100px displacement demonstrates a significant improvement, effectively smearing out the rings, and offers an optimal balance between acquisition time and signal-to-noise ratio (SNR). A 150px displacement results in only a slight further improvement.

Table 4.1 The relationship between the random displacement used during scanning, the resulting SNR, and the corresponding acquisition time is shown for a pixel size of 10 nm.

Random Displacement (px)	Acquisition time (mins) for 4 distances (HXCT)	SNR
25	160	2.4
50	162	2.65
100	166	3.5
150	172	3.6

Among the available definitions [148,149], the straightforward expression provided in Eq. (4.1) has been utilized to calculate the SNR:

$$SNR = \frac{\mu\ (sample)}{\sigma\ (bkg)} \tag{4.1}$$

Here, μ (*sample*) represents the mean grey-level value measured within the sample, while σ (*bkg*) refers to the standard deviation of the background, which is measured in a region selected outside the sample, typically in the air or vacuum.

The data presented in Table 4.1 underscores the impact of varying random displacement ranges on both image quality and acquisition time, with a clear correlation between increased displacement and improved SNR (deduced from the radial slices). With a 25px displacement, ring artefacts are particularly pronounced, likely due to the characteristic size of the beam features. Increasing the displacement to 50px leads to a modest reduction in these artefacts. This progression highlights a significant enhancement in image quality at 100px displacement, where the SNR markedly improves from 2.65 to 3.5. However, the SNR gain from 100px to 150px is minimal, increasing only slightly.

In terms of acquisition time, it reflects a gradual increase in time required with larger displacements (for 10 nm pixel size). Despite the time increase, the 100px displacement strikes an effective balance by providing a substantial improvement in SNR and significantly smearing out ring artefacts, with only a modest additional time investment of 6 minutes over the 50px displacement for 10nm pixel size. The observed ring artefacts are not continuous, as typically seen, and their size is comparable to the sample features and the wavefront inhomogeneities. Additionally, the quality of the reconstructed image obtained with the optimal random motion facilitates easier post-processing. While the 100px displacement significantly mitigates the ring artefacts, it does not entirely remove them, indicating the need to explore other options for completely eliminating such artefacts in these types of samples.

4.4 Impact of the number of projections

In X-ray tomography, the number of projections acquired during a scan represents a fundamental parameter that directly influences the quality of the reconstructed image. The number of projections determines the resolution, reconstruction artefacts, and overall quality of the volumes. Increasing the number of projections generally improves resolution and reduces artefacts, but this improvement comes at the cost of longer acquisition times and increased computational demands. The relationship between the number of projections and the quality of the reconstructed tomographic image is inextricably linked to the angular separation between each projection. The angular separation should ideally match the voxel size, b_{vox}, at the edge of the field of view (FOV) for 180°. This can be estimated using a simple rule of thumb, where the number of projections is calculated using the equation:

$$N_{proj} \geq \frac{\pi}{2} \left(\frac{FOV}{b_{vox}}\right) \tag{4.2}$$

Although this formula provides a simplified representation of the underlying physics, it offers a practical starting point for estimating the minimum number of projections required to achieve a desired resolution. Furthermore, oversampling, or the acquisition of an excessive number of projections, has the potential to introduce practical complications. Prolonged scans may result in sample drift, particularly in cases where the samples are not stabilized. This can lead to a degradation in the quality of the reconstruction. This effect is particularly pronounced in the case of ultrafine microstructures, where it is of the utmost importance to achieve an optimal balance between resolution, scan duration and the minimisation of artefacts.

In HXCT, a standard number of projections is typically set at 2000, as this offers a balanced compromise between scan duration, spatial resolution, and artefact minimization, making it suitable for many experiments. However, according to eqn. 6.2, with a pixel size of 10 nm and a FOV of 2048 x 2048 pixels, the minimum number of projections required for optimal reconstruction is approximately 3200. To investigate the effects of varying projection numbers on tomographic reconstruction quality, a systematic experiment was carried out on an Al-1Fe-1Zr sample.

The projection numbers of 1000, 2000, 4000, and 8000 were selected based on a systematic geometric progression designed to investigate the impact of the number of projections on reconstructions. The calculation from eqn. 4.2 indicates the selection of 4000 as a value slightly

above the minimum threshold for high-resolution imaging. Given that 2000 projections represent the standard for HXCT, this figure was selected as a baseline for typical acquisition conditions. The doubling of the projection number to 4000, and then again to 8000, permitted the assessment of incremental enhancements in image quality, while 1000 projections served as an undersampling case for comparison.

A total of 8000 projections were acquired in a single scan to acquire all necessary data at four increasing distances from the X-ray focus for HXCT. Subsequently, the data was reconstructed using subsets of 1000, 2000, 4000, and 8000 projections. The scan was performed with a pixel size of 10 nm, an exposure time of 0.3 seconds per projection, and an energy of 33.35 keV. Additionally, a random displacement of 100 pixels was applied to reduce ring artefacts.

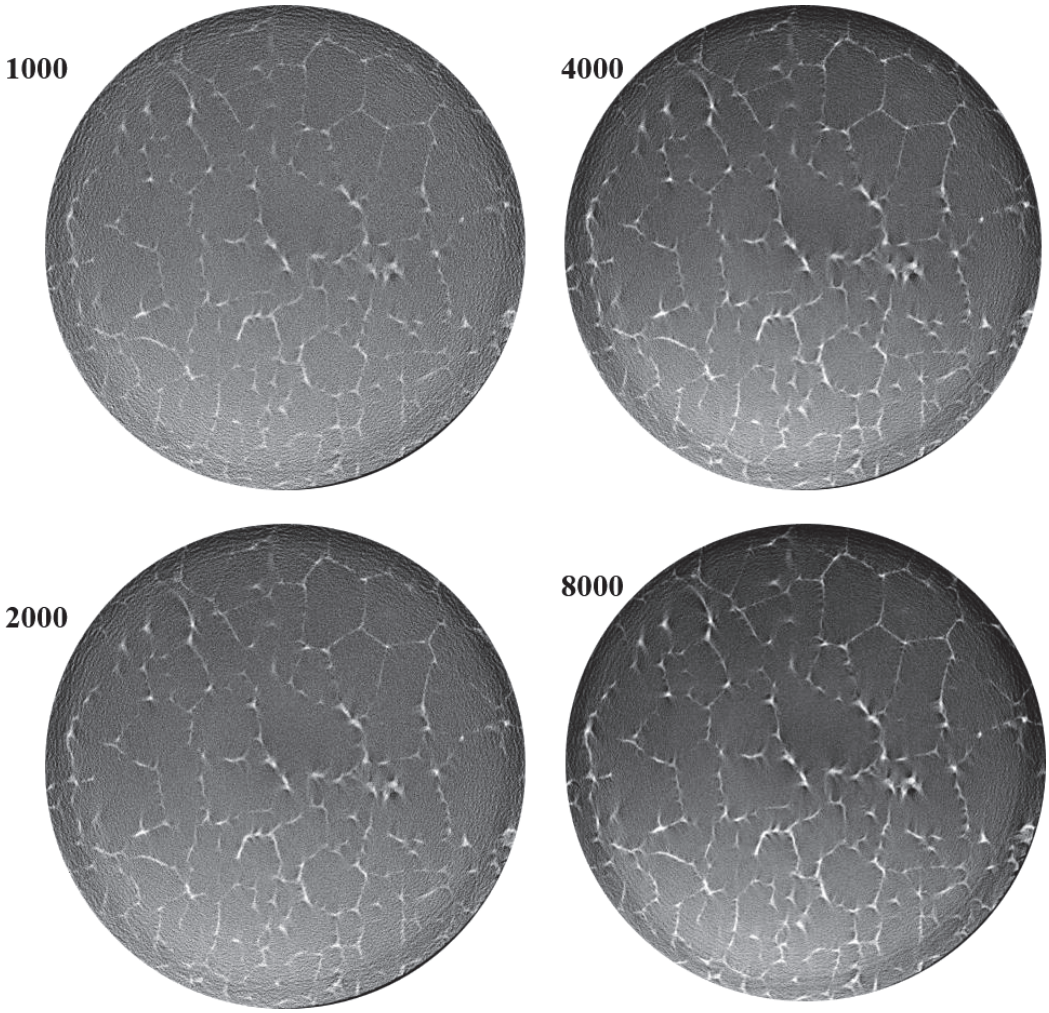

Fig. 4.6 Radial slices of reconstructed tomographic volumes using 1000, 2000, 4000, and 8000 projections, demonstrating the effect of projection count on image quality and noise.

Fig. 4.6 presents the radial slices of the reconstructed tomographic volumes for 1000, 2000, 4000, and 8000 projections, which illustrates the impact of projection count on image quality.

At 1000 projections, the image is significantly undersampled, resulting in the emergence of pronounced reconstruction artefacts and noise. The corresponding signal-to-noise ratio (SNR) is notably low, at 2.9. As the number of projections increases, there is a considerable improvement in image quality, with an increase in the signal-to-noise ratio.

Table 4.2 Influence of projection count on tomographic volume reconstruction and corresponding SNR

N_{proj}	SNR
1000	2.9
2000	3.5
4000	4
8000	4.2

Using 2000 projections, a considerable enhancement in image clarity and a reduction in artefacts can be observed, indicating that this number of projections represents a significant improvement over the undersampled case. At 4000 projections, the image quality attains an optimal level, exhibiting minimal noise and clear structural detail. Nevertheless, when the number of projections is increased to 8000, the improvement in image quality becomes marginal, with the signal-to-noise ratio rising only slightly from 4.0 to 4.2. These results indicate that the additional benefits of acquiring more than 4,000 projections may be minimal, particularly when considering the associated costs in terms of time and data management.

As illustrated in Fig. 4.7, the presentation of a selected region of interest from the axial slices of each reconstruction serves to demonstrate the reduction of stripe artefacts as the number of projections increases. Stripe artefacts, which are commonly observed in data obtained from undersampled tomography, represent a significant source of image degradation. At 1000 projections, these artefacts are highly visible, contributing to a noisy image. As the number of projections increases to 2000 and 4000, the artefacts are progressively reduced. By 4000 projections, the stripe artefacts are minimal, and no significant further reduction is observed at 8000 projections. This indicates that 4000 projections provide an optimal balance between artefact suppression and practical scan time.

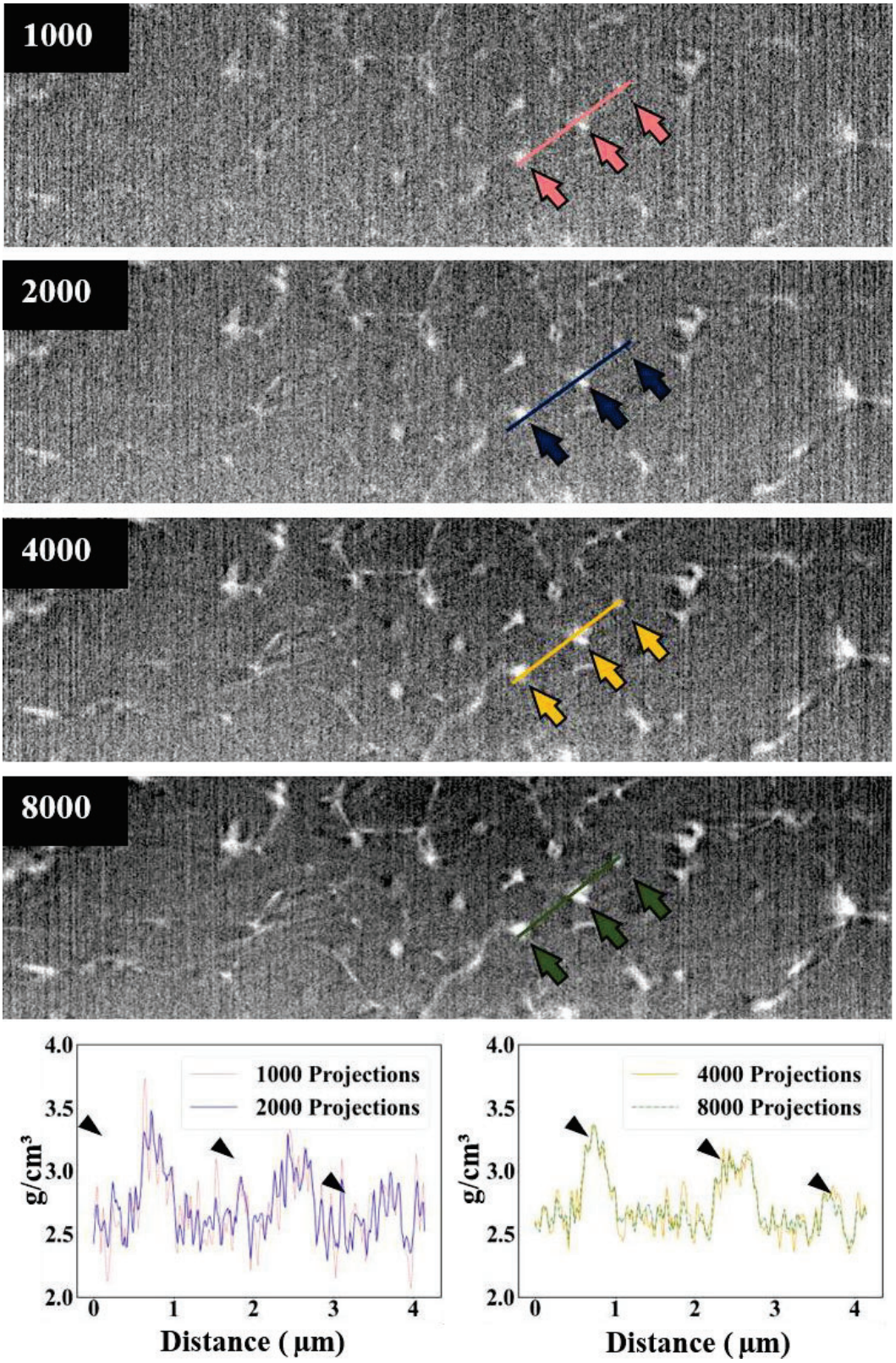

Fig. 4.7 Axial slices of a region of interest from reconstructions using 1000, 2000, 4000, and 8000 projections, showing the reduction of stripe artefacts with increasing projections. Line

profile plots of mass density demonstrate significant variations at 1000 projections, with smoother profiles observed as projection numbers increase.

A quantitative analysis of the reconstructed volumes was conducted through the examination of the line profiles extracted from each volume. The profiles demonstrate considerable variability and noise at 1000 projections, which impairs the precision of the representation of the sample's total mass density distribution. As the number of projections increases, the line profiles become progressively smoother, particularly at 4000 projections, which accurately represent the actual density variations within the sample. Although the profile for 8000 projections exhibits a slight further improvement in smoothness, the difference is minimal, thereby reinforcing the conclusion that 4000 projections are sufficient for the generation of high-quality reconstructions within the context of this experimental procedure.

These findings are crucial for optimizing synchrotron-based tomography experiments, where the balance between scan time, data quality, and artefact minimization must be meticulously managed. Furthermore, as techniques such as HXCT and NFPXCT are employed for the quantitative analysis of microstructures, selecting the optimal number of projections ensures that the reconstructed volumes accurately reflect the internal architecture of the material, free from undersampling or excessive noise.

4.5 Faster nano-positioning using a real-time control system

Precise and faster nano-positioning control system is essential for achieving high-resolution imaging within practical acquisition times, while also maintaining spatial resolution fidelity. The implementation of a real-time control system at the ID16A beamline of the European Synchrotron Radiation Facility (ESRF), commercially known as Speedgoat, marked a significant advancement in nanoscale synchrotron imaging capabilities. Integrated by Thomas Dehaez, Francois Villar (ISDD/ESRF) and the ID16A beamline staff, it delivered notable improvements in acquisition times and data quality.

In this work, the upgraded real-time control system was applied for the first time to high-resolution 3D FXCT imaging (Chapter 6), leading to a significant improvement in acquisition efficiency. For HXCT scans at a voxel size of 15 nm^3 and a random displacement of 25 pixels, acquisition time was reduced from ~2.5 hours to 2 hours. Although relatively modest, the improvements were more substantial for FXCT. A direct benchmark comparison between the legacy and upgraded systems, conducted under identical scan conditions, demonstrated a substantial enhancement in FXCT acquisition performance. Previously, an FXCT scan

covering a 36 × 36 × 8 μm^3 height FoV with a 100 nm step size required approximately 22 hours. Post-upgrade, a comparable scan of 40 × 40 × 8 μm^3 height using the same step size was completed in just 8.5 hours - a threefold reduction in acquisition time. The real-time control system mitigates mechanical vibrations during high-speed scanning and, due to the reduction in overall scan duration, significantly limits sample drift. Both factors are critical for preserving alignment accuracy and maintaining high-fidelity reconstruction, particularly in long-duration tomography acquisitions. Fig. 4.8 compares reconstructed volumes of the same sample before and after the upgrade, using the parameters outlined above.

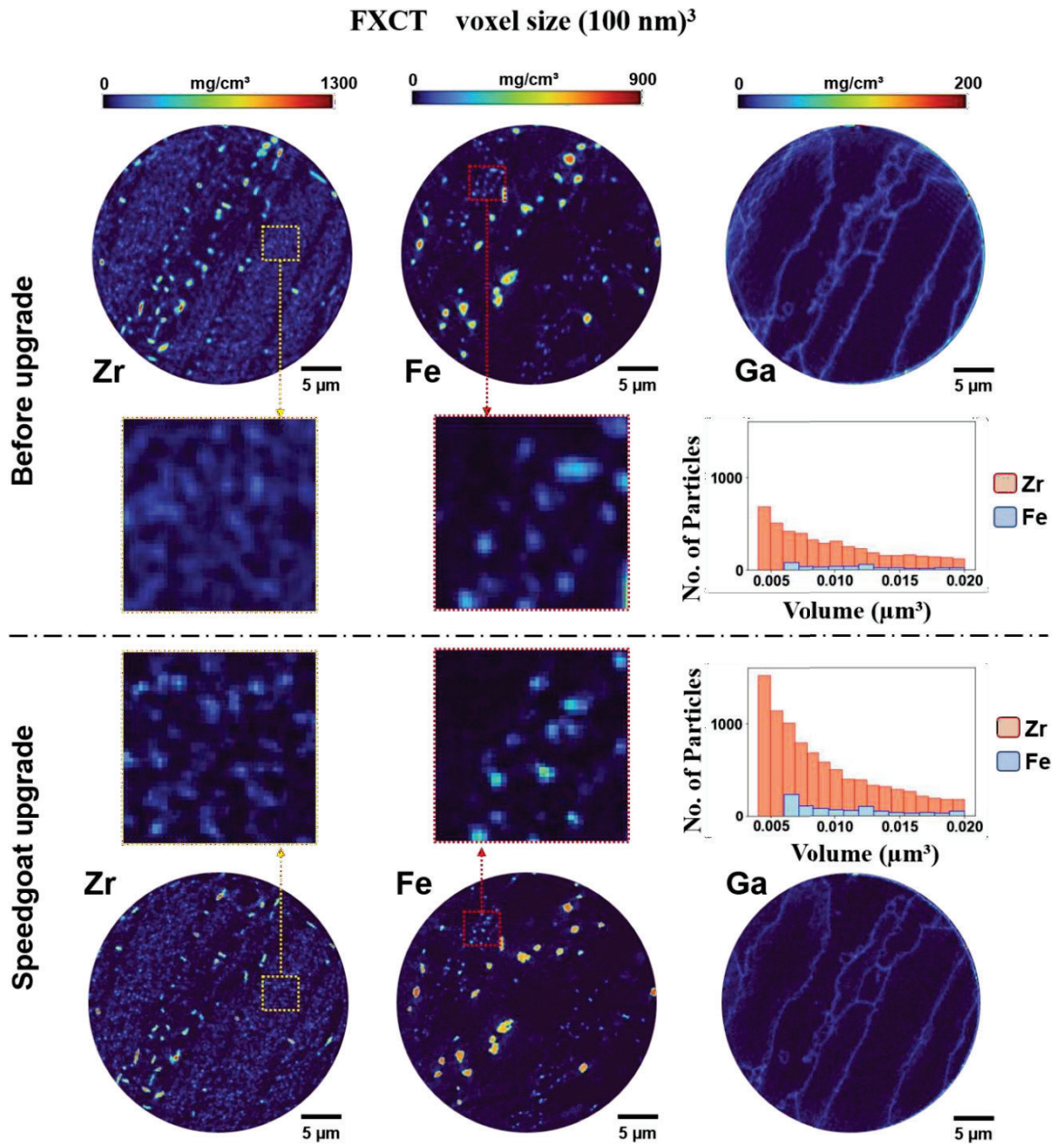

Fig. 4.8 Comparison of nanoscale imaging and particle quantification before and after the Speedgoat system upgrade at the ID16A beamline. The top and bottom rows display Zr, Fe,

and Ga elemental maps of the analyzed sample, with the top row representing pre-upgrade data and the bottom row showing post-upgrade results. The middle panel highlights enlarged views of Zr and Fe distributions before and after the upgrade, illustrating improved resolution and particle detection. Histograms on the right quantify Zr and Fe nanoparticle distributions, demonstrating a significant increase in detected particles post-upgrade, attributed to enhanced imaging precision and accuracy in the positioning and scanning. Quantification was performed using consistent parameters, ensuring comparability of particle volumes and distribution.

The upgrade's benefits are evident in the histograms representing the distribution of particle volumes, showing significantly improved particle quantification. ImageJ 3D object counter analysis revealed that, after the upgrade, nearly twice as many Zr-rich nano-intermetallic particles were detected compared to the legacy system. The analysis was standardized, counting particles ranging within 6 to 20 voxels in size with a threshold value of 20, ensuring consistency between the datasets.

The improved acquisition speed, enhanced stability, and minimized drift achieved with the upgraded control system enabled significant advancements in FXCT imaging resolution. High-efficiency data collection facilitated ultrafine-resolution scans with a voxel size of 36 nm^3 over a 35 × 35 × 3.6 μm^3 FoV, using 192 projections acquired in 40 hours. These scans provided unprecedented insights into the microstructural evolution and spatial distribution of Fe- and Zr-rich intermetallics in LPBF-processed Al–1Fe–1Zr alloys, substantially advancing our understanding of their behaviour. As demonstrated in Chapter 6, the capabilities of the upgraded system were pivotal in enabling such high-resolution FXCT imaging, underscoring the critical role of continuous technological progress in synchrotron-based materials characterization.

4.6 Image alignment for high resolution nano imaging

Achieving high spatial resolution in HXCT requires careful attention during both acquisition and data processing. One essential aspect in this context is image alignment, which becomes increasingly critical as voxel sizes approach the nanometric regime. At such resolutions, even minor misalignments between successive projections can introduce artefacts that obscure fine features and compromise the spatial fidelity of the reconstruction. These artefacts become especially problematic when the goal is to resolve nanoscale intermetallic particles.

In standard tomographic acquisition, parameters such as X-ray energy, exposure time, and number of projections are generally selected based on established protocols. However, in the context of nano-imaging, specific steps such as phase retrieval and image alignment require careful adjustment. As spatial resolution increases, the sensitivity of the reconstruction to small deviations also increases, amplifying the importance of precise image registration.

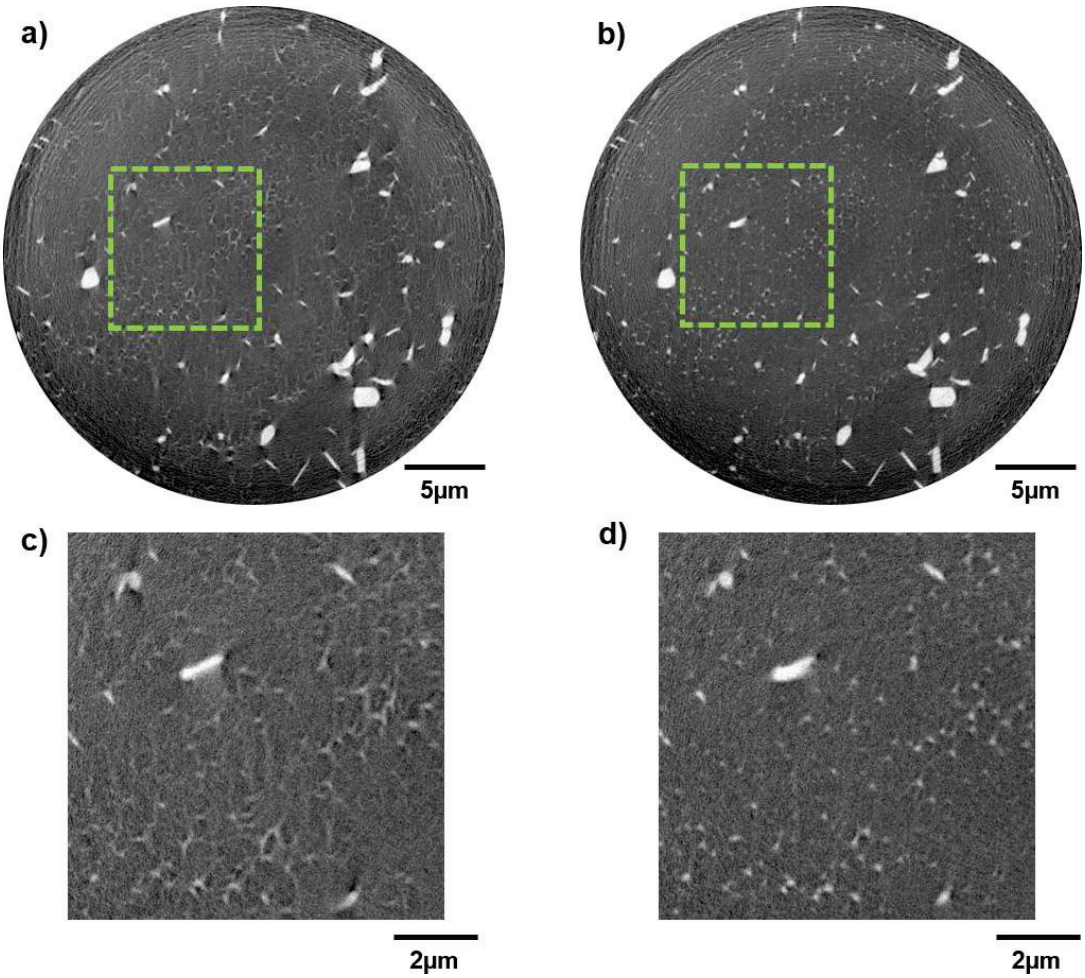

Fig. 4.9 Comparison of HXCT slice quality before and after image alignment. (a) and (b) shows HXCT slices before and after alignment, respectively. The respective enlarged images are shown in (c) and (d) highlighting distortions before the alignment and enhanced delineation of microstructural features and improved resolution following alignment correction, respectively.

Despite efforts to stabilize the sample stage and reduce acquisition times to minimize drift, misalignment artefacts may still persist. These artefacts are particularly detrimental when attempting to visualize ultrafine features, such as nanoscale intermetallics or precipitates. This is clearly demonstrated in Fig. 4.9 (a), where an HXCT slice prior to alignment correction shows noticeable artefacts. The enlarged view in Fig. 4.9 (c) highlights the extent of these

distortions. After applying alignment corrections, the same slice (Fig 4.9 (b) and (d)) shows a marked improvement in image quality, with clear delineation of microstructural features that were previously obscured. The alignment procedure follows a newly developed approach that describes the parasitic sample movement during thousands of projections with a limited (<10) number of parameters. An image quality metrics is minimized as a function of those parameters to find the optimal alignment corrections.

Also, in the context of FXCT, image alignment plays an important role. Here, the alignment is used extensively to correct the projections prior to the volume reconstruction. Vertical alignment is achieved by registering the vertical mass profile, exploiting the fact that the 'mass' within a tomographic slice is invariant to a rotation. The horizontal alignment is performed using a tomographic consistency approach [139,140]. These steps ensure that the reconstructed elemental volumes accurately reflect their true spatial distribution. Therefore, image alignment is not merely a procedural step but a fundamental requirement for achieving true nanoscale resolution. Continued development and refinement of alignment techniques will remain crucial for advancing the capabilities of synchrotron-based imaging and for enabling high-fidelity characterization of nanoscale microstructural features.

4.7 Nanoscale 3D characterization of Al-1Fe-1Zr Alloy

In order to elucidate the complex internal structure of the new Al-1Fe-1Zr alloy at the nanoscale, this study employs the three imaging techniques of the beamline to unravel the alloy's ultrafine internal structure, morphology, and mass density with high resolution. A comparative analysis of HXCT and NFPXCT was conducted, with a particular focus on acquisition and reconstruction times, as well as the quality of the reconstructed volumes. The objective of this study was to identify the most effective approach for resolving the complex microstructural features of the alloy. To ensure consistency and accuracy in the evaluation, all experiments were conducted using the same sample and instrumentation setup. Furthermore, complementary X-ray fluorescence computed tomography (FXCT) was used to provide quantitative data on the elemental distribution. These investigations gave a comprehensive understanding of the spatial distribution of Fe-rich and Zr-rich intermetallics within the Al matrix. The integration of these imaging techniques provides a comprehensive understanding of both the microstructural and elemental distribution characteristics of the Al-1Fe-1Zr alloy.

4.7.1 Materials and methods

Samples of the Al-1Fe-1Zr alloy were produced using a custom-designed, miniaturized LPBF system, at the Paul Scherrer Institute's MicroXAS beamline of the Swiss Light Source (SLS) [150]. The system is specifically designed to be installed at synchrotron beamlines and incorporates the fundamental features of commercially available LPBF machines. To prevent oxygen contamination, the build chamber was continuously purged with high-purity argon gas, and the oxygen levels were carefully monitored. The samples were fabricated with a wall geometry of $2 \times 0.2 \times 1$ mm^3 (length × width × height), using the following process parameters: laser power (E) of 370 W, hatch spacing of 130 µm, scanning speed (v) of 1400 mm/s, and a layer thickness of 60 µm (corresponding to 1–2 hatch layers).

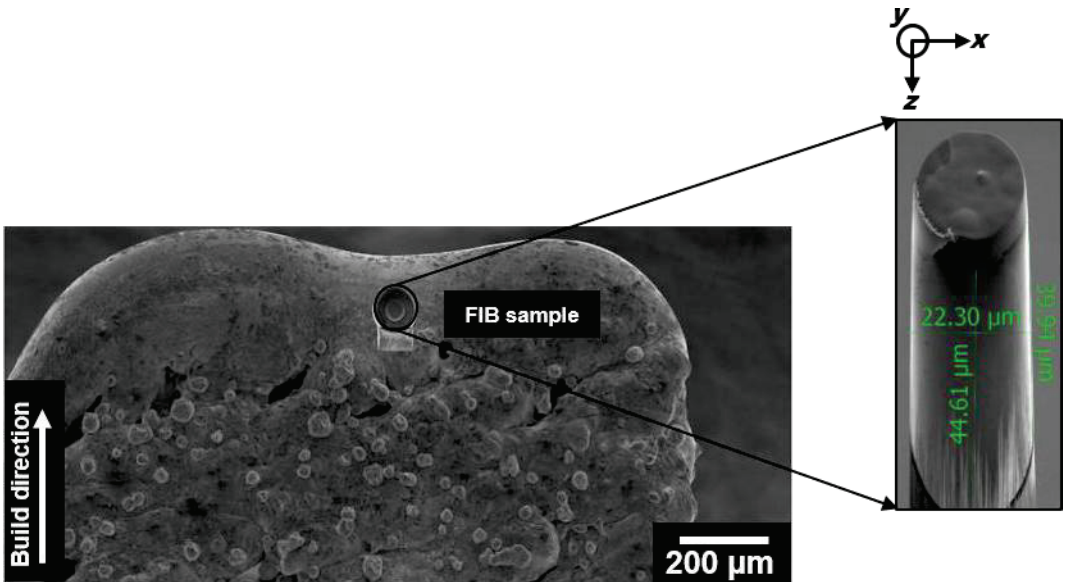

Fig. 4.10 SEM image of the additively manufactured wall showing the position of the extracted sample (marked in black) for high-resolution 3D characterization.

A cylindrical sample, approximately 22 µm in diameter and 45 µm in length was extracted from the additively manufactured wall (Fig. 4.10) using focused ion beam (FIB) milling with an FEI Helios Nanolab 600i dual-beam system (electron and Ga+). Prior to the milling process, a platinum coating was applied to the extraction area to protect the region of interest from potential damage. Following extraction, the sample was mounted onto a modified tungsten Omniprobe needle using platinum deposition and subsequently attached to a Huber sample holder.

4.7.1.1 3D Characterization

To demonstrate the potential of the two full-field coherent imaging techniques, HXCT and NFPXCT, and to accentuate the accuracy of the results, both measurements were carried out at 33.35keV, with the same voxel size of $(15\ nm)^3$ and 4000 projections with an exposure time of 0.3 s/projection.

For HXCT, tomography scans were done at 3 increasing distances from the focus. The phase retrieval and reconstruction of HXCT and NFPXCT are discussed in detail in section 3.3. For the case of NFPXCT, the phase retrieval of the first projection was done using one iteration of Alternating Projections [134] followed by Maximum Likelihood optimization [135] for 4000 iterations while updating the probe. The following projections were started with the previous

reconstruction as an initial guess and then improved by Maximum Likelihood optimization [135] for 100 iterations without updating the probe followed by 200 iterations updating the probe. The tomographic reconstructions are carried out on the horizontal derivative of the phase maps using the FBP method with a Hilbert filter[136] with the ESRF in-house software NABU [130]. After deriving the quantitative results from the resulting tomographic volumes, they were further processed for visualization purposes using bandpass filters available in ImageJ [151] to correct for gray value gradients caused by the Pt deposition.

For FXCT, a total number of 65 projections over 180° were acquired with 2 sub-tomograms of 32 projections each and a final projection at 180° to improve the alignment of the projections. This setting provides the best compromise between the target resolution and the field of view while still having a sufficient number of projections. Taking into account the step pixel size of 100 nm and dwell time of 50 ms for each pixel step, and the acquisition overhead time, each projection took ~18 minutes to acquire, resulting in a total scan time of a about 20 hours.

4.7.2 Results

The microstructure in the tomographic reconstructions consists of a grey aluminium matrix and bright intermetallic phases, likely rich in Fe and Zr [92]. Representative 2D reconstructed slices of the alloy, obtained using HXCT (Fig. 4.11 (a), (e)) and NFPXCT (Fig. 4.11 (b), (f)), are shown in Fig. 4.11. These phase-contrast tomography techniques reveal the morphology, distribution, and connectivity of intermetallic phases that decorate fine equiaxed Al grains (<10 µm) (Fig. 4.11). Fe-rich intermetallics form an intergranular network along the grain boundaries, while compact cuboidal Zr-rich primary particles are found within some Al grains (marked in Fig. 4.11 (a)), consistent with previous findings [92,100].

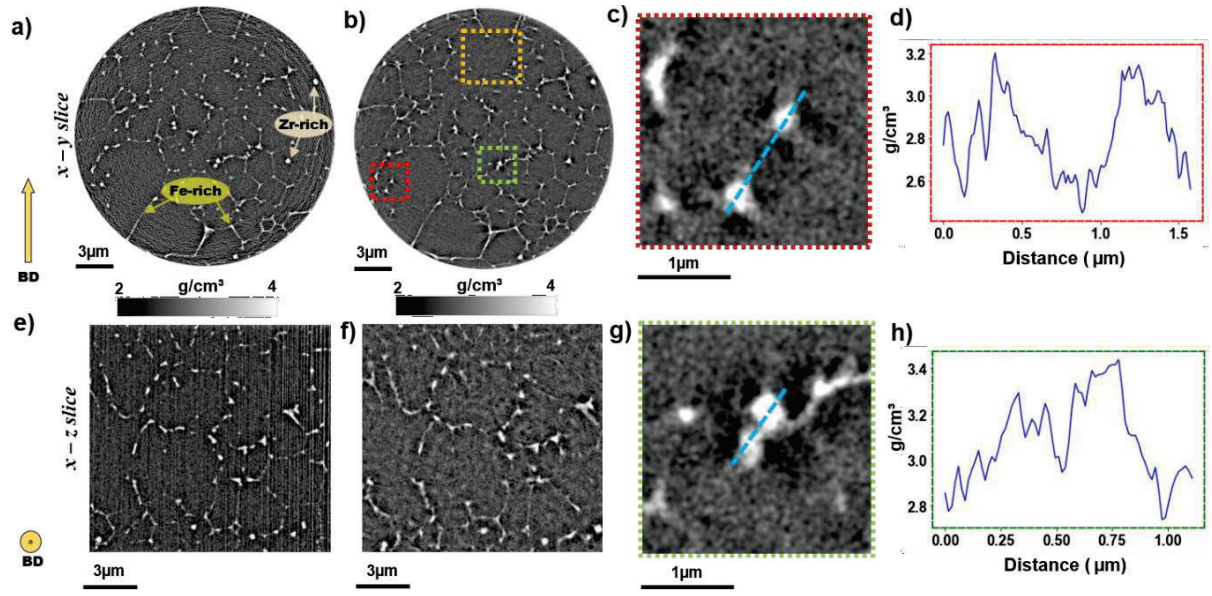

Fig. 4.11 Comparison of phase-contrast nano-tomography slices from HXCT ((a), (e)) and NFPXCT ((b),(f)) showing intra- and intergranular structures in the Al-Fe-Zr sample. The mass density maps are displayed both parallel ((a) and (b), x-y slices) and perpendicular ((e) and (f), x-z slices) to the Build Direction (indicated by the gold arrow labelled BD). Fe-rich intermetallics and Zr-rich primary particles are visible in (a). Enlarged images (c and g) highlight regions of interest from the NFPXCT slice marked in (b) by red and green boxes. Plots in (d) and (h) correspond to the line profiles (blue lines in (c and g)) of the respective regions, showing the total mass density of the intermetallic phases.

NFPXCT, which separately reconstructs the object (transmission function) and probe (incident illumination function), offers enhanced spatial resolution, as evaluated by Fourier shell correlation (FSC), achieving 57 nm for NFPXCT compared to 70 nm for HXCT (Fig. 4.12).

Additionally, NFPXCT provides a superior signal-to-noise ratio (15 to 10) as it bypasses the flat-field correction approximation required in HXCT [152].

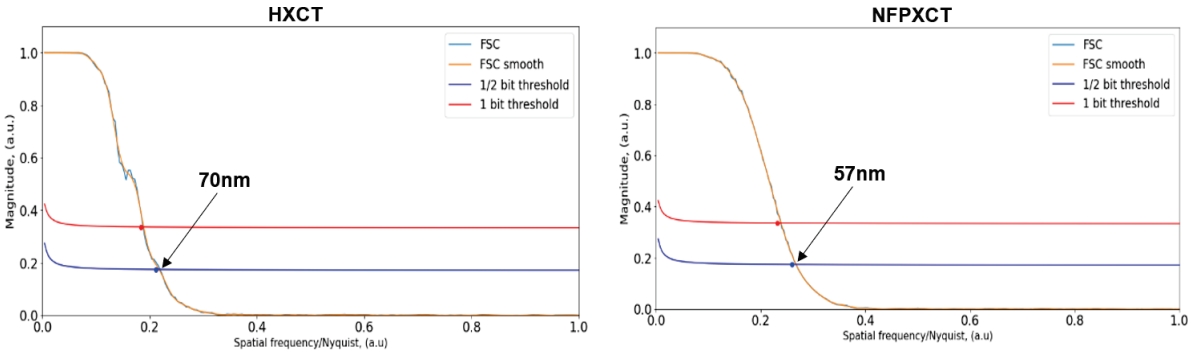

Fig. 4.12 Fourier shell correlation (FSC) analysis of the HXCT (left) and NFPXCT (right) volumes, performed on a central region of each volume measuring (500)³ pixels. The FSC curve represents the raw correlation, while the FSC smooth - reduces noise for clearer interpretation. The 1/2-bit threshold indicates the spatial frequency where the reconstruction contains statistically significant information, commonly used to define resolution. The stricter 1-bit threshold marks the frequency where structural features are reconstructed with high certainty.

Despite this, HXCT still produces reconstructions of sufficient quality. Fig. 4.11 (e) shows vertical line artefacts in the axial HXCT slices, while NFPXCT is free from such artefacts. Enlarged regions of interest from the NFPXCT slices (marked by red and green rectangles in Fig. 4.11 (b) are shown in Fig. 4.11 ((c) and (g)), where intermetallic phases with similar 2D morphologies but slight differences in mass density are observed, as highlighted by the line profiles in Fig. 4.11 ((d) and (h)). The accuracy of the mass density estimations from the NFPXCT reconstructions suggests potential compositional variations within these intermetallic phases. To further investigate local elemental concentrations, FXCT was employed as a crucial complementary technique. Given the extended acquisition times required for FXCT, a reduced field of view (5 µm in height and 28 µm in width) was selected in a region rich in intermetallics. For detailed correlative analysis, the FXCT results in Fig. 4.13 depict the same region as the phase-contrast slices shown in Fig. 4.11 (a and b).

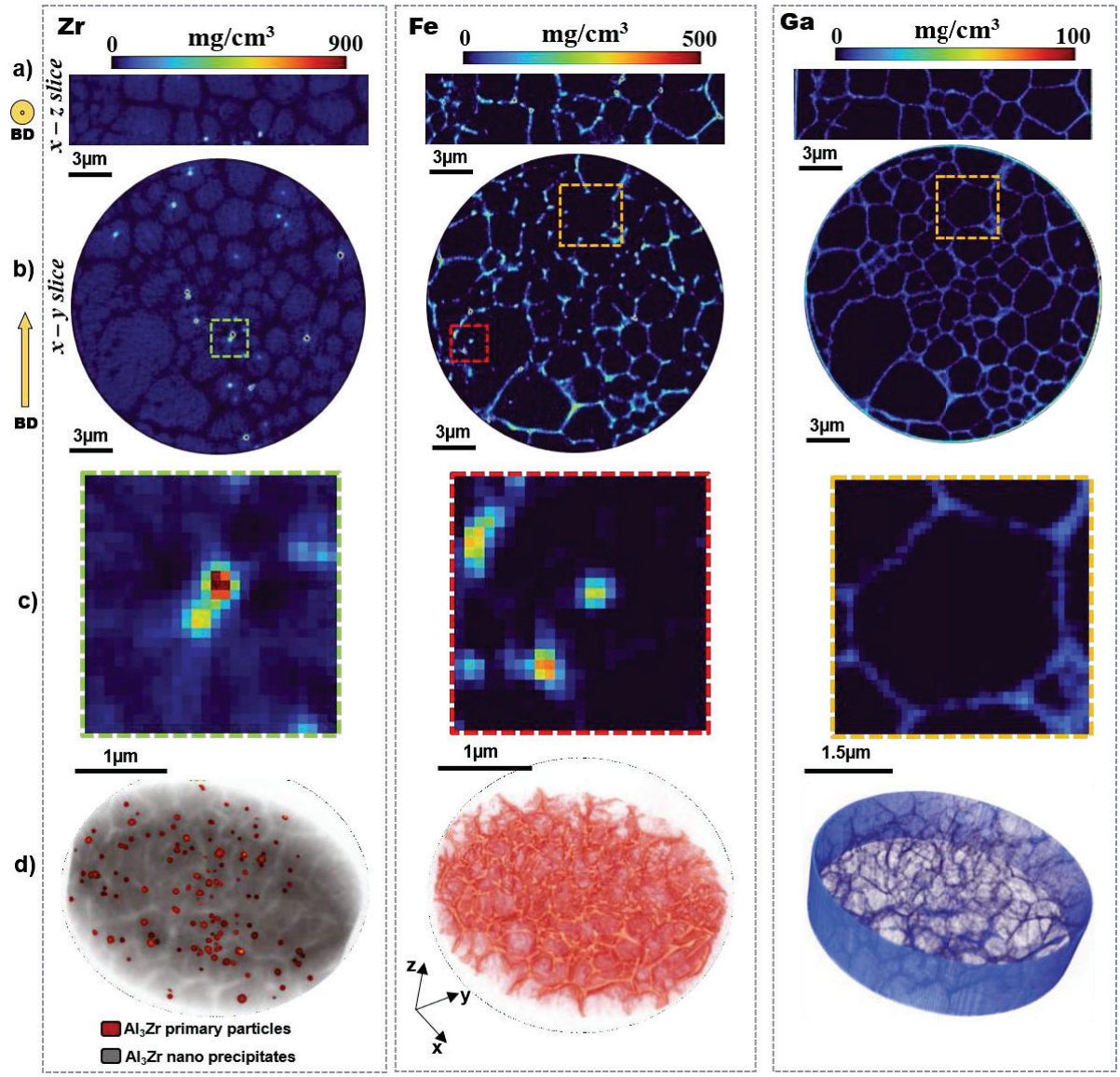

Fig. 4.13 Orthogonal views of X-ray fluorescence tomography volumes illustrating the distributions of Zr (left), Fe (middle), and Ga (right). The axial (a) and radial (b) slices (same as those in the phase contrast tomography, Fig. 4.11) reveal the localized concentrations of the alloying elements Zr and Fe, along with Ga, which was introduced during sample preparation. Enlarged regions of interest (c) show Zr (green) and Fe (red), corresponding to the areas in Fig. 4.11 (NFPXCT), indicating distinct intermetallics. The enlarged view of Ga highlights the presence of a grain boundary, while the corresponding Fe region shows no observable intermetallic accumulation (orange, also see Fig. 4.11 b). 3D volume renderings of the element distributions are presented in (d).

The elemental quantification from FXCT data provides two key insights: 1) The detection of Zr within the Al grains suggests that Zr is either partially incorporated in solid solution within the aluminium matrix or forming nanoscale Al_3Zr precipitates, and 2) Ga is observed decorating the Al grain boundaries. Ga was introduced into the alloy during sample preparation through focused ion beam (FIB) milling with Ga+ ions. Given Ga's known affinity for aluminium grain boundaries [153], it serves as a useful marker for identifying individual grains. Fig. 4.13 (a and b) display axial and radial FXCT maps for Zr, Fe, and Ga. The enlarged regions of interest in Fig. 4.13 (highlighted by the green and red rectangles in Fig. 4.13 (b)) confirm the presence of distinct intermetallic phases, despite the phases having a similar 2D morphology and only minor differences in total mass density (as seen in Fig. 4.11 d and h). The right side of Fig. 4.13 (c) reveals Ga clearly outlining a grain boundary, while the central region of Fig. 4.13 (b) (marked in orange) illustrates a discontinuous Fe distribution along a grain. Additional direct comparisons of elemental content (FXCT), mass density (NFPXCT) for the three enlarged regions are provided in Fig. 4.14.

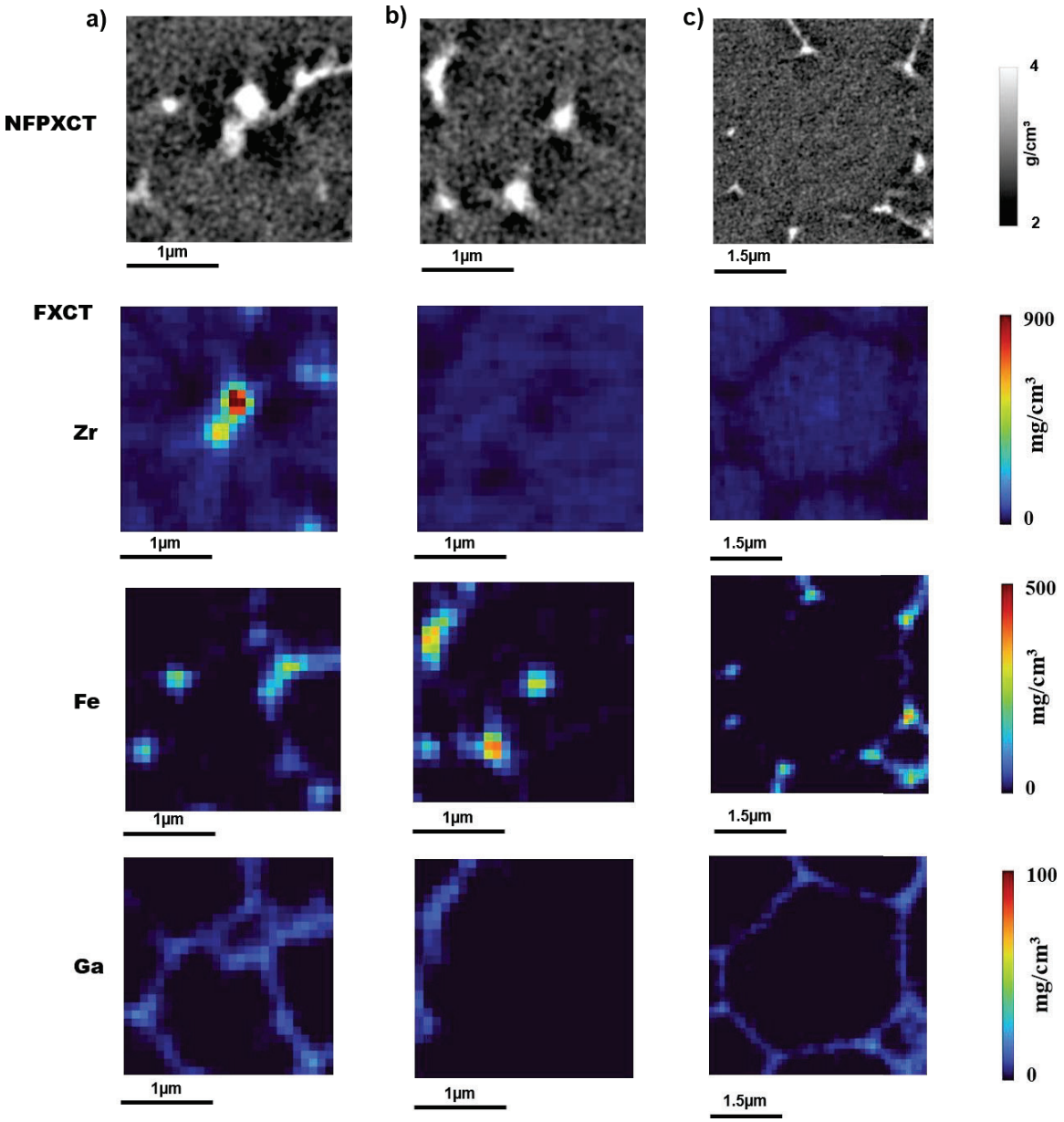

Fig. 4.14 Direct comparison of the enlarged regions of interest from NFPXCT with the corresponding regions from FXCT for the various elements.

Fig. 4.15 (a) presents the elemental distribution and mass density obtained from FXCT and NFPXCT reconstructions, with a single grain enlarged in Fig. 4.15 (b). Additionally, Fig. 4.15 (c) displays element concentrations and mass density along a line profile, with logarithmic scales used for Zr and Fe profiles to leverage the wide dynamic range of the reconstructions. The Zr line profile reveals a high concentration, likely corresponding to a primary Al_3Zr particle, located at the center of an Al grain. Surrounding this particle is a uniform Zr

concentration of approximately 25 mg/cm³ within the Al grain, equivalent to 0.9 wt%, which aligns with the alloy's nominal composition.

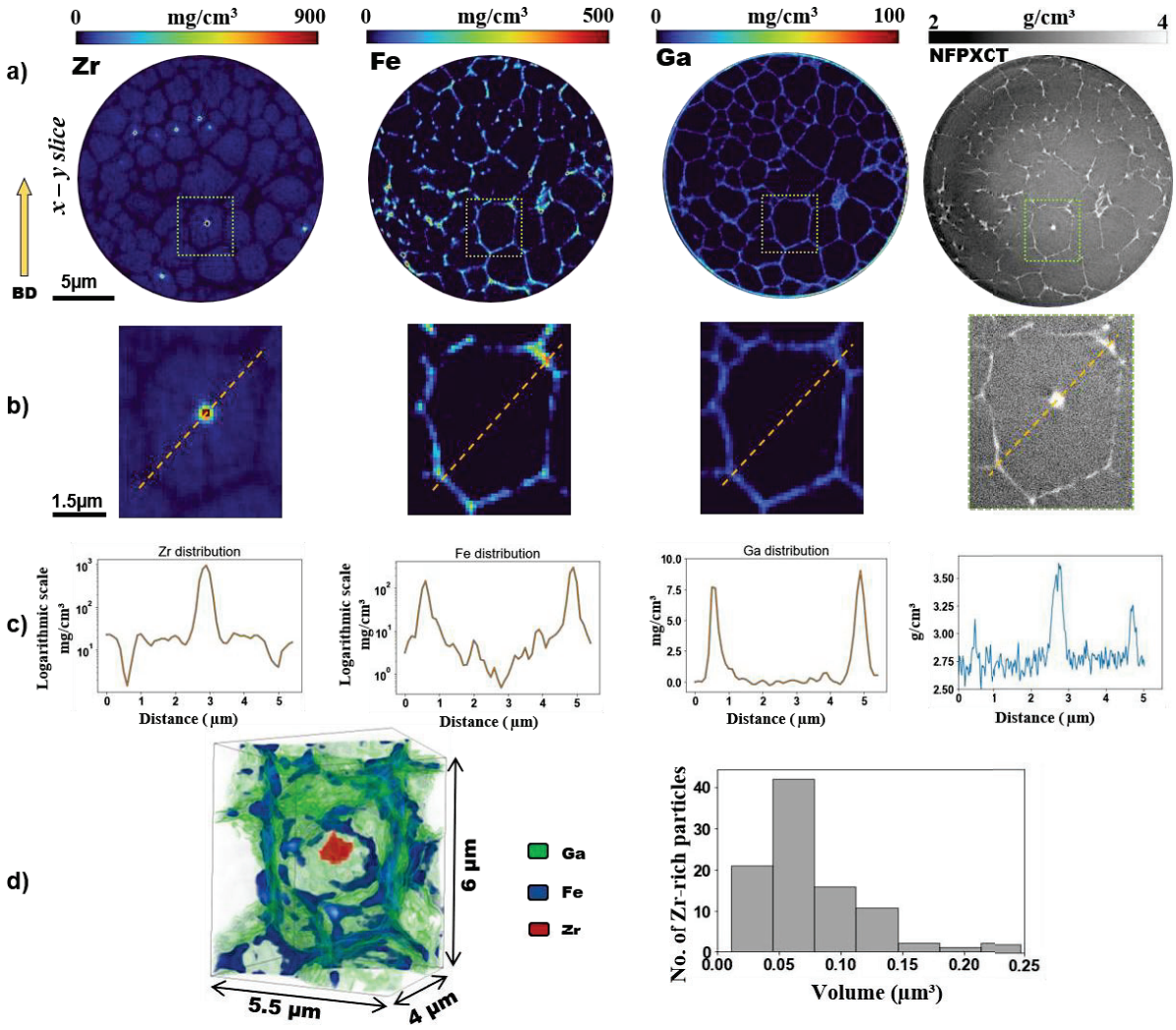

Fig. 4.15 Quantitative analysis of a single grain using FXCT and NFPXCT. (a) Radial slice showing elemental maps from FXCT alongside a mass density map obtained from NFPXCT. (b) Magnified images of a representative grain, and (c) line profile plots along the grain's diagonal, comparing elemental concentrations from FXCT with mass density from NFPXCT. (d, left) 3D rendering of the grain's elemental composition (see also supplementary movie 2), and (d, right) a histogram displaying the number of Zr-rich primary particles across the total volume (imaged via FXCT) as a function of their volume (µm³)

In contrast, Fe concentration is higher at the grain boundaries, with trace amounts of Fe retained in solid solution within the Al grain. Fig. 4.15 ((d), left) provides a 3D rendering of the Al grain from Fig. 4.15 (b), showing the heterogeneous distribution of Fe-rich intermetallics along the

grain boundary, as well as a cuboidal Al_3Zr primary particle located at the grain's center. In the FXCT-measured region, the volume fractions of Fe- and Zr-rich intermetallics are 0.23% and 0.37%, respectively. The 3D size distribution of primary Al_3Zr particles within the analysed volume is shown on the right side of Fig. 4.15 (d), with nearly half of the Al_3Zr particles ranging between 300 and 400 nm in size.

4.7.3 Discussion

When comparing HXCT and NFPXCT, one key factor is the time required for data acquisition. HXCT takes approximately 4 hours to collect data, while NFPXCT requires roughly three times longer to capture the same number of projections (4000). This difference is due to NFPXCT needing more positions per angle (16 vs. 3). Despite HXCT's advantage in faster acquisition and processing times, it relies on prior knowledge of the average sample composition to estimate the δ/β ratio, which is necessary for sufficient contrast in the final reconstructed volumes. In contrast, NFPXCT does not require any prior knowledge of the material composition [154,155].

NFPXCT also offers superior spatial resolution and a higher signal-to-noise ratio, as it eliminates the need for flat-field correction approximations required in HXCT. While HXCT volumes may exhibit line artefacts, which are absent in NFPXCT, these artefacts can be mitigated using a combined wavelet-FFT filter (stripes filter), available as the ImageJ plugin Xlib [156,157]. This filter can be applied to HXCT phase maps or x-z slices after reconstruction to reduce artefacts, although its effectiveness depends on the severity of the artefacts [56]. In this case, applying the stripes filter preserved most of the image information while enhancing the visual quality of the HXCT data. Nonetheless, NFPXCT generates higher-quality volumes with less noise, making it more suitable for samples where noise could interfere with the analysis. Fig. 4.16 shows a comparison of an *x-z* slice from HXCT volumes before and after applying the stripes filter, alongside the same region imaged by NFPXCT.

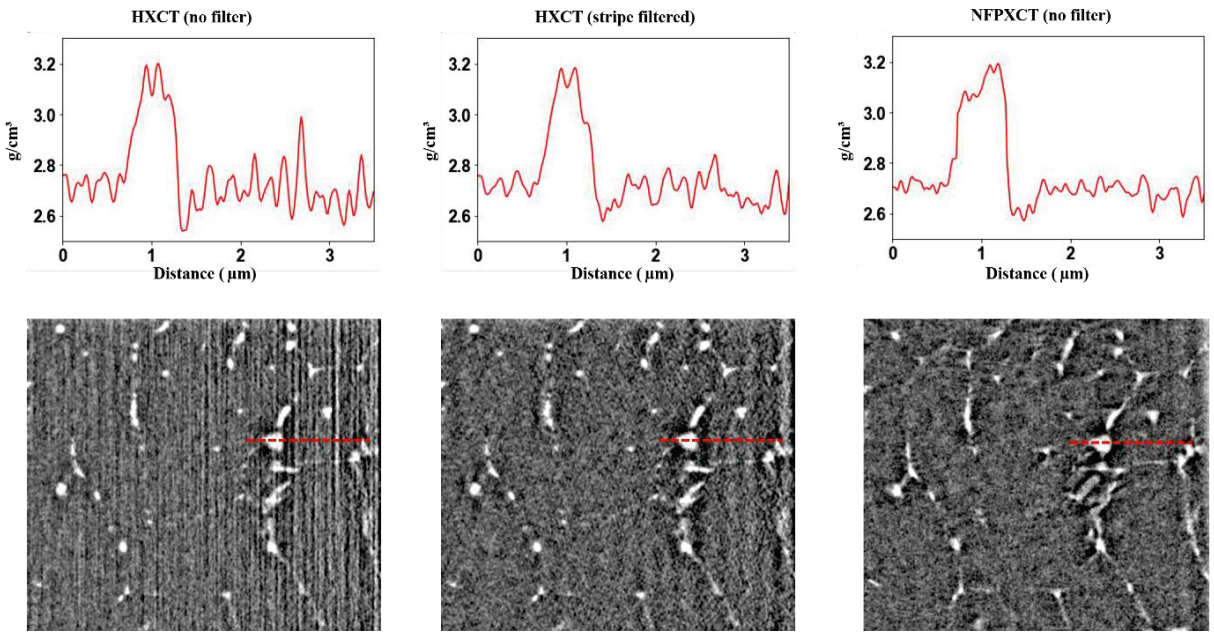

Fig. 4.16 Comparison of an x-z slice from HXCT volumes before and after applying the stripe filter. The corresponding region of interest from the NFPXCT volume is also displayed.

These techniques enable both qualitative and quantitative 3D analysis of the Al-1Fe-1Zr alloy microstructure, allowing precise determination of the local mass density of the aluminium matrix and intermetallic phases, with a spatial resolution of 57 nm and a mass density detection limit of 0.1 g/cm³. However, when phases or regions exhibit similar mass densities, their identification may rely on other microstructural characteristics, such as 3D morphology, which can lead to uncertainty. This underscores the importance of FXCT, which provides quantitative elemental information in 3D. For the alloy under study, individual elemental concentrations could be measured with a voxel size of 100 nm and a concentration resolution of 3 mg/cm³ (0.1wt%) for Zr, 1.5 mg/cm³ (0.05wt%) for Fe, and 0.3 mg/cm³ for Ga, across a broad dynamic range. This is particularly relevant for detecting Zr within the Al matrix, where it may exist either in solid solution or as nanoscale Al_3Zr precipitates.

In the development of the Al-1Fe-1Zr alloy, elements were chosen based on their low vapor pressure and diffusivity [92], with Zr serving two key roles: (i) as a grain refiner, forming primary Al_3Zr particles to promote heterogeneous nucleation at the melt pool boundaries, preventing hot cracking [158], and (ii) as an age-hardening agent, strengthening the alloy through nanoprecipitation of coherent Al_3Zr intermetallics during heat treatment [159]. The grain refinement can be explained by considering that the velocity of the solidification front is lowest for the first solidifying liquid, while the thermal gradient decreases as solidification

progresses [160,161]. At the melt pool boundary, the conditions support the formation of primary cuboidal Al_3Zr particles (Fig. 4.15 d), which serve as nucleation sites for equiaxed Al grains [162]. As solidification proceeds, Zr may become trapped in solid solution if the cooling rate is fast enough, as indicated by FXCT (Fig. 4.15). Conversely, Fe is rejected into the liquid at the periphery of the grains, leading to the formation of $Al_{13}Fe_4$ intermetallics that form a 3D network along the grain boundaries (Fig. 4.15). This is further evidenced by the Ga concentration, which acts as a grain marker in the FXCT results (Fig. 4.15). The theoretical mass densities for Al_3Zr (4.1g/cm^3 [163–165]) and $Al_{13}Fe_4$ phases (3.8 g/cm^3 [166–168]), were compared with the total mass densities calculated from the FXCT dataset, which were found to be 3.9 g/cm^3 and 3.4 g/cm^3, for Al_3Zr and $Al_{13}Fe_4$ phases, respectively. The estimated total mass densities of the intermetallic phases from NFPXCT and HXCT were 3.65 g/cm^3 for Al_3Zr and 3.25 g/cm^3 for $Al_{13}Fe_4$. These values are underestimated by ~12% while FXCT based estimates were slightly closer (~5%) to the theoretical densities. The applied techniques demonstrate high sensitivity in detecting compositional variations, it is important to note that the quantitative accuracy, particularly in terms of absolute elemental concentrations, is not always consistent with the stoichiometry of expected phases. This highlights the need for further methodological refinement and calibration to improve reliability in phase identification and quantification.

4.8 Key messages

The analyses conducted in this chapter facilitate a comprehensive discussion of the questions outlined in the Motivation (Chapter 2). The following conclusions provide answers to the pertinent research questions:

What methodological optimizations and parameter modifications were introduced to the experimental setup to enable a comprehensive 3D characterization of the microstructures?

A number of crucial parameters were investigated with the objective of optimizing the 3D characterisation of the microstructures present in the Al-1Fe-1Zr alloy. The selection of X-ray energy, specifically 33.35 keV, was to achieve an optimal equilibrium between contrast, the minimization of artefacts, and the enhancement of image quality. This energy was particularly effective for the purposes of complementary phase-contrast imaging and X-ray fluorescence analysis, which are essential for the quantification of elemental distributions. The impact of the random displacement technique was examined with the objective of reducing ring artefacts, thereby enhancing the SNR and the quality of the reconstructed volumes. Furthermore, the

number of projections during tomography was investigated with the objective of ensuring high-resolution reconstruction while simultaneously minimizing scan time and the occurrence of artefacts. An experimental upgrade using a real-time control system for nano-positioning (Speedgoat) significantly reduced X-ray fluorescence acquisition times, improving overall efficiency. Refinement of alignment techniques shows a marked improvement in image quality. The collective implementation of these adaptations enabled the precise 3D characterisation of the alloy's microstructures, thereby facilitating the gain of valuable insights into its internal architecture and spatial distribution.

What are the capabilities of the different 3D Synchrotron-Based X-ray Imaging Techniques available at the ID16A Nano-Imaging beamline of the ESRF and how can they be optimally applied to characterize Al-1Fe-1Zr alloy?

The study highlights the efficacy of nanotomography techniques at the ID16A beamline, including HXCT, NFPXCT, and FXCT, for the characterization of the Al-1Fe-1Zr alloy tailored for LPBF. Comparative analyses performed using these methods revealed the 3D microstructural features with high precision, achieving spatial resolution down to 57 nm, mass density resolution of 0.1 g/cm³, and elemental concentration resolution ranging from 0.3 to 3 mg/cm³ (which corresponds to 0.1wt%), depending on the element. Full-field coherent imaging techniques, particularly, offer advantages for these investigations due to their larger field of view and the capability to select regions of interest for FXCT. The enhanced spatial resolution of NFPXCT (57 nm compared to 70 nm for HXCT) proved especially valuable, given the ultrafine microstructural features of the alloy. HXCT being significantly faster (factor three), using more straightforward data processing and still providing high quality reconstructions, remains the most used method in the following of the work. X-ray phase contrast experiments provided accurate mapping and quantification of these microstructures. Integrating these methods with FXCT enabled clear identification of elements and their local distribution. The estimated total mass densities of the intermetallic phases from NFPXCT and HXCT were 3.65 g/cm^3 for Al_3Zr and 3.25 g/cm^3 for $Al_{13}Fe_4$. These values are underestimated by ~12% while FXCT based estimates were slightly closer (~5%) to the theoretical densities. The applied techniques demonstrate high sensitivity in detecting compositional variations, it is important to note that the quantitative accuracy, particularly in terms of absolute elemental concentrations, is not always consistent with the stoichiometry of expected phases. This highlights the need for further methodological refinement and calibration to improve reliability in phase identification and quantification.

5 From Powder to Process: Elucidating 3D Microstructural features of LPBF Al-1Fe-1Zr Alloy

5.1 Introduction

As discussed in the previous chapters, LPBF has significant potential, but several factors, including the processing conditions and the processability of the alloys under consideration, must be understood. In LPBF processes, the initial step is to optimize and screen the manufacturing parameters [169,170]. It aims for defect-free manufacturing. Many alloys employed in LPBF today were originally developed for conventional manufacturing processes and are not suitable for the high cooling conditions typical of LPBF. The typical cooling rates, e.g., ~10^6–10^7 K s^{-1}, can result in non-equilibrium microstructures, which may influence the materials' performance and even lead to defects [171,172]. Moreover, Mg and Zn in some Al alloys are susceptible to evaporation during LPBF, shifting the alloy's composition [173–176].

In LPBF, a 3D part is fabricated from a series of layers, each consisting of adjacent scanned tracks. The process involves the overlapping and metallurgical bonding of these tracks into a layer and the layers into a part. In each layer, the laser locally melts the powder particles line by line, leading to the formation of distinct melt pools. These melt pools usually present a semi-circular or a semi-cylindrical 3D shape formed as a result of surface tension [21]. A comprehensive characterization of the microstructures formed in these melt pools is crucial, as it impacts their stability and, consequently, the quality of the part [177]. While the majority of research in single-track experimentation is focused on the identification of defects and the delineation of zones of regularity [178–180], their significance extends beyond these traditional objectives. In this study, single-track experiments have been leveraged to gain deeper insights into how LPBF processing conditions influence the resultant microstructures. The material's response to laser irradiation is directly determined by its physical properties, underscoring the importance of tailoring parameters for each material. It is crucial to note that findings from one material cannot be universally extrapolated, emphasizing the need for material-specific investigations. In this context, 3D characterisation plays a critical role in materials analysis by enabling precise evaluation of microstructural features, including precipitates, grains, and inclusions. These microstructural parameters are fundamental to understanding structure–property relationships, as they directly influence mechanical performance and functional behaviour. Furthermore, non-destructive 3D characterization can provide valuable insights

into how LPBF processing parameters influence microstructural formation, its distribution and the influence of heat-treatments.

The lack of optimization in the parameters employed in an LPBF operation can result in a range of defects that limit its commercial scalability. The most commonly observed issues include surface roughness, porosity[181], balling defects [182], incomplete powder melting [183], the presence of high residual stress [184], and the formation of undesired microstructures [185]. The dynamics and geometry of the melt pool are of significant importance in the control of defect formation, given that the rapid heating and cooling that occurs during the LPBF process significantly influences the stability of its microstructures. As previously discussed in section 3.1.5, Pauzon et al. reported an enhancement in the Al-1Fe-1Zr alloy's material properties after heat treatment for 4 hours at 400°C owing to the nanoprecipitation of the $L1_2$-Al_3Zr [100]. Furthermore, Guo et al. used high-speed synchrotron radiography to investigate vapor depression and spatter dynamics during the LPBF of this alloy [109].

Building on this knowledge, we conducted an extensive experimental investigation with the primary objective to elucidate the influence of LPBF processing conditions on the formation and spatial distribution of Fe-rich and Zr-rich intermetallics within prior melt pools. To achieve this objective, X-ray imaging techniques available at the ID16A beamline were employed to characterize the internal architecture and the elemental distribution within a prior melt pool. The non-destructive nature of these techniques offers the benefit of enabling the examination of the same sample both before and after heat treatment, thereby enabling the investigation of microstructural changes in a specific location. As an additional investigation to gain a more comprehensive understanding, first a single powder particle of the alloy was analyzed to elucidate the elemental distribution in its original state. Therefore, in this chapter, we consider the following issues:

- *How does the variation of LPBF processing parameters influence microstructural formation?*
- *How do microstructural constituents, their architecture, and chemistry vary within a prior melt pool?*
- *How do heat treatments affect element distribution within a prior melt pool?*

5.2 Materials and Methods

5.2.1 Powder particles

The Al-1Fe-1Zr powder was produced by gas atomization by Constellium. The particle sizes range from 25.2 µm (D10) to 65.6 µm (D90), with average particle size of 42 µm (D50). The apparent density was 1.27 g/cm³ in accordance with ISO 3923/1, and the Carney flowability was 15 seconds per 50 g, as per ASTM B964 [186]. A single powder particle of about ~40 µm was glued to a pulled glass capillary using a micromanipulator. The glass capillary was fabricated using a laser-based puller to achieve a fine tapered tip [187]. The powder particle was fixed to the tip using UV glue. The glass capillary was then attached to a Huber sample pin (Fig. 5.1). Prior to mounting on the sample holder, the extended portion of the capillary below the Huber pin was trimmed to ensure compatibility with the ID16A experimental setup (Fig. 5.1, marked in white).

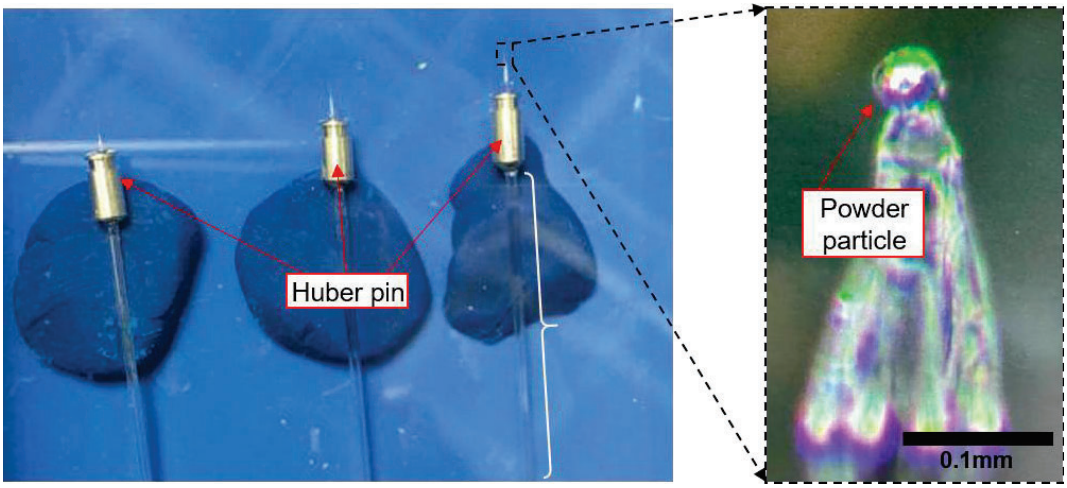

Fig. 5.1 Picture of the powder particles prepared for the high-resolution tomography at ID16A. The enlarged image shows the optical micrograph of the glass capillary with the particle. Note: The glass capillary that is extended below the Huber pin (marked in white) has to be shortened before mounting on the sample holder.

5.2.2 LPBF processing and sample extraction

The LPBF processing parameters covering a range of linear energy densities from 210 Jm^{-1} to 840 Jm^{-1} were selected, as explained in [109]. *In-operando* experiments of single tracks were performed at the ID19 beamline of the ESRF in collaboration with a research team from University College London [109]. The experiments were conducted using a custom-built additive manufacturing system known as the Quad-laser *in-situ* and operando process replicator (Quad-ISOPR) [109]. This system integrates four lasers and the scan head from a RenAM 500Q

(Renishaw plc., UK) system, along with a specially designed environmental chamber. A substrate, 1 mm in thickness and 15 mm in height, is positioned inside the chamber, where a thin layer of powder is deposited (Fig. 5.2). The substrates were fabricated by LPBF using the Al-1Fe-1Zr powder feedstock to replicate the deposition of a thin powder layer on top of a 15 mm tall additively manufactured part. Argon shielding gas was employed throughout the LPBF process [109].

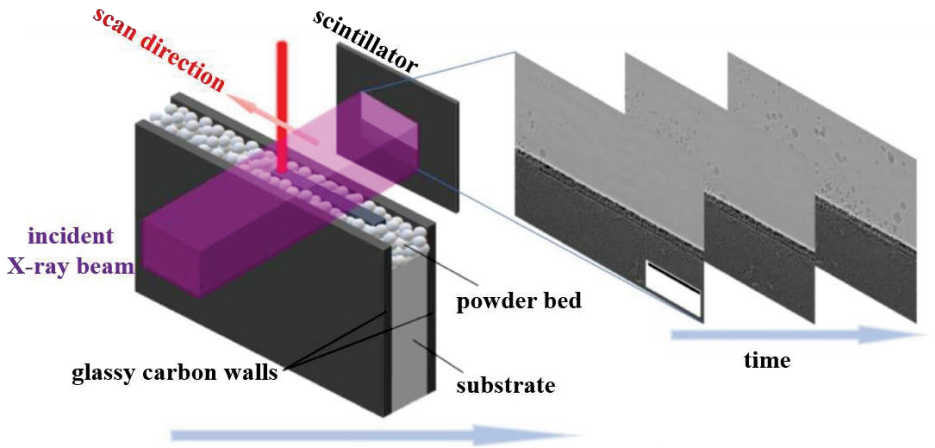

Fig. 5.2 Schematic representation of the in-operando X-ray imaging setup during LPBF, illustrating the laser scan and the data acquisition scheme at the ID19 beamline of the ESRF. Taken from [109].

In alignment with findings in [109], three specific conditions were selected for comparative analysis to investigate how the microstructure responds to varying LPBF processing parameters. These conditions were chosen based on their relatively higher productivity compared to other settings. The parameters are presented in the table 5.1.

Table 5.1 Processing parameters for LPBF of Al-1Fe-1Zr during the in-operando experiments

Sample	Laser power **W**	Scan speed **mm/s**	Exposure time **µs**	Laser mode	Linear energy density **J/m**
C1	420	1500	20	CW	280
C2	420	2000	20	CW	210
C3	400	800	40	PWM	500

The laser modes in the Table 5.1 are Continuous Wave (CW) mode delivering a constant, uninterrupted energy beam, providing uniform heat input and Pulse Width Modulation (PWM)

mode operating by emitting energy in periodic pulses, defined by a specific pulse width and duty cycle. Condition C1 was selected to closely match those reported in [92,100], where laser melting was conducted with a 370W laser power, a 1400 mm/s scan speed, a 130 µm hatch distance, and a 60 µm layer thickness. In our case, the C1 parameters were 420W and 1500mm/s. C2 was chosen to test a faster scanning speed, with 420W and 2000 mm/s. C3 was designed to assess the effect of a slower scan speed leading to higher liner energy density, using 400W, 800 mm/s, and operating in pulse width mode.

The ID16A experiments were divided into two sessions:

Session 1: Aimed to examine how variations in LPBF processing parameters influence microstructural development.

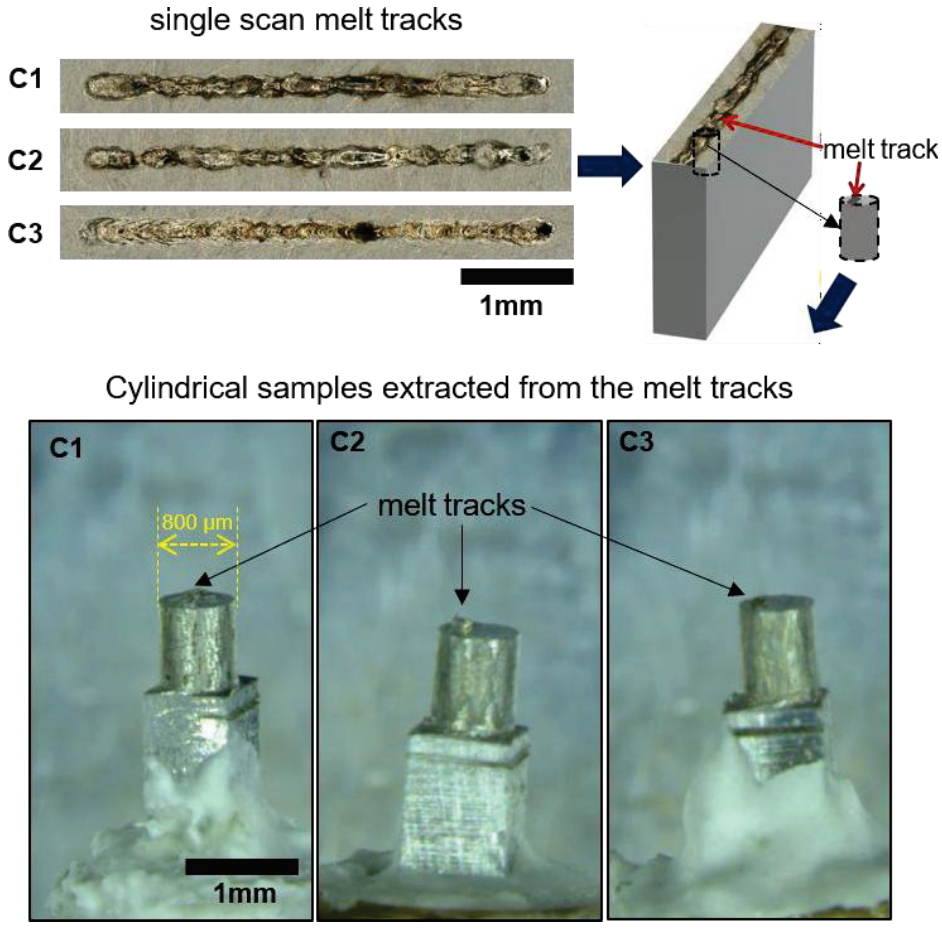

Fig. 5.3 Optical microscopy images of the LPBF single melt tracks for conditions C1, C2, and C3, with an illustration of cylindrical sample extraction, indicated on the right. The laser-machined cylindrical samples of ~800 µm in diameter from each melt track are displayed below.

The systematic investigation focused on HXCT imaging of the entire melt pool before and after heat treatment, with an emphasis on evaluating how heat treatments impact the evolution of the Fe-rich and Zr-rich intermetallics. Cylindrical samples of ~800 µm in diameter were laser-machined at the UCL from the 4 mm long LPBF single tracks from each processing condition mentioned above for the nanotomography experiments at the ID16A beamline (Fig. 5.3).

Each step of the investigation was planned to ensure consistency in the samples' integrity, particularly identifying the orientation and LPBF scan direction with respect to tomography. To ensure mechanical stability of the specimens during the tomographic experiments and the subsequent heat treatment, these cylindrical samples were mounted onto brass Huber pins using heat-resistant ceramic adhesive. This approach eliminated the need to unmount the samples for heat treatment, maintaining consistency and accuracy in the comparative analysis of the microstructural evolution.

Fig. 5.4 Samples subjected to heat treatment at Constellium at 400°C for 4 hours. (a) Sample mounted on the Huber pin. (b) Individual samples placed in designated crucibles. (c) Industrial furnace utilized at Constellium for the heat treatment process.

Large FoV HXCT (400 x 400 x 400 μm^3) was performed on the cylindrical samples extracted from the single tracks, covering approximately half of the sample's diameter, which measured 800 µm. After the first set of HXCT scans in the as-built condition, the samples from the 3 conditions were taken to Constellium, Vorrepe, France, to undergo heat treatment at 400°C for 4 hours (Fig. 5.4). Post heat treatment, HXCT scans were performed on the same regions of the cylindrical samples to elucidate the evolution of the microstructures.

Session 2: Dedicated to characterizing the microstructural constituents, their architecture, and chemical composition within a prior melt pool after the heat treatment. This required the extraction by FIB-SEM of *sub*-samples of ~30 µm in diameter to be extracted from different regions of the prior melt pools after session 1.

For the second session, a meticulous sample preparation process was undertaken to ensure precision during the sample polishing to reveal the melt pool. The primary objective was to selectively remove material from the cylindrical LPBF samples while maintaining their structural integrity, allowing for accurate extraction of the *sub*-samples for high-resolution tomography measurements. The HXCT scans from Session 1 with a large FoV scan (400 x 400 x 400 μm^3), were conducted with a pixel size of 125 nm. This pixel size provided a good balance between achieving a sufficiently large FoV and maintaining the resolution needed to sufficiently resolve intermetallics after heat treatment. This allowed only half of the cylindrical sample to be effectively scanned, and it was evident that material removal to expose the melt pool should be selective and precise (Fig. 5.5). The radial slice of the melt track exhibits a darker contrast than the substrate, which can be attributed to the global offset applied during reconstruction to compensate for intensity variations arising from the local HXCT. Additionally, to avoid undesirable features such as pores, the amount of material to be removed was planned using the previously acquired HXCT volumes as a reference.

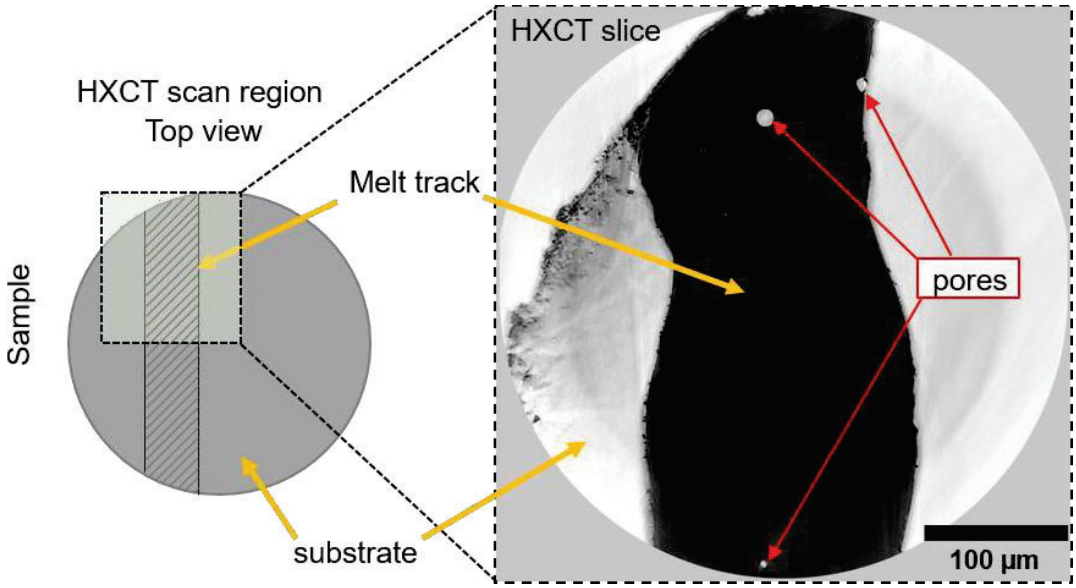

Fig. 5.5 Schematic top view of the sample (left) illustrating the location where the large FoV HXCT scan was conducted. The HXCT slice (right) from this region displays the corresponding radial slice of the melt track.

In order to be able to reveal the melt pool by optical microscopy and to expose the desired region for FIB extraction, the following steps were undertaken:

1. The cylindrical samples were grinded to remove between 100 µm and 150 µm of material. This process was carried out using a Buehler Minimet 1000 machine, equipped with Buehler diamond lapping film discs. Varying grit sizes- 9 µm, 3 µm, and 1 µm were used to remove the material (Fig. 5.6). The amount of material removed was closely monitored by regular diameter measurements along the melt track (Fig. 5.6) to ensure the sample remained within the HXCT scan range.
2. Once the desired region of the sample was exposed, the samples were glued (Fig. 5.6) on a polishing device formed by a steel ring which acts as a barrier and a glass slide to hold the sample at a specific depth. The device allowed for adjustments with a minimum step size of 1 µm, ensuring precise control over the amount of material removed during polishing. This setup prevented the removal of more material than intended, ensuring a controlled and precise polishing process.

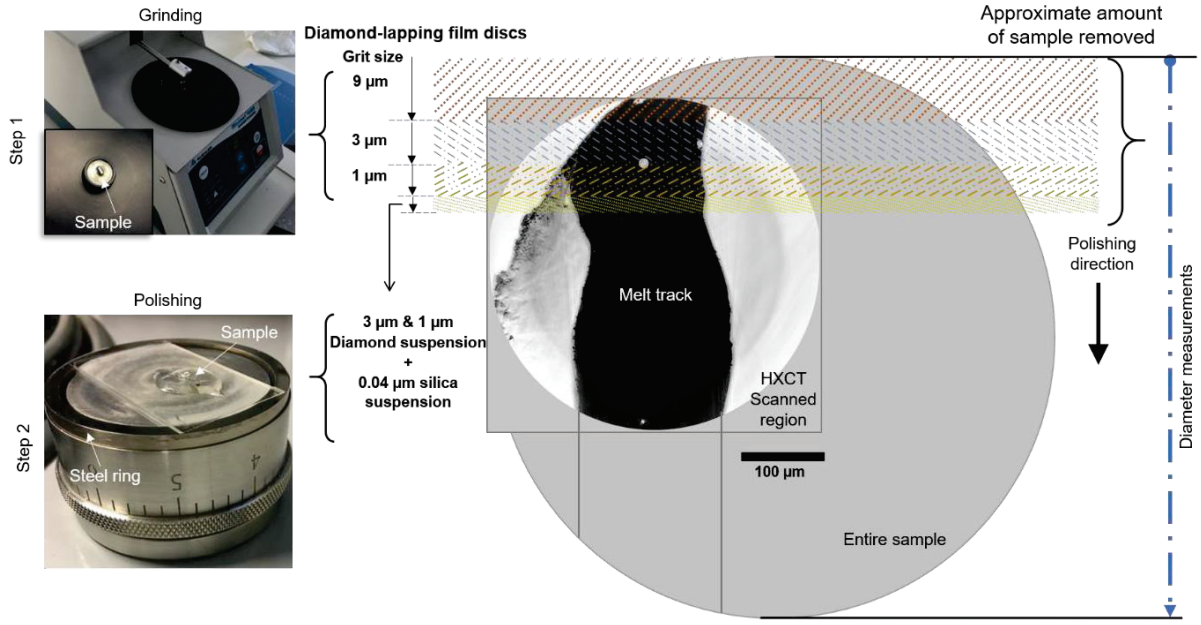

Fig. 5.6 Sample preparation process for high-resolution nanotomography. (Top left) Grinding of the cylindrical LPBF sample, with an inset image showing the sample during the process. The polishing device used to control material removal features the sample glued to a glass slide for secure handling during polishing (bottom left). (Right) Pictorial representation of the

grinding steps with varying grit sizes (9 µm, 3 µm, 1 µm) followed by the final polishing step with a 0.04 µm colloidal silica suspension.

2.1 With the sample secured, an ATM SAPHIR 550 polishing machine was used for the next steps. Firstly, any excess hot glue on the surface of the sample was polished away. Following this, the sample was examined under a light microscope to verify that the surface was flat and free of any residual glue.

2.2 Once a clean, even surface was obtained, the sample was set into the device, and an additional ~5 µm of material was polished away, with adjustments made in 1 µm increments as necessary.

2.3 It was followed by polishing using a 3 µm diamond suspension spray for 5 minutes and 1 µm diamond suspension spray for 3-5 minutes, aided by an ethanol spray for lubrication.

2.4 A final polish with a 0.04 µm colloidal silica suspension was applied for 5 minutes to achieve a high-quality finish. After polishing, the samples were thoroughly washed with dish soap and tap water to remove any remaining debris.

The material removal was monitored after each polishing step using a light microscope.

3. To improve the visibility of the melt pool during light microscopy, the samples were treated with a 5% NaOH solution for 90 seconds while still attached to the glass slide. The NaOH etching effectively highlighted the melt pool boundaries, aiding in subsequent sample preparation.

This entire procedure was fine-tuned after multiple trials on “dummy” Al-1Fe-1Zr substrate samples of the same dimensions. These tests allowed ensuring reproducibility and optimizing each step, from grinding and polishing to chemical etching, before applying the final protocol to the samples of interest.

The dimensions of the melt pools were measured using light microscopy, and specific regions were identified for *sub*-sample extraction (Fig. 5.7). Cylindrical *sub*-samples, ~30 µm in diameter, were extracted from the bottom and center of the melt pool to evaluate the microstructural variations across different depths. To achieve this, focused ion beam (FIB) milling was employed using an FEI Helios Nanolab 600i dual-beam system (electron and Ga+). Prior to milling, a protective carbon layer was deposited over the extraction area to shield the region of interest from potential damage during the process. This carbon patch also served as

a marker for sample identification and orientation, ensuring that the build direction remained accessible in the high-resolution tomography volumes. Once extracted, each sample was attached to a modified tungsten Omniprobe needle via platinum deposition and then mounted on a Huber sample pin for high-resolution investigations.

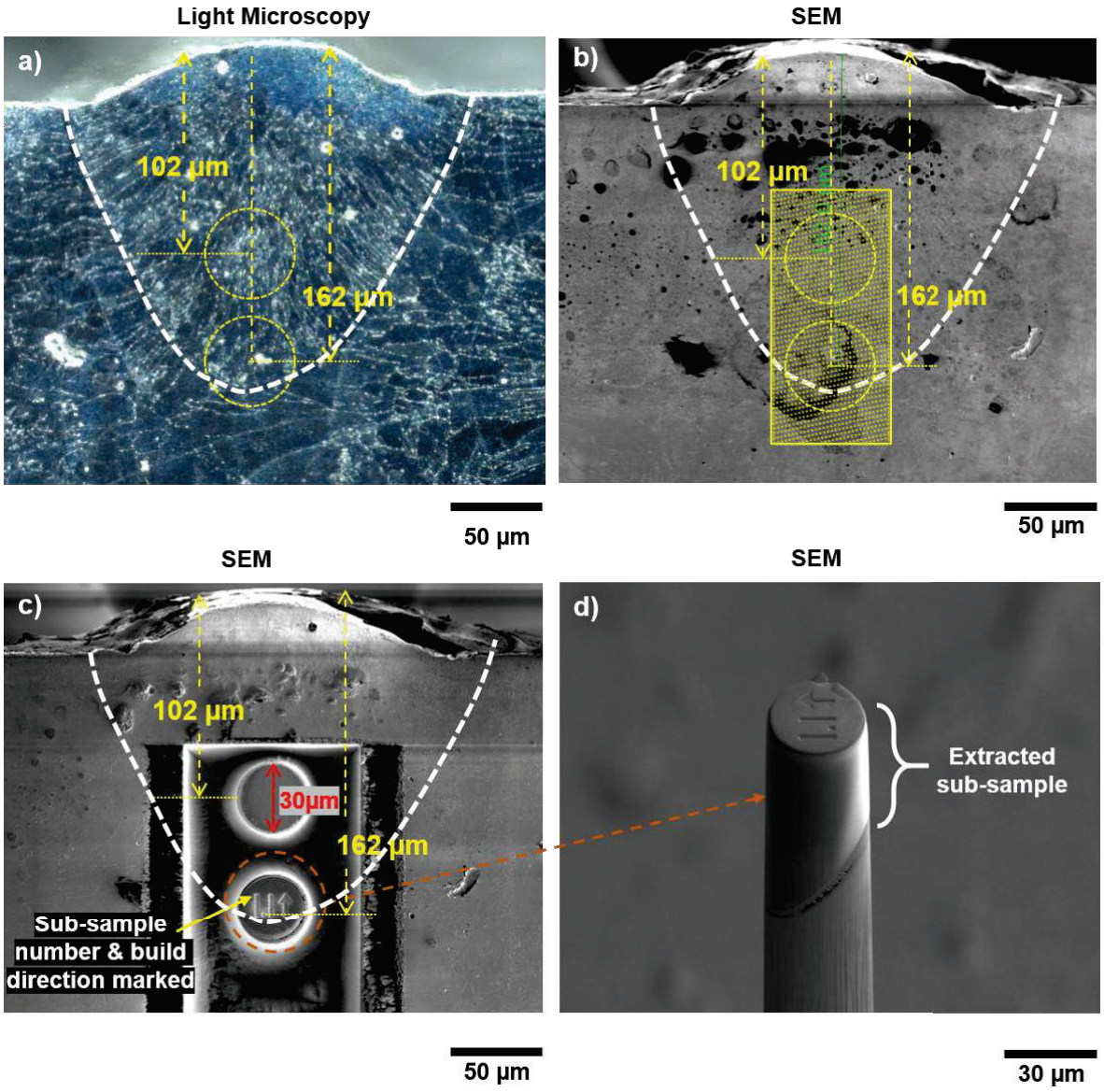

Fig. 5.7 Sub-sample extraction process for microstructural analysis. (a) Light microscopy image of the melt pool (C3) with marked dimensions, indicating regions selected for sub-sample extraction. (b) SEM image showing the marked extraction locations for focused ion beam (FIB) milling, based on references from the light microscopy measurements. (c) Cylindrical sub-samples milled from the bottom and middle of the melt pool, with the carbon patches on the top used for sample identification and marking the build direction. (d) The final extracted sub-sample. The white dashed lines indicate the melt pool border.

5.2.3 3D microstructural characterization

The general methodology, as outlined in section 3.3, remains largely consistent across experiments, with slight variations depending on the specific sample requirements. In this study, all 3D characterization measurements were performed at the ID16A beamline using an energy of 33.35 keV.

i. For the powder particle analysis, HXCT was performed by acquiring tomography scans at four increasing distances, with the initial distance corresponding to a voxel size of $(15\ nm)^3$. A total of 2000 projections were acquired, each with an exposure time of 0.3 seconds at each distance. For FXCT, 33 projections were collected with a 200 nm pixel step over a 180° rotation. Two sub-tomograms, consisting of 16 projections each, were captured, followed by a final projection at 180° to improve alignment. A bidirectional scanning approach was employed to accommodate the relatively large field of view (FoV) of 45 µm x 45 µm. This configuration provided an optimal balance between resolution and FoV, with an acquisition time of approximately 40 minutes per projection, resulting in a total scan time of about 22 hours.

ii. For the cylindrical samples extracted from the three distinct LPBF processing conditions (C1, C2, and C3), large FoV HXCT (400 x 400 x 400 μm^3) scans were conducted with the first distance corresponding to a voxel size of $(125\ nm)^3$. As explained in section 3.3, 2000 projections were acquired with an exposure time of 0.3 seconds per projection at 4 increasing distances from the focus. Local HXCT (120 µm x 120 µm) scans targeting regions of interest were carried out with a finer voxel size of $(40\ nm)^3$, with the same number of projections and exposure time. Both large FoV and local scans were performed before and after heat treatment, focusing on the same region of interest to assess microstructural changes.

iii. During the second session, *sub*-samples (~30 µm in diameter) extracted from various depths within the melt pools of the three different LPBF processing conditions (C1, C2, and C3) were analyzed using HXCT and FXCT. For these *sub*-samples, high-resolution HXCT scans with FoV 45 µm x 45 µm, were performed at four different distances, with the first distance corresponding to a voxel size of $(15\ nm)^3$. A total of 2000 projections were acquired, each with an exposure time of 0.3 seconds. Fig. 5.8 displays SEM images of the samples with details of the scans performed for each sample, and the scanning methodologies.

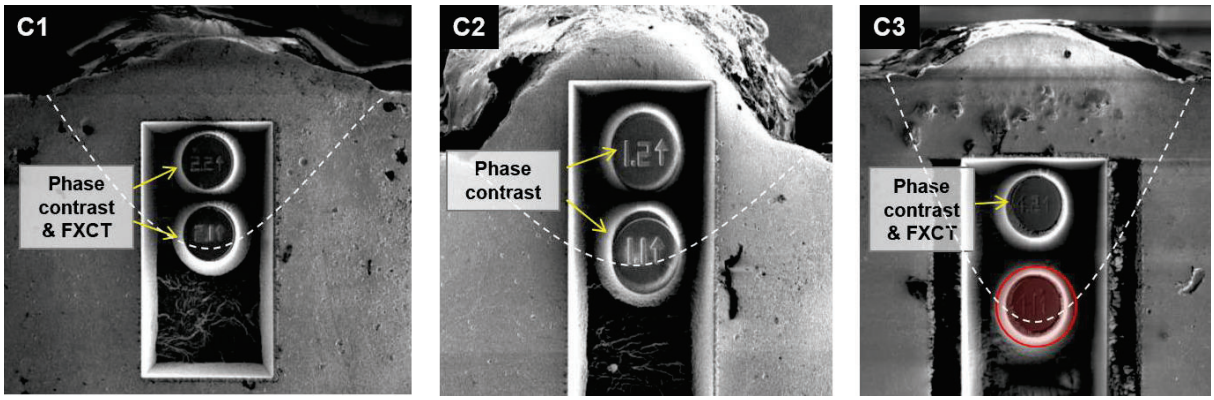

Fig. 5.8 SEM images of C1, C2, and C3 after FIB milling before extraction, showing the sub-samples prepared for high-resolution tomography. Details of the specific scans (Phase contrast tomography and FXCT) performed for each sample are indicated. In the case of C3, the sub-sample extracted from the bottom of the melt pool was lost during handling (marked red), and therefore, only the middle melt pool region was scanned. The white dashed lines indicate the melt pool border.

FXCT, which required the longest acquisition time, was performed using a 100 nm pixel step and 65 projections with over a 180° rotation. Two sub-tomograms of 32 projections each and a final projection at 180° were collected to enhance projection alignment. The field of view for these scans was 35 µm x 35 µm. Due to the dwell time of 40 ms per pixel step and the overhead associated with the acquisition process, each projection took approximately 18 minutes to capture, resulting in a total scan time of over 20 hours. Given the extended acquisition time, FXCT was prioritized for the most critical *sub*-samples of interest.

For the C1 and C2 processing conditions, *sub*-samples were successfully extracted from the bottom and middle regions of the melt pool. However, in C3, the *sub*-sample from the bottom of the melt pool was unfortunately lost during handling, leaving only the middle melt pool region for analysis. This underscores the delicate nature of *sub*-samples and handling at such fine scales.

5.3 Results

5.3.1 Powder particle

The HXCT results provide detailed insight into the microstructure of a single powder particle of the alloy, revealing a cellular microstructure by the bright intermetallic phases in the grey Al matrix. As shown in Fig. 5.9 (a) and (b), the *x-y* and *x-z* slices of the powder particle clearly illustrate the cellular network of these intermetallic phases spread throughout the volume. A

3D rendering of a representative region from the particle's midsection further illustrates this network, as presented in Fig. 5.9 (d). The total mass density distribution, represented by the plot of a line profile drawn across the sample in Fig. 5.9 (c), indicates an average density of ~2.6 g/cm³. However, discerning the specific intermetallic phases rich in Zr from those rich in Fe proves to be challenging using this technique alone.

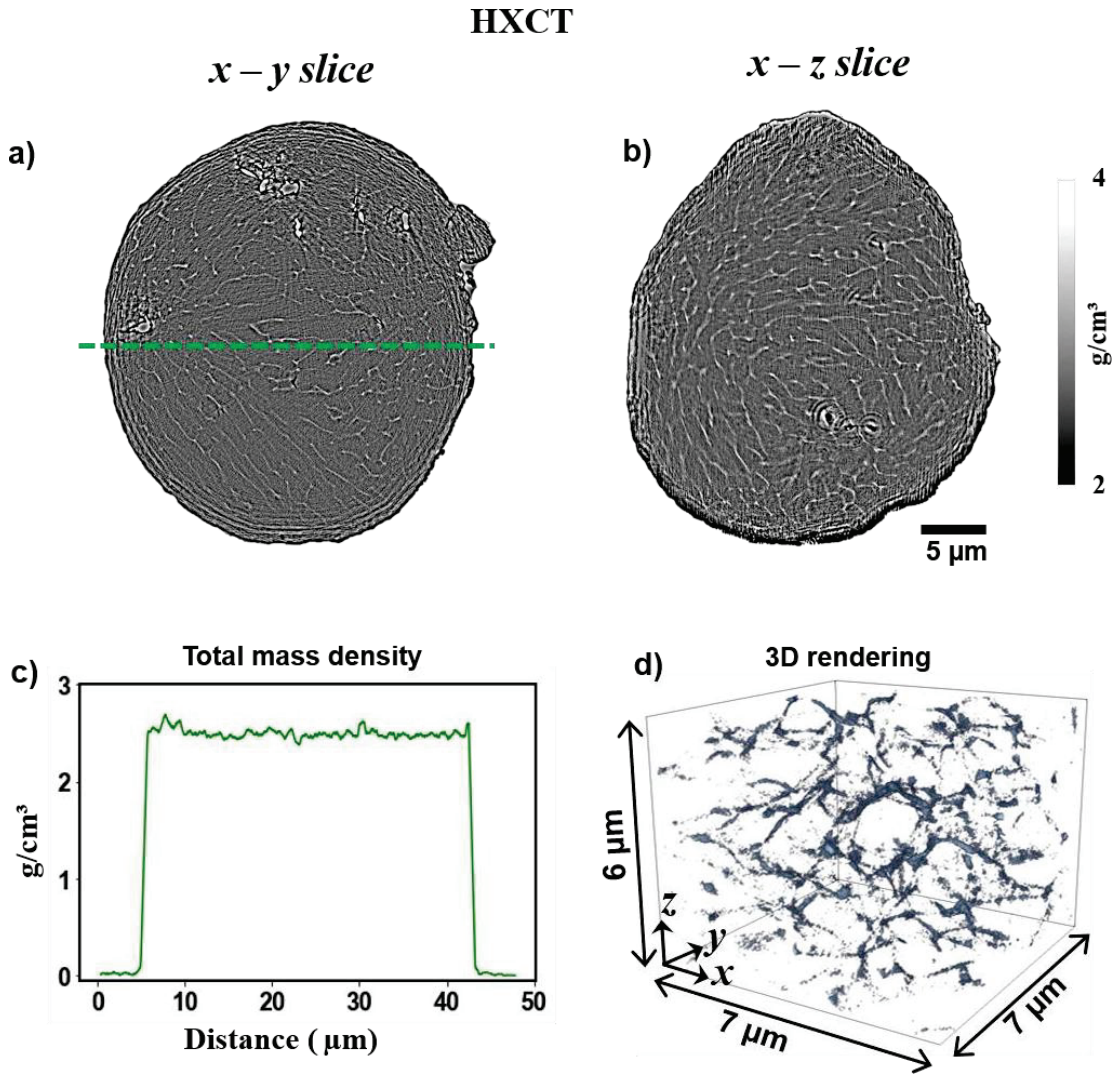

Fig. 5.9 HXCT mass density maps of (a) x-y slice and (b) x-z slice of a single powder particle. The slices reveal the interconnected network of bright intermetallic phases within the grey Al matrix. (c) Mass density distribution plot along the line profile drawn in (a), showing a density of ~2.6 g/cm³ across the sample. (d) 3D rendering of the cellular network of the intermetallics.

To address this limitation and accurately differentiate between these intermetallics, FXCT was incorporated as part of a correlative analysis. FXCT enables us to visualize the local elemental concentrations, providing a clearer distinction between the Zr- and Fe-rich intermetallics. Fig.

5.10 presents the FXCT results corresponding to the same region as the HXCT slice in Fig. 5.9 (a). The quantification of individual elements, as shown in the FXCT results, demonstrates that the Fe-rich intermetallics form a cellular network in the microstructure. Due to the relatively coarse voxel size (200 nm^3), the connectivity of this network is not as clearly distinguishable (compared to HXCT). At the junctions where these cellular structures intersect, localized regions of high Fe concentration emerge, with Fe-rich particles ranging in volume from 0.13 to 0.52 μm^3. In contrast, Zr is more uniformly distributed throughout the Al matrix. Specifically, Fig. 5.10 shows the FXCT elemental maps for (a) Zr and (b) Fe, illustrating both the morphology and concentration of these elements within the powder particle. In some regions, the increased Fe content leads to a displacement of Zr, as indicated by the yellow arrows in Fig. 5.10 (a) and (b).

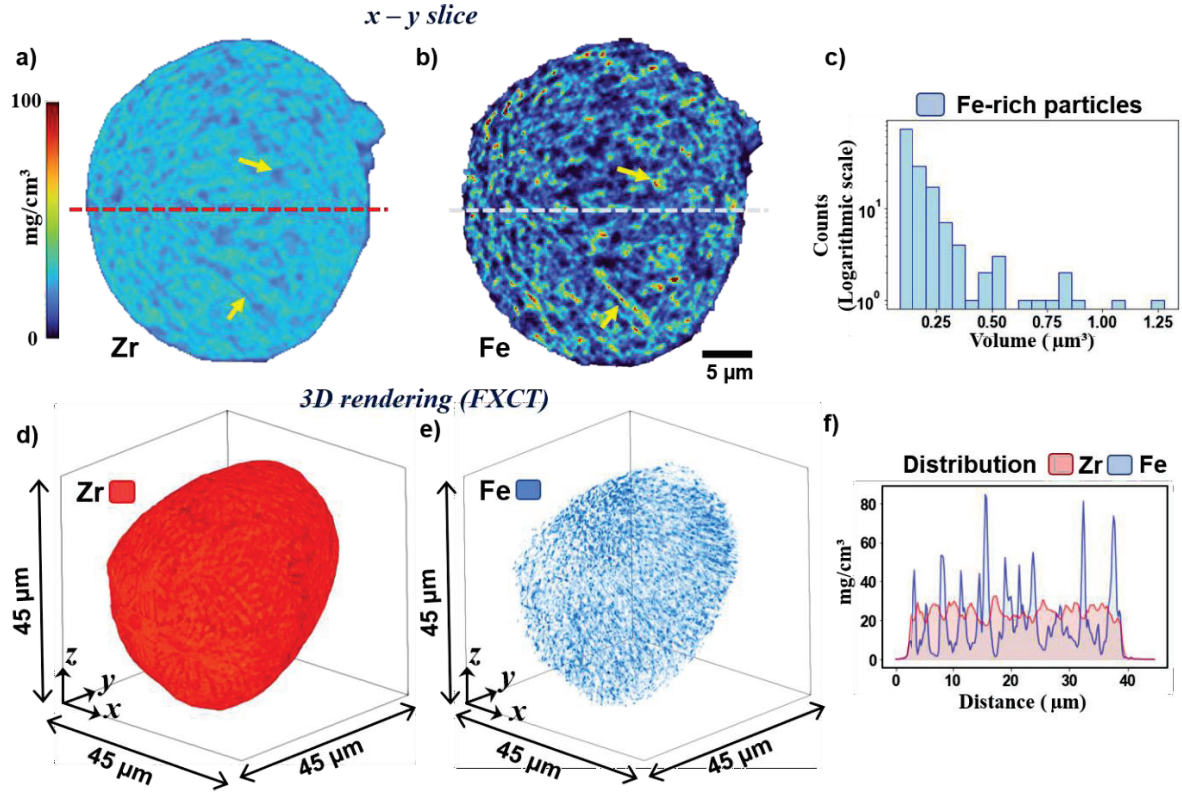

Fig. 5.10 FXCT maps of the same region shown in Fig. 5.9 (a), providing elemental concentrations. FXCT map of (a) Zr distribution and (b) Fe distribution. (c) Volume distribution of Fe-rich particles within the FXCT volume. (d, e) 3D renderings of Zr and Fe concentrations within the powder particle from the FXCT volume. (f) Line profile plots of Zr and Fe concentrations illustrate the relatively uniform concentration of Zr and the distinct formation of Fe-rich intermetallic structures.

Fig. 5.10 (c) shows the distribution of the Fe-rich particles within the Al matrix that are formed at the intersection of the cellular network, showing the volume distribution of these intermetallic structures from the FXCT volume. The volume fraction of Fe-rich particles in this powder particle is approximately 0.33%, corresponding to ~1wt%, aligning with the nominal alloy composition. The 3D renderings of Zr and Fe concentrations within the powder particle from the FXCT volume, as shown in Fig. 5.10 (d) and (e), respectively, provide visualization of the spatial distribution of these elements. The Zr distribution is relatively uniformly spread throughout the matrix, indicative of its homogeneous incorporation into the Al matrix during the solidification process. A detailed comparison of the line profiles for Zr and Fe, as depicted in Fig. 5.10 (f), elucidates the uniform concentration of Zr, with a consistent value of ~28 mg/cm^3 throughout the volume. This uniform distribution corresponds to approximately ~1wt%, aligning with the nominal alloy composition. Conversely, in areas with lower Fe concentrations, a slight enrichment in Zr is observed, as demonstrated by the line profile distribution.

5.3.2 LPBF 3D microstructure and heat treatment evolution

The melt pool boundaries for conditions C1, C2, and C3 were distinctly revealed using optical microscopy after polishing the heat-treated samples for the *sub*-sample extraction (Fig. 5.11).

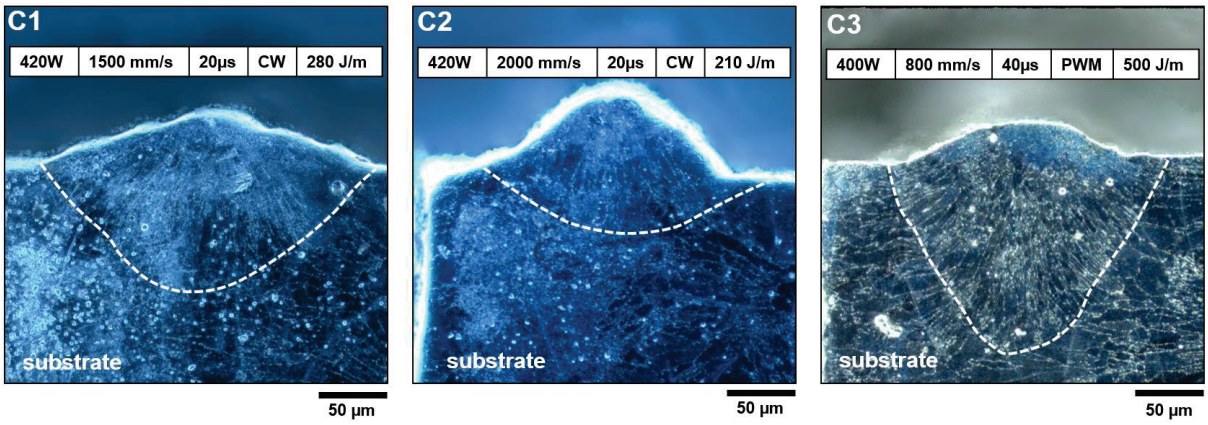

Fig. 5.11 Optical micrographs of polished samples for conditions C1, C2, and C3, showing the clearly defined melt pool boundaries marked with white dashed lines.

In the large FoV HXCT (voxel size (125 nm)^3) scans, the melt pool boundaries were not clearly visible due to insufficient contrast in the melt pool regions. Additionally, in the HXCT ROI

scans, only a specific portion of the melt pool was imaged, limiting the ability to capture the full melt pool depth.

Fig. 5.11 presents optical micrographs for the respective conditions, highlighting the melt pool boundaries and indicating accurately the melt depth for each condition. These micrographs offer a more complete representation of the melt pool geometry, complementing the high-resolution but localized insights from the HXCT ROI scans. For condition C1, the melt pool depth was measured to be 120 µm from the substrate height. For condition C2, the melt pool depth was significantly shallower at 60 µm, and condition C3 exhibited the deepest melt pool depth at 170 µm.

HXCT measurements were conducted for both the as-built and heat-treated samples for C1, C2, and C3 conditions. Condition C1 was processed with a 420 W laser power and 1500 mm/s scanning speed, resulting in a stable, continuous melt tracks with a well-formed melt pool.

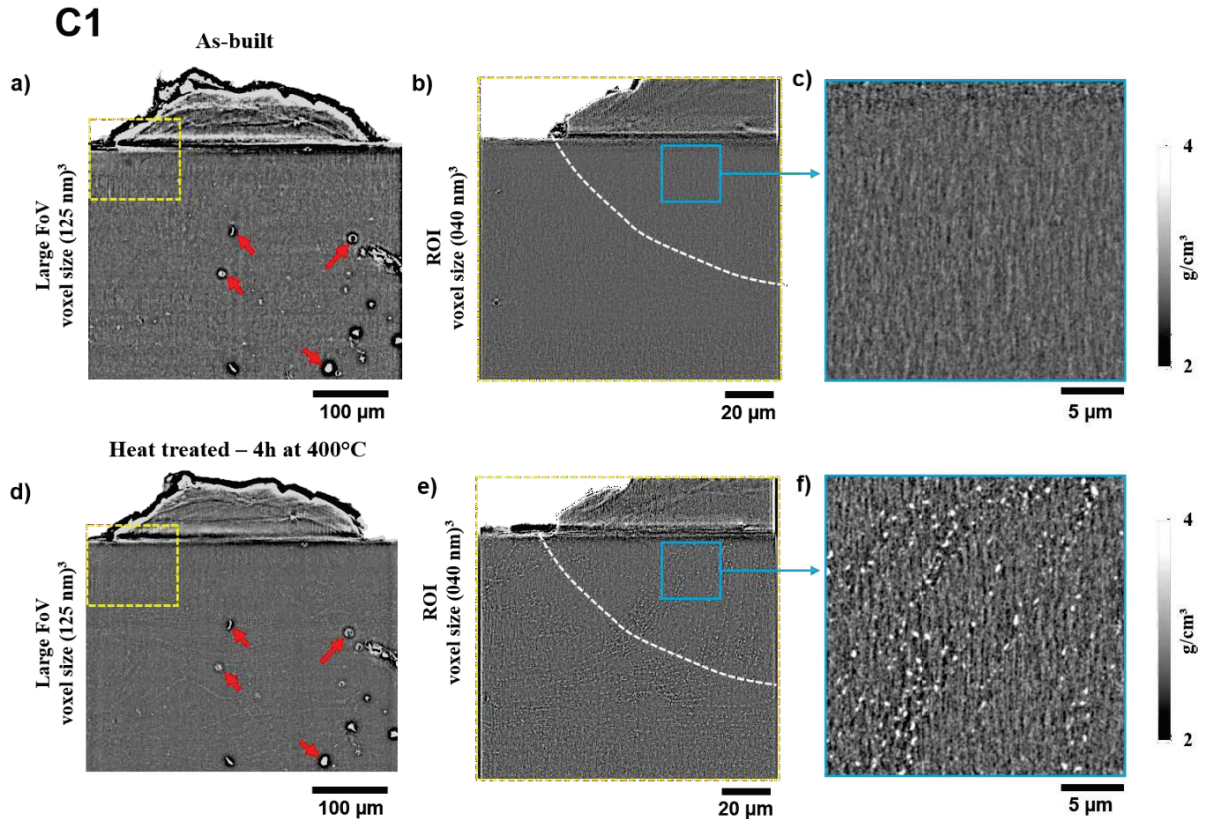

Fig. 5.12 HXCT slices with voxel size 125 nm, showing the cross-sectional view of the melt track in (a) as-built and (d) heat treated condition for condition C1. The HXCT ROI scans, with a finer voxel size of 40 nm (b and e), were measured in the region marked in yellow aiming

to resolve the melt pool boundary, marked with a white dashed line. The enlarged images (c and f) of the region marked in blue from the HXCT ROI scans elucidate the microstructure after heat treatment. The red arrows mark pores which also appear bright due to the bandpass filter applied to correct for gray value gradients.

Fig. 5.12 (a) and (d) present HXCT slices depicting the cross-sectional view of the melt pool in the as-built and heat-treated conditions for Condition C1, respectively. The corresponding ROI slices (b) and (e) reveal a microstructural evolution: no distinct microstructural features are observed in the as-built state, while bright phases appear in the heat-treated condition. The enlarged images (c) and (f) distinctly highlight the developed microstructures following heat treatment. Notably, intermetallic particles appear to have coalesced, likely aligning along elongated grain boundaries, as reported previously [92,100]. These formations indicate coarsening of intermetallics driven by the heat treatment.

Pores smaller than 20 µm appear in the sample as bright features. This is due to the application of a bandpass filter to the HXCT slices, which corrects for gray value gradients. A key distinction between pores and intermetallics is that pores exhibit a characteristic dark contour, allowing them to be differentiated from the intermetallics. The cross-sectional analysis (Fig. 5.11) of the single-track melt pool for C1 revealed a melt depth of ~120 µm, an optimal balance between height above the substrate and remelted depth, ensuring strong bonding between subsequent layers and a stable melt track. Fig. 5.12 illustrates the stability of the melt pool under these parameters, showing a defined melt track (as seen in ROI scans) and consistent remelted depth. While this figure provides a representative slice, the homogeneity of the melt track can be inferred from the HXCT slice shown in Fig. 5.5, under the applied processing parameters.

Condition C2, designed to test a faster scanning speed (2000 mm/s) while maintaining the same 420 W laser power, demonstrated different melt pool characteristics. At this higher scanning speed, the remelted depth was notably reduced compared to C1, reflecting the reduced time for heat to penetrate the substrate.

Fig. 5.13 (a) and (d) display HXCT slices of the melt pool cross-section for condition C2 in the as-built and heat-treated states, respectively. The melt pool was relatively shallow (~ 60 µm, see also Fig. 5.11), and a larger portion of the molten material remained above the substrate, which may indicate weaker fluid flow and less heat dissipation into the substrate.

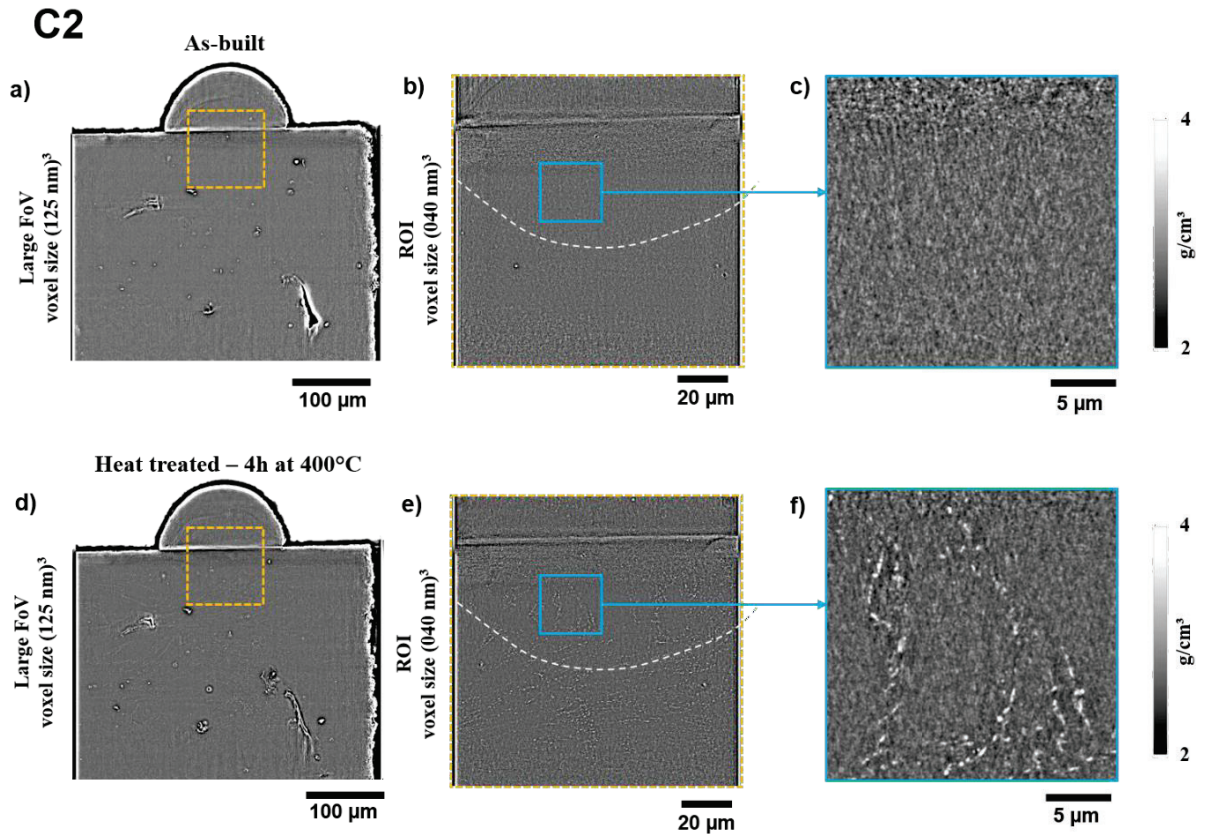

Fig. 5.13 HXCT slices with a voxel size of 125 nm, showing the cross-sectional view of the melt track in (a) as-built and (d) heat-treated conditions for condition C2. The HXCT ROI scans, with a finer voxel size of 40 nm (b and e), were measured in the region marked in orange to resolve the melt pool boundary, marked with a white dashed line. The enlarged images (c and f) of the region marked in blue from the HXCT ROI scans highlight the microstructure before and after heat treatment. The melt pool boundary indicates a shallower melt depth.

The heat treatment at 400°C led to similar evolution and distribution of intermetallics as in C1. The ROI slices (Fig. 5.13 (b) and (e)) indicate a clear microstructural evolution, with initially barely resolved features in the as-built condition becoming more pronounced after heat treatment. Enlarged images (Fig. 5.13 (c) and (f)) reveal intermetallic particles aligning along elongated structures, likely Al grain boundaries.

For condition, C3, where a lower scanning speed of 800 mm/s was combined with 400 W laser power and operation in pulse width mode, a significant increase in the melt pool depth was observed. Fig. 5.14 (a and d) present HXCT slices of the melt pool cross-section for Condition C3 in the as-built and heat-treated states, respectively. The combination of slower scanning speed and pulsed laser resulted in a significantly deeper melt pool (~170 µm, as also shown in Fig. 5.11) compared to C1 and C2.

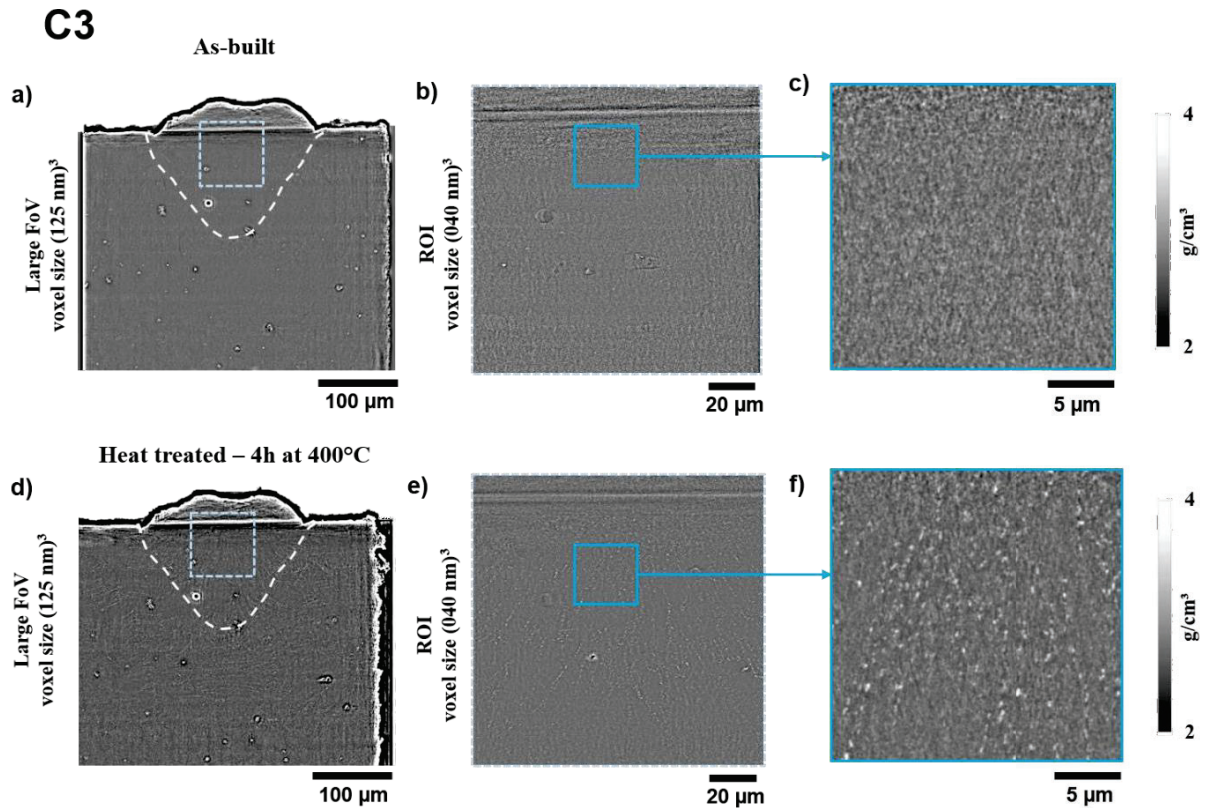

Fig. 5.14 HXCT slices with voxel size 125 nm, showing the cross-sectional view of the melt track in (a) as-built and (b) heat treated condition for condition C3. The HXCT ROI scans (b and e), with a finer voxel size of 40 nm, were measured in the region marked in cyan. The enlarged images (c and f) of the region marked in blue from the HXCT ROI scans highlight the microstructure before and after heat treatment. The melt pool depth inferred from the optical micrographs is marked in the large FoV slice in white dashed lines as it exceeds the ROI field of view.

The remelted depth was significantly more pronounced, and the melt pool extended deeper into the substrate. The ROI slices in Fig. 5.14 (b) and (e), along with the enlarged images (c) and (f), reveal a distinct microstructural evolution, consistent with the trends observed in Conditions C1 and C2.

5.3.3 High-resolution characterizations within prior melt pools

Condition C1:

In both *sub*-samples, i.e., from the bottom and the center of the melt pool, the intermetallic particles were observed in elongated structures, likely aligning along Al grain

boundaries, as evident in both the large field of view (FoV) and region of interest (ROI) scans from session 1. HXCT slices revealed a clear depiction of the microstructures, as illustrated in Fig. 5.15 (a) and (d) from the center and the bottom of the melt pool, respectively, which provided a comprehensive view of the melt pool's microstructure.

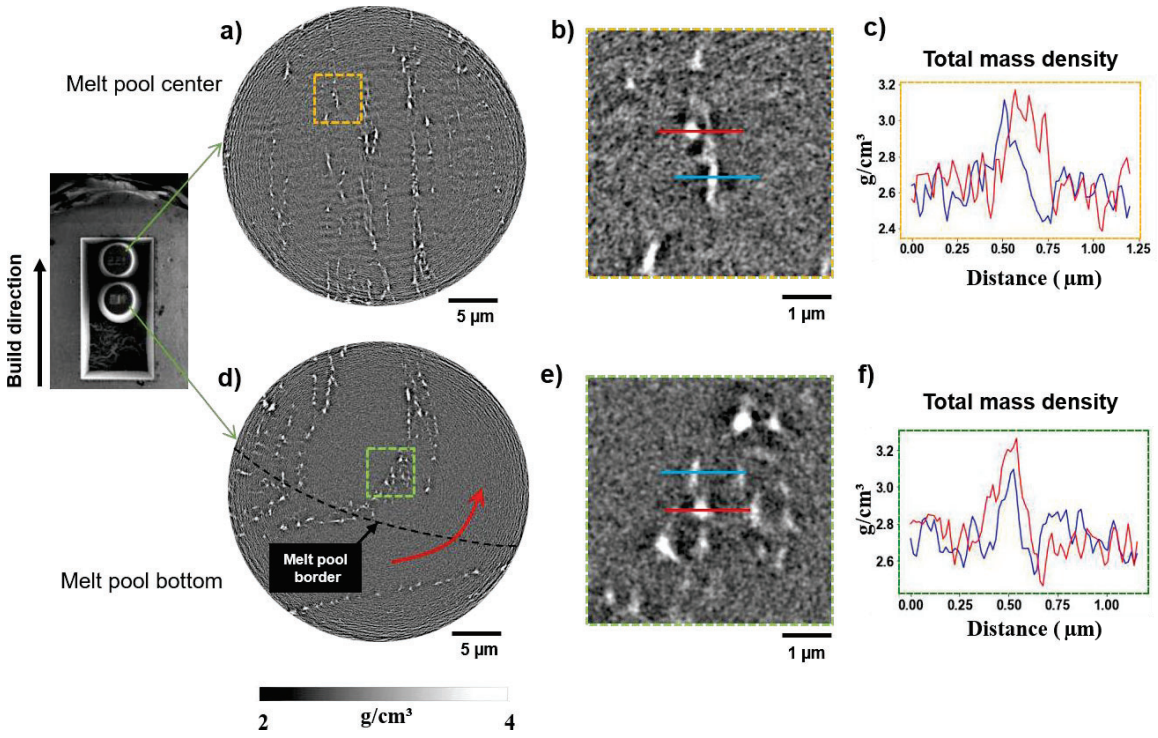

Fig. 5.15 HXCT mass density slices from the center and bottom of the melt pool from condition C1 are shown in (a) and (d), respectively, revealing intermetallic phases distributed within the Al matrix. The melt pool boundary is delineated a by black dashed line and the directional solidification of the grain is indicated by a red arrow in (d). (b) and (e) Enlarged region of interest from the center and bottom of the melt pool, highlighted by the orange and green square. (c) and (f) Line profile plot of the total mass density variations along the blue and red lines, showing density variations across the intermetallics.

The melt pool boundary is visible and appears slightly darker than the Al matrix in the reconstructed volume, a feature attributable to the reduced total mass density in this region. Grains extending from the previously solidified layer into the new melt pool were observed (Fig. 5.15 (d) marked by a red arrow), suggesting directional solidification. The enlarged views in Fig. 5.15 (b and e) highlight the intermetallic particles from the center and bottom of the melt pool. The intermetallics observed in both the bottom and center exhibited subtle differences in mass density detected between the two regions, as confirmed by line profile

analyses in Fig. 5.15 (c and f). However, distinguishing Fe-rich and Zr-rich intermetallics using mass density alone proved to be challenging due to the minimal variations in the HXCT data.

FXCT was employed to overcome the limitations of HXCT in differentiating Fe- and Zr-rich intermetallics. This method allowed for more precise identification of elemental content. Due to the extended acquisition times required for FXCT, the field of view was reduced to a height of 5 µm and a width of 35 µm, ensuring more detailed imaging of the intermetallic particles.

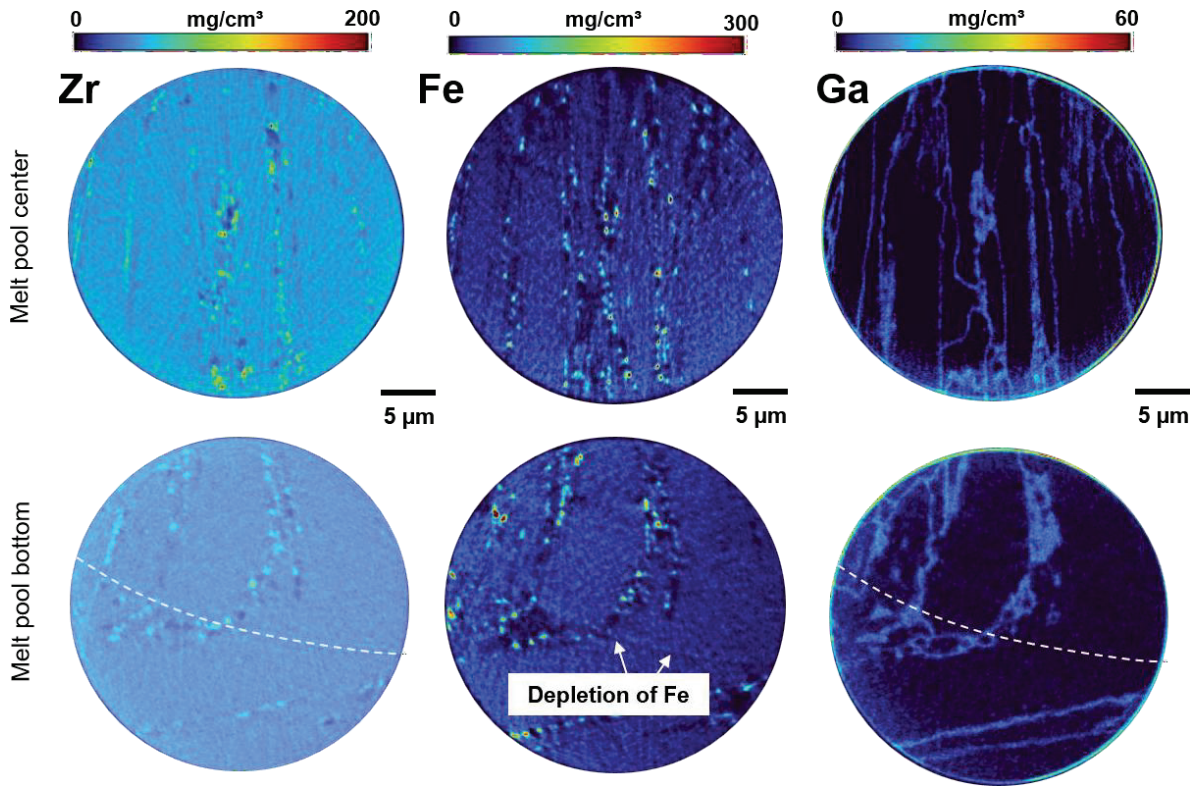

Fig. 5.16 FXCT elemental concentrations of Zr, Fe, and Ga from the same regions shown in the HXCT slices in Fig. 5.15, representing the center and bottom of the melt pool.

The FXCT results, as shown in Fig. 5.16, correspond to the same regions examined in the HXCT phase contrast slices, facilitating a direct correlative analysis. Fig. 5.17 shows additional direct comparisons of elemental concentration (FXCT) and mass density (HXCT) for the enlarged regions. It shows that the intermetallics in the enlarged images from Fig. 5.15 (b and e) are different, some being rich in Fe and others being rich in Zr. Due to the finite resolution in FXCT, the two distinct particles are not properly resolved (Fig. 5.17 FXCT top panels of Zr and Fe)

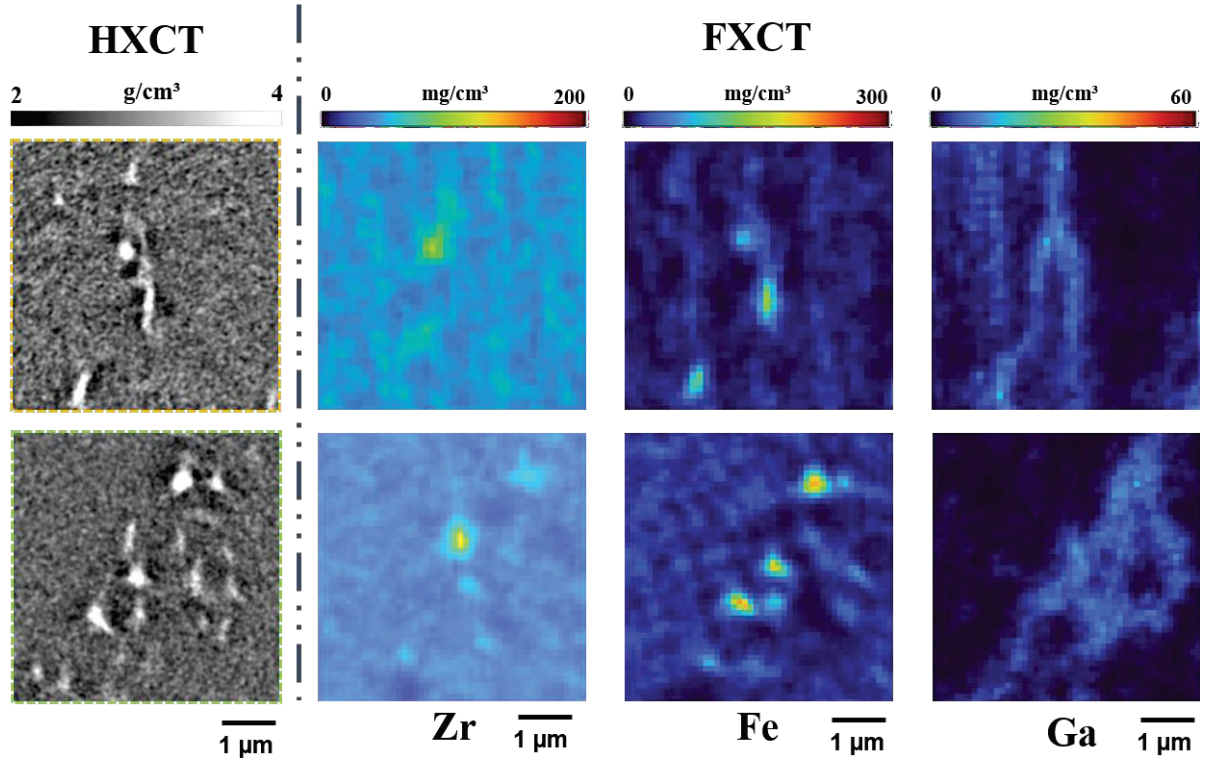

Fig. 5.17 Direct comparison of the enlarged regions of interest from HXCT (Fig. 5. 15 (b) and (e)) with the corresponding regions from FXCT for the various elements.

FXCT revealed several key observations: the background level of Fe and Zr within the Al grains shows a uniform concentration of ~15.5 mg/cm³ for Fe and ~26 mg/cm³ for Zr, at both the bottom and center of the melt pool. This corresponds to 0.56wt% Fe and 0.96wt% Zr that are either partially dissolved in the solid solution or exist forming nanometer-sized metastable precipitates throughout the Al matrix. Additionally, a distinct depletion of Fe is observed at the melt pool boundary, followed by a slight Fe enrichment in the adjacent region (Fig. 5.16 – Fe, bottom sample). As previously reported, Ga, which is introduced as a result of FIB extraction, acts as a grain boundary marker and shows that the intermetallic particles are, in fact, decorating the grain boundary. However, a notable difference emerged in the distribution of intermetallic particles between the bottom and center of the melt pool regions, even visually obvious in the 3D rendering of the FXCT volumes shown in Fig. 5.18. At the bottom of the melt pool, the volume fraction of Fe-rich intermetallics was measured at 0.78%, while Zr-rich intermetallics constituted 0.52% of the volume, calculated from corresponding histograms for the number of Zr-rich and Fe-rich particles in the volume as shown in Fig. 5.18. The analysis was performed on the FXCT volumes using intensity-based thresholding to segment the particles followed by 3D particle quantification with the 3D Object Counter plugin in ImageJ

[188]. It is to be noted that these calculations were done only in the volume of the melt pool (the substrate region was not used for calculations).

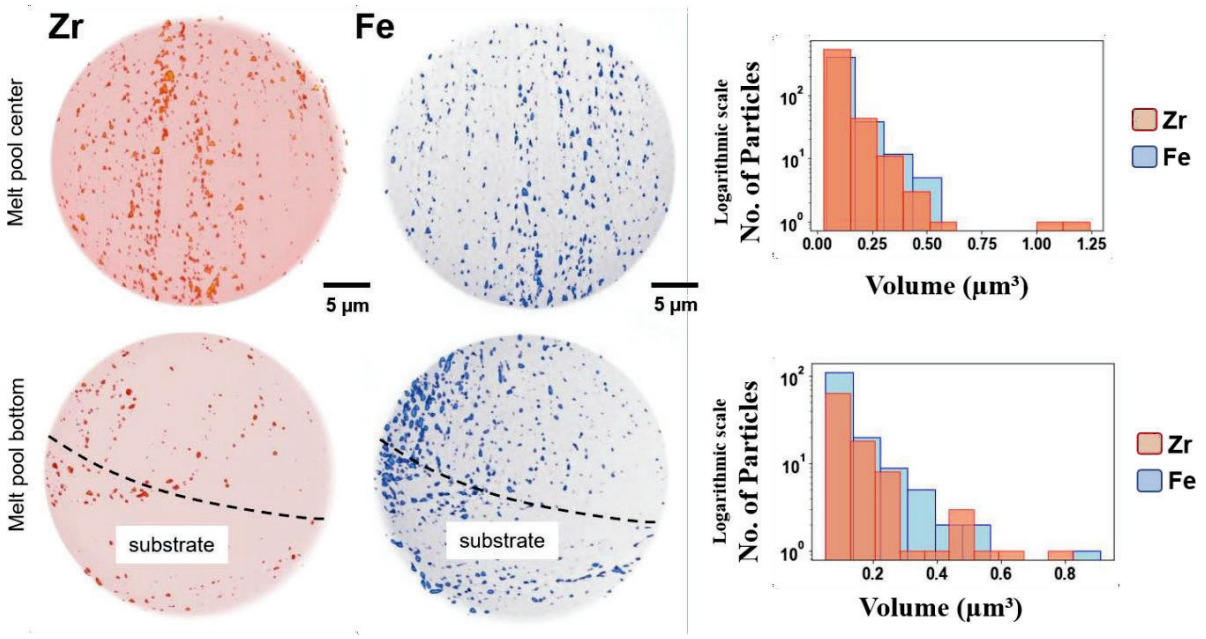

Fig. 5.18 3D rendering of Zr and Fe FXCT volume, elucidating the distribution of particles from the bottom and the center of the melt pool. The corresponding histograms for the number of Zr-rich and Fe-rich particles in the volume (imaged by FXCT) are shown as a function of their volume (µm³) analysed using 3D Object Counter plugin in ImageJ [188]. Volume fractions of Zr-rich and Fe-rich particles are presented for both the bottom and center of the melt pool, highlighting the distribution of these elements.

In contrast, the center of the melt pool exhibited higher volume fractions of intermetallics. The Fe-rich particles accounted for 0.92%, and the Zr-rich particles reached 0.98%. This is a nearly twofold increase in Zr-rich particles' volume fraction.

Condition C2:

The HXCT slices in Fig. 5.19 (a and b) present the mass density maps from the center and bottom of the melt pool. Notably, the melt pool boundary was clearly visible marked by a distinct darker contrast indicative of a reduced total mass density. The bright intermetallic particles enriched in Fe and Zr, were predominantly located along elongated structures, likely following Al grain boundaries, as identified in both large FoV and ROI scans from previous analyses.

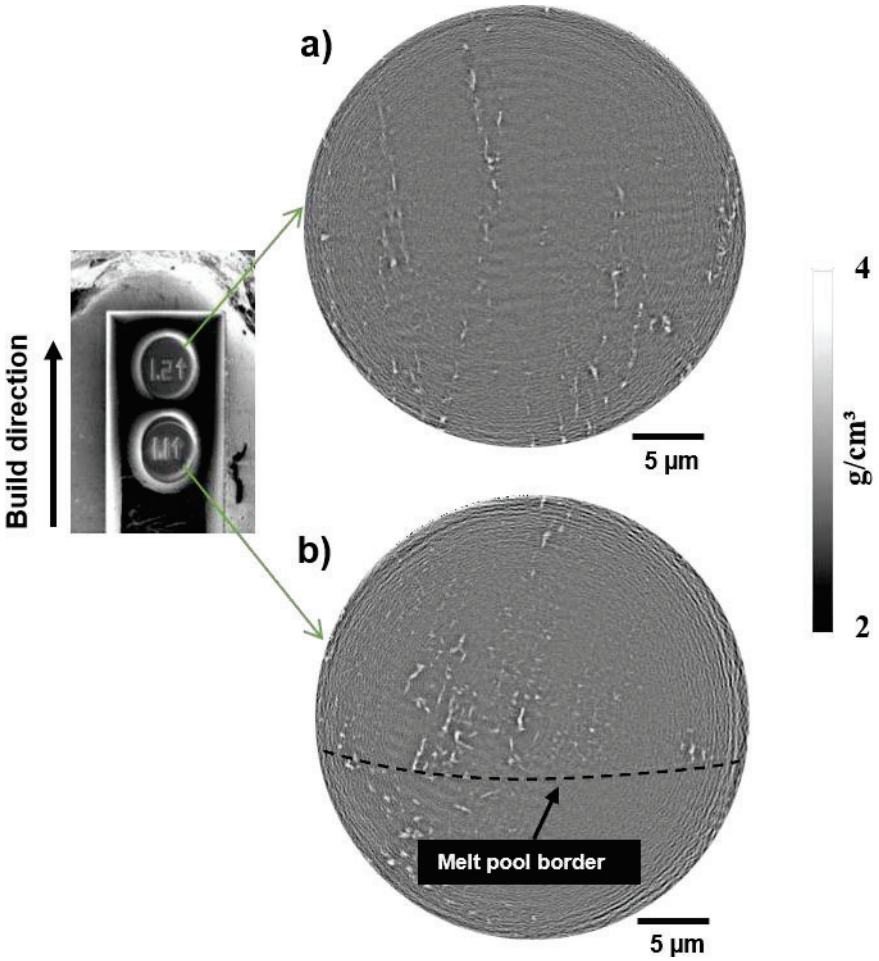

Fig. 5.19 HXCT mass density slices from the center and bottom of the melt pool from condition C2 are shown in (a and b), respectively, revealing intermetallic phases distributed within the Al matrix.

Since no significant changes in the morphology or distribution of the intermetallics were observed compared to C1, FXCT measurements were deemed unnecessary for the *sub*-samples.

Condition C3:

HXCT measurements were performed on *sub*-samples extracted from the center of the melt pool. Unfortunately, the *sub*-sample from the bottom of the melt pool was lost during handling, limiting the analysis to the center region. These scans revealed clear intergranular structures, as depicted in Fig. 5.20 (a), with a grey Al matrix interspersed with bright intermetallic phases, rich in either Fe or Zr. The HXCT slice provided a representation of the intermetallic distribution within the Al matrix. In contrast to conditions C1 and C2, the amount of intermetallics observed in condition C3 was significantly higher. The higher concentration

of intermetallic particles observed in the center of the melt pool prompted further investigation using FXCT to obtain a more detailed understanding of the elemental distribution and the behaviour of Fe- and Zr-rich phases. The elemental concentrations of Zr, Fe, and Ga are shown in Fig. 5.20 (b), (c), and (d), respectively.

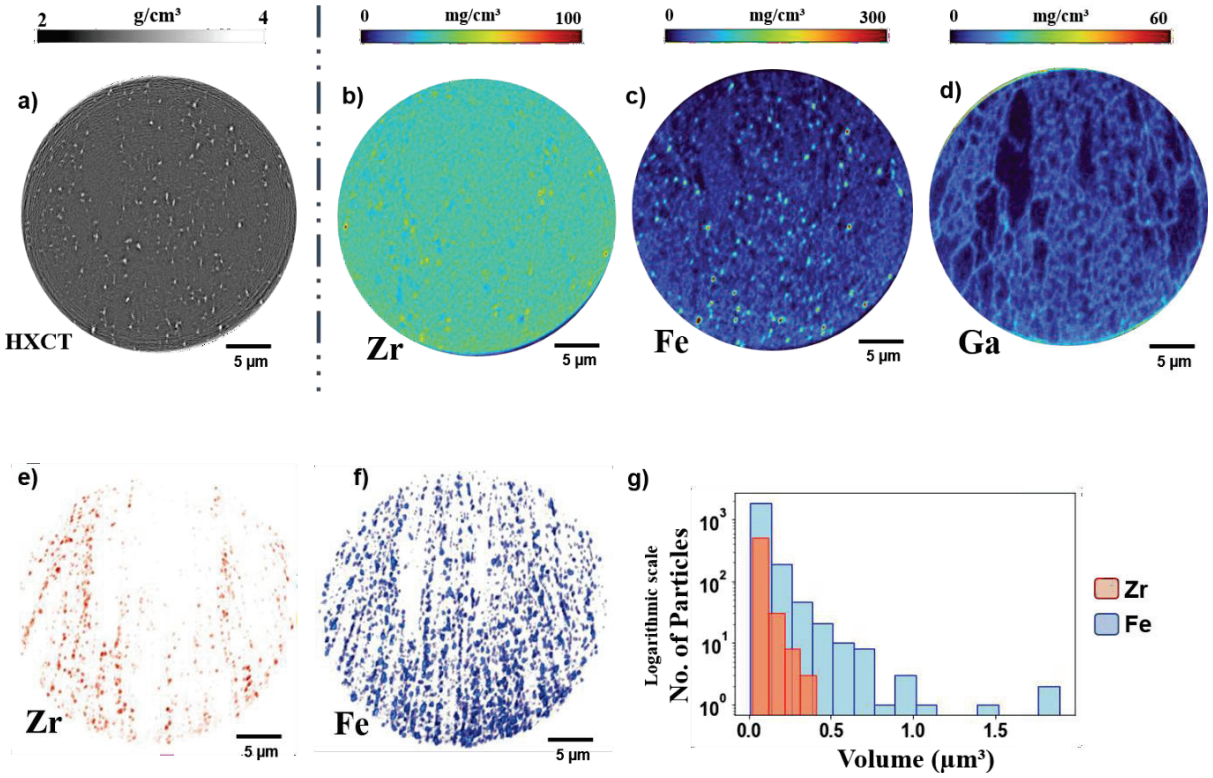

Fig. 5.20 (a) HXCT mass density slice of the sub-sample extracted from the center of the melt pool, revealing intermetallic phases within the Al matrix. (b–d) FXCT elemental concentrations for Zr, Fe, and Ga, respectively, show the spatial distribution of these elements in the same region as (a). (e and f) 3D volume rendering of Zr-rich of Fe-rich intermetallic particles, respectively. (g) Histogram displaying the size distribution of Zr and Fe particles in the FXCT measured region analysed using 3D Object Counter plugin in ImageJ [188].

The background level of Fe and Zr within the Al grains shows a uniform concentration of ~17 mg/cm³ for Fe and ~30 mg/cm³ for Zr. These concentrations correspond to ~0.65wt% Fe and ~1wt% Zr, which are either partially trapped in the Al matrix or present forming nanometer-sized precipitates dispersed throughout the grains. The introduction of Ga during FIB extraction, which acts as a grain boundary marker, revealed a significant difference in condition C3: a notably high density of finer grain boundaries, forming along the direction associated with columnar growth. The majority of the grain sizes measures much less than ~5 µm.

Moreover, it indicates that the intermetallic particles are predominantly accumulated at the grain boundaries, in line with previous findings, with no evidence of cuboidal Al_3Zr particles at the center of the grains. Further 3D rendering of the Zr and Fe intermetallic particles, as shown in Fig. 5.20 (e) and (f), revealed distinct differences in their accumulation. In this region, Fe accumulation was notably higher, with a volume fraction of 3.4%, compared to the Zr-rich intermetallics, which accounted for only 0.62% of the total volume in the measured FXCT region. A histogram of the size distribution of the Zr and Fe particles from FXCT volumes, displayed in Fig. 5.20 (g), provides further evidence of the differences in particle size and distribution between the two elements. The analysis was performed on the FXCT volumes using intensity-based thresholding to segment the particles followed by 3D particle quantification with the 3D Object Counter plugin in ImageJ [188]. The Fe-rich particles were more numerous and larger in size compared to the Zr particles, indicating a more pronounced segregation and accumulation of Fe in the center region of the melt pool.

5.4 Discussion

5.4.1 Powder particle

The microstructural characterization of the Al-1Fe-1Zr alloy powder was conducted using HXCT and FXCT, to understand the spatial distribution and morphology of Fe- and Zr-rich intermetallics. HXCT imaging revealed a cellular structure of bright intermetallic phases embedded within the Al matrix, indicative of solidification features formed during the rapid cooling process of gas atomization (Fig. 5.9). FXCT analysis confirmed that Fe-rich intermetallics are primarily responsible for the cellular structures observed in HXCT (see Fig. 5.10). The cellular structures, distributed throughout the powder particle, are the result of hypo eutectic solidification, following the transformation pathway of liquid (L) → α-Al followed by liquid (L) → α-Al + θ-$Al_{13}Fe_4$. However, due to the relatively coarse voxel size (200 nm^3), the connectivity of this network is not as clearly distinguishable compared to HXCT. At the junctions where these cellular structures intersect, localized regions of high Fe concentration emerge. These findings support a solidification mechanism in which Fe-rich intermetallics preferentially nucleate in the intercellular regions, with volumes ranging from 0.13 - 0.5 μm^3 . The presence of homogeneously distributed Zr in the Al matrix indicates that during solidification, Zr either remains in solid solution or forming nanoscale metastable $L1_2$-Al_3Zr precipitates. Quantitative analysis elucidates Zr maintains a consistent concentration of approximately 28 mg/cm³ (~1wt%) in the Al matrix, aligning with the nominal alloy

composition. A higher-resolution FXCT would be necessary to characterize the cellular network of Fe intermetallics more accurately.

5.4.2 Microstructural characterization and effects of heat treatment

Under condition C1, a melt pool with well-defined geometry was observed, exhibiting a width of approximately 250 µm and a depth of 120 µm, corresponding to a width-to-depth (W/D) ratio of ~2 (Fig 5.11). This ratio falls within the generally accepted optimal range of 1.5–2.5 for single-track LPBF experiments, which is indicative of conduction-mode melting [189–191]. In this regime, a stable balance between energy input and thermal dissipation is achieved, promoting uniform melting. The moderate CW (Continuous Wave) scanning speed provided a steady and sufficient heat input, resulting in balanced melting and heat dissipation into the substrate. This corresponds to typical observations at moderate scanning speeds [192]. In contrast, condition C2 employing a higher CW scanning speed produced a melt pool with a reduced depth of ~60 µm and a width of ~200 µm (W/D > 3). This elevated W/D ratio indicates a transition toward shallow, less penetrating melt pool, characteristic of reduced energy density and limited remelting. Such geometries are commonly associated with insufficient bonding between layers and an increased risk of lack-of-fusion defects, particularly at higher scan speeds where heat input is insufficient [193]. Condition C3, involving a PWM (Pulsed Width modulation) laser mode at a slower scanning speed, resulted in a deeper melt pool, with a width of ~200 µm and a depth of ~170 µm (W/D ≈ 1.2). This relatively low W/D ratio reflects a shift toward keyhole-mode melting, where excessive energy input leads to deeper penetration into the substrate [189,194]. These observations underscore the sensitivity of melt pool morphology to scanning speed and highlight the critical role of thermal input in the LPBF process (see Fig. 5.11).

A fundamental difference between CW and PWM in LPBF is their mode of energy delivery, which in turn affects solidification kinetics [195]. In CW- LPBF, the continuous laser beam provides a steady heat source that establishes a more homogeneous thermal field and slower cooling rates [195]. These conditions favour the development of coarser microstructures [196]. In contrast, PWM-LPBF delivers energy intermittently, leading to rapid heating–cooling cycles and higher cooling rates [197]. The smaller volume of molten metal at any given time under PWM conditions can promote the formation of finer microstructures.

Understanding the microstructure formation mechanisms in LPBF requires consideration of the melt pool geometry and thermal gradients. The optical microscopy images in Fig. 5.21

provide a clearer visualization of the melt pool boundaries, delineating the width-to-depth ratio for each condition. The heat flow direction (maximum thermal gradient, marked in white arrows), nearly perpendicular to the melt pool boundary, dictates the solidification path and subsequent grain growth direction [198,199]. This is schematically represented in Fig. 5.21 bottom panel, where black arrows indicate the heat flow direction and the grain morphology is illustrated in gray (inferred from optical micrographs). Conditions C1 and C2, exhibited predominantly almost vertical grain growth. Conversely, in C3, the deeper melt pool suggested a grain growth direction with a strong horizontal component. As solidification progresses, the junctions where grains intersect can disrupt columnar grain growth, leading to the formation of multiple grain boundaries along the columnar direction. Post heat treatment, intermetallic particles exhibited a tendency to coalesce into larger intermetallics, aligning preferentially along grain boundaries, across all conditions.

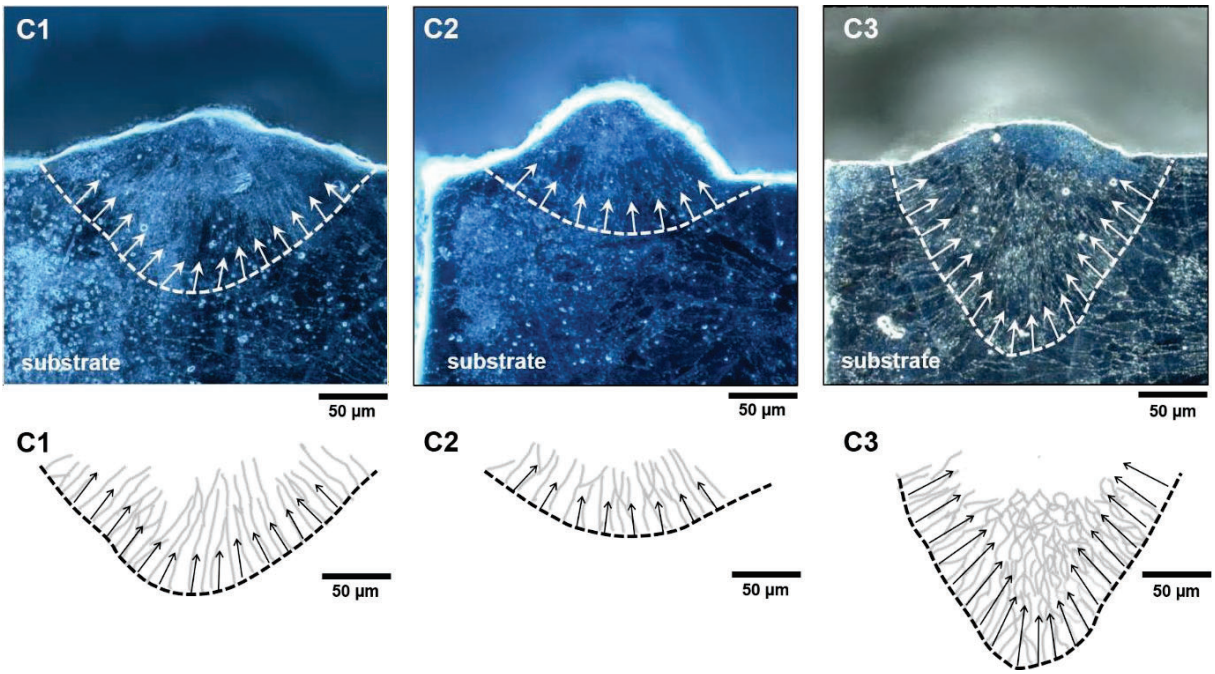

Fig. 5.21 Optical micrography images of the three conditions. The heat flow direction (thermal gradients) are marked with white arrows in the top panel. The respective schematic representation of the melt pool and the heat flow direction (black arrows) are shown in the bottom panels along with the grain morphology in gray (inferred from the optical micrographs).

HXCT imaging revealed an aluminum matrix interspersed with bright intermetallic particles, while the melt pool boundary appeared with a darker contrast due to Fe depletion, immediately followed by a slight enrichment in the adjacent region (confirmed by FXCT, Fig. 5.16), see

also [100]. FXCT further enabled the differentiation of Zr- and Fe-rich intermetallics and provided a detailed mapping of these elements (Fig. 5.17). The accumulation of larger Zr- and Fe- rich intermetallics at the grain boundaries and the presence of Fe and Zr in the matrix, either as solute atoms in solid solution or nanoscale intermetallic particles below the resolution limit of high-resolution tomography, were also identified. These observations can be explained by the non-equilibrium solidification conditions inherent to LPBF. For Fe-rich intermetallics, the process leads to the formation of both stable $Al_{13}Fe_4$ and metastable Al_6Fe phases [92,200]. For Zr-rich intermetallics, nanoscale $L1_2$-Al_3Zr precipitates can be formed [92,95,100,201]. These metastable phases, which remain below the detection threshold in the studied conditions, undergo thermodynamically driven transformations upon heat treatment. The heat treatment facilitated the coarsening of Fe- and Zr-rich intermetallics at the grain boundaries. In Fe-rich intermetallics, the nanoscale metastable Al_6Fe phase in the Al matrix, transforms into the more stable $Al_{13}Fe_4$ phase at the grain boundaries [202–204]. Similarly, the nanoscale $L1_2$-Al_3Zr, can undergo a transformation into the thermodynamically stable $D0_{23}$-Al_3Zr phase, accumulating and coarsening along the grain boundaries during heat treatment [205]. Notably, Zr coarsening at the grain boundaries was not observed in 2D characterizations conducted in [92,100]. This emphasizes the critical importance of 3D characterization techniques over 2D methods in capturing the complete spatial complexity of microstructures. Across all three conditions, the intermetallic particles exhibited consistent size and distribution after heat treatment. ImageJ analysis showed that the average volume of these particles ranged between 0.07 and 0.35 μm^3, with no significant variation across the solidified melt pools.

The thermal gradient and heat flow direction could further contribute to solute redistribution and microstructural evolution within different depths of the prior melt pool, under CW (slower cooling rates, C1) and PWM (faster cooling rates, C3) processing modes. The FXCT results for C1 (center and bottom) show uniform background concentrations of Fe (15.5 mg/cm³, 0.56wt%) and Zr (26 mg/cm³, 0.96wt%) throughout the volume. In contrast, for condition C3 (center), the background levels of Fe and Zr within the Al grains are slightly higher with uniform concentrations of ~17 mg/cm³ (~0.65wt%) for Fe and ~30 mg/cm³ (~1wt%) for Zr. These concentrations suggest that these elements are either partially trapped in the Al matrix or present forming nanoscale Al_6Fe and $L1_2$-Al_3Zr phases (Fig. 5.18 and 5.20). The uniformity of this distribution implies that a portion of Fe and almost all of Zr is either partially trapped in the Al matrix or present forming nanoscale precipitates after heat treatment.

For larger intermetallics in C1, continuous wave laser irradiation produces a steady heat source, leading to relatively uniform and slower cooling rates comparatively. At different depths within the melt pool, the Fe-rich intermetallic volume fraction increased slightly from 0.78% at the bottom to 0.92% at the center, whereas Zr exhibited a more significant increase from 0.52% to 0.98%. This suggests that during solidification, Fe maintains a relatively constant distribution, increasing only slightly in volume fraction throughout the melt pool, indicating its consistent presence across the different depths. While Zr tends to remain either partially trapped in the Al matrix or present in its nanoscale metastable $L1_2$-Al_3Zr form. The concentration of the larger Zr-rich intermetallics increases towards the upper regions of the melt pool, where cooling rates are slower, leading to a more pronounced accumulation in these areas.

For C3, the pulsed irradiation in PWM mode introduced rapid thermal cycling, significantly altering the melt pool dynamics. Fe-rich intermetallics demonstrated a pronounced accumulation in the center of the melt pool, with a volume fraction of 3.4%, compared to only 0.62% for Zr-rich intermetallics (Fig. 5.20). This discrepancy may be attributed to the altered melt pool morphology and the disruption of columnar grain growth at the center. During heat treatment, the coarsening of $Al_{13}Fe_4$ may have been further accelerated in grain boundary-dense regions, where shorter diffusion pathways enhance solute transport. The background level of uniform Zr concentration that is either partially trapped in the Al matrix or present as the nanoscale $L1_2$-Al_3Zr is slightly more compared to condition C1. Given the comparatively faster solidification rates due to PWM laser mode and the increased melt pool depth (high linear energy density), Zr solute distribution may be different with that observed in C1. However, due to the loss of the bottom sample in C3, definitive trends across different melt pool depths cannot be established.

5.5 Key messages

The analyses in this chapter allow for a thorough examination of the hypotheses introduced in the Motivation (Chapter 2). The following conclusions offer direct answers to the core research questions.

How does the variation of LPBF processing influence microstructural formation?

The variation in LPBF processing influences microstructural formation. Particularly laser scanning speed, energy density and Continuous Wave (slower cooling rates) vs. Pulsed Width Modulation modes (faster cooling rates), influence melt pool characteristics, thermal gradients, cooling rates, and solidification dynamics. These parameters, in turn dictate grain morphology, solute redistribution, and intermetallic formation. For instance, continuous laser scanning at moderate speeds and energy input can promote stable melt pools, with a balanced width-to-depth ratio (W/D ~2) and grain structures (C1). Faster scanning speeds with same laser mode and energy, results in shallower melt pool limiting heat penetration (C2) (W/D >3). While a pulsed laser at a higher energy density results in a deeper melt pool and could potentially alter the grain growth patterns (C3, W/D ~1.2). In C1 and C2, the grain growth followed a clear columnar direction along the thermal gradient. In C3, deeper melt pools and comparatively faster solidification could disrupt the columnar grain growth, leading to a higher density of grain boundaries to form at the center. Additionally, variations in processing parameters can affect the segregation and accumulation of alloying elements, in this case, Fe and Zr, influencing their distribution within the aluminum matrix. Overall, these processing variations highlight the intricate relationship between LPBF parameters that dictate the microstructural characteristics.

How do microstructural constituents, their architecture, and chemistry vary within a prior melt pool? How do heat treatments affect the elemental distribution and variation within a prior melt pool?

Within a prior melt pool, the microstructural constituents, their spatial distribution, and elemental composition vary under the influence of thermal gradients and cooling rates during solidification and evolve during subsequent heat treatment. Heat flow direction and thermal gradients further dictate solute redistribution across different melt pool depths, particularly

under varying laser energy densities and processing modes such as CW and PWM. FXCT results for C1 (bottom and center) reveal the background level of uniform concentrations of Fe (15.5 mg/cm³, 0.56 wt%) and Zr (26 mg/cm³, 0.96 wt%), indicating that they are either partially trapped in the Al matrix or their presence in nanoscale metastable phases, Al_6Fe and $L1_2$-Al_3Zr, respectively. For condition C3 (center) the background levels of Fe and Zr within the Al grains are slightly higher with uniform concentrations of ~17 mg/cm³ (~0.65wt%) for Fe and ~30 mg/cm³ (~1wt%) for Zr. This suggests that after heat treatment, a portion of Fe remains either partially trapped or in its metastable form Al_6Fe, and mostly transforms to the $Al_{13}Fe_4$. Whereas Zr is primarily retained either partially trapped in Al matrix or present as nanoscale metastable precipitates and only minimal fraction preferentially coarsens at the grain boundaries. In heat-treated samples, intermetallic particles exhibited consistent volumes ranging from 0.13 to 0.52 μm^3 across different melt pool regions, suggesting that heat treatments do not significantly alter particle size variations in different conditions but promotes the transformation from metastable to respective stable phases along grain boundaries.

In C1, the continuous laser irradiation results in slower cooling rates, leading to a slight increase in Fe-rich intermetallic volume fractions from 0.78% at the bottom to 0.92% at the center, while Zr exhibits a more significant increase from 0.52% to 0.98%. This suggests that Fe follows a relatively consistent solidification pattern, while Zr distribution becoming more concentrated towards the upper melt pool regions where the cooling rates decrease. In C3, the pulsed laser irradiation in PWM mode introduces rapid thermal cycling, significantly altering the melt pool dynamics. Fe-rich intermetallics exhibit a very pronounced accumulation at the center (3.4% volume fraction), whereas Zr-rich intermetallics remain lower (0.62%). This discrepancy may be due to melt pool morphology and disrupted columnar grain growth. During heat treatment, the coarsening of the stable $Al_{13}Fe_4$ is likely accelerated in grain boundary-dense regions, where shorter diffusion pathways enhance solute transport. The background Zr concentration, either partially trapped in the Al matrix or present as nanoscale $L1_2$-Al_3Zr, is slightly higher compared to condition C1. The faster solidification rates in PWM laser mode and the increased melt pool depth (due to high linear energy density) can likely alter the Zr solute distribution compared to C1. However, due to the loss of the bottom sample in C3, definitive trends across melt pool depths cannot be established.

6 Aging and Overaging Effects on the Coarsening of Intermetallics in Al-1Fe-1Zr Alloy

6.1 Introduction

The rapid cooling in LPBF, combined with the repeated heating and cooling cycles from the layer-by-layer laser processing, can produce microstructural features that cannot be easily replicated using conventional manufacturing methods. The formation of supersaturated solid solutions, residual stresses, and texture are key metallurgical phenomena inherent to LPBF that can significantly influence the mechanical behaviour of the fabricated components [206]. Al alloys processed by LPBF face notable challenges, including high reflectivity, strong oxidation tendency, and high thermal conductivity [207]. Moreover, in the case of alloys with a wide solidification range the risk of defects such as solidification cracking exists [206,208]. The fine microstructures created through the rapid cooling and directional solidification of the LPBF process can offer attractive properties [56], but they may remain far from optimized for broader applications.

This chapter examines the microstructural evolution of the Al-1Fe-1Zr alloy as a result of aging and overaging heat treatments. It has been reported in [100], that upon aging for 4 hr at 400°C, the alloy undergoes dual-phase precipitation, with the formation of nanoscale $L1_2$-Al_3Zr precipitates within the Al grains and faceted $Al_{13}Fe_4$ intermetallics at the grain boundaries. The partitioning behaviour of these elements is influenced by the diffusion-dependent partition coefficients, with Fe exhibiting a stronger tendency to form intermetallic compounds, while Zr remains predominantly in the solid solution [100]. Thermodynamic models predict that the metastable solubility limit of Zr for the $L1_2$ phase is 0.17 wt% (0.05 at.%) under equilibrium conditions at 530°C. As an upper bound it is assumed that in the LPBF as-built state, Zr is retained in solid solution (i.e., 0.3 at.%)[100]. Similarly, Fe remains in solid solution in quantities of approximately 0.2 at.%, as inferred from image analysis comparing intermetallic fractions in the LPBF as-built and upon aging at 400°C for 4 hours [100]. However, many of these intermetallics remain too small to be fully resolved in 3D in the as-built condition and even after aging at 400°C for 4 hours. To enable 3D analysis and quantification of spatial distribution of Zr- and Fe-rich nanoprecipitates using X-ray tomography their dimensions must exceed the resolution limit of the imaging techniques employed. Previous studies indicate that aging at 400°C for 4 hours results in Al_3Zr nanoprecipitates with an average diameter of ~2

nm, which remains below the detection threshold of high-resolution tomography [92,100]. Consequently, based on the thermodynamic model predictions, an overaging treatment at 530°C for 24 hours was selected to induce precipitate coarsening, targeting an estimated size range of 30–50 nm, allowing for direct visualization and quantitative analysis. This coarsening process provides valuable insights into the spatial distribution of Zr- and Fe-rich microstructures.

The primary objective of this chapter is to investigate the effects of heat treatments on the coarsening behaviour of intermetallics in the Al-1Fe-1Zr alloy, specifically targeting the growth of Zr- and Fe-rich nano-precipitates to dimensions that can be accurately visualized using synchrotron-based imaging techniques. For this, a comprehensive characterization of a multi-layer build sample was conducted. By carefully varying the heat treatment parameters, it is possible to promote the growth of nano-sized intermetallics, enabling their visualization and quantification using techniques at the ID16A beamline. These methods provide high spatial resolution, allowing for a detailed analysis of how heat treatments influence the coarsening kinetics and distribution of intermetallics within the alloy.

This chapter aims to address two key research questions:

- *How do different heat treatments influence the microstructural evolution of the Al-1Fe-1Zr alloy manufactured via LPBF?*
- *Is it possible to image and quantify the nano-sized precipitates present in Al-1Fe-1Zr?*

6.2 Materials and Methods

Al-1Fe-1Zr alloy samples, with dimensions of 10 mm in diameter and 60 mm in length, were fabricated using LPBF on an EOS M290 machine (EOS GmbH). The system is equipped with a Yb-fibre laser featuring a 100 µm spot size. LPBF parameters were as follows: a 370 W laser power (continuous mode), a scan speed of 1400 mm/s, a hatch distance of 130 µm, and a layer thickness of 60 µm. A striped scanning pattern was implemented with a 67° rotation between successive layers to promote isotropic material properties. From this batch, one cylindrical sample was further machined to a reduced diameter of 350–550 µm and a length of 6 mm. This machined sample was then glued on a Huber pin using UV glue (Fig. 6.1) for the tomography scans at the ID16A beamline.

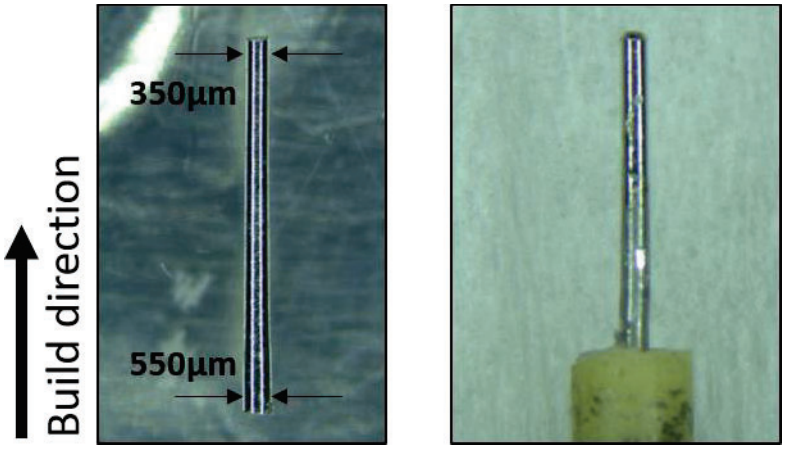

Fig. 6.1 Light microscopy images of the machined Al-1Fe-1Zr sample. The left image shows the sample geometry and build direction, while the right image shows the same sample glued on a Huber pin.

The sample underwent a two-step heat treatment. First, it was aged at 400°C for 4 hours to observe microstructural transformations at peak aging and to correlate with previous findings reported in [92,100]. This was followed by an overaging heat treatment at 530°C for 24 hours to stimulate the growth of nano-sized intermetallic phases, specifically Al_3Zr and Al_6Fe, thus facilitating detailed compositional analysis within the Al matrix. Both large field of view and high-resolution phase-contrast tomography scans were performed on the as-built sample and repeated after each heat treatment to monitor microstructural evolution over the treatment stages.

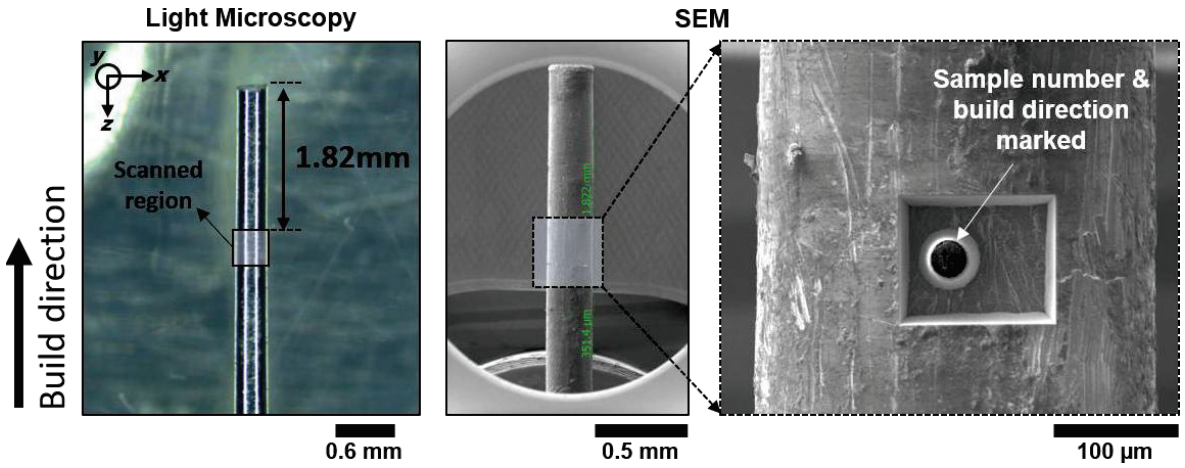

Fig. 6.2 (Left) Light microscopy image of the Al-1Fe-1Zr sample showing the region where large FoV HXCT scans were conducted. (Center) SEM image of the same region, and (right) the enlarged image showing the extraction site of the ~30 µm diameter sub-sample. The build direction is indicated for reference.

For further high-resolution analysis, a smaller *sub*-sample (~30 µm in diameter) was extracted from the final heat-treated sample (Fig. 6.2, right). This extraction was achieved through focused ion beam (FIB) milling on an FEI Helios Nanolab 600i dual-beam system, equipped with both electron and Ga^+ ion beams, at the Institute of Materials Research, German Aerospace Center (DLR). A protective carbon layer was deposited over the area of interest prior to milling to shield it from potential damage and to act as a fiducial marker for maintaining the sample orientation. The extracted sub-sample was attached to a modified tungsten Omniprobe needle via platinum deposition and then mounted on a Huber sample pin for high-resolution tomographic and compositional analysis.

6.2.1 3D Characterization Techniques

The general methodology outlined in section 3.3 was employed with minor adaptations for each sample condition. HXCT scans with FoV of 400 x 400 x 400 μm^3 and local HXCT ROI scans of 45 x 45 x 45 μm^3 and local high-resolution tomography NFPXCT scans (FoV 60 x 60 x 60 μm^3) were conducted using an energy of 17.1 keV.

For the extracted *sub*-sample, the scans were performed using 33.35 keV to excite the K-edge of Zr for improved X-ray fluorescence imaging. This energy minimized the self-attenuation of emitted radiation, allowing for correlative high-resolution phase contrast and X-ray fluorescence data acquisition. High-resolution HXCT scans were carried out at four different distances from the focal point, starting with an initial pixel size of 15 nm. For FXCT, the FoV

was 35 µm x 35 µm with an 8 µm height along the sample's build direction. A total of 65 projections were acquired over 180°, consisting of two sub-tomograms of 32 projections each, with an additional 180° projection for enhanced alignment. With a 100 nm step pixel size and a 10 ms dwell time per pixel, each projection required ~7 minutes, totaling just over 8 hours per scan. For further investigation, a higher-resolution FXCT scan was conducted with 192 projections acquired over 180° using four sub-tomograms, with a FoV of 36 µm x 36 µm and a 3.6 µm height. A step pixel size of 36 nm and a dwell time of 6.5 ms per pixel were used, with each projection taking ~13 minutes, resulting in a total scan time of around 40 hours (!).

6.3 Results

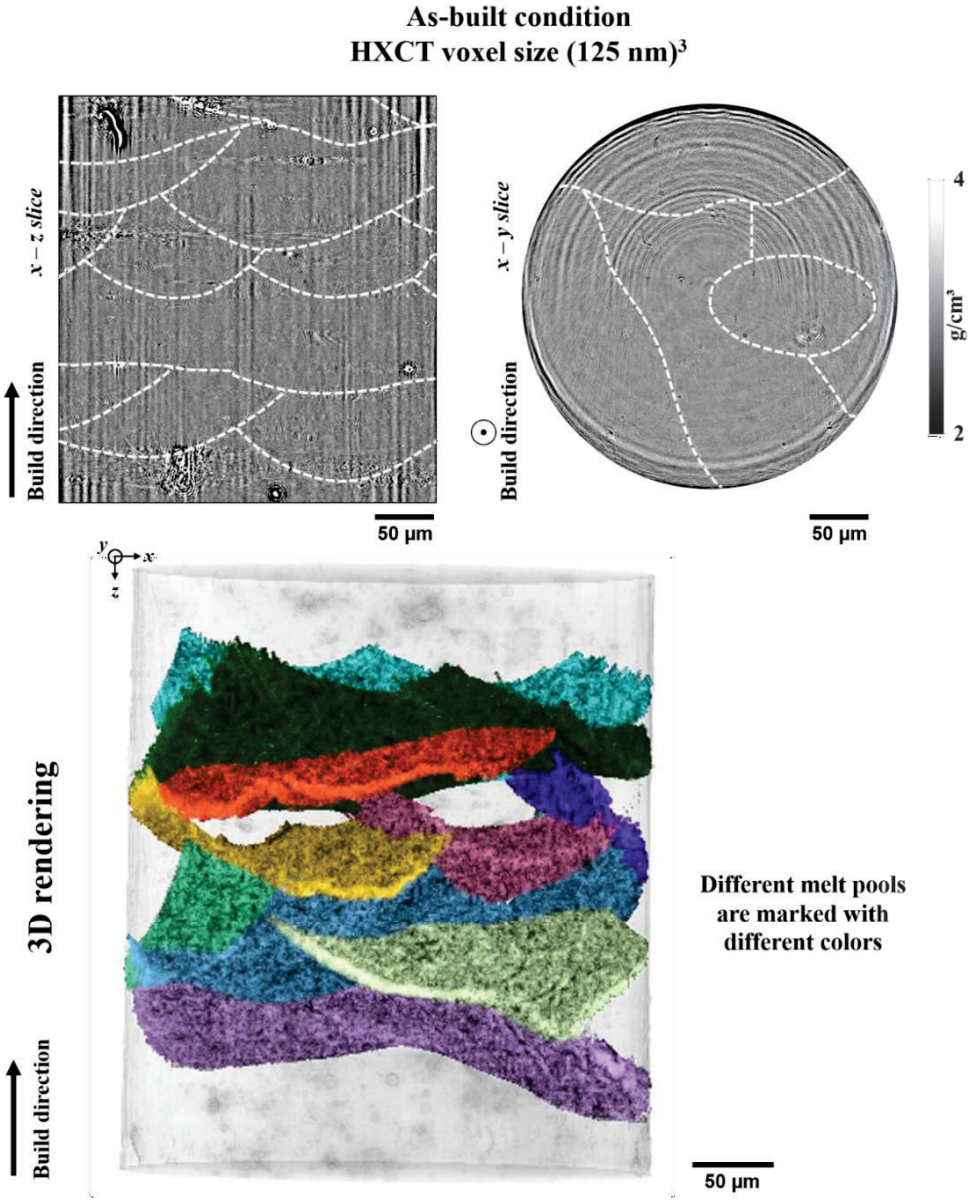

*Fig. 6.3 HXCT slices illustrating the continuous stacking of melt pools in the LPBF-fabricated Al-1Fe-1Zr alloy. (Left) The **x-z** plane reveals elongated and semi-cylindrical melt pools, and (right) in the **x-***

y *plane, the melt pools appear as rounded or elongated stripes depending on the LPBF scan strategy. The melt pool boundaries are delineated by white dashed lines in the HXCT slice. The 3D rendering of the sample in the bottom panel elucidates the morphology of melt pool boundaries, each marked with a different colour.*

The microstructure of LPBF Al-1Fe-1Zr alloy in the as-built condition using the same LPBF processing parameters, has been previously documented in 2D [92,100]. Due to the layer-by-layer nature of the LPBF process, the as-built parts inherently exhibit anisotropic characteristics. As shown in Fig. 6.3, the bulk material along the build direction consists of a continuous stacking of melt pools whose orientation depends on the laser scan direction. The 3D rendering of the sample in the bottom panel elucidates the morphology of melt pool boundaries, each marked with a different colour.

In the as-built condition, HXCT analysis, both in the large field of view (FoV) and at higher resolution (Fig. 6.4). ROI1 and ROI2 were strategically chosen to encompass melt pool border for detailed characterization.

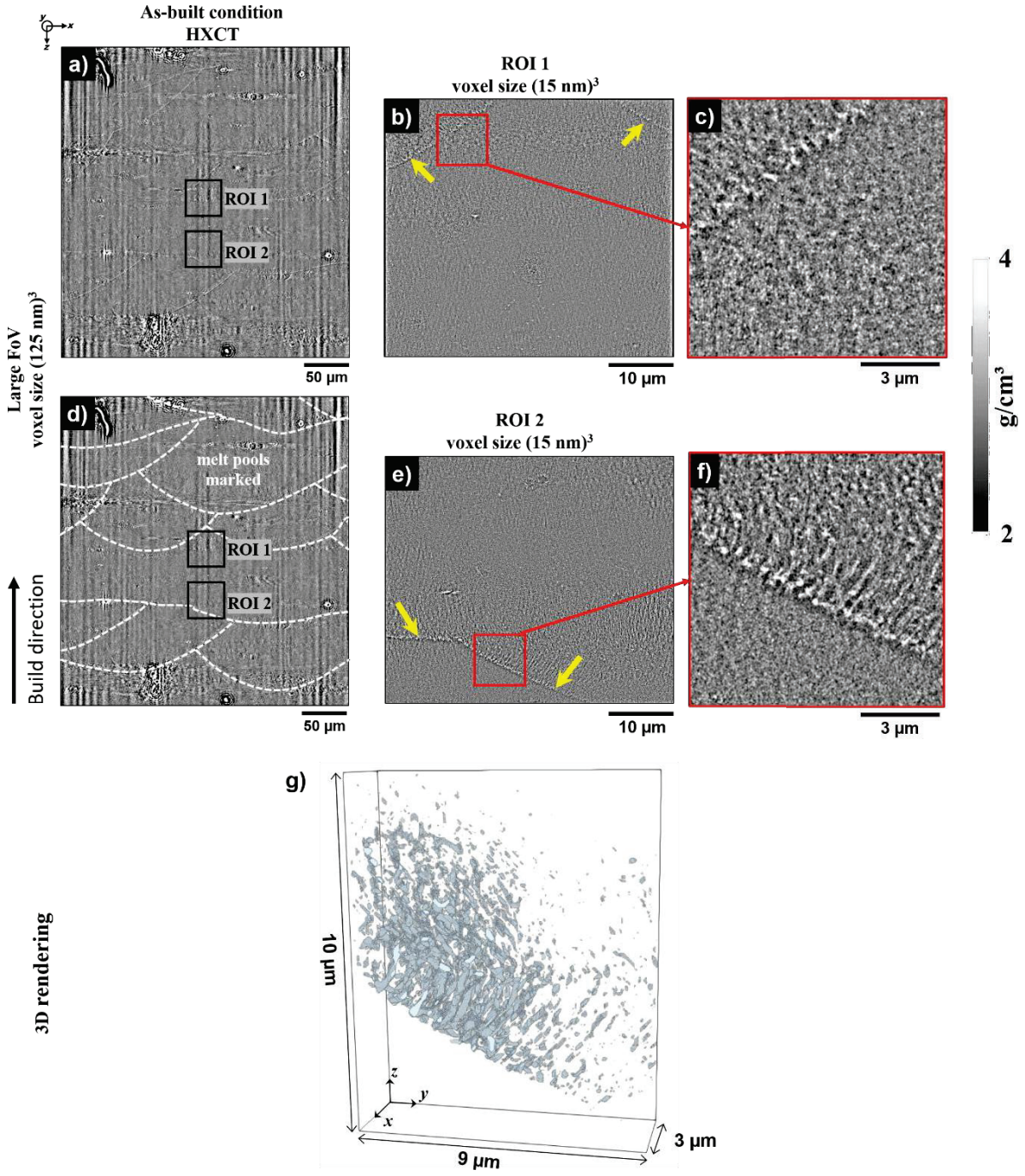

Fig. 6.4 HXCT slices and volume rendering of the as-built Al-1Fe-1Zr alloy. The large field of view (FoV) slice (a) reveals the characteristic semi-cylindrical melt pool (same slice shown in (d) with the melt pools borders marked in white) morphology along the build direction. ROI1 (b) focuses on the upper region of a melt pool, while ROI2 (e) captures the lower region of the same melt pool (melt pools borders marked in yellow arrows). The enlarged images (c and f) highlight cellular intermetallics (bright features) just above the melt pool boundaries in the as-

built condition. The 3D rendering of the cellular intermetallics is shown in (g), corresponding to a region within (f).

The melt pool boundaries were clearly visible, marked by a distinct darker contrast (marked with yellow arrows in Fig. 6.4 (b and e) indicative of a reduced total mass density. Immediately above these boundaries, intermetallic-enriched regions exhibiting higher mass density were observed to align with the direction of solidification, indicating a potential accumulation of intermetallic phases during the solidification process. As shown in Fig. 6.4 (c and f), magnified views of selected melt pool regions reveal melt pool borders with a width of approximately 200 nanometres (corresponding to 2 to 4 voxels), along with the presence of cellular intermetallic structures (Fig. 6.4 (g)) situated directly above the melt pool boundaries in the as-built condition.

Following the initial heat treatment at 400°C for 4 hours, as described in [100], HXCT slices from both the large FoV and the high-resolution ROI scans of the same regions were analyzed (Fig. 6.5). In the large FoV slices, the intermetallic particles align forming elongated structures, probably decorating Al grain boundaries. These structures display what seem to be grain growth patterns.

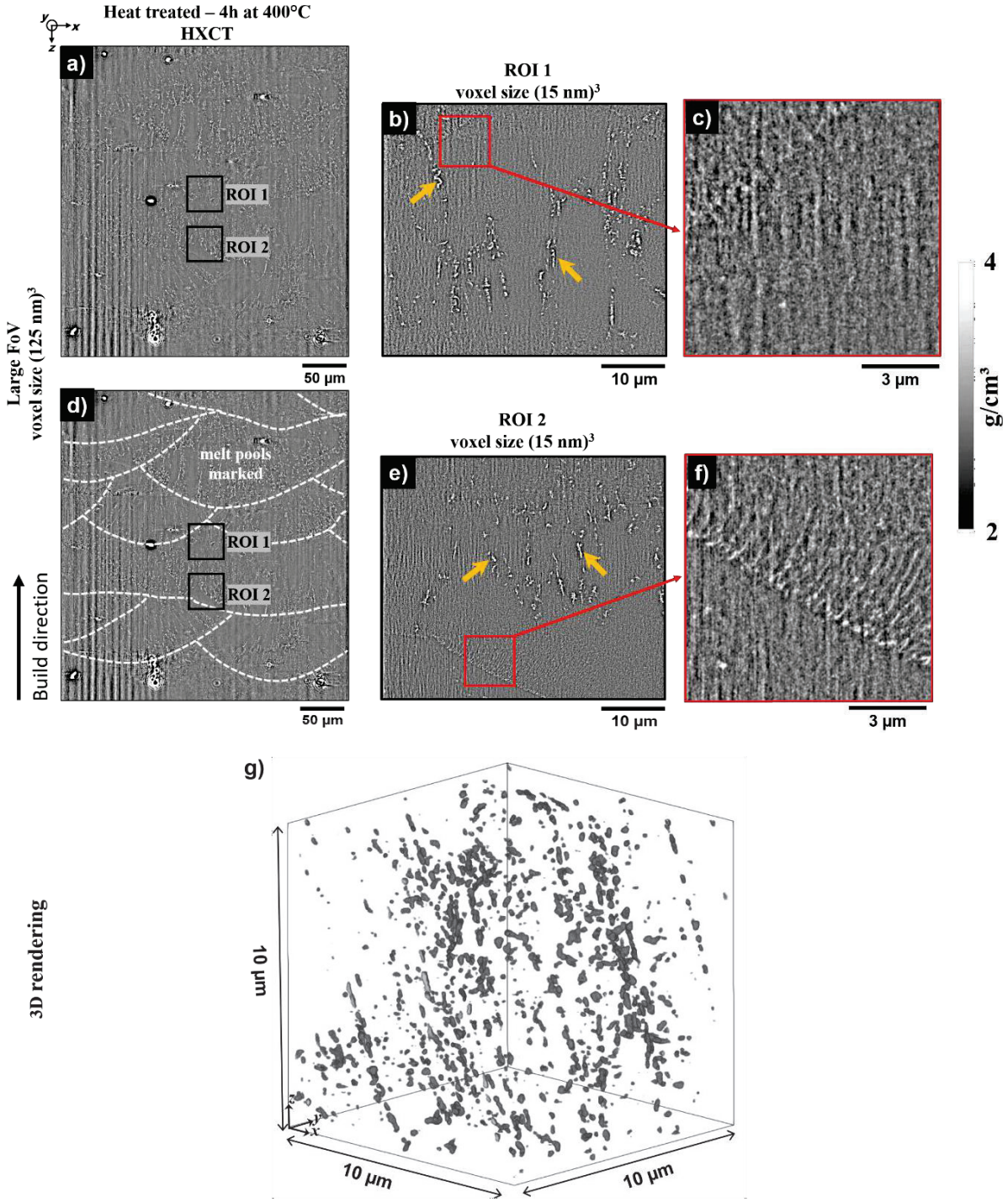

Fig. 6.5 HXCT slices and volume rendering of the Al-1Fe-1Zr alloy after heat treatment at 400°C for 4 hours. The large FoV slice ((a), (d) same slice with melt pools marked) shows the aligned intermetallic particles forming elongated structures, probably decorating grain boundaries. ROI1 (b) highlights the top region of a melt pool with intermetallic particles, while ROI2 (e) reveals similar features in the lower region of the melt pool with intermetallic sizes ranging from ~400 nm to ~1 µm (marked with orange arrows). The cellular intermetallics (bright features) appear relatively more coarsened compared to the as-built condition, just

above the melt pool boundaries in the enlarged images in (c) and (f). The 3D rendering shown in (g) elucidates the intermetallics particles corresponding to a region within (b).

High-resolution ROI slices (Fig. 6.5 (b) and (e)) provided more detailed insights into the microstructures. Intermetallics were found to accumulate predominantly in elongated patterns probably along grain boundaries (orange arrows in Fig. 6.5 (b) and (e), also see (g)). The melt pools boundaries are still distinctly visible and the cellular intermetallics just above the melt pool boundary appear relatively more coarsened, as seen in the enlarged images (Fig. 6.5 c and f).

After the overaging heat treatment at 530°C for 24 hours, significant microstructural changes are observed in the HXCT volumes. The large FoV slice (Fig. 6.6 (a)) reveals a pronounced growth of intermetallics. These intermetallics, now appear more globular and voluminous, emphasizing the grain boundary decoration. This growth suggests the visibility of the grain boundaries within the large FoV, making them more distinctly delineated compared to the as-built and 400°C heat-treated states. The accumulation of these globular intermetallics along the grain boundaries reflects the overaging heat treatment's role in promoting the coarsening of secondary phases.

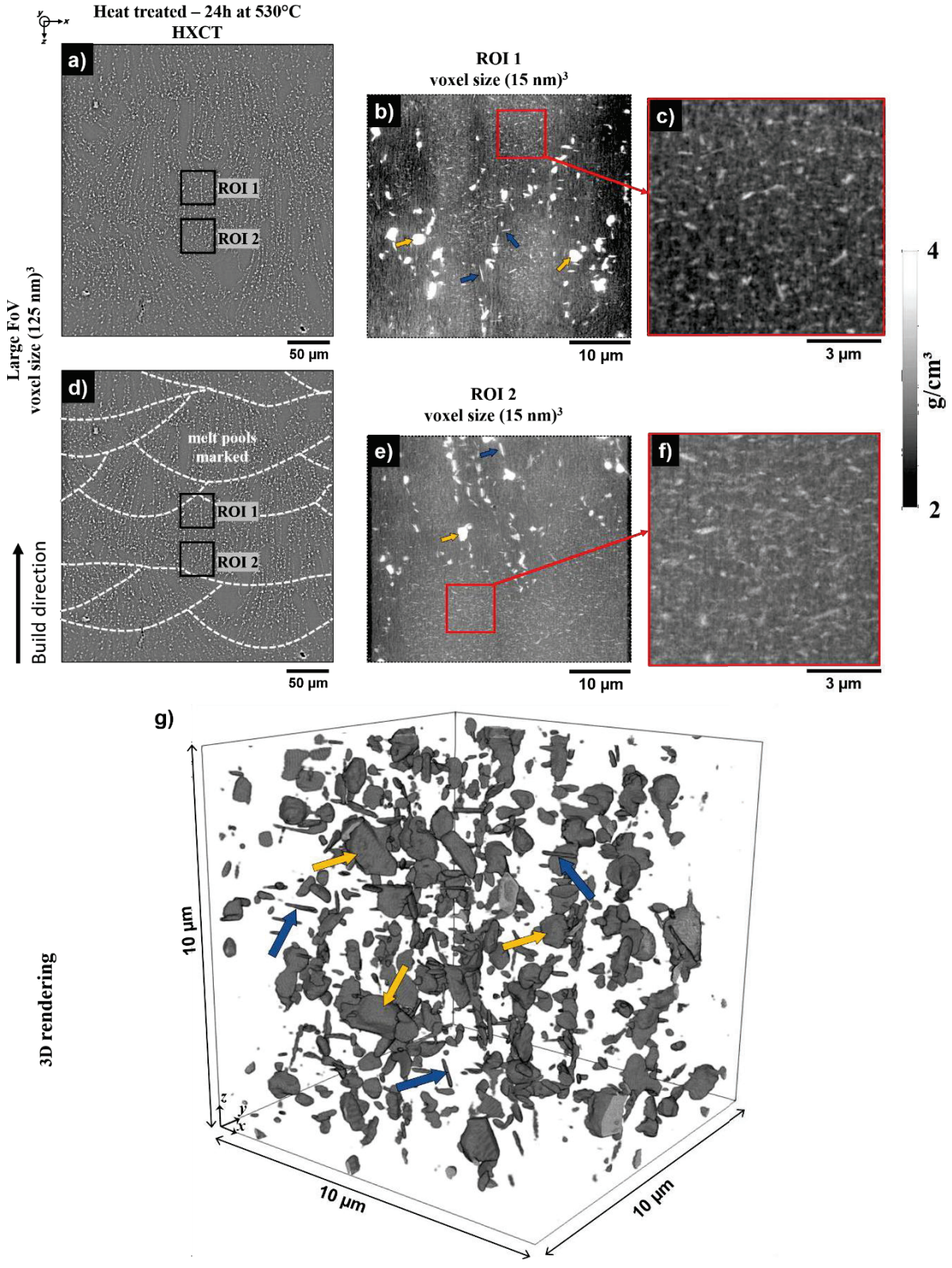

Fig. 6.6 HXCT slices and volume rendering illustrating the microstructure of the Al-1Fe-1Zr alloy after extended heat treatment at 530°C for 24 hours. The left panel shows a Large FoV HXCT slice ((a) and (d)- initial melt pool boundaries marked), highlighting the overall growth of intermetallics, which appear as globular or plate-like structures. The ROI1 (b) represents a

detailed view of the top region of a melt pool, while the ROI2 (e) shows the bottom region of the same melt pool. The 3D rendering (Fig. 6.6 (g)) shows the intermetallics from ROI1. Blue arrows in ROI1, ROI2 and the 3D rendering mark plate-like intermetallic features (~1–2 µm along their longest axis), while yellow arrows indicate bigger globular intermetallic structures. Red squares marked in ROI1 and ROI2 highlight nano-precipitates, enlarged in (c) and (f) which exhibit rod-like, cubic or spherical morphologies and are a few tens of nanometers in size. These precipitates were a focal point for quantification.

In the high-resolution HXCT scans (ROI1 and ROI2), which correspond to the upper and lower regions of the same melt pool, further insights into the microstructure are obtained (Fig. 6.6, b and e). In these regions, intermetallic particles are observed with increased detail, showing diverse morphologies. Globular intermetallics dominate, but plate-like structures up to 1–2 µm along their longest axis, are also present (see Fig. 6.6 - 3D rendering). Additionally, small bright features are observed within the Al grains, as seen in the enlarged images (Fig. 6.6 c and f). These features, measuring only a few tens of nanometers in size, exhibit rod-like, cubic or spherical morphologies. Unlike the as-built and 400°C-treated states, the visibility of the melt pool boundaries is reduced in the high-resolution ROI volumes. As the melt pool boundaries can no longer be identified, Fig. 6.6 (d) shows the approximate regions of the initial melt pools boundaries marked in white for reference, inferred from the as-built and 400°C-treated conditions.

A direct comparison of the same x-z slices from HXCT volumes is shown in Fig. 6.7, illustrating the microstructural evolution of the Al-1Fe-1Zr alloy from the as-built condition (left) to aged (4 h at 400 °C, center) and overaged (24 h at 530 °C, right) states.

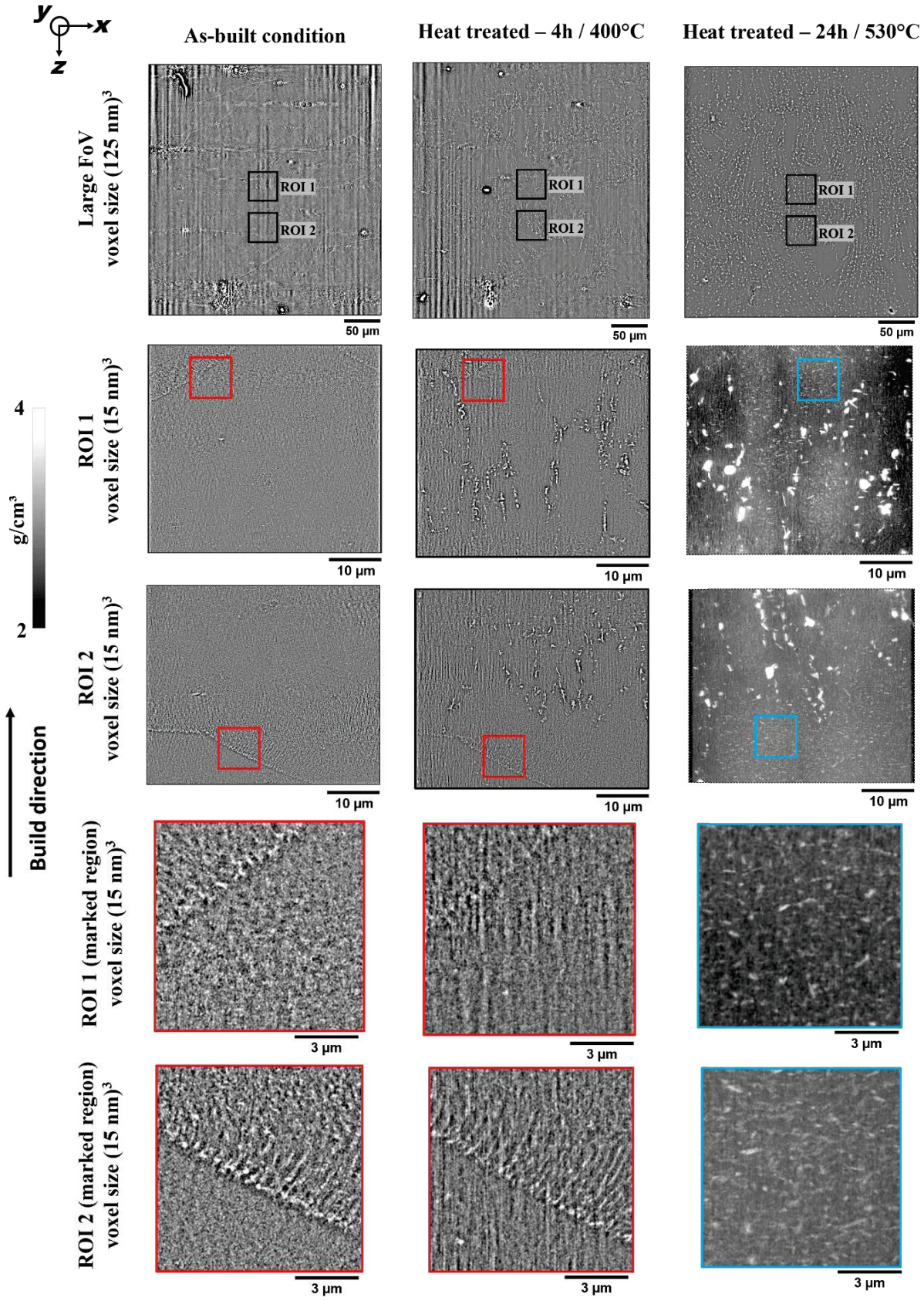

Fig. 6.7 Direct comparison of the same x-z slices from HXCT volumes corresponding to Figures 6.4, 6.5, and 6.6, illustrating the microstructural evolution of the Al-1Fe-1Zr alloy

from the as-built condition (left) to aged (4 h at 400 °C, center) and overaged (24 h at 530 °C, right) states.

To further investigate the microstructural evolution at the nanoscale, NFPXCT was performed at a newly defined region, ROI3 marked in Fig. 6.8 (a). This region was strategically selected to examine the junction of multiple melt pool boundaries, located just above ROI1. The voxel size for NFPXCT in this region was set to $(30\ nm)^3$ while still preserving a large FoV (60 x 60 x 60 μm^3), enabling high-resolution imaging of fine microstructural features. NFPXCT scans were conducted at the same ROI3 location for the sample heat-treated at 400°C for 4 hours and after overaging at 530°C for 24 hours, facilitating a direct comparative analysis of the microstructural changes. Fig. 6.8 illustrates the results of these investigations. The NFPXCT slice of ROI3 after the 400°C heat treatment and the corresponding slice after the overaging treatment at 530°C for 24 hr in shown in Fig. 6.8 (b) and (c), respectively. The 3D renderings of a portion of the volume representing the corresponding conditions are shown in (f) and (g), respectively. In both cases, the scans provide a comprehensive view of the region, highlighting the microstructural features at the junction of multiple melt pool boundaries. Fig. 6.8 (h) overlays the volumes shown in (f) and (g), which enables direct comparison of microstructural evolution from the aged to the overaged condition. The yellow boxed areas in the NFPXCT slices mark regions of interest, which are enlarged in Fig. 6.8 (d) and (e), to focus on the nano intermetallics.

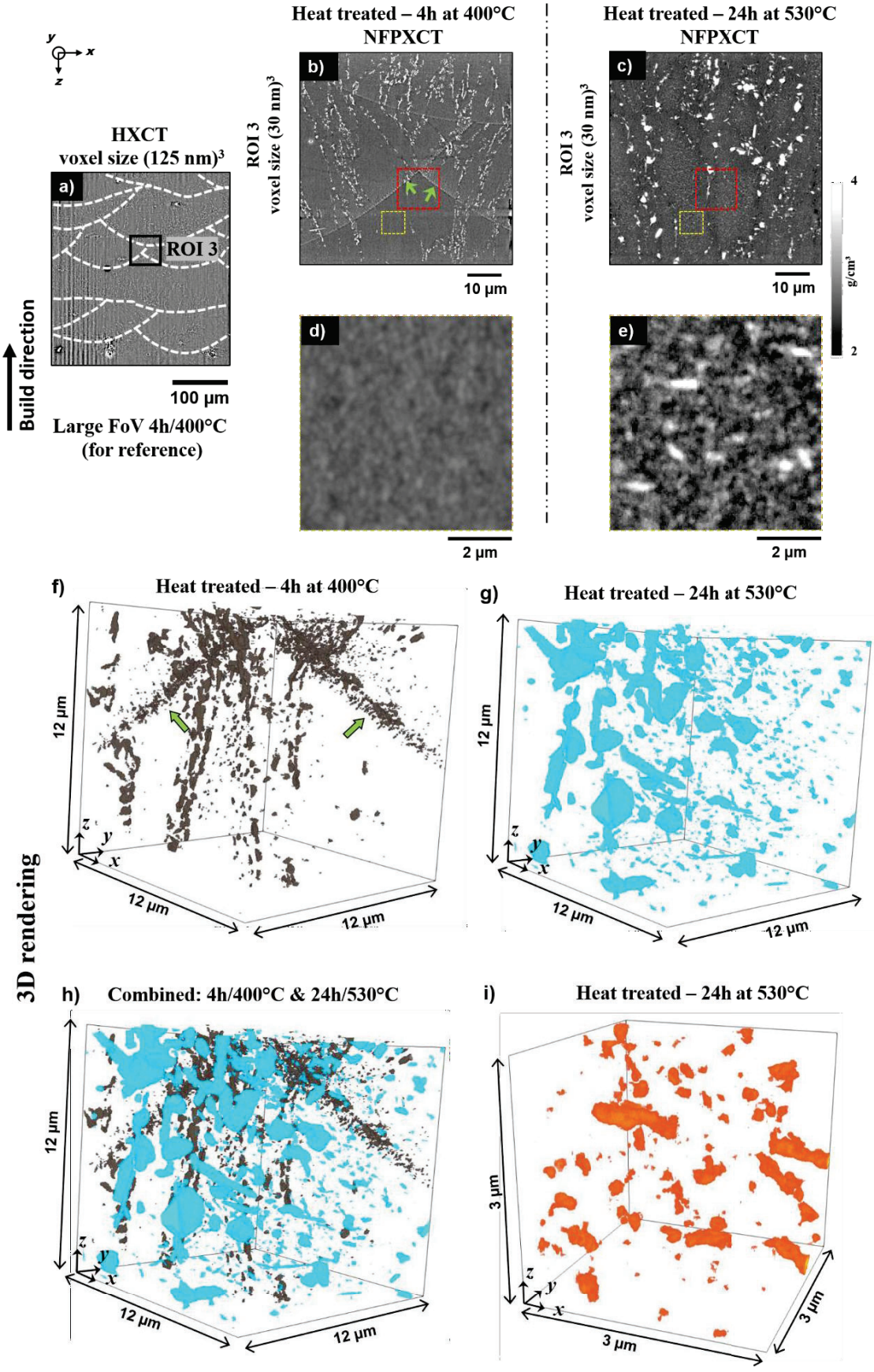

Fig. 6.8 (a) HXCT slice of the Al-1Fe-1Zr alloy acquired after heat treatment at 400°C for 4 hours, with ROI3 located at the junction of multiple melt pool boundaries. Panels (b) and (c)

present NFPXCT slices of the 400°C/4 h and 530°C/24 h conditions, respectively. The yellow boxes indicate the regions enlarged in (d) and (e), which provide enlarged views of nanoscale intermetallic precipitates that emerge more distinctly after overaging. Panel (f) shows a 3D rendering of a portion of the NFPXCT volume from the 400°C/4 h condition (marked in red dashed box in (b)), highlighting the distribution of intermetallics above the melt pool boundary (marked in green arrows, also see (b)) and along Al grain boundaries. Panel (g) displays the corresponding 3D rendering from the 530°C/24 h condition (marked in red dashed box in (c)), illustrating coarsening and redistribution of intermetallics upon overaging. Panel (h) overlays the volumes shown in (f) and (g), enabling direct comparison of microstructural evolution. Panel (i) presents a high-resolution 3D rendering of nano-precipitates within the Al grains extracted from the 530°C/24 h condition, corresponding to a region within the volume shown in panel (e).

The enlarged NFPXCT slices from the 530°C overaged sample (Fig. 6.8 (e) and (i)) distinctly reveal the nanoscale intermetallics that can be hardly identified in the 400°C condition. The nano-intermetallics appear as bright, well-defined features against the Al matrix. Their enhanced visibility after the overaged heat treatment is indicative of their growth during prolonged thermal exposure. The detailed nanoscale imaging achieved with NFPXCT, particularly in capturing both the larger and nano intermetallics, is critical for understanding the interplay between what seems to be the grain morphology and the evolution of nano-intermetallics.

6.3.1 Correlative High-Resolution HXCT and FXCT Characterization

A small *sub*-sample (Fig 6.2) was extracted from the previously analyzed sample to perform high-resolution HXCT and FXCT measurements, providing a more detailed characterization of the intermetallic phases. In Fig. 6.9, HXCT data is presented in two orthogonal slices: an *x-y* slice aligned with the build direction and an *x-z* slice perpendicular to it. The enlarged regions in the *x-y* and *x-z* slice, highlighted with an orange and green square, are shown in the respective right panels. The enlarged images illustrate the presence of roughly cubical (black arrows) and rod-like (blue arrows) nano intermetallics. Similarly, larger plate-like (red arrow) and globular intermetallics (yellow arrow) are also observed.

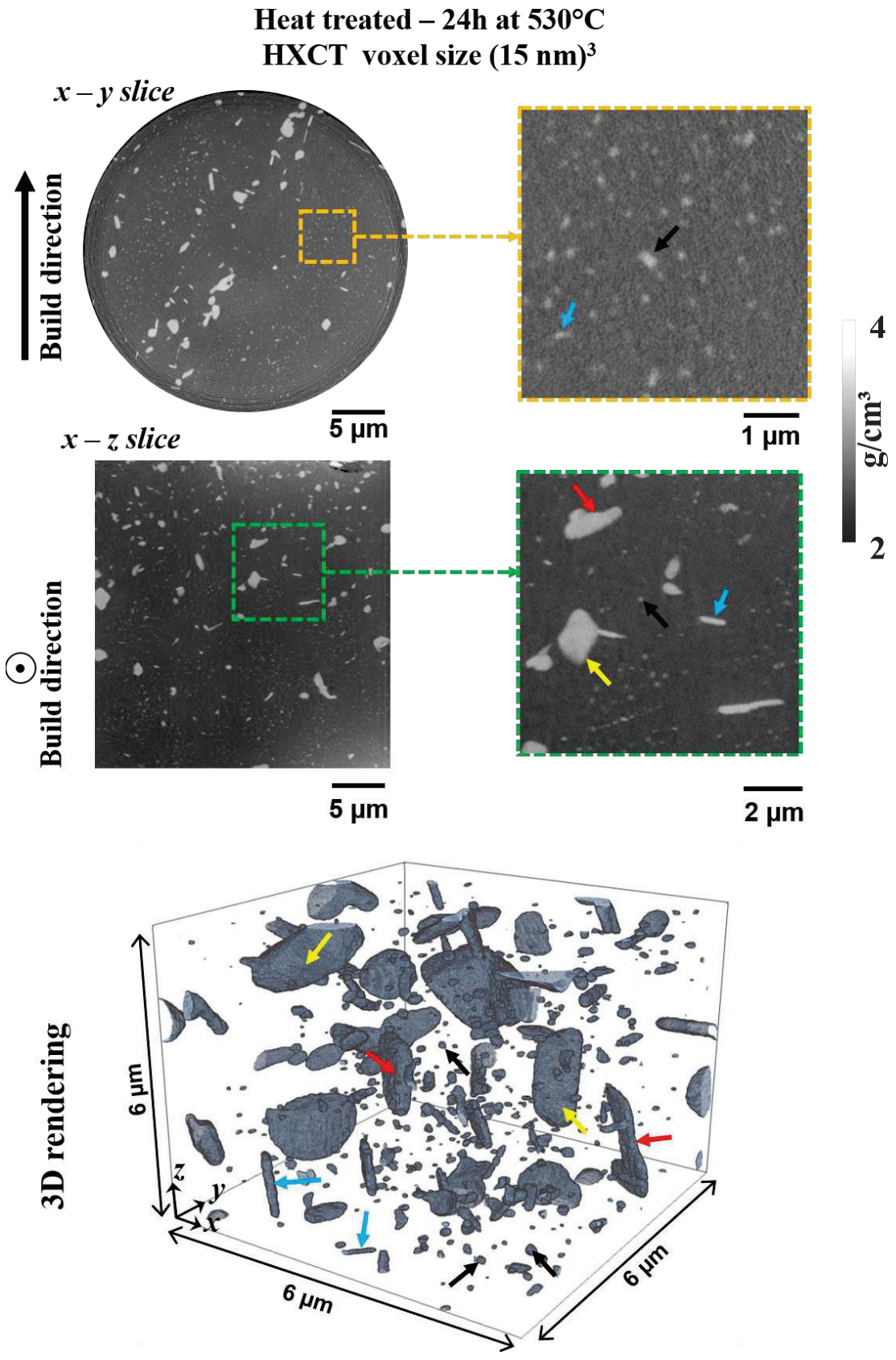

Fig. 6.9 High-resolution HXCT slices of the sub-sample extracted for detailed microstructural characterization. (Left) x-y slice aligned with the build direction and (bottom) x-z slice

perpendicular to the build direction. Enlarged regions highlighted by orange and green squares, are presented in the right panel for detailed visualization. The enlarged images and the 3D rendering reveal the presence of nano-sized intermetallics exhibiting distinct morphologies, including cubic (black arrows) and rod-like (blue arrows) structures. Larger intermetallics, such as plate-like structures (red arrows) and globular precipitates (yellow arrows), are also observed.

Despite the clarity provided by HXCT in resolving structural details, the differentiation between intermetallics rich in Zr and Fe proves challenging due to their similar total mass densities, as discussed in earlier chapters. This limitation underscores the necessity of FXCT in providing elemental specificity. In Fig. 6.10, FXCT maps corresponding to the same HXCT *x-y* slice are shown for direct comparison, enabling the identification of elemental distributions, along with Ga decoration that will permit the identification of the grain boundaries.

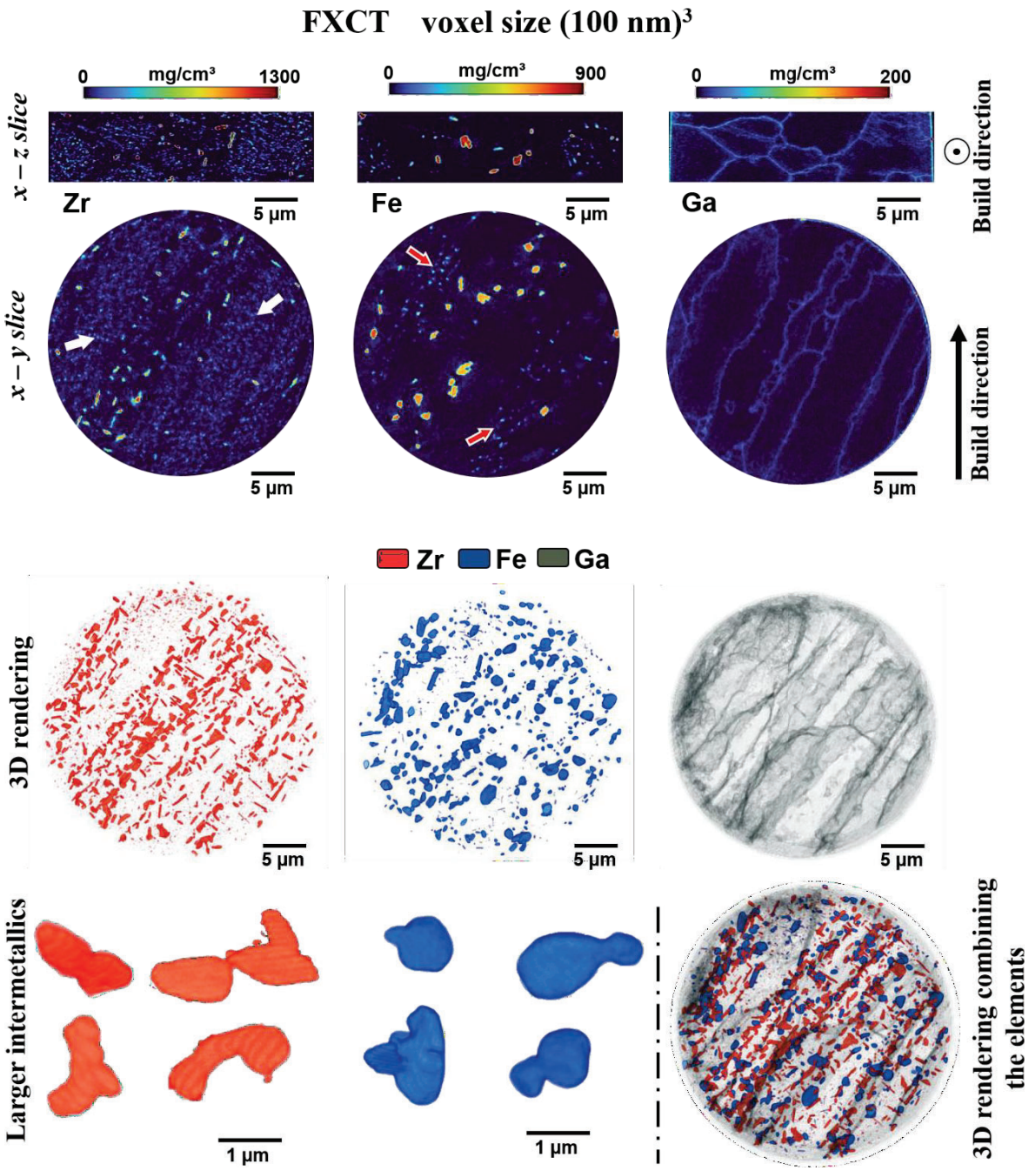

Fig. 6.10 FXCT elemental maps of the sub-sample corresponding to the x-y slice shown in Fig. 6.9 for direct comparison. x-z and x-y slice (build directions marked) of the Zr map and the Fe map highlight the elongated plate-like intermetallics predominantly rich in Zr and globular morphology of Fe-rich intermetallics. The Zr map shows a much higher population of nano intermetallics (white arrows) comparatively than the Fe map (red arrows). Ga map distinctly outlines the grain boundaries, confirming the formation of larger intermetallics at these boundaries and nano intermetallics within the grains. The 3D renderings of the volumes of Zr, Fe and Ga allow to visualize the morphology and spatial distribution of the intermetallics and

the grains. Some of these larger intermetallics are isolated and shown in the bottom panels. Zr-rich intermetallics have plate-like morphology and Fe tends to form more irregular globular structures.

The FXCT elemental analysis reveals distinct morphological tendencies for Zr-rich and Fe-rich intermetallics. Zr-rich phases predominantly form bulky plate-like structures, whereas Fe-rich intermetallics exhibit an irregular globular morphology (Fig. 6.10 *x-z* and *x-y* slice). The grain boundaries are distinctly highlighted in the Ga map, confirming the preferential formation of the larger intermetallics at these boundaries. The FXCT *x-z* and *x-y* slices of Zr maps further illustrates the population of nano intermetallics uniformly distributed within the grains (Fig. 6.10 white arrows), whereas in Fe maps the nano intermetallics are sparsely found in certain regions (Fig. 6.10 red arrows). This suggests that the relatively bigger nanoscale Zr- and Fe-rich precipitates, initially dispersed throughout the grains, coarsen during heat treatment and subsequent overaging to sizes that are detectable at a voxel size of 100 nm^3. This observation is consistent across both the *x-y* and *x-z* slices, as depicted in the corresponding elemental maps. It is also important to note that due to the low detection limits and high contrast sensitivity in FXCT, even precipitates smaller than the voxel size may contribute to the measured signal, enabling partial detection of features below the nominal resolution.

6.3.2 High resolution FXCT

To enhance the spatial resolution and improve the quantitative analysis of nano-sized intermetallics, FXCT was performed with a voxel size of $(36\ nm)^3$, a significant improvement compared to the previous dataset acquired at $(100\ nm)^3$ voxel size. Fig. 6.11 provides a comparative assessment of elemental maps for Zr, Fe, and Ga.

In Fig. 6.11, the top row presents elemental maps of Zr (left), Fe (center), and Ga (right) corresponding to the same slice shown in Fig. 6.10, providing insight into the morphology and spatial distribution of intermetallics in high resolution. The central images display 3D renderings of Zr and Fe distributions overlaid with Ga, further highlighting the intermetallic-phase arrangement relative to the grain boundaries.

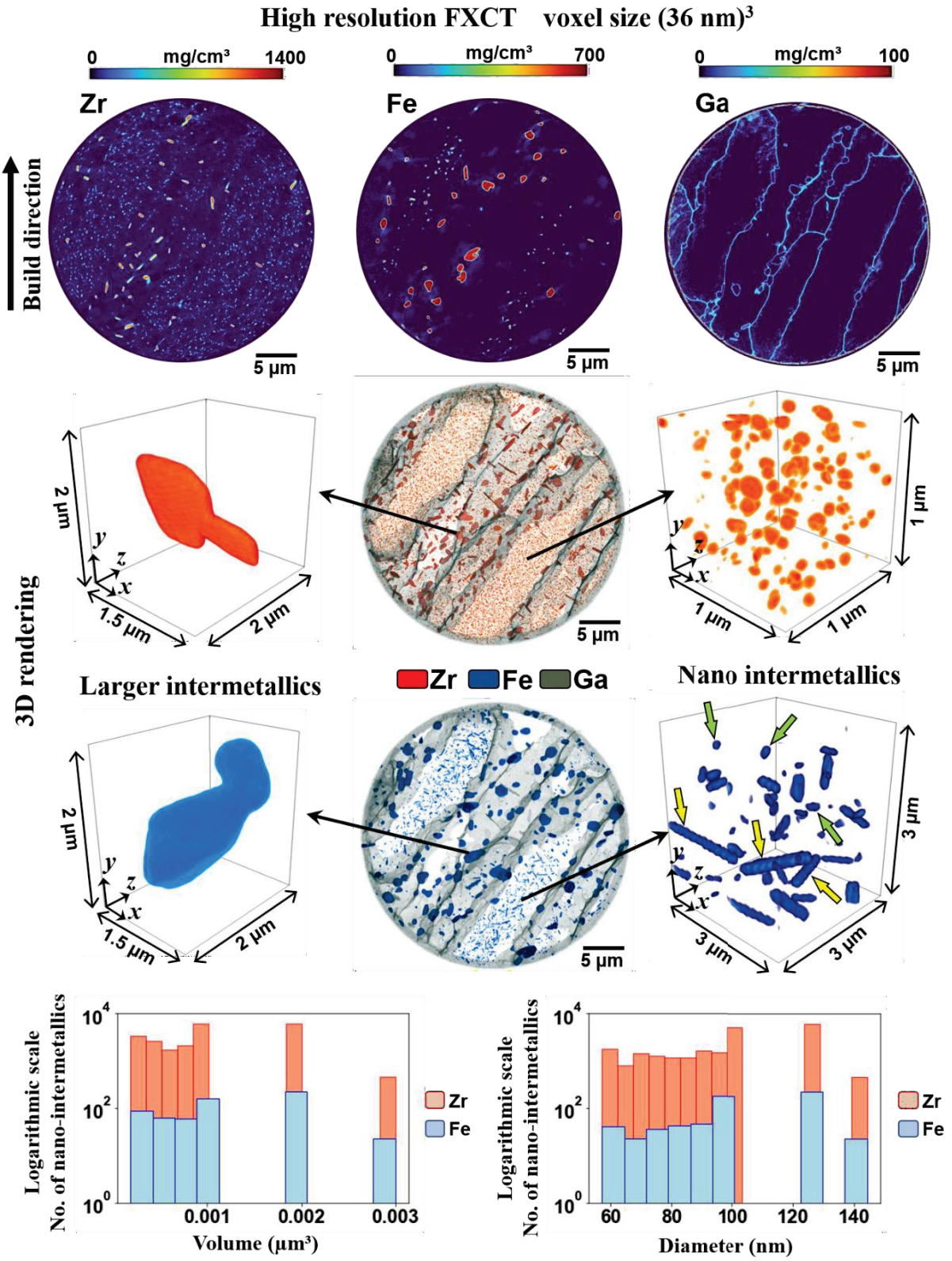

Fig. 6.11 Comparative analysis of intermetallic distributions using high-resolution FXCT with a voxel size of (36 nm)³. Top row: Elemental maps of Zr (left), Fe (center), and Ga (right) of the same x-y slice shown in Fig. 6.10. The central images present 3D renderings of Zr and Fe distribution, overlaid with Ga to delineate grain boundaries. On the left, larger Zr- and Fe-

rich intermetallics are shown, while the right panel focuses on nanoscale intermetallics. The Zr-rich intermetallics predominantly exhibit disc-like or spherical morphologies, whereas the Fe-rich intermetallics appear as both spherical and rod-like structures, indicated by green and yellow arrows, respectively. Bottom row: Histograms of the size distribution of the nano intermetallics. The left histogram shows the particle volume distribution, emphasizing the dominance of Zr-rich particles in smaller volume ranges compared to Fe-rich particles. The right histogram illustrates the diameter distributions of the nano-particles, with Zr-rich particles predominantly within the 60−100nm range, highlighting their finer size.

In Fig. 6.11, larger Zr- and Fe-rich intermetallics are depicted on the left that are predominantly formed at the edge of the Al grains, whereas the right panel emphasizes nanoscale intermetallics, distributed within the grains. These observations are critical in understanding microstructural evolution. Morphological analysis reveals that nanoscale Zr-rich intermetallics predominantly exhibit disc-like or spherical morphology. In contrast, nanoscale Fe-rich intermetallics appear in both spherical and rod-like morphologies, as indicated by green and yellow arrows (Fig. 6.11, right panel of 3D renderings), which may reflect differences in growth mechanisms under aging and subsequent overaging. The histograms at the bottom of Fig. 6.11 provide quantitative observations. The particle volume distribution (bottom left) shows a stark disparity, with Zr-rich intermetallics dominating the smaller volume ranges ($0.003\mu m^3$) and Fe-rich particles being less frequent across the sizes. Similarly, the diameter distribution (bottom right) reinforces the fine-scale nature of Zr-rich intermetallics, with the majority falling within the 60−100nm range. The analysis revealed the total of particle volumes of 24.2 μm^3 and 0.78 μm^3, of Zr- and Fe-rich nano-particles distributed within the scanned volume, respectively. This corresponds to volume fractions of ~0.95% (~0.5wt%) for Zr-rich intermetallics and ~0.03% (~0.008wt%) for Fe-rich intermetallics (without accounting the larger intermetallics).

6.4 Discussion

6.4.1 Multilayer Melt Pool Boundaries

At the melt pool scale, HXCT analyses of the as-built sample revealed distinct melt pool boundaries characterized by darker contrast, indicative of a reduced mass density over a thickness of ~200 nm (Fig. 6.4). Previous 2D characterizations of this alloy system with the same LPBF processing parameters reported Fe depletion along these melt pool boundaries,

which was correlated with high ductility, as evidenced by *in-situ* tensile tests [100]. The Fe depletion at the melt pool boundaries is shown in the FXCT results of the previous chapter. HXCT results corroborate these findings in 3D, clearly resolving Fe-depleted zones along the melt pool boundaries. The localized depletion in Fe, within these melt pool boundary zones, results in a softer region [100]. Melt pool boundaries, forming a 3D interconnected softer network (Fig. 6.3), coexist with the microstructure's overall high ductility in the as-built state. These features remained morphologically unchanged after initial heat treatment at 400°C/4 h (Fig. 6.5). However, prolonged thermal exposure at 530°C/24 h (Fig. 6.6) facilitated the homogenization across the microstructures, thereby reducing the contrast of the distinct melt pool boundary regions.

In contrast, the presence of cellular intermetallic phases just above the melt pool boundaries could likely correspond to the stable θ-$Al_{13}Fe_4$ (Fig. 6.4, 6.5, (c) and (f)). This also aligns with findings by Qi et al., who demonstrated similar features in LPBF-fabricated Al-2.5Fe alloys, where Fe-rich intermetallics formed a coarser network developed above the melt pool boundary [209]. This localization suggests a preferential formation mechanism at the solid-liquid interface during LPBF solidification [210]. Solid phases are known to nucleate and grow under conditions of high thermal gradients and relatively low solidification rates, particularly in the early stages of solidification [106,211,212]. The lower solidification rate facilitates the formation of stable intermetallic phases, which aligns with the observed θ-phase at the melt pool boundaries. Additionally, the extensive two-phase region in the Al-Fe binary system (Fig. 3.2), consisting of solid θ-$Al_{13}Fe_4$ and liquid Al, suggests that fragments of the θ-phase may persist in the melt pool during laser scanning. These undissolved θ-phase particles, residing at the solid-liquid interface, could act as preferential nucleation sites, thereby enhancing the formation and growth of θ-phase at the melt pool boundaries region with subsequent laser passes [210], and also during the aging and subsequent overaging.

6.4.2 Microstructural Evolution of Zr- and Fe-rich intermetallics

The high-resolution FXCT enables precise quantification of nanoscale intermetallics of the Al-1Fe-1Zr allow after overaging, offering detailed insights into their size distribution and volume fraction. Analysis of the diameter distribution shows that nanoscale Zr-rich intermetallics predominantly range between 60 and 100 nm. The Zr-rich particles are significantly more abundant than their Fe-rich counterparts, with total measured volumes of ~24.2 μm³ and ~0.78 μm³, respectively and corresponds to volume fractions of ~0.95%

(~0.5wt%) for Zr-rich and ~0.03% (~0.008wt%) for Fe-rich nanoscale intermetallics. This suggests that nearly half of Zr and only a very small fraction of Fe from the nominal alloy composition is at this scale.

The rapid solidification conditions inherent to LPBF processing lead to the formation of metastable intermetallic phases. For Fe-rich intermetallics, it results in the formation of both stable $Al_{13}Fe_4$ and metastable Al_6Fe phases [92,200]. For Zr-rich intermetallics, it is Al_3Zr phase predominantly in its nanoscale $L1_2$ form [92,95,100,201]. These metastable phases, which remain undetectable in the as-built state using high-resolution tomography, undergo a series of thermodynamically driven transformations during aging and subsequent overaging. The microstructural evolution of these Fe-rich and Zr-rich intermetallics is governed by solute redistribution, diffusion kinetics, and phase stability considerations. A key observation during aging and subsequent overaging is the progressive coarsening of Fe- and Zr-rich intermetallics at the grain boundaries (marked by the FXCT Ga map, Fig. 6.10), primarily driven by Ostwald ripening [213]. This mechanism drives the coarsening of intermetallics by promoting the dissolution of smaller metastable particles and the subsequent diffusion of atoms toward larger, more stable precipitates.

In Fe-rich intermetallics, the nanoscale metastable Al_6Fe formed due to non-equilibrium solidification undergoes a transformation into the more stable $Al_{13}Fe_4$ phase at the grain boundaries [202–204]. This process is further accelerated in regions with a higher density of grain boundaries or narrower grains, where shorter diffusion distances facilitate more efficient solute transport. Consequently, Fe-free zones develop in the grain interiors as Fe atoms preferentially migrate towards the grain boundaries, leaving behind an Al matrix with significantly reduced Fe content. The extent of this Fe depletion is particularly pronounced in areas where grains are narrower, as the limited available space accelerates the diffusion of solute atoms towards the grain boundaries (Fig. 6.12, Areas 1 and 3). Simultaneously, within larger intragranular regions, where diffusion distances are greater, the transformation pathway diverges from that observed at the grain boundaries. The metastable nanoscale Al_6Fe continue to grow to form larger spherical particles. The extended diffusion lengths limit the complete dissolution of Al_6Fe , resulting in its transformation into rod-like particles that are most likely Al_3Fe, a more thermodynamically stable intermetallic phase [214]. This transformation is favoured in regions with relatively larger grains, where the energy barrier for Fe diffusion to the grain boundaries becomes increasingly prohibitive (Fig. 6.12, Areas 2 and 4). Unlike the globular $Al_{13}Fe_4$, which nucleates and coarsens at the grain boundaries, Al_3Fe exhibits a strong

preference for linear growth, adopting a rod-like morphology. As heat treatment continues, smaller Al_6Fe particles coalesce and elongate into rod-like Al_3Fe.

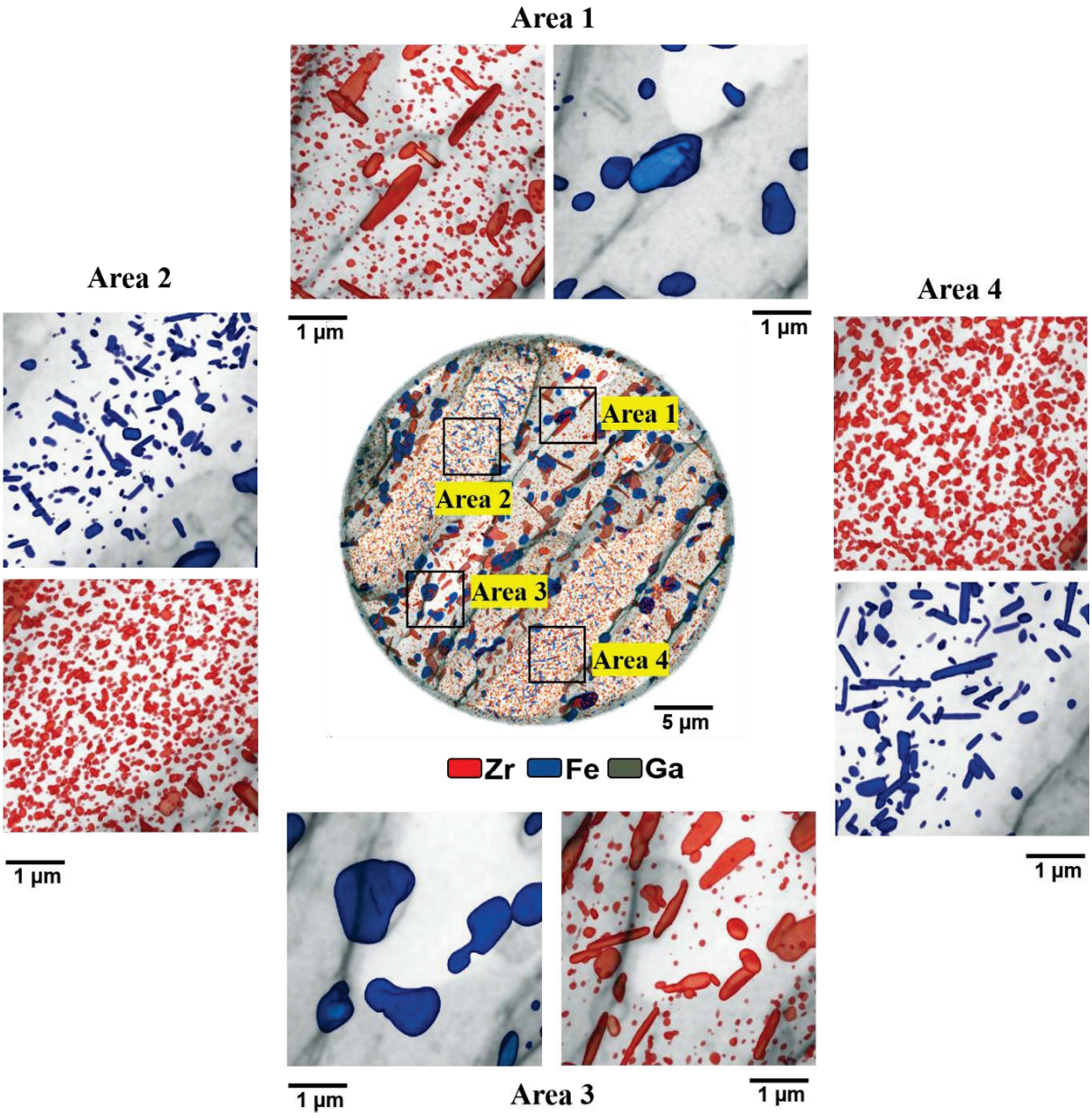

Fig. 6.12 3D rendering of the high-resolution FXCT dataset, highlighting regions of interest (marked Areas 1-4) to illustrate the spatial distribution of larger Zr- and Fe-rich intermetallics. Enlarged views of the marked areas provide a detailed visualization of their morphology and distribution.

Similarly, for Zr-rich intermetallics, the nanoscale $L1_2$-Al_3Zr possibly undergoes a transformation into the more thermodynamically stable $D0_{23}$-Al_3Zr phase, leading to its accumulation and coarsening along the Al grain boundaries [205], with plate-like morphology.

Analogous to the behaviour observed in Fe-rich intermetallics, regions with a high density of grain boundaries or narrower grains exhibit a reduced population of the $L1_2$-Al_3Zr, accompanied by a higher proportion of coarsened Zr-rich plate-like particles (Fig. 6.12, Areas 1 and 3) . In contrast, within larger intragranular regions, the nanoscale cubic $L1_2$-Al_3Zr precipitates continue to grow, resulting in the formation of smaller disc-like or spherical precipitates suggesting its change into $D0_{23}$-structure during overaging (Fig. 6.12, Areas 2 and 4). The diffusion-mediated $L1_2$ to $D0_{23}$ phase transition proposed here, is in line with previous findings in [215], which suggest that the $D0_{22}$ phase may serve as an intermediate state, eventually transforming into the stable $D0_{23}$ structure upon extended heat treatments. This further substantiates the feasibility of the transformation mechanisms described above.

6.5 Key messages

The analyses presented in this chapter provide a detailed examination of the hypotheses introduced in the Motivation (Chapter 2), addressing the influence of heat treatments on microstructural evolution and the feasibility of imaging nano-intermetallics in the LPBF-fabricated Al-1Fe-1Zr alloy.

How do different heat treatments influence the microstructural evolution of the Al-1Fe-1Zr alloy manufactured via LPBF?

In the as-built condition, the melt pool boundaries were distinctly visible, characterized by a lower mass density and Fe depletion. Upon heat treatment at 400°C/4 h, these boundaries remained largely unchanged but overaging facilitated microstructural homogenization, strongly reducing contrast at the melt pool boundaries. The cellular intermetallic phases just above the melt pool boundaries corresponding to the stable θ-$Al_{13}Fe_4$ coarsened during the heat treatment and subsequent overaging. The thermal treatments applied to the alloy significantly impact the hierarchical microstructure. A key observation during heat treatment and subsequent overaging is the progressive coarsening of Fe- and Zr-rich intermetallics at the grain boundaries, primarily driven by Ostwald ripening. At 400°C for 4 hours, intermetallic phases begin to coarsen at grain boundaries, transforming to the stable $Al_{13}Fe_4$ and $D0_{23}$-Al_3Zr. Subsequent overaging, at 530°C for 24 hours drives further coarsening of intermetallics, forming $Al_{13}Fe_4$ irregular globular particles and plate-like $D0_{23}$-Al_3Zrparticles at grain boundaries.

In larger intragranular regions, Fe diffusion barriers result in the coarsening of the nanoscale metastable Al_6Fe and its partial transformation into rod-like Al_3Fe. Similarly, for Zr-rich intermetallics, nanoscale $L1_2$-Al_3Zr coalesces into disc-like or spherical precipitates, suggesting a gradual diffusion-mediated transformation into the more stable $D0_{23}$-Al_3Zr.

Is it possible to image and quantify the nano-sized precipitates?

Using high-resolution synchrotron-based X-ray computed tomography techniques it is possible to image and quantify nano-sized precipitates. Moreover, extended heat treatments played a crucial role in coarsening these nano-sized precipitates to sizes resolvable by high-resolution imaging, demonstrating that such thermal exposure is essential for accurate visualization and quantification. The combination of high-resolution NFPXCT and HXCT provided crucial

insights into the spatial distribution and morphological evolution of nano-intermetallics, serving as a mapping tool to track the effects of heat treatments. However, the precise quantification of individual elemental phases at the nanoscale was achieved through high-resolution FXCT with a voxel size of $(36\ nm)^3$. The FXCT data revealed that Zr-rich intermetallics predominantly ranged between 60 and 100 nm, whereas Fe-rich intermetallics were significantly less abundant. The total measured volumes of Zr-rich and Fe-rich nanoscale intermetallics were 24.2 μm^3 and 0.78 μm^3, corresponding to volume fractions of 0.95% (0.5wt%) and 0.031% (0.008wt%), respectively. This suggests that nearly half of Zr and only a very small fraction of Fe from the nominal alloy composition is at this scale and the rest have transformed to the stable counterparts.

7 Conclusion

This research investigates the microstructural properties of the Al-1Fe-1Zr alloy (Constellium Aheadd® CP1) processed via LPBF, addressing critical gaps in understanding the process-microstructure-property relationship. Given the vast number of variables influencing LPBF, a comprehensive experimental assessment of all influencing factors is impractical. However, precise nanoscale characterization enables predictions of material behaviour and performance, bridging rigorous academic research with industrial applications. This study utilizes the advanced X-ray nano-imaging capabilities of the ID16A beamline at ESRF to achieve high-resolution, non-destructive 3D visualization and quantification of microstructural features. These techniques provide deeper insights into the morphology, spatial distribution, and phase evolution of Fe- and Zr-rich intermetallics during LPBF processing and subsequent heat treatments. The ability to conduct repeated non-destructive investigations before and after heat treatments provides a robust framework for understanding phase transformations and solute redistribution. Prior to applying these techniques to microstructural analysis, this study also optimizes experimental methodologies and beamline parameters for high-resolution imaging in AM. Refining synchrotron-based techniques enhances data quality, reduces acquisition times, and improves cost-efficiency, extending the applicability of these methods to a broader range of metallic systems. This work contributes to addressing key challenges in materials characterization, advancing the understanding of the process-microstructure-property relationship, and enhancing experimental efficiency through synchrotron-based 3D characterization techniques.

In chapter 3, the principles of LPBF were described along with its adoption in various sectors due to its capabilities in design efficiency. The Al-Fe and Al-Zr binary, and the ternary Al-Fe-Zr alloy systems were discussed to understand their rapid solidification behaviour, forming a theoretical foundation for subsequent investigations. Previous studies on Constellium Aheadd® CP1 were described in detail, particularly a comprehensive study employing 2D multiscale characterizations to analyze the mechanical properties of the alloy in as-built and peak-aged states. After peak aging for 4 h at 400°C, the alloy exhibits a yield strength of 310 MPa and thermal conductivity of 180 W/m.K, compared to 130 MPa and 122 W/m.K, respectively, in the as-built condition. Additionally, *in-operando* synchrotron X-ray radiography was employed to analyze laser-matter interactions, demonstrating that scan speed significantly affects spatter trajectory more than laser power. The impact of different layer thicknesses and the effects of a remelting strategy were also assessed. It was concluded that a

30 μm layer thickness provides the most robust process window, yielding material densities above 99.85% when processed with a 400 W laser. Furthermore, this chapter described the X-ray principles and the propagation-based phase contrast methods, along with X-ray fluorescence. The experimental setup of the ID16A beamline was explained, along with the imaging methods HXCT, NFPXCT, and FXCT. The workflow of each technique was outlined, detailing the sequential steps from raw data acquisition to 3D reconstruction.

In chapter 4, the full potential of these imaging techniques was realized through meticulous optimization of experimental parameters, tailored to the material and microstructures under investigation. Experimental strategies included optimizing parameters such as X-ray energy, number of projections, and the application of techniques like random displacement to improve data quality. The X-ray energy of 33.3 keV was preferred for corelative phase contrast and fluorescence imaging (to excite the K-edge of Zr). However, for NFPXCT the phase maps reconstructed at 17.1 keV exhibit considerably enhanced clarity, with minimal noise, thereby demonstrating the superior performance of this lower energy setting in capturing fine structural details. An experimental upgrade using a real-time control system for nano-positioning significantly reduced X-ray fluorescence acquisition times, improving overall efficiency. Refinement of alignment techniques shows a marked improvement in image quality. This chapter also provided a detailed examination of the ultrafine internal structure, morphology, and local mass density of an Al-1Fe-1Zr alloy in 3D. A comparative evaluation of HXCT and NFPXCT was conducted, assessing their performance in terms of acquisition time, reconstruction quality, and spatial resolution. NFPXCT offered improved spatial resolution and reduced artefacts, primarily due to its ability to accurately account for inhomogeneities in the incident beam (probe). Nevertheless, the majority of the analyses presented in the following sections were conducted using HXCT for several practical and technical reasons: (1) significantly shorter acquisition times, typically 3–4 times faster than NFPXCT; (2) more established and computationally efficient data processing workflows; and (3) improved imaging performance at 33.3 keV X-ray energy, which also aligns with the optimal energy range required for FXCT measurements. These insights were complemented by FXCT, which provided element-specific chemical analysis in 3D. The phase contrast and element sensitive techniques enabled both qualitative and quantitative analysis of phase morphology, mass density, and chemistry with spatial resolutions of 57 nm and elemental concentration detection limits of 3 mg/cm³ for Zr, 1.5 mg/cm³ for Fe, and 0.3 mg/cm³ for Ga. FXCT elucidated the Al_3Zr primary particles at the center of the equiaxed grain and the heterogenous accumulation

$Al_{13}Fe_4$ at the grain boundaries. Additionally, we also observed a uniform concentration of 25 mg/cm^3 of nanoscale $L1_2$-Al_3Zr equivalent to 0.9wt% aligning with the nominal alloy composition. Ga, used in the FIB milling process, turned out to be very valuable to identify the location of the grain boundaries.

In chapter 5, the primary objective was to elucidate the influence of LPBF processing conditions on the formation and spatial distribution of Fe-rich and Zr-rich intermetallics within prior melt pools and the effect of heat treatment. Three specific conditions (C1, C2, and C3) were selected for comparative analysis to investigate how the microstructure responds to varying LPBF processing parameters. The Al-1Fe-1Zr alloy powder was also analyzed to understand the microstructure in its original state. HXCT imaging of a powder particle revealed a cellular structure of bright intermetallic phases embedded within the Al matrix, indicative of rapid solidification features formed during gas atomization. Total mass density observed in the HXCT slices were 2.6 g/cm^3. FXCT showed that the cellular structure predominantly consists of Fe-rich intermetallics, likely θ-$Al_{13}Fe_4$, following an eutectic reaction during solidification, with a measured volume fraction of 0.33% (1.02wt%). Zr, in contrast, was homogeneously distributed in the volume with uniform concentrations of ~28 mg/cm³, corresponding to 1.03wt% and aligning with the nominal alloy composition. As part of this study, an optimized sample preparation workflow was established to ensure reliable and targeted high-resolution characterization. This workflow combined mechanical polishing, optical microscopy, and FIB milling, enabling precise localization and extraction of sub-samples from specific regions within the melt pool architecture. This approach was essential for accessing well-defined areas of interest and ensuring the suitability of the extracted samples for subsequent analysis using advanced high-resolution X-ray characterization techniques. Variations in LPBF processing significantly influenced microstructural formation, particularly through laser scanning speed, energy density, and laser mode. CW laser scanning at moderate speeds resulted in stable melt pools with a balanced width-to-depth ratio and well-defined columnar grain structures (C1). Higher scanning speeds (C2) produced shallower melt pools due to reduced thermal penetration, while the use of higher energy density and PWM (C3) created deeper melt pools and disrupted columnar grain growth at the center. FXCT results for the C1 center and bottom samples revealed uniform background concentrations of Fe (~15.5 mg/cm^3, ~0.56 wt%) and Zr (~26 mg/cm^3, ~0.96 wt%) throughout the volume. In comparison, the C3 center sample showed slightly elevated background concentrations, with Fe at ~17 mg/cm^3 (~0.65 wt%) and Zr at ~30 mg/cm^3 (~1 wt%). These concentrations are compatible with the presence of Fe and

Zr in their respective nanoscale metastable phases, Al_6Fe and $L1_2$–Al_3Zr. Fe depletion at the melt pool boundary was observed in C1 (bottom sample). Heat treatment influenced intermetallic transformations, where Al_6Fe transformed into stable $Al_{13}Fe_4$ at grain boundaries, and nanoscale $L1_2$-Al_3Zr evolved into the more stable $D0_{23}$-Al_3Zr phase at grain boundaries.

In chapter 6, the effects of heat treatments on the coarsening behaviour of intermetallics were investigated, specifically targeting the growth of Fe- and Zr-rich nano-precipitates to dimensions resolvable using synchrotron-based imaging. A multi-layer build sample was studied in the as-built state, after heat treatment at 400°C for 4 h, and following overaging at 530°C for 24 h. In the as-built condition, melt pool boundaries were distinctly visible, characterized by Fe depletion. Upon heat treatment, these boundaries remained largely unchanged at 400°C, but overaging at 530°C facilitated microstructural homogenization, strongly reducing contrast at the melt pool boundaries. Cellular intermetallic phases adjacent to the melt pool boundaries, likely corresponding to stable θ-$Al_{13}Fe_4$, coarsened during heat treatment and subsequent overaging. Thermal treatments significantly influenced the hierarchical microstructure, where Ostwald ripening promoted the coarsening of intermetallics at grain boundaries. Our observations are compatible with a transformation of metastable Al_6Fe into $Al_{13}Fe_4$ and $L1_2$-Al_3Zr into $D0_{23}$-Al_3Zr, indicating thermodynamically driven phase stability changes. The high-resolution FXCT experiment, performed at a voxel size of $(36\ nm)^3$, represents the first of its kind to enable 3D quantification of nanoscale intermetallics at this resolution. It allowed precise characterization of the Zr-rich particles, which were predominantly observed in the size range of 60-100 nm. Zr-rich intermetallics were significantly more abundant than Fe-rich ones, with total measured volumes of 24.2 μm^3 and 0.78 μm^3, corresponding to volume fractions of 0.95% (0.5 wt%) and 0.03% (0.008 wt%) for Zr- and Fe-rich nanoscale intermetallics, respectively. This is indicative that half of Zr and only a very small fraction of Fe from the nominal alloy composition exist at this scale.

This thesis provides a comprehensive study of the spatial distribution, morphology, and chemistry of microstructural features in the Al-1Fe-1Zr alloy. The findings have significant implications for both academic and industrial research, particularly within the scope of the InnovaXN doctoral program, which integrates large-scale research infrastructures with industrial R&D needs. By addressing key challenges in materials characterization and experimental efficiency, this work could contribute to the development of advanced materials and the optimization of AM processes, paving the way for improved process control and enhanced material performance in various applications.

8 Outlook

The following studies could be considered as outlook of the current work:

- While current 3D reconstructions account for many factors for good quality reconstruction, the possibilities for further improving the reconstructions are available. In particular, novel iterative algorithms for NFPXCT could enhance phase information extraction, improving both quality and efficiency. Such possibilities could be explored.

- Recent advancements such as probe retrieval in HXCT offer a more accurate alternative to conventional flat-field correction, reducing artefacts and improving reconstruction quality [216]. Integrating such methods can further enhance imaging fidelity in future studies.

- The inferred precipitation behaviour, non-equilibrium solidification, and associated phase transformations (as drawn from the literature) could be validated through X-ray diffraction experiments.

- Scanning-diffraction tomography could be used to show the grain solidification direction and orientation, providing complementary insights into the Ga-induced grain boundary wetting mechanism.

- Given that LPBF produces complex geometries - with multiple heat-affected zones, re-melting events, and other influencing factors - further investigation into the microstructure–property relationships in these parts could be interesting.

- The characterization approaches demonstrated in this work are broadly applicable to other alloys developed or under development for additive manufacturing applications.

9 Bibliography

[1] M. Armstrong, H. Mehrabi, N. Naveed, An overview of modern metal additive manufacturing technology, Journal of Manufacturing Processes 84 (2022) 1001–1029. https://doi.org/10.1016/j.jmapro.2022.10.060.

[2] B. Blakey-Milner, P. Gradl, G. Snedden, M. Brooks, J. Pitot, E. Lopez, M. Leary, F. Berto, A. du Plessis, Metal additive manufacturing in aerospace: A review, Materials & Design 209 (2021) 110008. https://doi.org/10.1016/j.matdes.2021.110008.

[3] F. Kerstens, A. Cervone, P. Gradl, End to end process evaluation for additively manufactured liquid rocket engine thrust chambers, Acta Astronautica 182 (2021) 454–465. https://doi.org/10.1016/j.actaastro.2021.02.034.

[4] Metal Additive Manufacturing in the aerospace sector, Metal Additive Manufacturing (2023). https://www.metal-am.com/articles/metal-am-in-the-aerospace-sector-from-early-successes-to-the-transformation-of-an-industry/ (accessed April 3, 2025).

[5] M. Attaran, The rise of 3-D printing: The advantages of additive manufacturing over traditional manufacturing, Business Horizons 60 (2017) 677–688. https://doi.org/10.1016/j.bushor.2017.05.011.

[6] T. DebRoy, H.L. Wei, J.S. Zuback, T. Mukherjee, J.W. Elmer, J.O. Milewski, A.M. Beese, A. Wilson-Heid, A. De, W. Zhang, Additive manufacturing of metallic components – Process, structure and properties, Progress in Materials Science 92 (2018) 112–224. https://doi.org/10.1016/j.pmatsci.2017.10.001.

[7] J. Gussone, K. Bugelnig, P. Barriobero-Vila, J.C. da Silva, U. Hecht, C. Dresbach, F. Sket, P. Cloetens, A. Stark, N. Schell, J. Haubrich, G. Requena, Ultrafine eutectic Ti-Fe-based alloys processed by additive manufacturing – A new candidate for high temperature applications, Applied Materials Today 20 (2020) 100767. https://doi.org/10.1016/j.apmt.2020.100767.

[8] A. Savini, G.G. Savini, A short history of 3D printing, a technological revolution just started, in: 2015: pp. 1–8. https://doi.org/10.1109/HISTELCON.2015.7307314.

[9] A. Vafadar, F. Guzzomi, A. Rassau, K. Hayward, Advances in Metal Additive Manufacturing: A Review of Common Processes, Industrial Applications, and Current Challenges, Applied Sciences 11 (2021) 1213. https://doi.org/10.3390/app11031213.

[10] F. Pixner, F. Warchomicka, M. Lipińska, S. Elmiger, C. Jechtl, P. Auer, F. Riedlsperger, R. Buzolin, J. Domitner, M. Lewandowska, N. Enzinger, Thermal cycling effects on the local microstructure and mechanical properties in wire-based directed energy deposition of nickel-based superalloy, Additive Manufacturing 83 (2024) 104066. https://doi.org/10.1016/j.addma.2024.104066.

[11] T. Mishurova, I. Serrano-Munoz, T. Fritsch, A. Ulbricht, M. Sprengel, A. Evans, A. Kromm, M. Madia, G. Bruno, A Critical Discussion on the Diffraction-Based Experimental Determination of Residual Stress in AM Parts, in: 2020: pp. 122–138. https://doi.org/10.1520/stp163120190148.

[12] A. Charmi, R. Falkenberg, L. Ávila, G. Mohr, K. Sommer, A. Ulbricht, M. Sprengel, R. Saliwan Neumann, B. Skrotzki, A. Evans, Mechanical anisotropy of additively manufactured stainless steel 316L: An experimental and numerical study, Materials Science and Engineering: A 799 (2021) 140154. https://doi.org/10.1016/j.msea.2020.140154.

[13] N. Sanaei, A. Fatemi, Defects in additive manufactured metals and their effect on fatigue performance: A state-of-the-art review, Progress in Materials Science 117 (2021) 100724. https://doi.org/10.1016/j.pmatsci.2020.100724.

[14] D. Herzog, V. Seyda, E. Wycisk, C. Emmelmann, Additive manufacturing of metals, Acta Materialia 117 (2016) 371–392. https://doi.org/10.1016/j.actamat.2016.07.019.

[15] S. Yim, H. Bian, K. Aoyagi, K. Yamanaka, A. Chiba, Effect of powder morphology on flowability and spreading behavior in powder bed fusion additive manufacturing process: A particle-scale modeling study, Additive Manufacturing 72 (2023) 103612. https://doi.org/10.1016/j.addma.2023.103612.

[16] S. Chowdhury, N. Yadaiah, C. Prakash, S. Ramakrishna, S. Dixit, L.R. Gupta, D. Buddhi, Laser powder bed fusion: a state-of-the-art review of the technology, materials, properties & defects, and numerical modelling, Journal of Materials Research and Technology 20 (2022) 2109–2172. https://doi.org/10.1016/j.jmrt.2022.07.121.

[17] S.R. Narasimharaju, W. Zeng, T.L. See, Z. Zhu, P. Scott, X. Jiang, S. Lou, A comprehensive review on laser powder bed fusion of steels: Processing, microstructure, defects and control methods, mechanical properties, current challenges and future trends, Journal of Manufacturing Processes 75 (2022) 375–414. https://doi.org/10.1016/j.jmapro.2021.12.033.

[18] J. Weaver, J. Heigel, B. Lane, Laser spot size and scaling laws for laser beam additive manufacturing, Journal of Manufacturing Processes 73 (2022) 26–39. https://doi.org/10.1016/j.jmapro.2021.10.053.

[19] G. Nordet, C. Gorny, Y. Mayi, J. Daligault, M. Dal, A. Effernelli, E. Blanchet, F. Coste, P. Peyre, Absorptivity measurements during laser powder bed fusion of pure copper with a 1 kW cw green laser, Optics & Laser Technology 147 (2022) 107612. https://doi.org/10.1016/j.optlastec.2021.107612.

[20] M.C. Sow, T. De Terris, O. Castelnau, Z. Hamouche, F. Coste, R. Fabbro, P. Peyre, Influence of beam diameter on Laser Powder Bed Fusion (L-PBF) process, Additive Manufacturing 36 (2020) 101532. https://doi.org/10.1016/j.addma.2020.101532.

[21] J. Wang, R. Zhu, Y. Liu, L. Zhang, Understanding melt pool characteristics in laser powder bed fusion: An overview of single- and multi-track melt pools for process optimization, Advanced Powder Materials 2 (2023) 100137. https://doi.org/10.1016/j.apmate.2023.100137.

[22] W. Guo, B. Feng, Y. Yang, Y. Ren, Y. Liu, H. Yang, Q. Yang, L. Cui, X. Tong, S. Hao, Effect of laser scanning speed on the microstructure, phase transformation and mechanical property of NiTi alloys fabricated by LPBF, Materials & Design 215 (2022) 110460. https://doi.org/10.1016/j.matdes.2022.110460.

[23] Q. Chen, Y. Zhao, S. Strayer, Y. Zhao, K. Aoyagi, Y. Koizumi, A. Chiba, W. Xiong, A.C. To, Elucidating the effect of preheating temperature on melt pool morphology variation in Inconel 718 laser powder bed fusion via simulation and experiment, Additive Manufacturing 37 (2021) 101642. https://doi.org/10.1016/j.addma.2020.101642.

[24] D. Zheng, Z. Li, Y. Jiang, R. Li, Y. Wu, Y. Tu, X. Cheng, P. Fu, L. Peng, H. Tang, Effect of multiple thermal cycles on the microstructure evolution of GA151K alloy fabricated by laser-directed energy deposition, Additive Manufacturing 57 (2022) 102957. https://doi.org/10.1016/j.addma.2022.102957.

[25] J. Gong, K. Wei, M. Liu, W. Song, X. Li, X. Zeng, Microstructure and mechanical properties of AlSi10Mg alloy built by laser powder bed fusion/direct energy deposition hybrid laser additive manufacturing, Additive Manufacturing 59 (2022) 103160. https://doi.org/10.1016/j.addma.2022.103160.

[26] M. Liu, K. Wei, X. Zeng, High power laser powder bed fusion of AlSi10Mg alloy: Effect of layer thickness on defect, microstructure and mechanical property, Materials Science and Engineering: A 842 (2022) 143107. https://doi.org/10.1016/j.msea.2022.143107.

[27] V.A. Medrano, E. Arrieta, J. Merino, B. Ruvalcaba, K. Caballero, B. Ramirez, J. Diemann, L.E. Murr, R.B. Wicker, D. Godfrey, M. Benedict, F. Medina, A comprehensive and comparative study of microstructure and mechanical properties for post-process heat

treatment of AlSi7Mg alloy components fabricated in different laser powder bed fusion systems, Journal of Materials Research and Technology 24 (2023) 6820–6842. https://doi.org/10.1016/j.jmrt.2023.04.129.

[28] H. Hyer, L. Zhou, A. Mehta, S. Park, T. Huynh, S. Song, Y. Bai, K. Cho, B. McWilliams, Y. Sohn, Composition-dependent solidification cracking of aluminum-silicon alloys during laser powder bed fusion, Acta Materialia 208 (2021) 116698. https://doi.org/10.1016/j.actamat.2021.116698.

[29] C. Böhm, M. Werz, S. Weihe, Practical Approach to Eliminate Solidification Cracks by Supplementing AlMg4.5Mn0.7 with AlSi10Mg Powder in Laser Powder Bed Fusion, Materials 15 (2022) 572. https://doi.org/10.3390/ma15020572.

[30] S. Wu, Z. Lei, B. Li, J. Liang, Y. Chen, Hot cracking evolution and formation mechanism in 2195 Al-Li alloy printed by laser powder bed fusion, Additive Manufacturing 54 (2022) 102762. https://doi.org/10.1016/j.addma.2022.102762.

[31] R.F. Fernandes, J.S. Jesus, R. Branco, L.P. Borrego, J.D. Costa, J.A.M. Ferreira, Influence of post-processing heat treatment on the cyclic deformation behaviour of AlSi10Mg aluminium alloy subjected to laser powder bed fusion, International Journal of Fatigue 164 (2022) 107157. https://doi.org/10.1016/j.ijfatigue.2022.107157.

[32] A. Maamoun, M. Elbestawi, G.K. Dosbaeva, S.C. Veldhuis, Thermal Post-processing of AlSi10Mg parts produced by Selective Laser Melting using recycled powder, Additive Manufacturing 21 (2018) 234–247. https://doi.org/10.1016/j.addma.2018.03.014.

[33] P.A. Rometsch, Y. Zhu, X. Wu, A. Huang, Review of high-strength aluminium alloys for additive manufacturing by laser powder bed fusion, Materials & Design 219 (2022) 110779. https://doi.org/10.1016/j.matdes.2022.110779.

[34] E. Louvis, P. Fox, C.J. Sutcliffe, Selective laser melting of aluminium components, Journal of Materials Processing Technology 211 (2011) 275–284. https://doi.org/10.1016/j.jmatprotec.2010.09.019.

[35] J. Gong, K. Wei, M. Liu, W. Song, X. Li, X. Zeng, Microstructure and mechanical properties of AlSi10Mg alloy built by laser powder bed fusion/direct energy deposition hybrid laser additive manufacturing, Additive Manufacturing 59 (2022) 103160. https://doi.org/10.1016/j.addma.2022.103160.

[36] L. Zhao, L. Song, J.G. Santos Macías, Y. Zhu, M. Huang, A. Simar, Z. Li, Review on the correlation between microstructure and mechanical performance for laser powder bed fusion AlSi10Mg, Additive Manufacturing 56 (2022) 102914. https://doi.org/10.1016/j.addma.2022.102914.

[37] Metal additive manufacturing in aerospace: A review - ScienceDirect, (n.d.). https://www.sciencedirect.com/science/article/pii/S0264127521005633 (accessed August 5, 2024).

[38] M. Rasch, D. Bartels, S. Sun, M. Schmidt, AlSi10Mg in Powder Bed Fusion with Laser Beam: An Old and Boring Material?, Materials (Basel) 15 (2022) 5651. https://doi.org/10.3390/ma15165651.

[39] M. Avateffazeli, S.I. Shakil, A. Hadadzadeh, B. Shalchi-Amirkhiz, H. Pirgazi, M. Mohammadi, M. Haghshenas, On microstructure and work hardening behavior of laser powder bed fused Al-Cu-Mg-Ag-TiB2 and AlSi10Mg alloys, Materials Today Communications 35 (2023) 105804. https://doi.org/10.1016/j.mtcomm.2023.105804.

[40] A. Ghasemi, E. Fereiduni, M. Balbaa, M. Elbestawi, S. Habibi, Unraveling the low thermal conductivity of the LPBF fabricated pure Al, AlSi12, and AlSi10Mg alloys through substrate preheating, Additive Manufacturing 59 (2022) 103148. https://doi.org/10.1016/j.addma.2022.103148.

[41] J.G. Santos Macías, T. Douillard, L. Zhao, E. Maire, G. Pyka, A. Simar, Influence on microstructure, strength and ductility of build platform temperature during laser powder

bed fusion of AlSi10Mg, Acta Materialia 201 (2020) 231–243. https://doi.org/10.1016/j.actamat.2020.10.001.
[42] S.-H. Li, Y. Zhao, U. Ramamurty, Role of the solidification cells on the yield strength of the Al-Si-Mg alloy manufactured using laser powder bed fusion: A micropillar compression study, Scripta Materialia 234 (2023) 115566. https://doi.org/10.1016/j.scriptamat.2023.115566.
[43] M.S. Bisht, V. Gaur, I.V. Singh, On mechanical properties of SLM Al–Si alloy: Role of heat treatment-induced evolution of silicon morphology, Materials Science and Engineering: A 858 (2022) 144157. https://doi.org/10.1016/j.msea.2022.144157.
[44] M. Prasad Behera, T. Dougherty, S. Singamneni, K. De Silva, Selective laser melting of aluminium metal-matrix composites and the challenges, Materials Today: Proceedings 33 (2020) 5729–5733. https://doi.org/10.1016/j.matpr.2020.05.086.
[45] S.I. Shakil, A. Hadadzadeh, B. Shalchi Amirkhiz, H. Pirgazi, M. Mohammadi, M. Haghshenas, Additive manufactured versus cast AlSi10Mg alloy: Microstructure and micromechanics, Results in Materials 10 (2021) 100178. https://doi.org/10.1016/j.rinma.2021.100178.
[46] F.H. (Sam) Froes, O.N. Senkov, E.G. Baburaj, Synthesis of nanocrystalline materials — an overview, Materials Science and Engineering: A 301 (2001) 44–53. https://doi.org/10.1016/S0921-5093(00)01391-5.
[47] Binary alloy phase diagrams, Metals Park, Ohio : American Society for Metals, 1986. http://archive.org/details/binaryalloyphase0002unse (accessed January 22, 2025).
[48] J. Valloton, A.A. Bogno, J. Chen, R. Lengsdorf, H. Henein, D.M. Herlach, U. Dahlborg, M. Calvo-Dahlborg, Microstructural Evolution in Undercooled Al–8wt%Fe Melts, in: TMS 2016 145th Annual Meeting & Exhibition, Springer International Publishing, Cham, 2016: pp. 51–57. https://doi.org/10.1007/978-3-319-48254-5_7.
[49] B. Badan, M. Magrini, A. Zambon, Al-Fe solid solutions in alloys obtained by melt spinning, Scripta Materialia 35 (1996) 13–16. https://doi.org/10.1016/1359-6462(96)00089-9.
[50] A. Aversa, G. Marchese, A. Saboori, E. Bassini, D. Manfredi, S. Biamino, D. Ugues, P. Fino, M. Lombardi, New Aluminum Alloys Specifically Designed for Laser Powder Bed Fusion: A Review, Materials 12 (2019) 1007. https://doi.org/10.3390/ma12071007.
[51] A. Kawahara, A. Niikura, T. Doko, Development of Aluminum Alloy Fin Stock for Heat Exchangers Using Twin-Roll Continuous Casting Method, in: 2003. https://www.semanticscholar.org/paper/Development-of-Aluminum-Alloy-Fin-Stock-for-Heat-Kawahara-Niikura/65b684cea66e9b161949ac0435d633e34a6d94c5 (accessed January 22, 2025).
[52] P. Rodriguez, Selection of Materials for Heat Exchangers, (n.d.).
[53] P.J. Black, The structure of FeAl3. I, Acta Crystallographica 8 (1955) 43–48. https://doi.org/10.1107/S0365110X5500011X.
[54] X. Wang, R.G. Guan, R.D.K. Misra, Y. Wang, H.C. Li, Y.Q. Shang, The mechanistic contribution of nanosized Al3Fe phase on the mechanical properties of Al-Fe alloy, Materials Science and Engineering: A 724 (2018) 452–460. https://doi.org/10.1016/j.msea.2018.04.002.
[55] C.A. Aliravci, M.Ö. Pekgüleryüz, Calculation of phase diagrams for the metastable Al-Fe phases forming in direct-chill (DC)-cast aluminum alloy ingots, Calphad 22 (1998) 147–155. https://doi.org/10.1016/S0364-5916(98)00020-0.
[56] X. Qi, N. Takata, A. Suzuki, M. Kobashi, M. Kato, Laser powder bed fusion of a near-eutectic Al–Fe binary alloy: Processing and microstructure, Additive Manufacturing 35 (2020) 101308. https://doi.org/10.1016/j.addma.2020.101308.

[57] H. KOSUGE, Intermetallic compounds in Al-Fe alloys, Journal of Japan Institute of Light Metals 30 (1980) 217–226. https://doi.org/10.2464/jilm.30.217.
[58] S.-L. Shang, H. Sun, B. Pan, Y. Wang, A.M. Krajewski, M. Banu, J. Li, Z.-K. Liu, Forming mechanism of equilibrium and non-equilibrium metallurgical phases in dissimilar aluminum/steel (Al–Fe) joints, Sci Rep 11 (2021) 24251. https://doi.org/10.1038/s41598-021-03578-0.
[59] X. Zhu, P. Blake, S. Ji, The formation mechanism of Al6(Fe, Mn) in die-cast Al–Mg alloys, CrystEngComm 20 (2018) 3839–3848. https://doi.org/10.1039/C8CE00675J.
[60] H. He, S. Lin, C. Yang, C. Fan, Z. Chen, Combination Effects of Nocolok Flux with Ni Powder on Properties and Microstructures of Aluminum-Stainless Steel TIG Welding-Brazing Joint, J. of Materi Eng and Perform 22 (2013) 3315–3323. https://doi.org/10.1007/s11665-013-0615-y.
[61] Intermetallics Synthesis in the Fe–Al System via Layer by Layer 3D Laser Cladding, (n.d.). https://www.mdpi.com/2073-4352/3/4/517 (accessed January 22, 2025).
[62] S. Lotfian, G. Rolink, A. Weisheit, M. Palm, Chemically graded Fe–Al/steel samples fabricated by laser metal deposition, MRS Advances 2 (2017) 1393–1398. https://doi.org/10.1557/adv.2017.124.
[63] B. Sundman, I. Ohnuma, N. Dupin, U.R. Kattner, S.G. Fries, An assessment of the entire Al–Fe system including D03 ordering, Acta Materialia 57 (2009) 2896–2908. https://doi.org/10.1016/j.actamat.2009.02.046.
[64] L.K. Walford, The structure of the intermetallic phase FeAl6, Acta Cryst 18 (1965) 287–291. https://doi.org/10.1107/S0365110X65000610.
[65] H. Jones, On the prediction of lattice parameter vs. concentration for solid solutions extended by rapid quenching from the melt, Scripta Metallurgica 17 (1983) 97–100. https://doi.org/10.1016/0036-9748(83)90078-9.
[66] T.T. Sasaki, T. Ohkubo, K. Hono, Microstructure and mechanical properties of bulk nanocrystalline Al–Fe alloy processed by mechanical alloying and spark plasma sintering, Acta Materialia 57 (2009) 3529–3538. https://doi.org/10.1016/j.actamat.2009.04.012.
[67] Z. Hu, H. Zhang, H. Zhu, Z. Xiao, X. Nie, X. Zeng, Microstructure, mechanical properties and strengthening mechanisms of AlCu5MnCdVA aluminum alloy fabricated by selective laser melting, Materials Science and Engineering: A 759 (2019) 154–166. https://doi.org/10.1016/j.msea.2019.04.114.
[68] T. Dorin, N. Stanford, N. Birbilis, R.K. Gupta, Influence of cooling rate on the microstructure and corrosion behavior of Al–Fe alloys, Corrosion Science 100 (2015) 396–403. https://doi.org/10.1016/j.corsci.2015.08.017.
[69] N.U. Deshpande, A.M. Gokhale, D.K. Denzer, J. Liu, Relationship between fracture toughness, fracture path, and microstructure of 7050 aluminum alloy: Part I. Quantitative characterization, Metall Mater Trans A 29 (1998) 1191–1201. https://doi.org/10.1007/s11661-998-0246-3.
[70] D. Dumont, A. Deschamps, Y. Brechet, A model for predicting fracture mode and toughness in 7000 series aluminium alloys, Acta Materialia 52 (2004) 2529–2540. https://doi.org/10.1016/j.actamat.2004.01.044.
[71] Y. Sun, D.R. Johnson, K.P. Trumble, Effect of Zr on recrystallization in a directionally solidified AA7050, Materials Science and Engineering: A 700 (2017) 358–365. https://doi.org/10.1016/j.msea.2017.06.026.
[72] F.J. Humphreys, M. Hatherly, Recrystallization and Related Annealing Phenomena, Elsevier, 2012.
[73] N. Ryum, Precipitation and recrystallization in an A1-0.5 WT.% Zr-alloy, Acta Metallurgica 17 (1969) 269–278. https://doi.org/10.1016/0001-6160(69)90067-4.

[74] E. Nes, Precipitation of the metastable cubic Al3Zr-phase in subperitectic Al-Zr alloys, Acta Metallurgica 20 (1972) 499–506. https://doi.org/10.1016/0001-6160(72)90005-3.
[75] R.D. Doherty, D.J. Srolovitz, A.D. Rollett, M.P. Anderson, On the volume fraction dependence of particle limited grain growth, Scripta Metallurgica 21 (1987) 675–679. https://doi.org/10.1016/0036-9748(87)90383-8.
[76] J.D. Robson, P.B. Prangnell, Dispersoid precipitation and process modelling in zirconium containing commercial aluminium alloys, Acta Materialia 49 (2001) 599–613. https://doi.org/10.1016/S1359-6454(00)00351-7.
[77] O. Engler, E. Sachot, J.C. Ehrström, A. Reeves, R. Shahani, Recrystallisation and texture in hot deformed aluminium alloy 7010 thick plates, Materials Science and Technology 12 (1996) 717–729. https://doi.org/10.1179/mst.1996.12.9.717.
[78] T. Wang, Z. Jin, J.-C. Zhao, Thermodynamic Assessment of the Al-Zr Binary System, Journal of Phase Equilibria 22 (2001) 544–551. https://doi.org/10.1361/105497101770332695.
[79] F. Xie, X. Yan, L. Ding, F. Zhang, S. Chen, M.G. Chu, Y.A. Chang, A study of microstructure and microsegregation of aluminum 7050 alloy, Materials Science and Engineering: A 355 (2003) 144–153. https://doi.org/10.1016/S0921-5093(03)00056-X.
[80] C. Guo, Z. Du, C. Li, B. Zhang, M. Tao, Thermodynamic description of the Al–Fe–Zr system, Calphad 32 (2008) 637–649. https://doi.org/10.1016/j.calphad.2008.08.007.
[81] P.B. Desch, R.B. Schwarz, P. Nash, Formation of metastable L12 phases in Al3Zr and Al-12.5%X-25%Zr (X ≡ Li, Cr, Fe, Ni, Cu), Journal of the Less Common Metals 168 (1991) 69–80. https://doi.org/10.1016/0022-5088(91)90035-3.
[82] C.C. Cheng, W.E. King, M.J. McNallan, Characterization and crystallization studies of melt-spun glassy Fe-22.5Al-10Zr Metal by analytical electron microscopy, Acta Metallurgica 37 (1989) 3399–3407. https://doi.org/10.1016/0001-6160(89)90212-5.
[83] Z. Jia, J. Friis, B. Forbord, J.K. Solberg, K. Marthinsen, The Effect of Alloying Elements on the Metastable Zr Solid Solubility and Precipitation of L12 Al3Zr Precipitates in Aluminium Alloys, (n.d.).
[84] F. B., H. H, M. K., J. Nie, A. Morton, B. Muddle (Eds.) Materials Forum, Insitute of Materials Engineering Australasia Ltd, Brisbane, Australia, (2004) 117–1185.
[85] N.A. Belov, A.N. Alabin, I.A. Matveeva, D.G. Eskin, Effect of Zr additions and annealing temperature on electrical conductivity and hardness of hot rolled Al sheets, Transactions of Nonferrous Metals Society of China 25 (2015) 2817–2826. https://doi.org/10.1016/S1003-6326(15)63907-3.
[86] F. Stein, G. Sauthoff, M. Palm, Phases and phase equilibria in the Fe–Al–Zr system, International Journal of Materials Research 95 (2004) 469–485. https://doi.org/10.1515/ijmr-2004-0096.
[87] H. Yoshida, Y. Baba, The Role of Zirconium to Improve Strength and Stress-corrosion Resistance of Al–Zn–Mg and Al–Zn–Mg–Cu Alloys, Transactions of the Japan Institute of Metals 23 (1982) 620–630. https://doi.org/10.2320/matertrans1960.23.620.
[88] O. Izumi, D. Oelschägel, On the decomposition of a highly supersaturated Al□Zr solid solution, Scripta Metallurgica 3 (1969) 619–621. https://doi.org/10.1016/0036-9748(69)90062-3.
[89] K.S. Vecchio, D.B. Williams, Convergent beam electron diffraction study of Al3Zr in Al-Zr AND Al-Li-Zr alloys, Acta Metallurgica 35 (1987) 2959–2970. https://doi.org/10.1016/0001-6160(87)90295-1.
[90] Y. Deng, Z. Yin, K. Zhao, J. Duan, Z. He, Effects of Sc and Zr microalloying additions on the microstructure and mechanical properties of new Al–Zn–Mg alloys, Journal of Alloys and Compounds 530 (2012) 71–80. https://doi.org/10.1016/j.jallcom.2012.03.108.

[91] J. Ye, R. Guan, H. Zhao, C. He, K. Xiong, Effect of Zr Microalloying on the Microstructures and Strengthening Mechanism of As-Cast Al-Fe-Zr Alloys, Materials 13 (2020) 4744. https://doi.org/10.3390/ma13214744.

[92] C. Pauzon, M. Buttard, A. Després, B. Chehab, J.-J. Blandin, G. Martin, A novel laser powder bed fusion Al-Fe-Zr alloy for superior strength-conductivity trade-off, Scripta Materialia 219 (2022) 114878. https://doi.org/10.1016/j.scriptamat.2022.114878.

[93] C-TEC, Constellium, Voreppe, France, (n.d.). https://www.constellium.com.

[94] J.H. Martin, B.D. Yahata, J.M. Hundley, J.A. Mayer, T.A. Schaedler, T.M. Pollock, 3D printing of high-strength aluminium alloys, Nature 549 (2017) 365–369. https://doi.org/10.1038/nature23894.

[95] A. Mehta, L. Zhou, T. Huynh, S. Park, H. Hyer, S. Song, Y. Bai, D.D. Imholte, N.E. Woolstenhulme, D.M. Wachs, Y. Sohn, Additive manufacturing and mechanical properties of the dense and crack free Zr-modified aluminum alloy 6061 fabricated by the laser-powder bed fusion, Additive Manufacturing 41 (2021) 101966. https://doi.org/10.1016/j.addma.2021.101966.

[96] M. Opprecht, J.-P. Garandet, G. Roux, C. Flament, M. Soulier, A solution to the hot cracking problem for aluminium alloys manufactured by laser beam melting, Acta Materialia 197 (2020) 40–53. https://doi.org/10.1016/j.actamat.2020.07.015.

[97] L. Zhou, H. Hyer, S. Park, H. Pan, Y. Bai, K.P. Rice, Y. Sohn, Microstructure and mechanical properties of Zr-modified aluminum alloy 5083 manufactured by laser powder bed fusion, Additive Manufacturing 28 (2019) 485–496. https://doi.org/10.1016/j.addma.2019.05.027.

[98] N. Kaufmann, M. Imran, T.M. Wischeropp, C. Emmelmann, S. Siddique, F. Walther, Influence of Process Parameters on the Quality of Aluminium Alloy EN AW 7075 Using Selective Laser Melting (SLM), Physics Procedia 83 (2016) 918–926. https://doi.org/10.1016/j.phpro.2016.08.096.

[99] S.Z. Uddin, D. Espalin, J. Mireles, P. Morton, C. Terrazas, S. Collins, L.E. Murr, R. Wicker, Laser Powder Bed Fusion Fabricated and Characterization of Crack-Free Aluminum Alloy 6061 Using In-Process Powder Bed Induction Heating, (2017). https://hdl.handle.net/2152/89814 (accessed January 18, 2025).

[100] C. Pauzon, M. Buttard, A. Després, F. Charlot, M. Fivel, B. Chehab, J.-J. Blandin, G. Martin, Direct ageing of LPBF Al-1Fe-1Zr for high conductivity and mechanical performance, Acta Materialia 258 (2023) 119199. https://doi.org/10.1016/j.actamat.2023.119199.

[101] T.-S. Liu, P. Chen, F. Qiu, H.-Y. Yang, N.T.Y. Jin, Y. Chew, D. Wang, R. Li, Q.-C. Jiang, C. Tan, Review on laser directed energy deposited aluminum alloys, Int. J. Extrem. Manuf. 6 (2024) 022004. https://doi.org/10.1088/2631-7990/ad16bb.

[102] J. Su, F. Jiang, J. Teng, L. Chen, M. Yan, G. Requena, L.-C. Zhang, Y.M. Wang, I.V. Okulov, H. Zhu, C. Tan, Recent innovations in laser additive manufacturing of titanium alloys, Int. J. Extrem. Manuf. 6 (2024) 032001. https://doi.org/10.1088/2631-7990/ad2545.

[103] S.R. Narasimharaju, W. Zeng, T.L. See, Z. Zhu, P. Scott, X. Jiang, S. Lou, A comprehensive review on laser powder bed fusion of steels: Processing, microstructure, defects and control methods, mechanical properties, current challenges and future trends, Journal of Manufacturing Processes 75 (2022) 375–414. https://doi.org/10.1016/j.jmapro.2021.12.033.

[104] M.-S. Pham, B. Dovgyy, P.A. Hooper, C.M. Gourlay, A. Piglione, The role of side-branching in microstructure development in laser powder-bed fusion, Nat Commun 11 (2020) 749. https://doi.org/10.1038/s41467-020-14453-3.

[105] A. Sonawane, G. Roux, J.-J. Blandin, A. Despres, G. Martin, Cracking mechanism and its sensitivity to processing conditions during laser powder bed fusion of a structural aluminum alloy, Materialia 15 (2021) 100976. https://doi.org/10.1016/j.mtla.2020.100976.
[106] N. Raghavan, R. Dehoff, S. Pannala, S. Simunovic, M. Kirka, J. Turner, N. Carlson, S.S. Babu, Numerical modeling of heat-transfer and the influence of process parameters on tailoring the grain morphology of IN718 in electron beam additive manufacturing, Acta Materialia 112 (2016) 303–314. https://doi.org/10.1016/j.actamat.2016.03.063.
[107] J. Yin, D. Wang, L. Yang, H. Wei, P. Dong, L. Ke, G. Wang, H. Zhu, X. Zeng, Correlation between forming quality and spatter dynamics in laser powder bed fusion, Additive Manufacturing 31 (2020) 100958. https://doi.org/10.1016/j.addma.2019.100958.
[108] L. Guo, H. Liu, H. Wang, Q. Wei, Y. Xiao, Z. Tang, Y. Wu, H. Wang, Identifying the keyhole stability and pore formation mechanisms in laser powder bed fusion additive manufacturing, Journal of Materials Processing Technology 321 (2023) 118153. https://doi.org/10.1016/j.jmatprotec.2023.118153.
[109] D. Guo, R. Lambert-Garcia, S. Hocine, X. Fan, H. Greenhalgh, R. Shahani, M. Majkut, A. Rack, P.D. Lee, C.L.A. Leung, Correlative spatter and vapour depression dynamics during laser powder bed fusion of an Al-Fe-Zr alloy, Int. J. Extrem. Manuf. 6 (2024) 055601. https://doi.org/10.1088/2631-7990/ad4e1d.
[110] Y. Chen, S.J. Clark, C.L.A. Leung, L. Sinclair, S. Marussi, M.P. Olbinado, E. Boller, A. Rack, I. Todd, P.D. Lee, In-situ Synchrotron imaging of keyhole mode multi-layer laser powder bed fusion additive manufacturing, Applied Materials Today 20 (2020) 100650. https://doi.org/10.1016/j.apmt.2020.100650.
[111] Y. Huang, T.G. Fleming, S.J. Clark, S. Marussi, K. Fezzaa, J. Thiyagalingam, C.L.A. Leung, P.D. Lee, Keyhole fluctuation and pore formation mechanisms during laser powder bed fusion additive manufacturing, Nat Commun 13 (2022) 1170. https://doi.org/10.1038/s41467-022-28694-x.
[112] D.T. Rees, C.L.A. Leung, J. Elambasseril, S. Marussi, S. Shah, S. Marathe, M. Brandt, M. Easton, P.D. Lee, *In situ* X-ray imaging of hot cracking and porosity during LPBF of Al-2139 with TiB2 additions and varied process parameters, Materials & Design 231 (2023) 112031. https://doi.org/10.1016/j.matdes.2023.112031.
[113] T. Weitkamp, P. Tafforeau, E. Boller, P. Cloetens, J. Valade, P. Bernard, F. Peyrin, W. Ludwig, L. Helfen, J. Baruchel, Status and evolution of the ESRF beamline ID19, AIP Conference Proceedings 1221 (2010) 33–38. https://doi.org/10.1063/1.3399253.
[114] L.M. Klamann, Materialuntersuchungen einer für LPBF optimierten Al-Fe-Zr Legierung im Hinblick auf die Etablierung von Prozessparametern für spezifische Anwendungsfälle, masters, Hochschule Bonn-Rhein-Sieg (HBRS), 2023. https://elib.dlr.de/198785/ (accessed February 6, 2025).
[115] X-Ray Fluorescence - an overview | ScienceDirect Topics, (n.d.). https://www.sciencedirect.com/topics/engineering/x-ray-fluorescence (accessed January 20, 2025).
[116] L.-M. Peng, Electron atomic scattering factors and scattering potentials of crystals, Micron 30 (1999) 625–648. https://doi.org/10.1016/S0968-4328(99)00033-5.
[117] A. Guinier, P. Lorrain, D.S.-M. Lorrain, X-RAY DIFFRACTION IN CRYSTALS, IMPERFECT CRYSTALS, AND AMORPHOUS BODIES, Dover publications, New York NY, 1963.
[118] P. Cloetens, W. Ludwig, E. Boller, L. Helfen, L. Salvo, R. Mache, M. Schlenker, Quantitative phase contrast tomography using coherent synchrotron radiation, in: U. Bonse (Ed.), San Diego, CA, USA, 2002: p. 82. https://doi.org/10.1117/12.452867.

[119] M. Stockmar, P. Cloetens, I. Zanette, B. Enders, M. Dierolf, F. Pfeiffer, P. Thibault, Near-field ptychography: phase retrieval for inline holography using a structured illumination, Sci Rep 3 (2013) 1927. https://doi.org/10.1038/srep01927.

[120] M.W. Vannier, Image Reconstruction from Projections, The Fundamentals of Computerized Tomography: G. T. Herman. New York, Academic Press, 1980, 316 pp, $29.50, Journal of Nuclear Medicine 23 (1982) 368–369.

[121] P. Kirkpatrick, A.V. Baez, Formation of Optical Images by X-Rays, J. Opt. Soc. Am., JOSA 38 (1948) 766–774. https://doi.org/10.1364/JOSA.38.000766.

[122] C. Morawe, R. Barrett, P. Cloetens, B. Lantelme, J.-C. Peffen, A. Vivo, Graded multilayers for figured Kirkpatrick-Baez mirrors on the new ESRF end station ID16A, in: Advances in X-Ray/EUV Optics and Components X, SPIE, 2015: pp. 8–14. https://doi.org/10.1117/12.2189279.

[123] F. Villar, L. Andre, R. Baker, S. Bohic, J.C. da Silva, C. Guilloud, O. Hignette, J. Meyer, A. Pacureanu, M. Perez, M. Salome, P. van der Linden, Y. Yang, P. Cloetens, Nanopositioning for the ESRF ID16A Nano-Imaging Beamline, Synchrotron Radiation News 31 (2018) 9–14. https://doi.org/10.1080/08940886.2018.1506234.

[124] P. Cloetens, W. Ludwig, J. Baruchel, D. Van Dyck, J. Van Landuyt, J.P. Guigay, M. Schlenker, Holotomography: Quantitative phase tomography with micrometer resolution using hard synchrotron radiation x rays, Applied Physics Letters 75 (1999) 2912–2914. https://doi.org/10.1063/1.125225.

[125] M. Stockmar, M. Hubert, M. Dierolf, B. Enders, R. Clare, S. Allner, A. Fehringer, I. Zanette, J. Villanova, J. Laurencin, P. Cloetens, F. Pfeiffer, P. Thibault, X-ray nanotomography using near-field ptychography, Opt. Express, OE 23 (2015) 12720–12731. https://doi.org/10.1364/OE.23.012720.

[126] S. Ünsal, R. Girod, C. Appel, D. Karpov, M. Mermoux, F. Maillard, V.A. Saveleva, V. Tileli, T.J. Schmidt, J. Herranz, Decoupling the Contributions of Different Instability Mechanisms to the PEMFC Performance Decay of Non-noble Metal O2-Reduction Catalysts, J. Am. Chem. Soc. 145 (2023) 7845–7858. https://doi.org/10.1021/jacs.2c12751.

[127] R. Mokso, P. Cloetens, E. Maire, W. Ludwig, J.-Y. Buffière, Nanoscale zoom tomography with hard x rays using Kirkpatrick-Baez optics, Applied Physics Letters 90 (2007) 144104. https://doi.org/10.1063/1.2719653.

[128] M. Hubert, A. Pacureanu, C. Guilloud, Y. Yang, J.C. da Silva, J. Laurencin, F. Lefebvre-Joud, P. Cloetens, Efficient correction of wavefront inhomogeneities in X-ray holographic nanotomography by random sample displacement, Applied Physics Letters 112 (2018) 203704. https://doi.org/10.1063/1.5026462.

[129] D. Paganin, S. Mayo, T. Gureyev, P. Miller, S. Wilkins, Simultaneous phase and amplitude extraction from a single defocused image of a homogenous object, Journal of Microscopy 206 (2002) 33–40. https://doi.org/10.1046/j.1365-2818.2002.01010.x.

[130] P. Paleo, J. Lesaint, H. Payno, alessandro mirone, N. Vigano, C. Nemoz, Nabu 2024.1, (2024). https://doi.org/10.5281/zenodo.11104029.

[131] A. Mirone, E. Brun, E. Gouillart, P. Tafforeau, J. Kieffer, The PyHST2 hybrid distributed code for high speed tomographic reconstruction with iterative reconstruction and a priori knowledge capabilities, Nuclear Instruments and Methods in Physics Research Section B: Beam Interactions with Materials and Atoms 324 (2014) 41–48. https://doi.org/10.1016/j.nimb.2013.09.030.

[132] A. Diaz, P. Trtik, M. Guizar-Sicairos, A. Menzel, P. Thibault, O. Bunk, Quantitative x-ray phase nanotomography, Phys. Rev. B 85 (2012) 020104. https://doi.org/10.1103/PhysRevB.85.020104.

[133] V. Favre-Nicolin, G. Girard, S. Leake, J. Carnis, Y. Chushkin, J. Kieffer, P. Paleo, M.-I. Richard, PyNX: high performance computing toolkit for coherent X-ray imaging based on operators, 2020.
[134] S. Marchesini, A. Schirotzek, C. Yang, H. Wu, F. Maia, Augmented projections for ptychographic imaging, Inverse Problems 29 (2013) 115009. https://doi.org/10.1088/0266-5611/29/11/115009.
[135] P. Thibault, M. Guizar-Sicairos, Maximum-likelihood refinement for coherent diffractive imaging, New J. Phys. 14 (2012) 063004. https://doi.org/10.1088/1367-2630/14/6/063004.
[136] M. Guizar-Sicairos, A. Diaz, M. Holler, M.S. Lucas, A. Menzel, R.A. Wepf, O. Bunk, Phase tomography from x-ray coherent diffractive imaging projections, Opt Express 19 (2011) 21345–21357. https://doi.org/10.1364/OE.19.021345.
[137] I. Hafizh, G. Bellotti, M. Carminati, G. Utica, M. Gugiatti, A. Balerna, V. Tullio, G. Borghi, A. Picciotto, F. Ficorella, N. Zorzi, A. Capsoni, S. Coelli, L. Bombelli, C. Fiorini, ARDESIA: A fast silicon drift detector X-ray spectrometer for synchrotron applications, X-Ray Spectrometry 48 (2019). https://doi.org/10.1002/xrs.3017.
[138] V.A. Solé, E. Papillon, M. Cotte, Ph. Walter, J. Susini, A multiplatform code for the analysis of energy-dispersive X-ray fluorescence spectra, Spectrochimica Acta Part B: Atomic Spectroscopy 62 (2007) 63–68. https://doi.org/10.1016/j.sab.2006.12.002.
[139] M. Guizar-Sicairos, J.J. Boon, K. Mader, A. Diaz, A. Menzel, O. Bunk, Quantitative interior x-ray nanotomography by a hybrid imaging technique, Optica, OPTICA 2 (2015) 259–266. https://doi.org/10.1364/OPTICA.2.000259.
[140] J.C. da Silva, J. Haubrich, G. Requena, M. Hubert, A. Pacureanu, L. Bloch, Y. Yang, P. Cloetens, High energy near- and far-field ptychographic tomography at the ESRF, in: Developments in X-Ray Tomography XI, SPIE, 2017: pp. 39–45. https://doi.org/10.1117/12.2272971.
[141] L.A. Shepp, Y. Vardi, Maximum likelihood reconstruction for emission tomography, IEEE Trans Med Imaging 1 (1982) 113–122. https://doi.org/10.1109/TMI.1982.4307558.
[142] W. Van Aarle, W.J. Palenstijn, J. Cant, E. Janssens, F. Bleichrodt, A. Dabravolski, J. De Beenhouwer, K. Joost Batenburg, J. Sijbers, Fast and flexible X-ray tomography using the ASTRA toolbox, Opt. Express 24 (2016) 25129. https://doi.org/10.1364/OE.24.025129.
[143] V. Elser, I. Rankenburg, P. Thibault, Searching with iterated maps, Proceedings of the National Academy of Sciences 104 (2007) 418–423. https://doi.org/10.1073/pnas.0606359104.
[144] M. Boin, A. Haibel, Compensation of ring artefacts in synchrotron tomographic images, Opt. Express, OE 14 (2006) 12071–12075. https://doi.org/10.1364/OE.14.012071.
[145] F.P. Vidal, J.M. Létang, G. Peix, P. Cloetens, Investigation of artefact sources in synchrotron microtomography via virtual X-ray imaging, Nuclear Instruments and Methods in Physics Research Section B: Beam Interactions with Materials and Atoms 234 (2005) 333–348. https://doi.org/10.1016/j.nimb.2005.02.003.
[146] R.A. Ketcham, W.D. Carlson, Acquisition, optimization and interpretation of X-ray computed tomographic imagery: applications to the geosciences, Computers & Geosciences 27 (2001) 381–400. https://doi.org/10.1016/S0098-3004(00)00116-3.
[147] M. Hubert, A. Pacureanu, C. Guilloud, Y. Yang, J.C. da Silva, J. Laurencin, F. Lefebvre-Joud, P. Cloetens, Efficient correction of wavefront inhomogeneities in X-ray holographic nanotomography by random sample displacement, Applied Physics Letters 112 (2018) 203704. https://doi.org/10.1063/1.5026462.
[148] V. Vanpeene, J. Villanova, J.-P. Suuronen, A. King, A. Bonnin, J. Adrien, E. Maire, L. Roué, Monitoring the morphological changes of Si-based electrodes by X-ray computed

tomography: A 4D-multiscale approach, Nano Energy 74 (2020) 104848. https://doi.org/10.1016/j.nanoen.2020.104848.
[149] M. Welvaert, Y. Rosseel, On the Definition of Signal-To-Noise Ratio and Contrast-To-Noise Ratio for fMRI Data, PLOS ONE 8 (2013) e77089. https://doi.org/10.1371/journal.pone.0077089.
[150] S. Hocine, S. Van Petegem, U. Frommherz, G. Tinti, N. Casati, D. Grolimund, H. Van Swygenhoven, A miniaturized selective laser melting device for *operando* X-ray diffraction studies, Additive Manufacturing 34 (2020) 101194. https://doi.org/10.1016/j.addma.2020.101194.
[151] C.A. Schneider, W.S. Rasband, K.W. Eliceiri, NIH Image to ImageJ: 25 years of image analysis, Nat Methods 9 (2012) 671–675. https://doi.org/10.1038/nmeth.2089.
[152] F. Monaco, M. Hubert, J.C. Da Silva, V. Favre-Nicolin, D. Montinaro, P. Cloetens, J. Laurencin, A comparison between holographic and near-field ptychographic X-ray tomography for solid oxide cell materials, Materials Characterization 187 (2022) 111834. https://doi.org/10.1016/j.matchar.2022.111834.
[153] L. Lilensten, B. Gault, New approach for FIB-preparation of atom probe specimens for aluminum alloys, PLoS ONE 15 (2020) e0231179. https://doi.org/10.1371/journal.pone.0231179.
[154] M. Stockmar, P. Cloetens, I. Zanette, B. Enders, M. Dierolf, F. Pfeiffer, P. Thibault, Near-field ptychography: phase retrieval for inline holography using a structured illumination, Sci Rep 3 (2013) 1927. https://doi.org/10.1038/srep01927.
[155] M. Stockmar, M. Hubert, M. Dierolf, B. Enders, R. Clare, S. Allner, A. Fehringer, I. Zanette, J. Villanova, J. Laurencin, P. Cloetens, F. Pfeiffer, P. Thibault, X-ray nanotomography using near-field ptychography, Opt. Express, OE 23 (2015) 12720–12731. https://doi.org/10.1364/OE.23.012720.
[156] Xlib, ImageJ Wiki (n.d.). https://imagej.github.io/plugins/xlib/index (accessed July 2, 2024).
[157] B. Münch, P. Trtik, F. Marone, M. Stampanoni, Stripe and ring artifact removal with combined wavelet — Fourier filtering, Opt. Express, OE 17 (2009) 8567–8591. https://doi.org/10.1364/OE.17.008567.
[158] X. Li, G. Li, M.-X. Zhang, Q. Zhu, Novel approach to additively manufacture high-strength Al alloys by laser powder bed fusion through addition of hybrid grain refiners, Additive Manufacturing 48 (2021) 102400. https://doi.org/10.1016/j.addma.2021.102400.
[159] S. Bahl, K. Sisco, Y. Yang, F. Theska, S. Primig, L.F. Allard, R.A. Michi, C. Fancher, B. Stump, R. Dehoff, A. Shyam, A. Plotkowski, Al-Cu-Ce(-Zr) alloys with an exceptional combination of additive processability and mechanical properties, Additive Manufacturing 48 (2021) 102404. https://doi.org/10.1016/j.addma.2021.102404.
[160] X. Zhang, B. Mao, L. Mushongera, J. Kundin, Y. Liao, Laser powder bed fusion of titanium aluminides: An investigation on site-specific microstructure evolution mechanism, Materials & Design 201 (2021) 109501. https://doi.org/10.1016/j.matdes.2021.109501.
[161] P. Van Cauwenbergh, V. Samaee, L. Thijs, J. Nejezchlebová, P. Sedlák, A. Iveković, D. Schryvers, B. Van Hooreweder, K. Vanmeensel, Unravelling the multi-scale structure–property relationship of laser powder bed fusion processed and heat-treated AlSi10Mg, Sci Rep 11 (2021) 6423. https://doi.org/10.1038/s41598-021-85047-2.
[162] S. Griffiths, J.R. Croteau, M.D. Rossell, R. Erni, A. De Luca, N.Q. Vo, D.C. Dunand, C. Leinenbach, Coarsening- and creep resistance of precipitation-strengthened Al–Mg–Zr alloys processed by selective laser melting, Acta Materialia 188 (2020) 192–202. https://doi.org/10.1016/j.actamat.2020.02.008.

[163] G. Gautam, A. Mohan, Effect of ZrB2 particles on the microstructure and mechanical properties of hybrid (ZrB2 + Al3Zr)/AA5052 *insitu* composites, Journal of Alloys and Compounds 649 (2015) 174–183. https://doi.org/10.1016/j.jallcom.2015.07.096.
[164] Al3Zr (ZrAl3 m) Crystal Structure - SpringerMaterials, (n.d.). https://materials.springer.com/isp/crystallographic/docs/sd_0261041 (accessed February 21, 2025).
[165] W. Zhang, K. Xu, W. Long, X. Zhou, Microstructure and Compressive Properties of Porous 2024Al-Al3Zr Composites, Metals 12 (2022) 2017. https://doi.org/10.3390/met12122017.
[166] P. (Pierre) Villars, Pearson's handbook : crystallographic data for intermetallic phases, Desk ed, ASM International, 1997. https://cir.nii.ac.jp/crid/1130282269714282880 (accessed February 21, 2025).
[167] Al13Fe4 (Fe4Al13) Crystal Structure - SpringerMaterials, (n.d.). https://materials.springer.com/isp/crystallographic/docs/sd_1930868 (accessed February 21, 2025).
[168] J. Gu, S. Gu, L. Xue, S. Wu, Y. Yan, Microstructure and mechanical properties of in-situ Al13Fe4/Al composites prepared by mechanical alloying and spark plasma sintering, Materials Science and Engineering: A 558 (2012) 684–691. https://doi.org/10.1016/j.msea.2012.08.076.
[169] S. Bergmueller, L. Gerhold, L. Fuchs, L. Kaserer, G. Leichtfried, Systematic approach to process parameter optimization for laser powder bed fusion of low-alloy steel based on melting modes, Int J Adv Manuf Technol 126 (2023) 4385–4398. https://doi.org/10.1007/s00170-023-11377-2.
[170] A. Khaimovich, A. Balyakin, M. Oleynik, A. Meshkov, V. Smelov, Optimization of Process Parameters for Powder Bed Fusion Additive Manufacturing Using a Linear Programming Method: A Conceptual Framework, Metals 12 (2022) 1976. https://doi.org/10.3390/met12111976.
[171] K. Kosiba, T. Gustmann, J.T. Kim, J. Seok, J. Jung, L. Beyer, S. Scudino, L. Giebeler, J. Han, J.K. Hufenbach, Experimental cooling rates during high-power laser powder bed fusion at varying processing conditions, Journal of Alloys and Compounds 967 (2023) 171773. https://doi.org/10.1016/j.jallcom.2023.171773.
[172] P.A. Hooper, Melt pool temperature and cooling rates in laser powder bed fusion, Additive Manufacturing 22 (2018) 548–559. https://doi.org/10.1016/j.addma.2018.05.032.
[173] J. Liu, P. Wen, Metal vaporization and its influence during laser powder bed fusion process, Materials & Design 215 (2022) 110505. https://doi.org/10.1016/j.matdes.2022.110505.
[174] L. Deillon, F. Jensch, F. Palm, M. Bambach, A new high strength Al–Mg–Sc alloy for laser powder bed fusion with calcium addition to effectively prevent magnesium evaporation, Journal of Materials Processing Technology 300 (2022) 117416. https://doi.org/10.1016/j.jmatprotec.2021.117416.
[175] Y. Zhou, J. Wang, Y. Yang, M. Yang, H. Zheng, D. Xie, D. Wang, L. Shen, Laser Additive Manufacturing of Zinc Targeting for Biomedical Application, Int J Bioprint 8 (2022) 501. https://doi.org/10.18063/ijb.v8i1.501.
[176] R. Mertens, L. Baert, K. Vanmeensel, B. Van Hooreweder, Laser powder bed fusion of high strength aluminum, Material Design & Processing Communications 3 (2021) e161. https://doi.org/10.1002/mdp2.161.
[177] N.T. Aboulkhair, I. Maskery, C. Tuck, I. Ashcroft, N.M. Everitt, On the formation of AlSi10Mg single tracks and layers in selective laser melting: Microstructure and nano-mechanical properties, Journal of Materials Processing Technology 230 (2016) 88–98. https://doi.org/10.1016/j.jmatprotec.2015.11.016.

[178] A. Aversa, M. Moshiri, E. Librera, M. Hadi, G. Marchese, D. Manfredi, M. Lorusso, F. Calignano, S. Biamino, M. Lombardi, M. Pavese, Single scan track analyses on aluminium based powders, Journal of Materials Processing Technology 255 (2018) 17–25. https://doi.org/10.1016/j.jmatprotec.2017.11.055.

[179] J. Patalas-Maliszewska, E. Feldshtein, O. Devojno, M. Śliwa, M. Kardapolava, N. Lutsko, Single Tracks as a Key Factor in Additive Manufacturing Technology—Analysis of Research Trends and Metal Deposition Behavior, Materials 13 (2020). https://doi.org/10.3390/ma13051115.

[180] Y. Guo, L. Jia, B. Kong, N. Wang, H. Zhang, Single track and single layer formation in selective laser melting of niobium solid solution alloy, Chinese Journal of Aeronautics 31 (2018) 860–866. https://doi.org/10.1016/j.cja.2017.08.019.

[181] K. Kempen, L. Thijs, J. Van Humbeeck, J.-P. Kruth, Processing AlSi10Mg by selective laser melting: Parameter optimisation and material characterisation, Materials Science and Technology 31 (2015) 917–923. https://doi.org/10.1179/1743284714Y.0000000702.

[182] R. Li, J. Liu, Y. Shi, L. Wang, W. Jiang, Balling behavior of stainless steel and nickel powder during selective laser melting process, Int J Adv Manuf Technol 59 (2012) 1025–1035. https://doi.org/10.1007/s00170-011-3566-1.

[183] K. Darvish, Z.W. Chen, T. Pasang, Reducing lack of fusion during selective laser melting of CoCrMo alloy: Effect of laser power on geometrical features of tracks, Materials & Design 112 (2016) 357–366. https://doi.org/10.1016/j.matdes.2016.09.086.

[184] D. Dai, D. Gu, Tailoring surface quality through mass and momentum transfer modeling using a volume of fluid method in selective laser melting of TiC/AlSi10Mg powder, International Journal of Machine Tools and Manufacture 88 (2015) 95–107. https://doi.org/10.1016/j.ijmachtools.2014.09.010.

[185] L. Wang, Q. Lu, S. Luo, W. Zhan, R. Chen, B. Lou, D. Xu, Effect of dietary lipid on growth performance, body composition, plasma biochemical parameters and liver fatty acids content of juvenile yellow drum *Nibea albiflora*, Aquaculture Reports 4 (2016) 10–16. https://doi.org/10.1016/j.aqrep.2016.05.002.

[186] B09 Committee, Test Methods for Flow Rate of Metal Powders Using the Carney Funnel, (n.d.). https://doi.org/10.1520/B0964-23.

[187] Laser-based puller, for use with glass LESS than 0.6 mm OD, (n.d.). https://www.wpiinc.com/su-p2000f-laser-based-puller-for-use-with-glass-less-than-0-6-mm-od.html (accessed April 10, 2025).

[188] S. Bolte, F.P. Cordelières, A guided tour into subcellular colocalization analysis in light microscopy, Journal of Microscopy 224 (2006) 213–232. https://doi.org/10.1111/j.1365-2818.2006.01706.x.

[189] V. Coen, L. Goossens, B.V. Hooreweder, Methodology and experimental validation of analytical melt pool models for laser powder bed fusion, Journal of Materials Processing Technology 304 (2022) 117547. https://doi.org/10.1016/j.jmatprotec.2022.117547.

[190] A.V. Gusarov, I. Yadroitsev, Ph. Bertrand, I. Smurov, Heat transfer modelling and stability analysis of selective laser melting, Applied Surface Science 254 (2007) 975–979. https://doi.org/10.1016/j.apsusc.2007.08.074.

[191] S.A. Khairallah, A.T. Anderson, A. Rubenchik, W.E. King, Laser powder-bed fusion additive manufacturing: Physics of complex melt flow and formation mechanisms of pores, spatter, and denudation zones, Acta Materialia 108 (2016) 36–45. https://doi.org/10.1016/j.actamat.2016.02.014.

[192] C.L.A. Leung, S. Marussi, R.C. Atwood, M. Towrie, P.J. Withers, P.D. Lee, In situ X-ray imaging of defect and molten pool dynamics in laser additive manufacturing, Nat Commun 9 (2018) 1355. https://doi.org/10.1038/s41467-018-03734-7.

[193] A.V. Gusarov, I. Yadroitsev, Ph. Bertrand, I. Smurov, Heat transfer modelling and stability analysis of selective laser melting, Applied Surface Science 254 (2007) 975–979. https://doi.org/10.1016/j.apsusc.2007.08.074.

[194] Y.J. Liu, S.J. Li, H.L. Wang, W.T. Hou, Y.L. Hao, R. Yang, T.B. Sercombe, L.C. Zhang, Microstructure, defects and mechanical behavior of beta-type titanium porous structures manufactured by electron beam melting and selective laser melting, Acta Materialia 113 (2016) 56–67. https://doi.org/10.1016/j.actamat.2016.04.029.

[195] C.A. Biffi, J. Fiocchi, P. Bassani, A. Tuissi, Continuous wave vs pulsed wave laser emission in selective laser melting of AlSi10Mg parts with industrial optimized process parameters: Microstructure and mechanical behaviour, Additive Manufacturing 24 (2018) 639–646. https://doi.org/10.1016/j.addma.2018.10.021.

[196] G.A. Ravi, C. Qiu, M.M. Attallah, Microstructural control in a Ti-based alloy by changing laser processing mode and power during direct laser deposition, Materials Letters 179 (2016) 104–108. https://doi.org/10.1016/j.matlet.2016.05.038.

[197] J.D. Roehling, S.A. Khairallah, Y. Shen, A. Bayramian, C.D. Boley, A.M. Rubenchik, J. DeMuth, N. Duanmu, M.J. Matthews, Physics of large-area pulsed laser powder bed fusion, Additive Manufacturing 46 (2021) 102186. https://doi.org/10.1016/j.addma.2021.102186.

[198] F.L. Vecchiato, H. de Winton, P.A. Hooper, M.R. Wenman, Melt pool microstructure and morphology from single exposures in laser powder bed fusion of 316L stainless steel, Additive Manufacturing 36 (2020) 101401. https://doi.org/10.1016/j.addma.2020.101401.

[199] M. Garibaldi, I. Ashcroft, M. Simonelli, R. Hague, Metallurgy of high-silicon steel parts produced using Selective Laser Melting, Acta Materialia 110 (2016) 207–216. https://doi.org/10.1016/j.actamat.2016.03.037.

[200] Y. Wu, T. Zhang, C. Chen, S.R.E. Hosseini, X. Zhang, K. Zhou, Microstructure and mechanical property evolution of additive manufactured eutectic Al-2Fe alloy during solidification and aging, Journal of Alloys and Compounds 897 (2022) 163243. https://doi.org/10.1016/j.jallcom.2021.163243.

[201] V. Raghavan, Al-Fe-Zr (Aluminum-Iron-Zirconium), J. Phase Equilib. Diffus. 31 (2010) 459–462. https://doi.org/10.1007/s11669-010-9746-0.

[202] D. Liang, H. Jones, The effect of growth velocity on growth temperature of the Al-Al3Fe and Al-Al6Fe eutectics, Zeitschrift Fur Metallkunde (1992). https://www.semanticscholar.org/paper/The-effect-of-growth-velocity-on-growth-temperature-Liang-Jones/06b26dee7deb5370996f5d34bd2106b540609211 (accessed January 31, 2025).

[203] R.M.K. Young, T.W. Clyne, An Al□Fe intermetallic phase formed during controlled solidification, Scripta Metallurgica 15 (1981) 1211–1216. https://doi.org/10.1016/0036-9748(81)90301-X.

[204] J. Arbeiter, M. Vončina, B. Šetina Batič, J. Medved, Transformation of the Metastable Al6Fe Intermetallic Phase during Homogenization of a Binary Al-Fe Alloy, Materials (Basel) 14 (2021) 7208. https://doi.org/10.3390/ma14237208.

[205] D. Miao, H. Jiang, X. Cai, Z. Wang, J. Zhou, F. Xue, Influence of Cooling Rate on the Segregation and Precipitation of Al-4.5zn-2.5mg-1.5cu-0.6zr Alloy Prepared by Directional Solidification, (2023). https://doi.org/10.2139/ssrn.4570627.

[206] J. Fiocchi, A. Tuissi, C.A. Biffi, Heat treatment of aluminium alloys produced by laser powder bed fusion: A review, Materials & Design 204 (2021) 109651. https://doi.org/10.1016/j.matdes.2021.109651.

[207] K. Bartkowiak, S. Ullrich, T. Frick, M. Schmidt, New Developments of Laser Processing Aluminium Alloys via Additive Manufacturing Technique, Physics Procedia 12 (2011) 393–401. https://doi.org/10.1016/j.phpro.2011.03.050.

[208] Revisiting fundamental welding concepts to improve additive manufacturing: From theory to practice - ScienceDirect, (n.d.). https://www.sciencedirect.com/science/article/pii/S0079642519300726 (accessed October 25, 2024).
[209] X. Qi, N. Takata, A. Suzuki, M. Kobashi, M. Kato, Controllable tensile performance of additively manufactured Al–Fe alloy, Materials Science and Engineering: A 855 (2022) 143893. https://doi.org/10.1016/j.msea.2022.143893.
[210] W. Wang, N. Takata, A. Suzuki, M. Kobashi, M. Kato, Formation of multiple intermetallic phases in a hypereutectic Al–Fe binary alloy additively manufactured by laser powder bed fusion, Intermetallics 125 (2020) 106892. https://doi.org/10.1016/j.intermet.2020.106892.
[211] Y. Zhao, Y. Koizumi, K. Aoyagi, D. Wei, K. Yamanaka, A. Chiba, Molten pool behavior and effect of fluid flow on solidification conditions in selective electron beam melting (SEBM) of a biomedical Co-Cr-Mo alloy, Additive Manufacturing 26 (2019) 202–214. https://doi.org/10.1016/j.addma.2018.12.002.
[212] Grain structure evolution in Inconel 718 during selective electron beam melting - ScienceDirect, (n.d.). https://www.sciencedirect.com/science/article/pii/S0921509316305536 (accessed February 3, 2025).
[213] M.E. Glicksman, Principles of Solidification: An Introduction to Modern Casting and Crystal Growth Concepts, Springer Science & Business Media, 2010.
[214] H. Qu, W.D. Liu, Study on the Stability and Phase Transition of Precipitated Phases Al6Fe and Al3Fe in Al-Fe Alloy, Advanced Materials Research 306–307 (2011) 438–442. https://doi.org/10.4028/www.scientific.net/AMR.306-307.438.
[215] S. Pan, C. Li, F. Qian, L. Hao, Y. Li, Diffusion controlled early-stage L12-D023 transitions within Al3Zr, Scripta Materialia 231 (2023) 115460. https://doi.org/10.1016/j.scriptamat.2023.115460.
[216] V. Nikitin, M. Carlsson, D. Gürsoy, R. Mokso, P. Cloetens, X-ray nano-holotomography reconstruction with simultaneous probe retrieval, Opt. Express, OE 32 (2024) 41905–41924. https://doi.org/10.1364/OE.537341.